



Incoherent Broadband Cavity-Enhanced Absorption Spectroscopy for NO₃ Radical and Aerosol Measurements: Application to Field and Chamber Studies

Lingshuo Meng

► To cite this version:

Lingshuo Meng. Incoherent Broadband Cavity-Enhanced Absorption Spectroscopy for NO₃ Radical and Aerosol Measurements: Application to Field and Chamber Studies. Earth Sciences. Université du Littoral Côte d'Opale, 2020. English. NNT : 2020DUNK0576 . tel-03399390

HAL Id: tel-03399390

<https://theses.hal.science/tel-03399390>

Submitted on 24 Oct 2021

HAL is a multi-disciplinary open access archive for the deposit and dissemination of scientific research documents, whether they are published or not. The documents may come from teaching and research institutions in France or abroad, or from public or private research centers.

L'archive ouverte pluridisciplinaire **HAL**, est destinée au dépôt et à la diffusion de documents scientifiques de niveau recherche, publiés ou non, émanant des établissements d'enseignement et de recherche français ou étrangers, des laboratoires publics ou privés.

N° d'ordre



Thèse de Doctorat

Discipline : Sciences de la Terre et de l'Univers, Espace

Spécialité : Terre, Enveloppes Fluides

présentée à *l'Ecole Doctorale SMRE 104 (Lille, Artois, ULCO, UVHC, Centrale Lille, Chimie Lille, IMT Lille Douai)*

de l'Université du Littoral Côte d'Opale

par

Lingshuo MENG

pour obtenir le grade de Docteur de l'Université du Littoral Côte d'Opale

Incoherent Broadband Cavity-Enhanced Absorption Spectroscopy for NO₃ Radical and Aerosol Measurements: Application to Field and Chamber Studies

Soutenue le 23 octobre 2020 devant le jury d'examen :

Rapportrice	Estelle ROTH, MCF HDR, Université de Reims, France
Rapportrice	Meriam TRIKI, Chef de Projet R&D, Terakalis, France
Examineur	Eric VILLENAVE, Professeur, Université de Bordeaux, France
Directeur de thèse	Weidong CHEN, Professeur, Université du Littoral Côte d'Opale, France
Co-directrice de thèse	Cécile CŒUR, MCF HDR, Université du Littoral Côte d'Opale, France
Co-directeur de thèse	Alexandre TOMAS, Professeur, IMT Lille Douai, France

Acknowledgements

Time does fly, and my doctoral career that is about to end has left me with a lot of valuable wealth, and I am full of hope and motivation to greet the following life. On the completion of this thesis full of scientific research results during the doctorate period, reviewing the good times of these years, at this moment, I would like to thank all the teachers, colleagues, friends and families who have given me guidance, training, care, encouragement and help.

First, I would like to express my sincere gratitude to my supervisors, Prof. Weidong Chen, Prof. Alexandre Tomas and Dr. Cécile Cœur. I am extremely lucky to have them for the PhD career. They spent an enormous amount of time to help me get familiar with fields of optics and atmospheric chemistry. They showed me how to observe, how to think and how to solve a problem as a independent researcher. They taught me how to write a scientific paper and how to present at seminars. They have always been patient with me and they were always there for me when I needed them.

I am grateful to Dr. Estelle Roth, Dr. Meriam Triki and Dr. Eric Villenave for the time they spent on my thesis and participation in my committee. They have given me helpful and brilliant comments.

I am also deeply thankful to all of my colleagues and the staff members at Laboratoire de Physico-Chimie de l'Atmosphère for the enjoyable environment, the discussions and the time we shared together during the past four years. I was lucky to have met Dr. Eric Fertein and Dr. Nguyen Tong who helped me in the first year in the installation of the instrument and offered me patient and care. And also thank Mr. Nicoals Houzel, who helped me in the physical operation of CHARME studies and the analysis of SOA products. I would also like show thanks to Dr. Patrick Augustin and Dr. Marc Fourmentin, with whose collaboration I have gained more knowledge of instruments. And big thanks to the constant help and support of those lab friends and office mates, Elena Maters, Anastasia Penkina, Hichem Bouzidi and Houceine Bouya.

I am grateful to my colleague and friend, Dr. Gaoxuan Wang, who have given me supports in data collection and communication. Also I would like to thank my friends Yiruiwen Xie, Hong Li, Hao Wu and Zihua Li, for their care and joys sharing with me anytime.

I would also like to take this opportunity to express my deepest appreciation to my precious families: thankful to my parents for the continuous support and love over the years, thankful to my sister Lingshuang for the understanding and companionship. Without them, this work would never have been possible.

Last but not least, my deepest gratitude and respect go to all the medical staff in the world during this COVID-19 health crisis. Life will get better and tough time will end.

Table of Contents

List of Figures	VI
List of Tables	IX
List of Abbreviations	X
Abstract	XII
Introduction	1
References	4
Chapter I General overview of atmospheric chemistry and focus on NO₃ and aerosols	5
1 General overview of atmospheric chemistry.....	5
2 Importance of NO ₃ radicals in the troposphere	6
2.1 Sources and photolysis	7
2.2 Reactions of NO ₃ radicals in troposphere with VOCs	8
2.3 Analytical techniques	9
2.3.1 Matrix isolation and electron spin resonance spectroscopy (MIESR).....	9
2.3.2 Chemical Ionization Mass Spectrometry (CIMS)	11
2.3.3 Differential optical absorption spectroscopy	12
2.3.4 Laser induced fluorescence (LIF).....	13
2.3.5 Cavity ring-down spectroscopy (CRDS).....	14
2.3.6 Incoherent broadband cavity enhanced absorption spectroscopy.....	15
2.4 Atmospheric concentrations	17
3 Atmospheric chemistry of aerosols	19
3.1 Sources and sinks	20
3.2 Measurement techniques	21
3.2.1 Optical particle counter (OPC)	22
3.2.2 Differential mobility analysers (DMA)	23
3.2.3 Light Detection And Ranging (LIDAR).....	24
3.2.4 Incoherent Broadband Cavity-enhanced absorption spectroscopy (IBBCEAS).....	25
4 Importance of field campaigns and chamber studies	26
5 Thesis motivation	26

References	28
Chapter II Experimental platforms	39
1 IBBCEAS technique	39
1.1 IBBCEAS for trace gas detection.....	39
1.2 Retrieval of trace gas concentrations and aerosol extinction coefficients.....	42
1.3 Development of two IBBCEAS systems for field and chamber measurements	44
1.3.1 A portable IBBCEAS for field measurement of aerosol extinction	45
1.3.2 Open-path IBBCEAS in CHARME chamber for monitoring NO ₃ radicals	46
2 The atmospheric simulation chamber CHARME	47
2.1 Description and features	47
2.2 Associated instruments.....	50
2.2.1 Gas-phase analysis.....	51
2.2.2 Particle-phase analysis.....	54
3 Conclusion of the chapter.....	55
References	57
Chapter III Portable IBBCEAS instrument for field measurement of aerosol extinction	59
1 Introduction and objectives	59
2 Description of the involved instruments	62
2.1 Lidar system and measurements.....	62
2.2 IBBCEAS instrument	63
3 Measurement details.....	65
3.1 Measurement by IBBCEAS	65
3.1.1 Calibration of the IBBCEAS instrument	65
3.1.2 Performance characteristics	67
3.1.3 Simultaneous measurement of aerosol extinction and NO ₂ concentration in ambient air	69
3.1.4 Sampling site	72
3.1.5 Potential interferences	74
3.2 Intercomparison of results from the IBBCEAS and the Lidar	74
4 Conclusion.....	76

References	77
Chapter IV Laboratory studies of the reactions of VOCs with nitrate radicals.....	81
1 Context of the study	81
2 Kinetics of the reaction of NO ₃ radical with guaiacol	82
2.1 Experimental section	82
2.1.1 Experimental system.....	82
2.1.2 Chemicals	83
2.1.3 Kinetic study methods	84
2.2 Results and discussion.....	86
2.2.1 Specifications of IBBCEAS	86
2.2.2 NO ₃ + guaiacol kinetics using the pseudo-first order method.....	91
2.2.3 NO ₃ + guaiacol kinetics using the relative rate method	93
3 SOAs formation from the gas-phase reaction of guaiacol with NO ₃ radicals.....	95
3.1 Experimental section	95
3.1.1 Experimental system and method.....	95
3.1.2 Chemicals	97
3.2 Results and discussion.....	97
3.2.1 SOA yields.....	98
3.2.2 SOA chemical composition	103
4 Conclusion.....	109
References	112
Conclusions and perspectives.....	115
References	118
Résumé	119
Appendices.....	137
Appendix I Minor/major compounds observed in the SOAs and LC/MS/MS product ion spectra for major compounds.....	137
Appendix II Article 1	144
Appendix III Article 2	168

List of Figures

Figure I-1 Schematic description of atmospheric processes involving NO ₃	7
Figure I-2 Spectrum of NO ₃ from 640 nm to 680 nm	8
Figure I-3 Schematic drawing of the cryosampler.....	10
Figure I-4 Schematic of CIMS for NO ₃ radical.....	12
Figure I-5 Instrumental setup of the DOAS system.....	13
Figure I-6 LIF instrument for NO ₃ measurement: (a) Top view; (b) Right view.....	14
Figure I-7 Schematic of CRDS for NO ₃ detection.....	15
Figure I-8 Schematic of IBBCEAS for NO ₃ radical.....	16
Figure I-9 Schematic of OPC laser system.....	23
Figure I-10 Schematic diagram of a DMA	24
Figure I-11 Schematic diagram of a LIDAR system	25
Figure II-1 Light transmission in an optical cavity.....	40
Figure II-2 Setup of IBBCEAS for field measurement. M1, M2, cavity mirrors; EV, electronic valve... ..	45
Figure II-3 Setup of IBBCEAS for chamber application. M1, M2: cavity mirrors.....	46
Figure II-4 Installation of CHARME: (a) Schematic of CHARME with main design; (b) Irradiation systems and general view; (c) Mixing fans inside CHARME. ..	47
Figure II-5 (a) Comparison of solar and filtered xenon spectra; (b) Quartz material transmission.	48
Figure II-6 The DMA and the CPC coupled to CHARME.. ..	52
Figure III-1 Schematic diagram of Lidar's geometric overlap factor η . θ and α are the width transmitter angle and the receiver acceptance angle, respectively. d_0 is the separation distance between the two axes. The overlap factor η is related to the θ , α , d_0 , and the diameters of both cross sections of laser beam and telescope FOV at the same distance.....	60
Figure III-2 Lidar system in an atmospheric mobile unit	63
Figure III-3 (a) Emission spectrum of the LED used; (b) Absorption spectrum of NO ₂ from 350 nm to 380 nm	64
Figure III-4 Band-pass filter transmission. Transmisson in the range of 320-1120 nm is noise limited to be near or below $3 \times 10^{-5}\%$, and transmisson in the wavelength of < 320 nm or > 1120 nm is near or below $3 \times 10^{-4}\%$	64

Figure III-5 (a) Cavity output spectra for pure N ₂ and standard NO ₂ mixture, and the Rayleigh scattering coefficient for N ₂ ; (b) Absorption cross sections of NO ₂ and the experimentally determined mirror reflectivity; (c) 361 ppbv NO ₂ absorption spectrum	66
Figure III-6 Allan variance plot as a function of averaging time. The optimum averaging time was found to be 69.6 s with an estimate of the measurement precision of 1.5 ppbv for NO ₂ , corresponding to an optimum averaging number of 116 with 600 ms integration time per spectrum.....	68
Figure III-7 Histogram showing the distribution of the estimated 0 ppbv NO ₂ concentrations by N ₂ flushing.....	69
Figure III-8 (a) and (b) The electronic valve in the experiment; (c) Working time sequence of the valve in the experiment; (d) Process to retrieve the aerosol extinction $\alpha_{\text{ext,aerosol}}(\lambda)$	70
Figure III-9 Typical data retrieval of NO ₂ (10.8 ppbv) and wavelength-dependent aerosol extinction coefficients ($1.05 \times 10^{-7} \text{ cm}^{-1}$ at 370 nm) from a measured IBBCEAS spectrum of ambient air.....	72
Figure III-10 Schematic of combined measurements of aerosol extinction near ground surface	73
Figure III-11 Time series of meteorological parameters (such as temperature, relative humidity, atmospheric pressure, solar radiation, wind speed and direction) during the measurement period at the measurement site (9:30-11:30, 14 September 2018)	73
Figure IV-1 Setups of N ₂ O ₅ formation: (a) Setups for the formation process; (b) Ethanol bath in dewar vessel; (c) N ₂ O ₅ crystal in the trap..	84
Figure IV-2 (a) NO ₂ and NO ₃ absorption cross sections around 650 nm, and Rayleigh scattering coefficient ; (b) Light intensities and mirror reflectivity; (c) 1295 ppbv NO ₂ absorption characteristic; (d) LED emission spectrum.	87
Figure IV-3 Typical data retrieval of NO ₂ (445.4 ppbv) and NO ₃ (2.0 ppbv) from a measured IBBCEAS spectrum of chamber sample..	88
Figure IV-4 NO ₂ (upper panel) and NO ₃ (lower panel) time profiles following injection of 2000 ppbv NO ₂ , ~30 min stabilization and injection of 1600 ppbv O ₃	90
Figure IV-5 Correlation plot of NO ₂ measured by IBBCEAS vs. NO ₂ measured by chemiluminescence before O ₃ injection.....	91
Figure IV-6 Time series of NO ₂ , O ₃ and NO ₃ in experiment of NO ₃ + guaiacol.	92
Figure IV-7 Plots of relative kinetics for NO ₃ reaction with guaiacol using cresols as references	94

Figure IV-8 Typical concentration-time profiles obtained for guaiacol (PTR-ToF-MS) and SOAs (SMPS; measured and corrected for wall losses). Experiment guaiacol#10 (initial mixing ratios: guaiacol (276 ppbv; 1429 $\mu\text{g m}^{-3}$); NO ₂ (750 ppbv) and O ₃ (500 ppbv)....	99
Figure IV-9 Aerosol growth curve: SOA mass concentration (M_0) against the reacted guaiacol concentration ($\Delta[\text{guaiacol}]$) measured at the end of the experiments. Each data point represents a separate experiment.....	101
Figure IV-10 Yield curve (SOA yield Y vs. the organic aerosol mass formed M_0) for guaiacol/NO ₃ experiments in LPCA-One (blue squares) and in CHARME (green circles). The line represents the best fit to the data considering one semi-volatile major product. The fitting parameters used are $\alpha = 0.32 \pm 0.04$ and $K_{om} = (4.2 \pm 1.0) \times 10^{-3} \text{ m}^3 \mu\text{g}^{-1}$	102
Figure IV-11 Chromatogram (ESI-LC-QToF-MS/MS analysis) of the SOAs formed from the gas-phase reaction of guaiacol with NO ₃ radicals. The compounds corresponding to the labelled peaks are displayed in Tab.IV-4. The indicated masses correspond to the $[\text{M-H}]^+$ product ions.....	105
Figure IV-12 Detailed chemical mechanism leading to the main products observed in the SOAs formed from the gas-phase reaction of guaiacol with NO ₃ radicals..	107

List of Tables

Table I-1 Comparison of the discussed techniques for NO ₃ measurement	17
Table I-2 Summary of NO ₃ concentrations in different environments.....	18
Table I-3 Methods to discuss for measurement of aerosols.....	22
Table II-1 Characteristics of CHARME	49
Table II-2 Analytical instruments associated to CHARME	50
Table III-1 Main parameters of LED	63
Table III-2 Parameters for QE 65000 spectrometer.....	65
Table IV-1 Chemical reaction system used to simulate the temporal profiles of NO ₃ , NO ₂ , O ₃ and N ₂ O ₅ concentrations with Facsimile	89
Table IV-2 Experimental rate constants for the reaction of NO ₃ radicals with guaiacol at 294 ± 2K.....	94
Table IV-3 Experimental conditions and results	100
Table IV-4 Major compounds observed in the SOAs (ESI-LC-QToF-MS/MS analyses) formed from the gas-phase reaction of guaiacol with NO ₃ radicals. The main fragments obtained by MS/MS analyses and the relative abundances (R, in %) are also indicated.....	105

List of Abbreviations

ATD	Thermodesorber
ATR-FTIR	Attenuated total reflection- fourier transform infrared spectroscopy
BBA	Biomass burning aerosols
CAPS	Cavity attenuated phase shift spectroscopy
CCD	Charge-coupled device
CDC	Collisional dissociation chamber
CHARME	Chamber for the atmospheric reactivity and the metrology of the environment
CIMS	Chemical ionization mass spectrometry
CRDs	Cavity ring-down spectroscopy
CPC	Condensation particle counter
DMA	Differential mobility analysers
DOAS	Differential optical absorption spectroscopy
ESI-LC- QToF-MS/MS	Electrospray ionization- Liquid chromatography- quadrupole time- of-flight- Tandem mass spectrometry
EV	Electronic valve.
FOV	Field of view
GC	Gas chromatograph
GFF	Geometrical form factor
GPC	Gas-to-particle conversion
HNO ₃	Nitric acid
IBBCEAS	Incoherent broadband cavity enhanced absorption spectroscopy
MIESR	Matrix isolation and electron spin resonance spectroscopy
MS	Mass spectrometry
N ₂ O ₅	Dinitrogen pentoxide
NO	Nitrogen monoxide
NO ₂	Nitrogen dioxide
NO ₃	Nitrate radicals

LC-MS	Liquid chromatography-mass spectrometry
LED	Light emitting diode
LIDAR	Light detection and ranging
LIF	Laser induced fluorescence spectroscopy
LPCA	Laboratoire de Physico-Chimie de l'Atmosphère
OH	Hydroxyl radicals
OPC	Optical particle counter
PM	Particulate matter
PMT	Photomultiplier tube
PTR-Tof-MS	Proton transfer reaction-time of flight mass spectrometry
RH	Relative humidity
RO ₂	Peroxy radicals
RPM	Revolutions per minute
SNR	Signal-to-noise ratio
SOAs	Secondary organic aerosols
TEC	Thermoelectric cooler
VOCs	Volatile organic compounds

Abstract

Particulate matter in the atmosphere is also one of the main components of air pollution. The inclusion of aerosols in global climate models is still at its infancy due to large uncertainties in particle properties, especially regarding organic aerosol of secondary origin. Therefore, studies are needed to improve our knowledge of aerosol physicochemical and optical properties that may help understand their impacts on both air quality and climate. In this work, one of the aims is to develop a developed custom-designed incoherent broadband cavity-enhanced absorption spectroscopy (IBBCEAS) instrument, and to apply it to the *in situ* measurement of aerosol extinction near the ground surface in effort to address the issue of missing data in the light detection and ranging (Lidar) blind zone in the first hundreds of meters of the observation range. Combined measurements of aerosol extinction at the same location using Lidar remote sensing at 355 nm and *in situ* IBBCEAS operating in the UV spectral region around 370 nm showed results with a good correlation ($R^2 = 0.90$) between the two measurement techniques, which provides a new strategy for near-end Lidar calibration, using a ground-based compact and robust IBBCEAS located at the Lidar measurement site to determine the vertical profile of the aerosol extinction coefficient with a higher accuracy.

The nitrate radical is one of the important nitrogen inorganic species in the atmosphere, and has been recognized for decades to play a key role in nocturnal chemistry. Its low concentrations in the troposphere and its rapid photolysis in sunlight make it challenging to detect. Kinetics and mechanistic studies on NO_3 -initiated oxidation of VOCs are also much less abundant in the literature compared to OH radical chemistry, thus limiting the understanding of NO_3 impact in atmospheric chemistry. This thesis aims to develop an IBBCEAS instrument for detecting the NO_3 on the simulation chamber CHARME, aiming at investigating NO_3 chemistry with biogenic VOCs. Chamber studies were performed to validate the IBBCEAS instrument by following nitrate radical concentrations during its production by reaction of NO_2 with O_3 in the simulation chamber. Furthermore, the reaction of guaiacol (2-methoxyphenol, a VOC emitted by biomass burning) with nitrate

radicals was investigated in both LPCA simulation chambers (CHARME and LPCA-ONE). The SOAs yield and products of $\text{NO}_3 + \text{guaiacol}$ have been studied. The rate coefficient determined using the relative rate method $((3.77 \pm 0.39) \times 10^{-11} \text{ cm}^3 \text{ molecule}^{-1} \text{ s}^{-1})$ leads to an atmospheric lifetime of about 53 s with respect to the oxidation of NO_3 with guaiacol. The formation of secondary organic aerosols from the reaction of guaiacol with nitrate radicals was also observed. The SOAs yields were shown to be influenced by the initial guaiacol concentration, leading to aerosol yields ranging from 0.01 to 0.21. A very good agreement was observed between the experiments performed in both chambers which gives confidence in the data obtained in this study.

Keywords: incoherent broadband cavity-enhanced absorption spectroscopy (IBBCEAS); aerosol extinction; nitrate radical; atmospheric simulation chamber; guaiacol; SOA yield.

Résumé

Les radicaux nitrates jouent un rôle important dans la chimie troposphérique nocturne, à la fois en tant qu'agent oxydant pour un grand nombre d'espèces organiques et en tant que voie d'élimination des NO_x . En outre, les études sur les aérosols atmosphériques suscitent un intérêt croissant en raison de leur impact sur le climat, sur la qualité de l'air et les problèmes de visibilité qu'ils engendrent.

Une bonne compréhension des processus physico-chimiques atmosphérique est nécessaire pour lutter efficacement contre la pollution de l'air et des expériences sont réalisées en laboratoire, sur le terrain et sont associées à de la modélisation.

Dans ce travail de thèse, la constante de vitesse pour la réaction du guaïacol avec les radicaux nitrate a été étudiée dans la chambre de simulation CHARME en utilisant la méthode relative. Les expériences effectuées avec la méthode du pseudo-premier ordre ont montré que celle-ci n'est applicable que pour les COV ayant une réactivité avec NO_3 modérée ($k_{\text{NO}_3} < 10^{-12} \text{ cm}^3 \text{ molécule}^{-1} \text{ s}^{-1}$). La constante de vitesse déterminée ($k_{\text{guaïacol}} = (3.77 \pm 0.39) \times 10^{-11} \text{ cm}^3 \text{ molécule}^{-1} \text{ s}^{-1}$) a permis de calculer une durée de vie atmosphérique de ≈ 53 s pour ce composé par rapport à sa réaction avec NO_3 .

La formation d'AOS pour cette réaction a été étudiée dans deux chambres de simulation atmosphérique (LPCA-ONE et CHARME) et un très bon accord a été observé entre les résultats obtenus dans les deux réacteurs. Les rendements en AOS sont compris entre 0,01 à 0,21 et les valeurs augmentent avec la concentration initiale en COV. Les données ont été traitées par le modèle de répartition gaz-particule à un produit développé par Pankow et Odum et al. (1996). L'extrapolation à une charge atmosphérique particulaire de $5 \mu\text{g m}^{-3}$ conduit à un rendement en AOS de $\approx 2\%$, ce qui indique que la contribution de la réaction entre le guaïacol et les radicaux NO_3 est mineure dans de nombreux environnements.

Des analyses ESI-LC-QToF-MS/MS ont été réalisées pour caractériser la composition chimique des aérosols. Les nitro-aromatiques ont été identifiés comme les principaux produits d'oxydation, confirmant des études antérieures sur les produits formés à partir de la réaction en phase gazeuse des radicaux NO_3 avec les dérivés du guaïacol.

Mots clés : spectroscopie d'absorption en cavité résonante par une source incohérente spectrale large bande (IBBCEAS); extinction d'aérosol; radical nitrate; chambre de simulation atmosphérique; gaiacol; rendements en AOS.

Introduction

Atmospheric chemistry is an important and complicated discipline for understanding air pollution and its impacts, dealing with atmospheric chemical composition and reactivity of its components, and the ways addressing the interactions of gas- and liquid-, solid-, and mixed-phase particles with terrestrial surfaces. This branch of atmospheric science focuses on chemical processes within the Earth's atmosphere, including photochemistry of gas compounds, formation and properties of airborne aerosol particles, gas-particle interactions, etc. [1].

The main gas components constituting the Earth's atmosphere are nitrogen (N_2 , 78.08% in dry air) and oxygen (O_2 , 20.95%) [2]. Besides, hundreds of gas-phase compounds called trace gases are present, like nitrogen dioxide (NO_2), nitrogen monoxide (NO), ozone (O_3) and volatile organic compounds (VOCs). In spite of their very low concentrations, they drive much of the atmosphere chemistry: one of the best example is the hydroxyl radical (OH), responsible for many diurnal oxidation reactions and known as important reaction chain initiators in most oxidation processes involving organic compounds [3]. To better understand the atmospheric chemistry, it is required to perform laboratory experiments, field campaigns and modelisation. Field measurements are often used to evaluate model predictions or to help identify poorly represented chemistry, while laboratory experiments provide an important bridge between field measurements and models, and extend the basic (or fundamental) physics and chemistry of the underlying mechanisms of phenomena observed in the field campaigns.

One of the important nitrogen inorganic species, the nitrate radical (NO_3), has been recognized for decades [4-6] to play a key role in nocturnal chemistry. However, its low concentrations (from a few pptv to a few hundred pptv [7, 8]) in the troposphere and its rapid photolysis in sunlight make it challenging to detect. Meanwhile, the nitrate radical is a strong oxidant, reacting with a wide variety of VOCs, including both saturated and unsaturated [9]. Although unsaturated VOCs may be even more efficiently removed by

NO₃ at night than that with daytime OH chemistry [10], laboratory studies with nitrate radicals have been much less undergone compared to that of hydroxyl radical, mainly due to detection difficulties. Developing an efficient instrument for NO₃ measurement is therefore essential for the study of NO₃ atmospheric chemistry.

Particulate matter (PM) in the atmosphere is also one of the main components of air pollution. Atmospheric aerosols display a wide range of composition, size, shape, and reactivity depending on their source and location. The inclusion of aerosols in global climate models is still at its infancy due to large uncertainties in particle properties, especially regarding organic aerosol of secondary origin. Therefore, studies are needed to improve our knowledge of aerosol physicochemical and optical properties that may help understand their impacts on both air quality and climate.

This thesis is divided into four chapters followed by a general conclusion and annexes.

The first introductory chapter presents a general overview of the context of the present work, which concerns the measurement of aerosol extinction and NO₃ concentrations in field measurements and in atmospheric simulation chambers.

The second chapter introduces and describes the experimental systems involved in the present PhD work, including: (1) the instruments based on Incoherent Broad-Band Cavity Enhanced Absorption Spectroscopy (IBBCEAS) dedicated to laboratory studies of NO₃ radicals and field campaign measurement of aerosol extinction; (2) the simulation chamber CHARME (CHamber for the Atmospheric Reactivity and the Metrology of the Environment), in which some validation tests and kinetic experiments were performed.

In Chapter 3, the development of a custom-designed incoherent broadband cavity enhanced absorption spectrometer and its application to *in situ* measurement of aerosol extinction near the ground surface are described in an effort to address the issue of missing data in the light detection and ranging (LIDAR) blind zone in the first hundreds of meters of the observation range. Combined measurements of aerosol extinction at the same location using LIDAR remote sensing at 355 nm and *in situ* IBBCEAS operating in the UV spectral region around 370 nm showed results with a good correlation ($R^2 = 0.90$) between the two measurement techniques. This Letter highlights a new strategy for near-

end LIDAR calibration, using a ground-based compact and robust IBBCEAS located at the LIDAR measurement site to determine the vertical profile of the aerosol extinction coefficient with a higher accuracy.

The 4th chapter is dedicated to chamber studies in CHARME. An IBBCEAS setup was developed and installed on the chamber to detect NO₃ time-concentration profiles during its production by NO₂ reaction with O₃. The objective was to validate the quantitative measurement of NO₃ concentration using IBBCEAS in a new simulation chamber. In parallel, gas-phase oxidation of a biomass-burning compound (guaiacol or 2-methoxyphenol) by NO₃ radicals was investigated: determination of the rate constant, product study and secondary organic aerosols (SOAs) formation in the presence of NO₃ radicals.

Finally, the main results obtained during this thesis are resumed in a general conclusion, and research perspectives are proposed. Only when we understand the chemical and physical processes involving trace gases and aerosols, as well as their interactions, will we be able to plan pollution control and energy usage strategies which lead to environmentally sound practices on all scales.

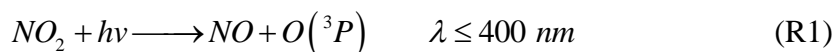
References

- [1] B.J. Finlayson-Pitts. Atmospheric chemistry. *Proceedings of the National Academy of Sciences*, 2010, 107(15): 6566. **10.1073/pnas.1003038107**
- [2] D. R. Lide. CRC handbook of chemistry and physics. CRC press, 2004.
- [3] S. Gligorovski, R. Strekowski, S. Barbati, D. Vione. Environmental implications of hydroxyl radicals (OH). *Chemical Reviews*, 2015, 115(24): 13051-13092. **10.1021/cr 500310b**
- [4] A. M. Winer, R. Atkinson, J. N. Pitts. Gaseous nitrate radical: possible nighttime atmospheric sink for biogenic organic compounds. *Science*, 1984, 224(4645): 156-159. **10.1126/science.224.4645.156**
- [5] U. Platt, D. Perner, J. Schröder, C. Kessler, A. Toennissen. The diurnal variation of NO₃. *Journal of Geophysical Research*, 1981, 86(C12): 11965-11970. **10.1029/JC086iC12p11965**
- [6] U. F. Platt, A. M. Winer, H. W. Biermann, R. Atkinson, J. N. Pitts. Measurement of nitrate radical concentrations in continental air. *Environmental Science & Technology*, 1984, 18(5): 365-369. **10.1021/es00123a015**
- [7] S. Wang, C. Shi, B. Zhou, H. Zhao, Z. Wang, S. Yang, L. Chen. Observation of NO₃ radicals over Shanghai, China. *Atmospheric Environment*, 2013, 70: 401-409. **10.1016/j.atmosenv.2013.01.022**
- [8] D. Stone, M. J. Evans, H. Walker, T. Ingham, S. Vaughan, B. Ouyang, O. J. Kennedy, M. W. McLeod, R. L. Jones, J. Hopkins, S. Punjabi, R. Lidster, J. F. Hamilton, J. D. Lee, A. C. Lewis, L. J. Carpenter, G. Forster, D. E. Oram, C. E. Reeves, S. Bauguitte, W. Morgan, H. Coe, E. Aruffo, C. Dari-Salisburgo, F. Giammaria, P. Di Carlo, D. E. Heard. Radical chemistry at night: comparisons between observed and modelled HO_x, NO₃ and N₂O₅ during the RONOCO project. *Atmospheric Chemistry and Physics*, 2014, 14(3): 1299-1321. **10.5194/acp-14-1299-2014**
- [9] R. Atkinson, J. Arey. Atmospheric degradation of volatile organic compounds. *Chemical Reviews*, 2003, 103(12): 4605-4638. **10.1021/cr0206420**
- [10] S. A. Penkett, R. A. Burgess, H. Coe, I. Coll, Ø. Hov, A. Lindskog, N. Schmidbauer, S. Solberg, M. Roemer, T. Thijssse, J. Beck, C. E. Reeves. Evidence for large average concentrations of the nitrate radical (NO₃) in Western Europe from the HANSA hydrocarbon database. *Atmospheric Environment*, 2007, 41(16): 3465-3478. **10.1016/j.atmosenv.2006.11.055**

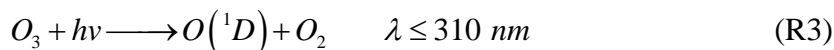
Chapter I General overview of atmospheric chemistry and focus on NO₃ and aerosols

1 General overview of atmospheric chemistry

The chemistry of nitrogen oxides has been a central theme in atmospheric chemistry since NO was identified as one of the ingredients necessary for producing photochemical smog. Later, a free radical catalytic cycle involving NO_x (NO_x = NO + NO₂) was identified as one of the key mechanisms of photochemical ozone production in urban areas (R1-2), and it was demonstrated that the same mechanism applied throughout the global troposphere [1] .



Appreciation of the importance of nitrogen oxides to atmospheric chemistry grew further with the improvement of detection methods of trace gases and radicals. The O₃ molecule produced in R2 can be photolysed and produce the hydroxyl radical OH in the presence of water vapor (R3-4) [2]:



The OH radical is a key atmospheric oxidant and is known as the prevailing “detergent” of the atmosphere from local to global scales, since it reacts with almost all VOCs, thus cleaning the atmosphere of our planet. In this cleaning process, peroxy radicals RO₂ are formed that will convert back NO into NO₂ (reaction R5), thus sustaining the oxidant capacity of the atmosphere.



The NO₃ radicals play an important role in the chemistry of the nighttime troposphere, both as an oxidizing agent for a large number of organic species [3-6], and as a route for the removal of NO_x. Although it has a quite low concentration (from a few pptv to a few hundred pptv), NO₃ controls the oxidation and loss of many trace gases [4, 7], in particular terpenes and alkenes. In addition, NO₃ also contribute to the formation and growth of particles. Its ability to oxidize VOCs in the night may equal or even exceed that of OH in the daytime [8, 9].

Taking into account the complicated synthesis and difficult detection of NO₃ radicals, reactivity studies are not widespread, and many uncertainties remain on its kinetics, chemical mechanisms and SOAs formation. Mechanistic studies are often limited to the determination of total organic nitrates and SOAs yields without any detection or quantification of individual nitrate species [10]. Thus, NO₃ chemistry remains much less understood than OH chemistry, the main uncertainties relying on the difficulty of identifying the organic nitrates products due to the lack of standards and the mechanisms leading to their production.

Atmospheric aerosols play a central role in the processes related to climate change and in air quality, which affects human health. There is an increasing interest in the studies of atmospheric aerosols due to their impact on the climate, their chemical heterogeneous reactions in the atmosphere, which particularly affect environmental air quality, and the associated problems of visibility and health issues [11].

In the next sections, emphasis will be put on NO₃ radicals and atmospheric aerosols to present their chemistry, including sources and sinks, their reactions in the troposphere and the detection techniques.

2 Importance of NO₃ radicals in the troposphere

As the results of the progress in the development of differential optical absorption spectroscopy (DOAS) involving long-path absorption, it becomes possible since 1990s to detect NO₃ radicals in the polluted atmosphere [12-14].

2.1 Sources and photolysis

Nocturnal radical chemistry, and in particular that of NO₃ and nitrogen pentoxide (N₂O₅), impacts a number of key atmospheric phenomena, as shown in Fig.I-1 [15], and the detailed reaction process will be present. Researches are made to understand the NO₃ reactions with the atmospheric gases.

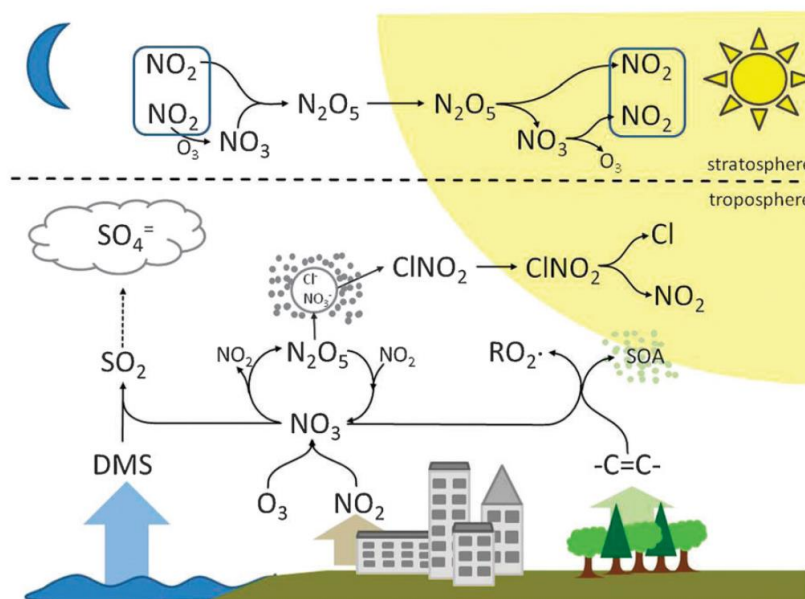


Figure I-1 Schematic description of atmospheric processes involving NO₃ radicals [15]. In stratosphere, NO₃ radicals are formed by the reaction of NO₂ + O₃, with a sequence reaction with NO₂ to form N₂O₅ in nocturnal, which works as a reservoir and can decompose into NO₃ in the daytime.

As indicated in Fig.I-1, in the atmosphere, NO₃ radicals are formed from the O₃ reaction with NO₂ (R6), which has a sequence reversible reaction R7 to form N₂O₅.





NO₃ radicals strongly absorb radiations in the red region of 650-670 nm of the electromagnetic spectrum (Fig.I-2).

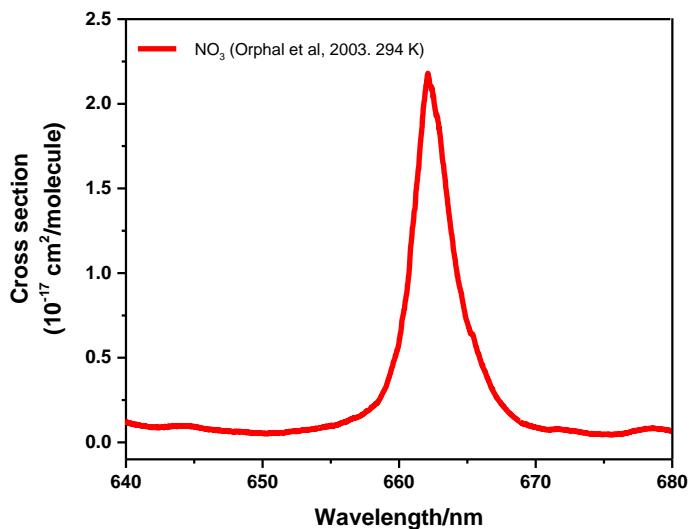
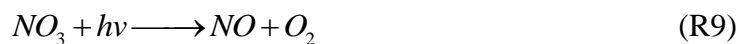
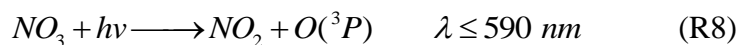


Figure I-2 Spectrum of NO₃ from 640 nm to 680 nm [16].

Therefore, during the day, NO₃ is rapidly ($\tau \approx 5$ s) converted to NO₂ (R8) or NO (R9) by photolysis, maintaining its abundance at sub-pptv mixing ratios [17].



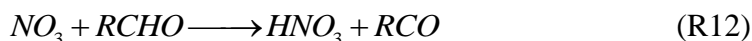
At night, when there is no photolysis, NO₃ accumulates and is available to react with NO₂ to form N₂O₅ (R7), which can also be hydrolyzed by contact with moist surfaces and form nitric acid (HNO₃) (reaction R10):



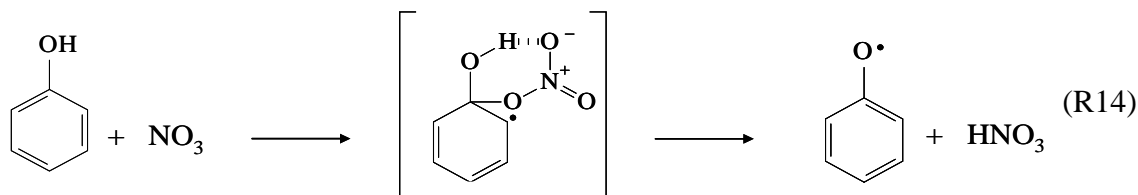
2.2 Reactions of NO₃ radicals in troposphere with VOCs

The reactions of organics with NO₃ are important in the troposphere, many of which are sufficiently fast to be important sinks of organics at night, often rivaling in magnitude with the loss by reaction with OH during the day [4]. In addition, they could provide a means of generating organic radicals [18, 19].

In general, NO₃ reactions with hydrocarbons are similar to those of the OH radicals. It abstracts an H-atom from saturated hydrocarbons (with $k < 10^{-16}$ cm³ molecule⁻¹ s⁻¹) (R11) and aldehydes (R12), and adds to unsaturated hydrocarbons (R13).



In terms of atmospheric importance, the main organic species concerned by reactions with NO₃ are alkenes (reaction rate magnitude 10⁻¹² cm³ molecule⁻¹ s⁻¹) and aldehydes (reaction rate magnitude 10⁻¹⁴ cm³ molecule⁻¹ s⁻¹). NO₃ radicals reactions with phenols have been postulated to proceed by an overall H-atom abstraction process after initial NO₃ radicals addition to the aromatic ring (NO₃-radical ipso-addition to the substituent OH site), through the intermediacy of a six-membered transition state (R14) [20].



2.3 Analytical techniques

Several conversion-based non direct or direct optical techniques are used to detect NO₃ radicals. These methods, including the principle, the setup, the process, and the advantages / disadvantages, are described below.

2.3.1 Matrix isolation and electron spin resonance spectroscopy (MIESR)

MI-ESR is the technique combined matrix isolation (MI) and electron spin resonance (ESR) spectroscopy to measure the highly reactive radical.

Electron spin resonance spectroscopy is a method for studying molecules with unpaired electrons [3, 21]. It is particularly useful for studying metal complexes or organic radicals. The basic concepts of ESR is to excite the electron spins of the molecules and then detect the transition of unpaired electrons in an external magnetic field. In an ESR spectrometer, the sample is loaded in a high frequency resonant cavity in a slowly varying, uniform magnetic field. When irradiated with microwave radiation at a fixed frequency, the unpaired electrons undergo resonant transitions between spin 'up' and spin 'down' states in a particular magnetic field. The amplitude of the resonant peak is determined by the concentration of the radical in the sample. Matrix isolation is to separate the unstable molecules by the matrix liquid, and make it possible to detect stably and safely.

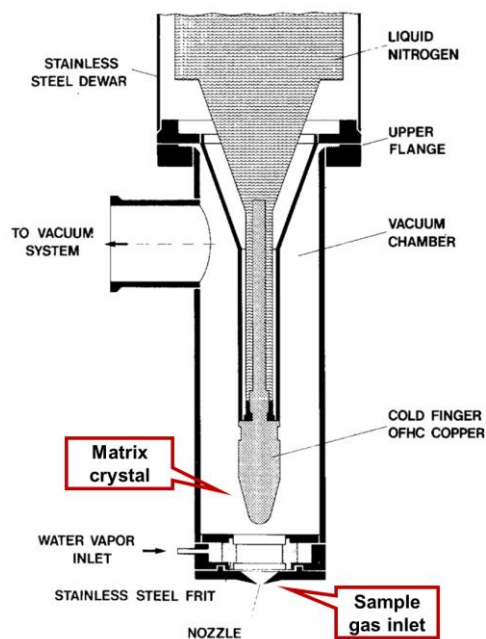


Figure I-3 Schematic drawing of the cryosampler [22]. The air sample is pumping into the cryosampler through the nozzle. The radicals were trapped on the copper cold finger in polycrystalline D₂O-ice matrix at a temperature of 77 K.

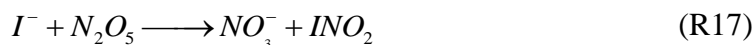
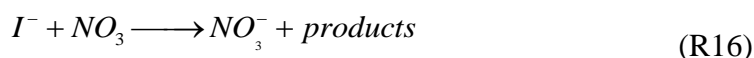
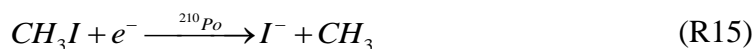
The unpaired electrons in NO₃ radicals are highly reactive. The analysis of NO₃ radicals concentrations by MIESR is carried out in two steps: *in situ* trapping of the NO₃ radicals followed by laboratory determination of the trapped radical concentrations by ESR. To collect a sample of ambient radicals, air is passed over a copper finger in a cryosampler (Fig.I-3), which is cooled by liquid nitrogen and located in a stainless steel vacuum chamber. The sampled air is introduced through a stainless steel nozzle. The radicals are trapped from ambient air in a polycrystalline D₂O matrix at a temperature of 77 K.

2.3.2 Chemical Ionization Mass Spectrometry (CIMS)

CIMS is a versatile and well established technique used for measurement of atmospheric trace gases [23, 24]. It is a non-optical, *in situ* method, based on a selective ionization process resulting from a reaction between a reagent ion and the compound of interest. In this technique, ionization of the gaseous analyte occurs via gas-phase ion-molecule reactions and gives rise to a set of ions that could be detected by mass spectrometry.

Measurement of the sum of NO₃ + N₂O₅ in air using CIMS [25] includes three steps (Fig.I-4):

- 1) CH₃I was flowed over a ²¹⁰Po source to generate I⁻ (R15). I⁻ is a very selective reagent ion because it is unreactive with almost all atmospheric species.
- 2) Ion-NO₃ reactions take place in a flow tube followed by a collisional dissociation chamber (CDC). Because I⁻ reacts with both NO₃ and N₂O₅ (R16 and R17), the technique could not differentiate between NO₃ and N₂O₅, resulting the sum results.



- 3) the NO₃⁻ is generated and detected by the following mass spectrometry at 62 amu (atomic mass unit).

A principal drawback of the CIMS method is that although I⁻ is reasonably specific for either NO₃ or N₂O₅, there is still background noise at the 62 amu. In some regions of the atmosphere, there may be additional interferences from the active nitrogen compounds, like HNO₃, PAN, ClONO₂ and BrONO₂, which could also generate NO₃⁻ by reaction with I⁻ [26].

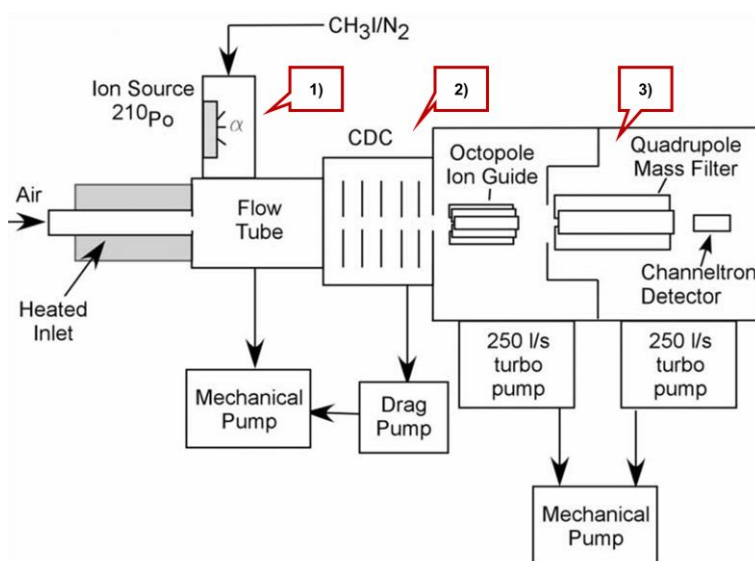


Figure I-4 Schematic of CIMS for NO₃ radicals measurement [25].

2.3.3 Differential optical absorption spectroscopy

DOAS is a widely used optical technique for NO₃ detection in both remote and highly polluted environments.

As shown in Fig.I-5, long-path DOAS instruments for tropospheric NO₃ measurement are composed of a light source, such as a xenon (Xe) arc lamp [27], and a coaxial sending/receiving telescope which emits a collimated beam to an array of retro-reflectors located at kilometer-scale away from the instrument [28] and the reflectors send the light back to the telescope where the narrow-band absorptions of various trace gases along the

light path are analyzed with a spectrograph-detector system. For NO₃, the window of wavelength range is between 610 and 680 nm.

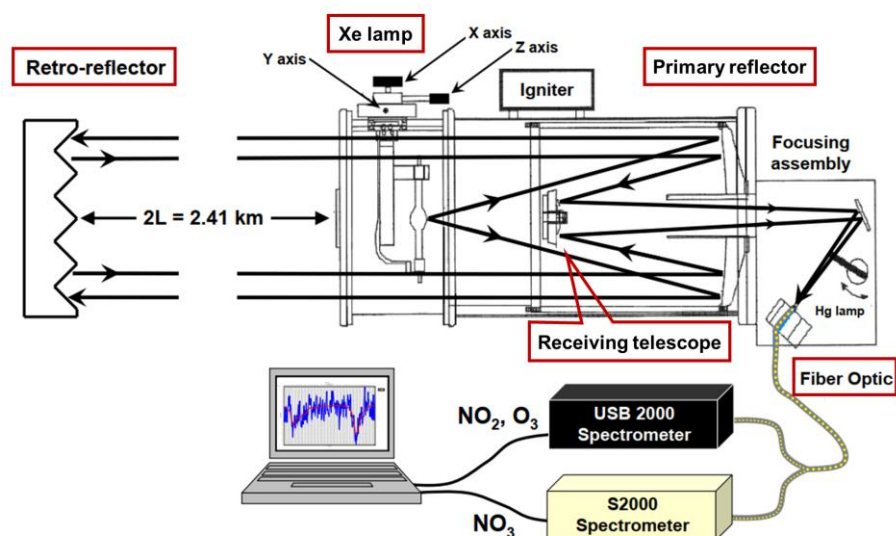


Figure I-5 Instrumental setup of the DOAS system [29]. A Xe arc lamp radiation is emitted towards the primary reflector where it is collimated and directed to an array of retro-reflector, and then the radiation is reflected back to the primary reflector and directed through the receiving telescope to a spectrometer via an optic fiber.

The advantages of DOAS lie in its ability to simultaneously measure multiple gaseous species in open-path, such as NO₂ and NO₃ without artifacts associated with wall losses in the pathlength. Owing to its good sensitivity and high time resolution, DOAS is considered as an absolute analytical technique [30]. However, this technique needs a large volume, and the result is the average value for the long optic path (hence low spatial resolution).

2.3.4 Laser induced fluorescence (LIF)

LIF has proven to be an accurate, sensitive, and selective method for measurement of trace atmospheric species, such as NO₃ and related nitrogen compounds using its strong and highly accessible visible absorption bands [31-34] throughout the troposphere and stratosphere.

The LIF instrument used to detect NO₃ (and N₂O₅) is shown in Fig.I-6. Ambient air is sampled through a heater tube to the optic cell. The laser source could be tuned around 662 nm where NO₃ has a strong absorption band to excite the NO₃ radicals to an excited electronic state, followed by the subsequent spontaneous emission of fluorescence. NO₃ fluorescence was then collected within a spectral window of 700-750 nm by a collimating lens and passed through a 750 nm short-pass filter and a 700 nm long-pass interference filter to eliminate the unneeded fluorescence wavelength. The final filtered fluorescence, being proportional to the NO₃ concentration, was focused onto the photomultiplier tube (PMT), which will be detected.

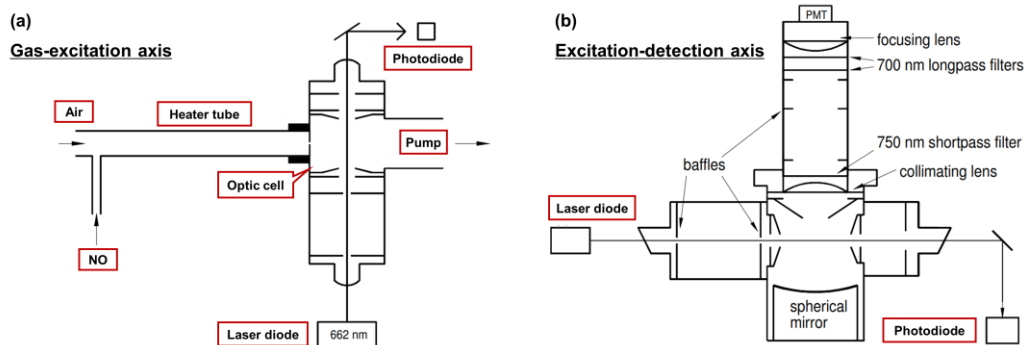


Figure I-6 LIF instrument for NO₃ measurement [35]: (a) Top view; (b) Right view.

This technique is highly selective. The utility of LIF for particular trace gas measurements depends on the accessibility and intensity of electronic transitions in regions where laser sources and the fluorescence yield [24] are available.

The LIF technique has the advantages of high sensitivity (≈ 76 pptv in 60 s for NO₃), but its application in field campaign is limited due to its high cost, complexity of instrument structure and bulky system.

2.3.5 Cavity ring-down spectroscopy (CRDS)

The principle to monitor NO₃ radicals using CRDS is straightforward [36-39] as shown in Fig.I-7. CRDS measures the loss rate of light intensity related to trace gas absorption within an optical cavity. The ring-down cavity consists of a set of mirrors (M1 and M2) with high reflectivity forming a stable optical resonator. By measuring the

change in cavity losses in the presence and absence of molecular sample, the absolute sample concentration can be quantified [40].

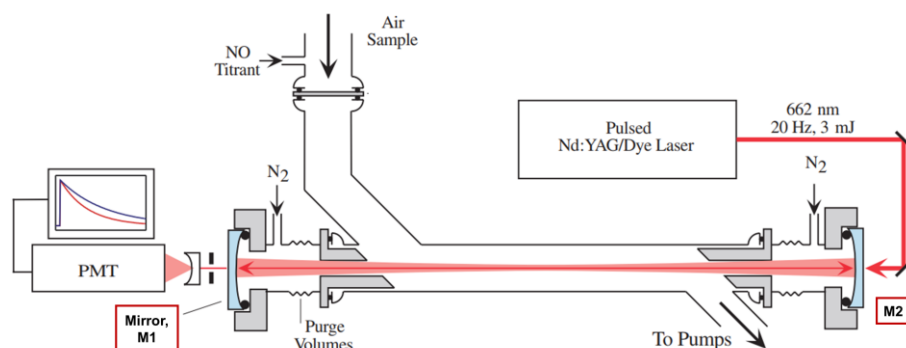


Figure I-7 Schematic of CRDS for NO₃ detection [41]. A laser was passed through a beam splitter, collimated with the lens and injected into the cavity conducted by the mirrors and a steel cell. Each of the signal beams transmitted the M1 and M2 to a photomultiplier tube, and finally digitized by the computer.

A pulse laser beam is directed into the cavity, once the optical intensity builds up in the cavity, the laser is then quickly turned off, allowing to establish a ring-down event in the cavity. The subsequent exponential decay τ_0 of the light intensity from the cavity in the absence of the absorber is characterized by a $1/e$ lifetimes, also known as the ring-down time. When an absorber is present, the exponential decay time constant τ is reduced, providing an absolute measurement of optical extinction, as given in Eq.1:

$$\alpha = \sigma[A] = \frac{R_l}{c} \left(\frac{1}{\tau} - \frac{1}{\tau_0} \right) \quad (\text{Eq.1})$$

where α is the optical extinction coefficient, σ is the absorption cross section corresponding to the absorber, $[A]$ is the concentration of the absorber, R_l is the ratio of the total cavity length to the length where the absorber is present, c is the light speed, τ and τ_0 are the exponential decay constants with and without the absorber in the cavity.

The CRDS technique has advantages of high sensitivity (1 pptv for NO₃ [42]), easy to operate, and measurement results without the effect of pulsed laser fluctuation, however this technique requires sophisticated optical elements.

2.3.6 Incoherent broadband cavity enhanced absorption spectroscopy

CRDS instruments detect NO₃ using its strong absorption at 662 nm with a single wavelength, while IBBCEAS detects NO₃ using its characteristic absorption band across a wider wavelength range [43]. Unlike CRDS method, IBBCEAS needs the calibration of the mirror reflectivity. The mirror reflectivity may be determined by the following methods [44-46]: (1) measuring light extinction by absorbing sample with known concentration or Rayleigh extinction coefficient by molecules with known Rayleigh cross sections [47]; (2) using an antireflection - coated optical substrate of known losses [48], or (3) using step - scan phase shift cavity ring - down spectroscopy [49]. A typical IBBCEAS setup is shown in Fig.I-8. IBBCEAS measurement is conducted by exciting a high finesse optical cavity, formed by two mirrors with high reflectivity ($R > 99\%$), with an incoherent broadband light source. The light trapped inside the cavity increases its average life time by a factor of $1/(1 - R(\lambda))$, corresponding to an effective absorption path length of 11.8 km at 660 nm through the intracavity medium [49].

The detailed technique description will be given in Chapter II.

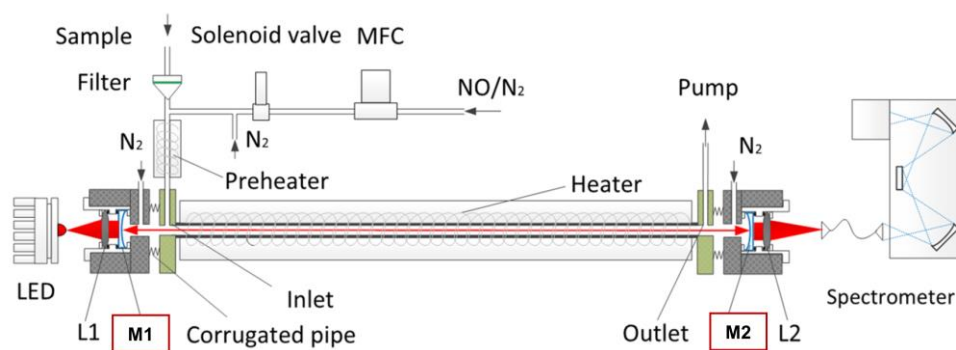


Figure I-8 Schematic of IBBCEAS for NO₃ radicals [50]. A LED was used as the light source and the beam was collimated by a lens to the cavity formed by two mirrors. The sample air was pumped into the cavity. The cavity output light was collimated by another lens and coupled to the spectrometer with the fiber.

Overall, the limit of detection and advantages / disadvantages for the NO₃ detection techniques discussed above are overviewed in Tab.I-1. In this work, the instrument

should be easily coupled to the simulation chamber, and it should be continuous measurement. MIESR could measure multi species of gases, like RO₂, NO₂ and NO₃, but it's off-line technique and harsh experiment condition limits its application. CIMS is an on-line technique and has a fast response, but it could be interfered by the other trace gases, like HNO₃, HO₂NO₂ and ClONO₂, and the results stand for the sum of NO₃ and N₂O₅. LIF is a continuous measurement, but it has disadvantages of high cost, large volume and complex calibration. DOAS is the classical technique with no-contact, open path measurement, which has sensitive, on-line and high time-resolution advantages, but the results are the integrated concentration in the long path length, which needs large volume. Both CRDS and IBBCEAS are the optic techniques available to perform on-line and no-sampling measurement, but CRDS has a narrow band, and a relatively higher requirement for the optic components. Thus to couple the instrument to the chamber and to have an on-line measurement, the IBBCEAS technique is chosen to develop in the lab.

Table I-1 Comparison of the discussed techniques for NO₃ measurement.

	Limit of detection (integration time)	Advantages	Drawbacks
MIESR	< 2 pptv [51] (30 min)	multi species of gas	off-line; harsh experimental conditions (low temperature)
CIMS	12 pptv [25] (1 s)	on-line; fast time response	interferences from other trace gases; measurement of sum of NO ₃ + N ₂ O ₅
DOAS	6.3 pptv [52] (300 s)	no sampling; direct measurement; high temporal resolution	large volume, integrated concentration measurement and so low spatial resolution
LIF	11 pptv [53] (10 min)	continuous observation	large setup volume, high cost and complex calibration
CRDS	1 pptv [42] (100 s)	no sampling; compact devices; point measurement	Narrow band, higher requirement of optic components

IBBCEAS	1 pptv [54] (1 s)	and hence high spatial resolution	calibration of mirror reflectivity; Affected by water vapor
---------	----------------------	--------------------------------------	---

2.4 Atmospheric concentrations

Many field campaigns described by previous researchers were conducted to measure NO₃ and/or N₂O₅ (see Tab.I-2) in various environments (marine, forest and urban).

In the daytime, in marine regions NO₃ peaks 140 pptv most and averages dozens pptv. In forest, it has an average of ~ 40 pptv. Indoor NO₃ has a value around several pptv, and in urban air, it normally averages hundred pptv and higher values at polluted conditions.

Table I-2 Summary of NO₃ concentrations in different environments.

Environment	Location/year	Technique	NO ₃ Concentration	Refs.
Marine	Mace Head on the west coast of Ireland, 2002	LP - DOAS	5 ~ 25 pptv	Saiz - Lopez et al. [55]
	Roscoff, France in 2006	DOAS	70 pptv	Mahajan et al. [56]
	Finokalia station on the island of Crete in the Mediterranean, 2001 - 2003	LP - DOAS	1~38 pptv avg 5 pptv	Vrekoussis et al. [6, 57, 58]
	Gulf of Maine MBL at the University of New Hampshire , 2004	LP - DOAS	80 pptv	Ambrose et al. [59]
	Izu - Oshima Island, 2004	LIF	30 pptv	Matsumoto et al. [60]
Forest	Sumas Eagle Ridge site in the eastern end of the Lower Fraser Valley, 2001	DOAS	Max. 45 pptv	McLaren et al. [13]
	Taunus Observatory, at the summit of a mountain, Germany, 2008	CRDS	20 - 40 pptv	Crowley et al. [61]
	United States Forest	CRDS	Max. 12 pptv	Fry et al. [62]

Urban Air	Service Manitou Forest Observatory in Pike National Forest, 2011			
	German Taunus mountains, 2011	CRDS LP - DOAS	Max. 200 pptv	Sobanski et al. [63]
	Los Angeles, 2010	CRDS; 1 - D model	200 pptv (low pollution) 300 pptv (high pollution)	Stark et al. [64]
	A ground site near Boulder, Colorado, 2001	CRDS	Max. 100 pptv	Brown et al. [65]
	Denver - Boulder area (Colorado, USA). 2004	DOAS	90 pptv	Brown et al. [66]
	Houston, Texas, and along the U.S. Gulf Coast 2006	CRDS	400 pptv	Brown et al. [67]
	Pabstthum near Berlin, Germany, 2001	DOAS	Max. 80 pptv	Geyer et al. [7]
	The BT Tower 160 m above street level in central London, 2017	IBBCEAS	Max. 800 pptv NO ₃ + N ₂ O ₅ Avg. 30 pptv	Benton et al. [68]
	Downwind of New York City, 2010-2011	IBBCEAS	Avg. 18.9 pptv	Stone et al. [69]
	Urban center of Hong-Kong, 2010	TD - CIMS	Avg. 102.5 pptv day Avg. 71.3 pptv night	Wang et al. [26]
Indoor	An office building in Denmark	Calculation	Max. 58 pptv NO ₃ + N ₂ O ₅	Nøjgaard [70]

3 Atmospheric chemistry of aerosols

An aerosol is a system of solid or liquid particles suspended in a mixture of gases. The term aerosols covers a wide spectrum of small particles, like sea salt particles, mineral dust, pollen, drops of sulphuric acid and many others [71].

Aerosol particles in the atmosphere have widely variable shapes (crystalline, aggregate, fractal and amorphous [72]). Their dimensions are usually characterized by a particle diameter, ranging in size over four orders of magnitude, from a few nanometers

to around 100 μm . Particle size is one of the most important parameters to describe the behavior of aerosols, affecting their lifetime, physical and chemical properties. Based on particle size distributions, different groups of atmospheric particles can be separated: a) nucleation (Aitken) mode, b) accumulation mode, c) coarse mode:

- a) Aerosol particles $< 0.1 \mu\text{m}$ form the nucleation mode which are produced by homogeneous and heterogeneous nucleation processes. They are generated from gas-to-particle conversion (gas-to-particle conversion, GPC) in the troposphere or during condensation of hot vapor in combustion processes.
- b) Larger aerosol particles in the size range from 0.1 to 1 μm , mainly generated through coagulation of small particles, could accumulate in the atmosphere because their removal mechanisms are least efficient with a typical lifetime of several days [73]. They are removed from the atmosphere mainly by wet deposition.
- c) The coarse mode contains particles with diameter $> 1.0 \mu\text{m}$. These particles are mostly emitted in the atmosphere during mechanical processes from both natural and anthropogenic sources (like sea-salt particles from ocean surface, soil and mineral dust, biological materials....). Due to their relatively large mass, they have short atmospheric lifetimes (in the order of minutes) because of their rapid sedimentation.

Particles in the nucleation mode constitute the majority of atmospheric particles expressed in number. However, due to their small sizes, their contribution to the total mass of aerosols is very small (around a few percent). The accumulation mode particles usually account for a substantial part of aerosol mass and for most of the aerosol surface area [74].

Atmospheric aerosol particles contribute significantly in the Earth radiation budget as they scatter and absorb both shortwave solar radiations and longwave terrestrial radiations [75]. The ability of aerosols to interact with radiation is dictated by their optical properties, which depend on their physical and chemical characteristics, and on the wavelength of the incident light. The main parameters in this respect are the

scattering and absorption coefficient, which can be summed as extinction coefficient, and expressed as $\alpha_{\text{extinction}} = \alpha_{\text{absorption}} + \alpha_{\text{scattering}}$ [76]. Scattering is a process that conserves the total amount of energy, but the direction in which the radiation propagates may be altered. Absorption is a process that removes energy from the electromagnetic radiation field, and converts it to another form. Extinction is the sum of scattering and absorption, so it represents total effect of medium on radiation passing the medium. In the atmosphere: aerosol particles can scatter and absorb solar and infrared radiation with changing air temperature and the rates of photochemical reactions.

The aerosols also have great impacts on the formation of clouds and precipitations. Meanwhile by chemical reactions they could affect the abundance and distribution of atmospheric trace gases and oxidants. Moreover, aerosols are a major factor in reducing air quality, and may adversely affect the environment and human health [77].

Due to the increasing anthropogenic emission of aerosols since the industrial revolution [78], aerosols can also affect the global climate change. However, the effects of aerosols on climate are not one-way, and are known with high uncertainties [79]. The climate forcing by aerosols can be realized in two ways, basically in direct and indirect radiative forcing:

- a) Aerosol particles could reflect part of shortwave solar radiations back into space, resulting a cooling effect on Earth's atmosphere. Pure sulfates and nitrates [80, 81] reflect nearly all radiations they encounter, cooling the atmosphere, while elemental carbon aerosols and dust particles has a warming influence on the atmosphere.
- b) Particles could also affect the radiative balance through the formation of cloud droplets by condensation of water vapor onto hygroscopic particles (cloud condensation nuclei, or ice nuclei) when the relative humidity exceeds the saturation level, otherwise the homogeneous condensation of water vapor would necessarily need a very large supersaturation without the particles [82].

3.1 Sources and sinks

The sources of aerosols includes both natural and anthropogenic sources. A wide variety of aerosol particles are produced through the combination of physical, chemical and biological processes, based on which different sources could be distinguished.

Atmospheric aerosol particles may be emitted directly (primary sources) or formed in the atmosphere from gaseous precursors (secondary sources). Primary particles directly emitted in the atmosphere include carbonaceous aerosol (organic matter, black carbon), industrial emissions, sea salt and mineral dust [82]. Secondary particles are formed by nucleation and condensation of gaseous precursor, for which high concentrations of SO₂, NH₃, and VOCs have always been served as the precursors [83].

Based on the particle size and disposition, aerosols could be removed from the atmosphere by different ways, two types of which are wet and dry depositions. Dry depositions refers to the deposition of particles through the direct delivery of mass to the surface (like gravitational settling, impaction, turbulent diffusion) [84]. Wet processes are often referred to as rain-out and washout, as well as cloud deposition. Wet deposition is the main sink of atmospheric particles, while dry deposition is less important on a global scale [85].

3.2 Measurement techniques

To correctly evaluate the effects of aerosols on various issues such as human health, air quality, and global climate, and ultimately establish effective control strategies, it is vital to increase our understanding of the physical and chemical properties of aerosols.

Different techniques have been developed based on the measurement of number, mass, morphology, chemical composition and optical properties of atmospheric particles. Four of the commonly-used methods concerning different parameters of aerosols will be discussed below.

Table I-3 Methods to discuss for measurement of aerosols.

Technique	Optic particle counter	Differential mobility analyzer	Light Detection And Ranging	IBBCEAS
Target	Particle number	Particle number, volume, mass	Aerosol scattering coefficient	Aerosol extinction coefficient

3.2.1 Optical particle counter (OPC)

Particle measurements by an OPC are based on the fact that when the particles pass through a beam of light, some of the light is scattered [86]. Detection of this scattered light is the basis of such instruments. Particle number can be determined simply by counting the pulses of scattered light reaching the detector.

A typical OPC system is shown in Fig.I-9, containing three major sections in an OPC (i) the airflow system; (ii) the optical system, and (iii) the electronics system.

The optical system allows measurement of a single particle by collecting the scattered light by the particle. Each scattered light pulse corresponds to a particle count, and electronics convert the pulse to the corresponding particle size and this will be added in the appropriate size category to obtain particle concentration in a given size interval.

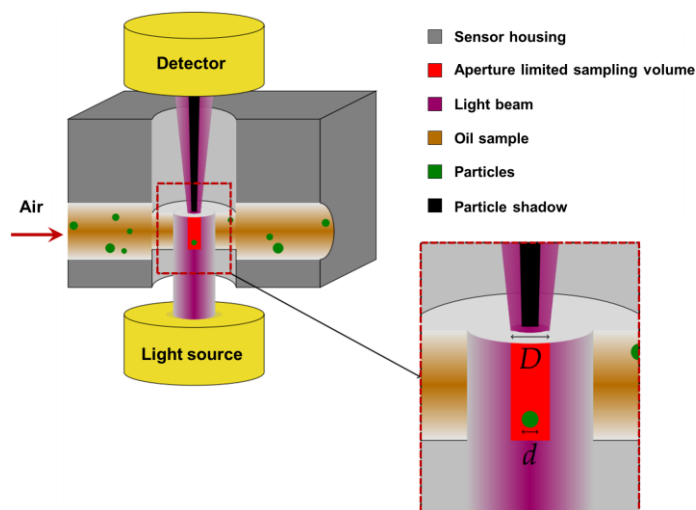


Figure I-9 Schematic of OPC laser system [87]. The diameters D and d stand for a circular aperture and a spherical particle, respectively. The air flows through the sampling area, and the light beam will be blocked by the particles, which results in that detector output signal will be the response of particle size d .

3.2.2 Differential mobility analysers (DMA)

Differential mobility analysers (DMA, also known as electrostatic classifiers) classify particles according to their electrical mobility, which depends on gas properties, particle charge, and the geometric size but is independent of other properties such as density [88].

The DMA (Fig.I-10) contains a hollow cylinder with a concentric rod in the center on which a positive voltage is applied. Particles with higher mobilities will migrate to the central rod before reaching the gap, while those with lower mobility will surpass the gap and be extracted. The size of the extracted particles could be controlled by adjusting the voltage on the center rod and the flow rate inside the DMA.

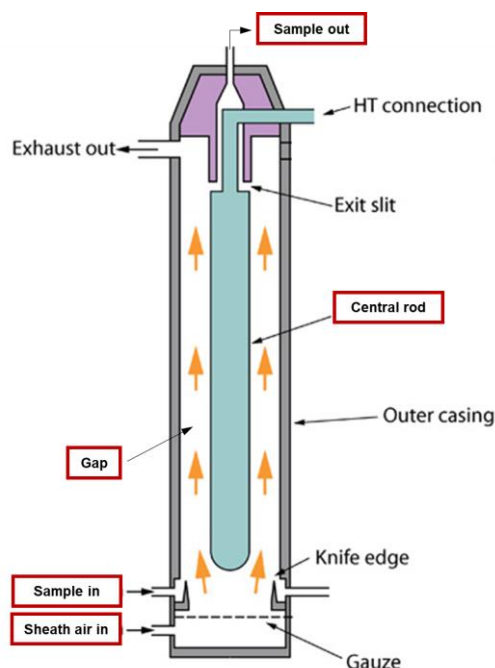


Figure I-10 Schematic diagram of a DMA ([http://www.cas.manchester.ac.uk/restools/instruments/aerosol/differential/Schem DMA/](http://www.cas.manchester.ac.uk/restools/instruments/aerosol/differential/Schem_DMA/)). The sheath air is the main flow of free particle. An electric field is placed between the central rod and outer casing. The particle will be separated depending on its charge, the strength of the electric field and sheath flow.

3.2.3 Light Detection And Ranging (LIDAR)

LIDAR (Fig.I-11) stands for **L**ight **D**etection **A**nd **R**anging and is a differential absorption system operating in the ultraviolet spectral region. It has widely been used for remote sensing of the atmosphere.

LIDAR performs temporal and spatial resolved measurements of backscattered photons. Light pulses are emitted into the atmosphere, where they are scattered at different heights by particles. Backscattered photons are collected through a telescope for detection. The strength of the received backscatter signal depends on the attenuation, due to scattering and absorption processes of the light along its path. From the backscattered signal, the backscatter and extinction coefficients can be derived together [89].

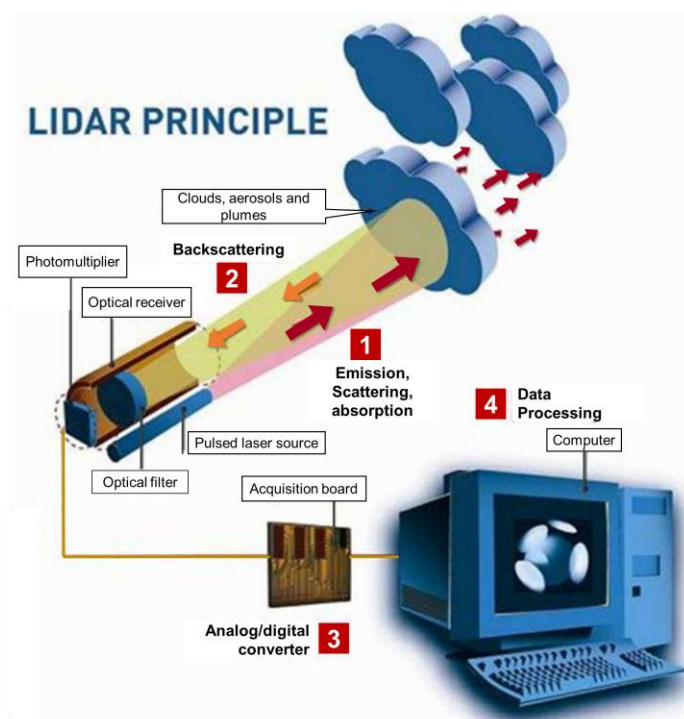


Figure I-11 Schematic diagram of a LIDAR system [90].

It should be noticed that there is an angle between the laser beam and telescope, which results in the incomplete overlap in the near field of the instrument, leading to the missing information in the area close to lidar, so called blind area.

3.2.4 Incoherent Broadband Cavity-enhanced absorption spectroscopy (IBBCEAS)

Methods based on absorption spectroscopy are used to measure the aerosol extinction coefficients. The detailed method to distinguish aerosol extinction from trace gas using IBBCEAS measurements will be presented in Chapter II.

For the thesis work, it is aimed to solve the lidar's blind area problem to get the aerosol extinction information in its blind area. And an optic technique will be introduced to gain the *in-situ* aerosol extinction. And no measurement of aerosol extinction by IBBCEAS near the ground surface in synergy with lidar has been previously reported.

4 Importance of field campaigns and chamber studies

A good understanding of atmospheric physical-chemistry is required to perform laboratory experiments, field campaigns and modelisation.

Although it has been quite extensive chemical kinetics databases for gas phase and heterogeneous reactions, like gas kinetic data evaluation of IUPAC (<http://iupac.pole-ether.fr/>) and JPL (<https://jpldataeval.jpl.nasa.gov/download.html>), there are still many gaps for the realistic and complex atmospheric chemistry. Laboratory studies supply a good approach to isolate and focus on an individual chemical reaction between simple components under relevant atmospheric conditions. And it also provides an effective method to conduct kinetic and mechanism studies. Such studies do provide a highly useful means of initially examining the emissions-air quality relationship under controlled conditions.

In the atmosphere, concentrations of trace gases depends on the rates of their chemical production and loss, as well as physical transport. Field measurements of atmospheric composition provide essential data and information on source mechanism, which can be used to test complement and accuracy of chemical mechanisms involved in atmospheric models and support to improve the model.

As presented above, this work will focus on NO₃ and aerosols. IBBCEAS instrument can be used to multi-species measurement. Considering the sensitivity, cost, operation, it can be used for several species, which will focus on NO₃ and aerosols in this work. To

better understand the sources, distribution and sinks of NO_3 and aerosols, the atmospheric concentrations are important to undertake a further study.

5 Thesis motivation

A thorough understanding and explanation of aerosol impact on light transmission in the atmosphere requires knowledge of aerosol optical properties. As introduced above, many techniques are devoted to detecting aerosol parameters. Lidar technique is a widely used method for field measurement of aerosol extinction. However due to its geometric structure, the missing information of aerosol extinction in its blind zone in the first hundreds of meters of the observation range is inevitable. One of the main objectives of this project involves the development of a portable IBBCEAS instrument for field measurements of aerosol optical properties and to test its agreement with lidar measurement results, in order to supply a potential solution for the missing information of aerosol extinction in the lidar blind zone.

And the bibliographic review has introduced and highlighted the concentrations in different environments and reactivities of NO_3 radicals, showing the challenge of detection in the atmosphere and laboratory. Another objective of the thesis is to build up an IBBCEAS system for laboratory studies of the $\text{NO}_3 + \text{VOCs}$ reactions, which could be used to simultaneously monitor the NO_3 temporal profiles.

References

- [1] P. J. Crutzen. The role of NO and NO₂ in the chemistry of the troposphere and stratosphere. *Annual review of earth and planetary sciences*, 1979, 7(1): 443-472. **10.1146/annurev.earth.07.050179.002303**
- [2] S. A. Penkett, P. S. Monks, L. J. Carpenter, K. C. Clemitshaw, G. P. Ayers, R. W. Gillett, I. E. Galbally, C. P. Meyer. Relationships between ozone photolysis rates and peroxy radical concentrations in clean marine air over the Southern Ocean. *Journal of Geophysical Research*, 1997, 102(D11)): 12805-12817. **10.1029/97JD00765**
- [3] B. J. Allan, N. Carslaw, H. Coe, R. A. Burgess, J. M. C. Plane. Observations of the nitrate radical in the marine boundary layer. *Journal of Atmospheric Chemistry*, 1999, 33(2): 129-154. **10.1023/A:1005917203307**
- [4] R. Atkinson, J. Arey. Gas-phase tropospheric chemistry of biogenic volatile organic compounds: a review. *Atmospheric Environment*, 2003, 37(Supplement 2): 197-219. **10.1016/s1352-2310(03)00391-1**
- [5] A. Geyer, B. Alicke, D. Mihelcic, J. Stutz, U. Platt. Comparison of tropospheric NO₃ radical measurements by differential optical absorption spectroscopy and matrix isolation electron spin resonance. *Journal of Geophysical Research*, 1999, 104(D21): 26097-26105. **10.1029/1999JD900421**
- [6] L. Vereecken, B. Aumont, I. Barnes, J. W. Bozzelli, M. J. Goldman, W. H. Green, S. Madronich, M. R. McGillen, A. Mellouki, J. J. Orlando, B. Picquet-Varrault, A. R. Rickard, W. R. Stockwell, T. J. Wallington, W. P. L. Carter. Perspective on mechanism development and structure-activity relationships for gas-phase atmospheric chemistry. *International Journal of Chemical Kinetics*, 2018, 50(6): 435-469. **10.1002/kin.21172**
- [7] M. Vrekoussis, M. Kanakidou, N. Mihalopoulos, P. J. Crutzen, J. Lelieveld, D. Perner, H. Berresheim, E. Baboukas. Role of the NO₃ radicals in oxidation processes in the eastern Mediterranean troposphere during the MINOS campaign. *Atmospheric Chemistry and Physics*, 2004, 4(1): 169-182. **10.5194/acp-4-169-2004**
- [8] A. Geyer, B. Alicke, S. Konrad, T. Schmitz, J. Stutz, U. Platt. Chemistry and oxidation capacity of the nitrate radical in the continental boundary layer near Berlin. *Journal of Geophysical Research: Atmospheres*, 2001, 106(D8): 8013-8025. **10.1029/2000jd900681**
- [9] U. Platt, B. Alicke, R. Dubois, A. Geyer, A. Hofzumahaus, F. Holland, M. Martinez, D. Mihelcic, T. Klüpfel, B. Lohrmann. Free radicals and fast photochemistry during BERLIOZ. *Journal of Atmospheric Chemistry*, 2002, 42(1): 359-394. **10.1023/A:1015707531660**

- [10] N. L. Ng, S. S. Brown, A. T. Archibald, E. Atlas, R. C. Cohen, J. N. Crowley, D. A. Day, N. M. Donahue, J. L. Fry, H. Fuchs, R. J. Griffin, M. I. Guzman, H. Herrmann, A. Hodzic, Y. Iinuma, J. L. Jimenez, A. Kiendler-Scharr, B. H. Lee, D. J. Luecken, J. Mao, R. McLaren, A. Mutzel, H. D. Osthoff, B. Ouyang, B. Picquet-Varrault, U. Platt, H. O. T. Pye, Y. Rudich, R. H. Schwantes, M. Shiraiwa, J. Stutz, J. A. Thornton, A. Tilgner, B. J. Williams, R. A. Zaveri. Nitrate radicals and biogenic volatile organic compounds: oxidation, mechanisms, and organic aerosol. *Atmospheric Chemistry and Physics*, 2017, 17(3): 2103-2162. **10.5194/acp-17-2103-2017**
- [11] Z. Ren-Jian, H. Kin-Fai, S. Zhen-Xing. The role of aerosol in climate change, the environment, and human health. *Atmospheric and Oceanic Science Letters*, 2012, 5(2): 156-161. **10.1080/16742834.2012.11446983**
- [12] J. Noxon, R. Norton, E. Marovich. NO₃ in the troposphere, *Geophysical Research Letters*, 1980, 7(2): 125-128. **10.1029/GL007i002p00125**
- [13] U. Platt, D. Perner, A. M. Winer, G. W. Harris, J. Pitts Jr. Detection of NO₃ in the polluted troposphere by differential optical absorption, *Geophysical Research Letters*, 1980, 7(1): 89-92. **10.1029/GL007i001p00089**
- [14] R. McLaren, R. A. Salmon, J. Liggitto, K. L. Hayden, K. G. Anlauf and W. R. Leitch. Nighttime chemistry at a rural site in the Lower Fraser Valley. *Atmospheric Environment*, 2004, 38(34): 5837-5848. **10.1016/j.atmosenv.2004.03.074**
- [15] S. S. Brown, J. Stutz. Nighttime radical observations and chemistry. *Chemical Society Reviews*, 2012, 41(19): 6405-6447. **10.1039/c2cs35181a**
- [16] J. Orphal, C. E. Fellows, P. M. Flaud. The visible absorption spectrum of NO₃ measured by high-resolution Fourier transform spectroscopy. *Journal of Geophysical Research*, 2003, 108(D3). **10.1029/2002jd002489**
- [17] S. S. Brown, H. D. Osthoff, H. Stark, W. P. Dubé, T. B. Ryerson, C. Warneke, J. A. de Gouw, A. G. Wollny, D. D. Parrish, F. C. Fehsenfeld, A. R. Ravishankara. Aircraft observations of daytime NO₃ and N₂O₅ and their implications for tropospheric chemistry. *Journal of Photochemistry and Photobiology A: Chemistry*, 2005, 176(1-3): 270-278. **10.1016/j.jphotochem.2005.10.004**
- [18] U. Platt, G. LeBras, G. Poulet, J. P. Burrows, G. Moortgat. Peroxy radicals from night-time reaction of NO₃ with organic compounds. *Nature*, 1990, 348(6297): 147-149. **10.1021/j100492a002**
- [19] S. R. Aliwell, R. L. Jones. Measurements of tropospheric NO₃ at midlatitude. *Journal of Geophysical Research: Atmospheres*, 1998, 103(D5): 5719-5727. **10.1029/97jd03119**

- [20] R. Atkinson, S. M. Aschmann, J. Arey. Reactions of hydroxyl and nitrogen trioxide radicals with phenol, cresols, and 2-nitrophenol at 296 ± 2 K. *Environmental Science & Technology*, 1992, 26(7): 1397-1403. **10.1021/es00031a018**
- [21] D. Mihelcic, A. Volz-Thomas, H. W. Pätz, D. Kley, M. Mihelcic. Numerical analysis of ESR spectra from atmospheric samples. *Journal of Atmospheric Chemistry*, 1990, 11(3): 271-297. **10.1007/bf00118353**
- [22] D. Mihelcic, P. Müsgen, D. H. Ehhalt. An improved method of measuring tropospheric NO₂ and RO₂ by matrix isolation and electron spin resonance. *Journal of Atmospheric Chemistry*, 1985, 3(3): 341-361. **10.1007/bf00122523**
- [23] L. G. Huey, D. R. Hanson, C. J. Howard. Reactions of SF₆⁻ and I⁻ with atmospheric trace gases. *The Journal of Physical Chemistry*, 1995, 99(14): 5001-5008. **10.1021/j100014a021**
- [24] W. L. Chang, P. V. Bhave, S. S. Brown, N. Riemer, J. Stutz, D. Dabdub. Heterogeneous atmospheric chemistry, ambient measurements, and model calculations of N₂O₅: a review. *Aerosol Science and Technology*, 2011, 45(6): 665-695. **10.1080/02786826.2010.551672**
- [25] D. L. Slusher, L. G. Huey, D. J. Tanner, F. M. Flocke, J. M. Roberts. A thermal dissociation–chemical ionization mass spectrometry (TD-CIMS) technique for the simultaneous measurement of peroxyacyl nitrates and dinitrogen pentoxide. *Journal of Geophysical Research*, 2004, 109(D19). **10.1029/2004JD004670**
- [26] X. Wang, T. Wang, C. Yan, Y. J. Tham, L. Xue, Z. Xu, Q. Zha. High concentrations of N₂O₅ and NO₃ observed in daytime with a TD-CIMS: chemical interference or a real atmospheric phenomenon? *Atmospheric Measurement Techniques Discussions*, 2013, 6(4): 7473-7504. **10.5194/amtd-6-7473-2013**
- [27] J. Nasse, P. G. Eger, D. Pöhler, S. Schmitt, U. Frieß, U. Platt. Recent improvements of long-path DOAS measurements: impact on accuracy and stability of short-term and automated long-term observations. *Atmospheric Measurement Techniques*, 2019, 12(8): 4149-4169. **10.5194/amt-12-4149-2019**
- [28] U. Brandenburger, T. Brauers, H. P. Dorn, M. Hausmann, D. H. Ehhalt. In-situ measurements of tropospheric hydroxyl radicals by folded long-path laser absorption during the field campaign POPCORN. *Journal of Atmospheric Chemistry*, 1998, 31(1/2): 181-204. **10.1023/a:1005909328924**
- [29] R. McLaren, P. Wojtal, D. Majonis, J. McCourt, J. D. Halla, J. Brook. NO₃ radical measurements in a polluted marine environment: links to ozone formation. *Atmospheric Chemistry and Physics*, 2010, 10(9): 4187-4206. **10.5194/acp-10-4187-2010**

- [30] S. Wang, R. Ackermann, J. Stutz. Vertical profiles of O₃ and NO_x chemistry in the polluted nocturnal boundary layer in Phoenix, AZ: I. Field observations by long-path DOAS. *Atmospheric Chemistry and Physics*, 2006, 6(9): 2671-2693. **10.5194/acp-6-2671-2006**
- [31] S. A. Nizkorodov, V. I. Makarov, I. V. Khmelinskii, S. A. Kotschubei, K. A. Amosov. LIF detection of NO₃ radical after pulsed excitation of NO₂ vapor at 436.45 nm. *Chemical Physics Letters*, 1994, 222(1-2): 135-140. **10.1016/0009-2614(94)00290-8**
- [32] T. Ishiwata, I. Fujiwara, Y. Naruge, K. Obi, I. Tanaka. Study of nitrate radical by laser-induced fluorescence. *The Journal of Physical Chemistry*, 1983, 87(8): 1349-1352. **10.1021/j100231a016**
- [33] E. Martinez, B. Cabañas, A. Aranda, P. Martin, S. Salgado. A temperature dependence study of the gas-phase reaction of the nitrate radical with 3-fluoropropene followed by laser induced fluorescence detection. *International Journal of Chemical Kinetics*, 1999, 29: 927-932. **10.1002/(SICI)1097-4601(1997)29:12<927::AID-KIN4>3.0.CO;2-O**
- [34] H. H. Nelson, L. Pasternack, J. R. McDonald. Laser-induced excitation and emission spectra of nitrate radical (NO₃). *The Journal of Physical Chemistry*, 1983, 87(8): 1286-1288. **10.1021/j100231a003**
- [35] E. C. Wood, T. H. Bertram, P. J. Wooldridge, R. C. Cohen. Measurements of N₂O₅, NO₂, and O₃ east of the San Francisco Bay. *Atmospheric Chemistry and Physics*, 2005, 5: 483-491. **10.5194/acp-5-483-2005**
- [36] M. D. King, E. M. Dick, W. R. Simpson. A new method for the atmospheric detection of the nitrate radical (NO₃). *Atmospheric Environment*, 2000, 34(5): 685-688. **10.1016/S1352-2310(99)00418-5**
- [37] S. S. Brown, H. Stark, S. J. Ciciora, A. R. Ravishankara. In-situ measurement of atmospheric NO₃ and N₂O₅ via cavity ring-down spectroscopy. *Geophysical Research Letters*, 2001, 28(17): 3227-3230. **10.1029/2001gl013303**
- [38] S. S. Brown, H. Stark, S. J. Ciciora, R. J. McLaughlin, A. R. Ravishankara. Simultaneous *in situ* detection of atmospheric NO₃ and N₂O₅ via cavity ring-down spectroscopy. *Review of Scientific Instruments*, 2002, 73(9): 3291-3301. **10.1063/1.1499214**
- [39] S. S. Brown. Absorption spectroscopy in high-finesse cavities for atmospheric studies. *Chemical Reviews*, 2003, 103(12): 5219-5238. **10.1021/cr020645c**
- [40] W. P. Dubé, S. S. Brown, H. D. Osthoff, M. R. Nunley, S. J. Ciciora, M. W. Paris, R. J. McLaughlin, A. R. Ravishankara. Aircraft instrument for simultaneous, *in situ*

- measurement of NO₃ and N₂O₅ via pulsed cavity ring-down spectroscopy. *Review of Scientific Instruments*, 2006, 77(3): 034101. **10.1063/1.2176058**
- [41] S. S. Brown, H. Stark, A. R. Ravishankara. Cavity ring-down spectroscopy for atmospheric trace gas detection: application to the nitrate radical (NO₃). *Applied Physics B*, 2002, 75(2-3): 173-182. **10.1007/s00340-002-0980-y**
- [42] M. Bitter, S. M. Ball, I. M. Povey, R. L. Jones. A broadband cavity ringdown spectrometer for in-situ measurements of atmospheric trace gases. *Atmospheric Chemistry and Physics*, 2005, 5(9): 2547-2560. **10.5194/acp-5-2547-2005**
- [43] S. M. Ball, R. L. Jones. Broad-band cavity ring-down spectroscopy. *Chemical Reviews*, 2003, 103(12): 5239-5262. **10.1021/cr020523k**
- [44] T. Wu, Q. Zha, W. Chen, Z. Xu, T. Wang, X. He. Development and deployment of a cavity enhanced UV-LED spectrometer for measurements of atmospheric HONO and NO₂ in Hong Kong. *Atmospheric Environment*, 2014, 95: 544-551. **10.1016/j.atmosenv.2014.07.016**
- [45] T. Wu, C. Coeur-Tourneur, G. Dhont, A. Cassez, E. Fertein, X. He, W. Chen. Simultaneous monitoring of temporal profiles of NO₃, NO₂ and O₃ by incoherent broadband cavity enhanced absorption spectroscopy for atmospheric applications. *Journal of Quantitative Spectroscopy and Radiative Transfer*, 2014, 133: 199-205. **10.1016/j.jqsrt.2013.08.002**
- [46] D. S. Venables, T. Gherman, J. Orphal, J. C. Wenger, A. A. Ruth. High sensitivity *in situ* monitoring of NO₃ in an atmospheric simulation chamber using incoherent broadband cavity-enhanced absorption spectroscopy. *Environmental Science & Technology*, 2006, 40(21): 6758-6763. **10.1021/es061076j**
- [47] R. Washenfelder, A. Langford, H. Fuchs, S. Brown. Measurement of glyoxal using an incoherent broadband cavity enhanced absorption spectrometer. *Atmospheric Chemistry and Physics*, 2008, 8(24): 7779-7793. **10.5194/acp-8-7779-2008**
- [48] R. M. Varma, D. S. Venables, A. A. Ruth, U. Heitmann, E. Schlosser, S. Dixneuf. Long optical cavities for open-path monitoring of atmospheric trace gases and aerosol extinction. *Applied Optics*, 2009, 48(4): B159-171. **10.1364/ao.48.00b159**
- [49] J. M. Langridge, S. M. Ball, A. J. Shillings, R. L. Jones. A broadband absorption spectrometer using light emitting diodes for ultrasensitive, *in situ* trace gas detection. *Review of Scientific Instruments*, 2008, 79(12): 123110. **10.1063/1.3046282**
- [50] H. Wang, J. Chen, K. Lu. Development of a portable cavity-enhanced absorption spectrometer for the measurement of ambient NO₃ and N₂O₅: experimental setup, lab characterizations, and field applications in a polluted urban environment. *Atmospheric Measurement Techniques*, 2017, 10: 1465-1479. **10.5194/amt-10-1465-2017**

- [51] A. Geyer, B. Alicke, D. Mihelcic, J. Stutz, U. Platt. Comparison of tropospheric NO₃ radical measurements by differential optical absorption spectroscopy and matrix isolation electron spin resonance. *Journal of Geophysical Research*, 1999, 104(D21): 26097-26105. **10.1029/1999jd900421**
- [52] J. Meinen, J. Thieser, U. Platt, T. Leisner. Technical Note: Using a high finesse optical resonator to provide a long light path for differential optical absorption spectroscopy: CE-DOAS. *Atmospheric Chemistry and Physics*, 2010, 10(8): 3901-3914. **10.5194/acp-10-3901-2010**
- [53] J. Matsumoto, N. Kosugi, H. Imai, Y. Kajii. Development of a measurement system for nitrate radical and dinitrogen pentoxide using a thermal conversion/laser-induced fluorescence technique. *Review of Scientific Instruments*, 2005, 76(6): 064101. **10.1063/1.1927098**
- [54] M. Le Breton, A. Bacak, J. B. A. Muller, T. J. Bannan, O. Kennedy, B. Ouyang, P. Xiao, S. Bauguette, D. E. Shallcross, R. L. Jones, M. Daniels, S. M. Ball, C. J. Percival. The first airborne comparison of N₂O₅ measurements over the UK using a CIMS and BBCEAS during the RONOCO campaign. *Analytical Methods*, 2014, 6(24): 9731-9743. **10.1039/c4ay02273d**
- [55] A. Saiz-Lopez, J.A. Shillito, H. Coe, J. M. C. Plane. Measurements and modelling of I₂, IO, OIO, BrO and NO₃ in the mid-latitude marine boundary layer. *Atmospheric Chemistry and Physics*, 2006, 6(6): 1513-1528. **10.5194/acp-6-1513-2006**
- [56] A. S. Mahajan, H. Oetjen, A. Saiz-Lopez, J. D. Lee, G. B. McFiggans, J. M. C. Plane. Reactive iodine species in a semi-polluted environment. *Geophysical Research Letters*, 2009, 36(16): L16803. **10.1029/2009gl038018**
- [57] M. Vrekoussis, E. Liakakou, N. Mihalopoulos, M. Kanakidou, P. Crutzen, J. Lelieveld. Formation of HNO₃ and NO₃⁻ in the anthropogenically-influenced eastern Mediterranean marine boundary layer. *Geophysical Research Letters*, 2006, 33 (L05811). **10.1029/2005GL025069**.
- [58] M. Vrekoussis, N. Mihalopoulos, E. Gerasopoulos, M. Kanakidou, P. J. Crutzen, J. Lelieveld. Two-years of NO₃ radical observations in the boundary layer over the Eastern Mediterranean. *Atmospheric Chemistry and Physics*, 2007, 7(2): 315-327. **10.5194/acp-7-315-2007**
- [59] J. Ambrose, H. Mao, H. Mayne, J. Stutz, R. Talbot, B. Sive. Nighttime nitrate radical chemistry at appledore island, maine during the 2004 international consortium for atmospheric research on transport and transformation, *Journal of Geophysical Research*, 2007, 112(D21302). **10.1029/2007JD008756**
- [60] J. Matsumoto, K. Imagawa, H. Imai, N. Kosugi, M. Ideguchi, S. Kato, Y. Kajii. Nocturnal sink of NO_x via NO₃ and N₂O₅ in the outflow from a source area in Japan.

- Atmospheric Environment*, 2006, 40(33): 6294-6302. **10.1016/j.atmosenv.2006.05.045**
- [61] J. N. Crowley, G. Schuster, N. Pouvesle, U. Parchatka, H. Fischer, B. Bonn, H. Bingemer, J. Lelieveld. Nocturnal nitrogen oxides at a rural mountain-site in south-western Germany. *Atmospheric Chemistry and Physics*, 2010, 10(6): 2795-2812. **10.5194/acp-10-2795-2010**
- [62] J. L. Fry, D. C. Draper, K. J. Zarzana, P. Campuzano-Jost, D. A. Day, J. L. Jimenez, S. S. Brown, R. C. Cohen, L. Kaser, A. Hansel, L. Cappellin, T. Karl, A. Hodzic Roux, A. Turnipseed, C. Cantrell, B. L. Lefer, N. Grossberg. Observations of gas- and aerosol-phase organic nitrates at BEACHON-RoMBAS 2011. *Atmospheric Chemistry and Physics*, 2013, 13(17): 8585-8605. **10.5194/acp-13-8585-2013**
- [63] N. Sobanski, M. J. Tang, J. Thieser, G. Schuster, D. Pöhler, H. Fischer, W. Song, C. Sauvage, J. Williams, J. Fachinger, F. Berkes, P. Hoor, U. Platt, J. Lelieveld, J. N. Crowley. Chemical and meteorological influences on the lifetime of NO₃ at a semi-rural mountain site during PARADE. *Atmospheric Chemistry and Physics*, 2016, 16(8): 4867-4883. **10.5194/acp-16-4867-2016**
- [64] H. Stark, S. Brown, K. Wong, J. Stutz, C. Elvidge, I. Pollack, T. Ryerson, W. Dube, N. Wagner, D. Parrish. City lights and urban air. *Nature Geoscience*, 2011, 4(11): 730-731. **10.1038/ngeo1300**
- [65] S. S. Brown, H. Stark, T. B. Ryerson, E. J. Williams, D. K. Nicks, M. Trainer, F. C. Fehsenfeld, A. R. Ravishankara. Nitrogen oxides in the nocturnal boundary layer: Simultaneous *in situ* measurements of NO₃, N₂O₅, NO₂, NO, and O₃. *Journal of Geophysical Research*, 2003, 108(D9). **10.1029/2002jd002917**
- [66] S. S. Brown, W. P. Dubé, H. D. Osthoff, D. E. Wolfe, W. M. Angevine, A. R. Ravishankara. High resolution vertical distributions of NO₃ and N₂O₅ through the nocturnal boundary layer. *Atmospheric Chemistry and Physics*, 2007, 7(1): 139-149. **10.5194/acp-7-139-2007**
- [67] S. S. Brown, W. P. Dubé, J. Peischl, T. B. Ryerson, E. Atlas, C. Warneke, J. A. de Gouw, S. te Lintel Hekkert, C. A. Brock, F. Flocke, M. Trainer, D. D. Parrish, F. C. Feshenfeld, A. R. Ravishankara. Budgets for nocturnal VOC oxidation by nitrate radicals aloft during the 2006 Texas Air Quality Study. *Journal of Geophysical Research*, 2011, 116(D24). **10.1029/2011jd016544**
- [68] A. K. Benton, J. M. Langridge, S. M. Ball, W. J. Bloss, M. Dall'Osto, E. Nemitz, R. M. Harrison, R. L. Jones. Night-time chemistry above London: measurements of NO₃ and N₂O₅ from the BT Tower. *Atmospheric Chemistry and Physics*, 2010, 10(20): 9781-9795. **10.5194/acp-10-9781-2010**

- [69] D. Stone, M. J. Evans, H. Walker, T. Ingham, S. Vaughan, B. Ouyang, O. J. Kennedy, M. W. McLeod, R. L. Jones, J. Hopkins, S. Punjabi, R. Lidster, J. F. Hamilton, J. D. Lee, A. C. Lewis, L. J. Carpenter, G. Forster, D. E. Oram, C. E. Reeves, S. Bauguitte, W. Morgan, H. Coe, E. Aruffo, C. Dari-Salisburgo, F. Giammaria, P. Di Carlo, D. E. Heard. Radical chemistry at night: comparisons between observed and modelled HO_x, NO₃ and N₂O₅ during the RONOCO project. *Atmospheric Chemistry and Physics*, 2014, 14(3): 1299-1321. **10.5194/acp-14-1299-2014**
- [70] J. K. Nøjgaard. Indoor measurements of the sum of the nitrate radical, NO₃, and nitrogen pentoxide, N₂O₅ in Denmark. *Chemosphere*, 2010, 79(8): 898-904. **10.1016/j.chemosphere.2010.02.025**
- [71] *Chapter 7 The Atmospheric Aerosol*. International Geophysics, Academic Press, 1988, 278-373.
- [72] *Chapter 4 Behavior of aerosol particles*. Inhaled Particles, Elsevier, 2005, 55-78.
- [73] J.T. Houghton, J. Bruce, H. Lee, B. A. Callander, E. Haites, N. Harris, K. Maskell. Climate change 1994: radiative forcing of climate change and an evaluation of the IPCC IS92 emission scenarios. *IPCC Report*, 1994.
- [74] J. H. Seinfeld, S. Pandis. Atmospheric chemistry and physics : from air pollution to climate change, John Wiley & Sons, 2016.
- [75] M. Pyrina, N. Hatzianastassiou, C. Matsoukas, A. Fotiadis, C. D. Papadimas, K. G. Pavlakis, I. Vardavas. Cloud effects on the solar and thermal radiation budgets of the Mediterranean basin. *Atmospheric Research*, 2015, 152: 14-28. **10.1016/j.atmosres.2013.11.009**
- [76] A. Abo Rizeq, C. Erlick, E. Dinar, Y. Rudich. Optical properties of absorbing and non-absorbing aerosols retrieved by cavity ring down (CRD) spectroscopy. *Atmospheric Chemistry and Physics*, 2007, 7: 1523-1536. **10.5194/acp-7-1523-2007**
- [77] M. Shiraiwa, K. Ueda, A. Pozzer, G. Lammel, C. J. Kampf, A. Fushimi, S. Enami, A. M. Arangio, J. Frohlich-Nowoisky, Y. Fujitani, A. Furuyama, P. Lakey, J. Lelieveld, K. Lucas, Y. Morino, U. Poschl, S. Takahama, A. Takami, H. Tong, B. Weber, A. Yoshino, K. Sato. Aerosol health effects from molecular to global scales. *Environmental Science & Technology*, 2017, 51(23): 13545-13567. **10.1021/acs.est.7b04417**
- [78] S. Undorf, M. A. Bollasina, G. C. Hegerl. Impacts of the 1900-74 increase in anthropogenic aerosol emissions from North America and Europe on Eurasian summer climate. *Journal of Climate*, 2018, 31(20): 8381-8399. **10.1175/jcli-d-17-0850.1**

- [79] G. Myhre, C. E. Myhre, B. H. Samset, T. Storelvmo. Aerosols and their relation to global climate and climate sensitivity. *Nature Education Knowledge*, 2013, 4(5):7.
- [80] B. L. Zhuang, S. Li, T. J. Wang, J. J. Deng, M. Xie, C. Q. Yin, J. L. Zhu. Direct radiative forcing and climate effects of anthropogenic aerosols with different mixing states over China. *Atmospheric Environment*, 2013, 79: 349-361. **10.1016/j.atmosenv.2013.07.004**
- [81] E. Marmer, B. Langmann, H. Fagerli, V. Vestreng. Direct shortwave radiative forcing of sulfate aerosol over Europe from 1900 to 2000. *Journal of Geophysical Research*, 2007, 112(D23). **10.1029/2006jd008037**
- [82] B. E. Wyslouzil, J. Wolk. Overview: Homogeneous nucleation from the vapor phase-The experimental science. *The Journal of Chemical Physics*, 2016, 145(21): 211702. **10.1063/1.4962283**
- [83] T. Chen, Y. Liu, Q. Ma, B. Chu, P. Zhang, C. Liu, J. Liu, H. He. Significant source of secondary aerosol: formation from gasoline evaporative emissions in the presence of SO₂ and NH₃. *Atmospheric Chemistry and Physics*, 2019, 19(12): 8063-8081. **10.5194/acp-19-8063-2019**
- [84] Y. Wu, J. Liu, J. Zhai, L. Cong, Y. Wang, W. Ma, Z. Zhang, C. Li. Comparison of dry and wet deposition of particulate matter in near-surface waters during summer. *PLoS One*, 2018, 13(6): e0199241. **10.1371/journal.pone.0199241**
- [85] M. O. Andreae, P. J. Crutzen. Atmospheric aerosols: biogeochemical sources and role in atmospheric chemistry. *Science (New York, N.Y.)*, 1997, 276(5315): 1052-1058. **10.1126/science.276.5315.1052**
- [86] W. J. Glantschnig, S. H. Chen. Light scattering from water droplets in the geometrical optics approximation. *Applied Optics*, 1981, 20(14): 2499-2509. **10.1364/AO.20.002499**
- [87] K. Krogs , M. Henneberg, R. Eriksen. Model of a light extinction sensor for assessing wear particle distribution in a lubricated oil system. *Sensors*, 2018, 18(12): 4091. **10.3390/s18124091**
- [88] T. Rosenberger, D. Kiesler, E. Hontela, D. Fuentes, E. Ramiro, F. E. Kruis. Design and optimization of a medium flow differential mobility analyzer (MF-DMA) for classification of high-density particles. *Aerosol Science and Technology*, 2019, 53(10): 1172-1185. **10.1080/02786826.2019.1642443**
- [89] A. Geisinger, A. Behrendt, V. Wulfmeyer, J. Strohbach, J. F rstner, R. Potthast. Development and application of a backscatter lidar forward operator for quantitative validation of aerosol dispersion models and future data assimilation. *Atmospheric Measurement Techniques*, 2017, 10(12): 4705-4726. **10.5194/amt-10-4705-2017**

- [90] EZ aerosol and cloud LIDAR ALS300, LEOSPHERE Company. http://www.lisa.u-pec.fr/~formenti/Tools/Manuals/LIDAR/ALS300-450_UserManual.pdf

Chapter II Experimental platforms

In this chapter, the experimental systems involved in the present PhD work will be introduced and discussed, including (1) instruments based on IBBCEAS dedicated to laboratory studies and field campaign applications, (2) simulation chamber and associated analytical instruments.

1 IBBCEAS technique

As optical methods being used for spectral absorption measurements, the IBBCEAS technique is the most suitable method for chamber application: optical observation of chemical reaction without sampling, non-invasive and *in situ* real time.

IBBCEAS was firstly introduced by Ruth's group in 2003 [1]. In this technique, an incoherent broadband light beam is coupled into a cavity, formed by two mirrors with high reflectivity, to probe absorption information of the target chemical species (gases or/and aerosols), light leaking from the high optical finesse cavity is then dispersed with a grating monochromator and detected by a sensitive photodiode array or charge-coupled device (CCD) array. Concentration of the absorbers or/and aerosol extinction coefficients could be retrieved by a least-square algorithm.

1.1 IBBCEAS for trace gas detection

A typical diagram of cavity enhanced spectroscopic method is shown in Fig.II-1. The optical cavity with a length of d is formed by two mirrors with reflectivities R_1 and R_2 , respectively. The input intensity of incoherent light to the cavity is represented by I_{in} .

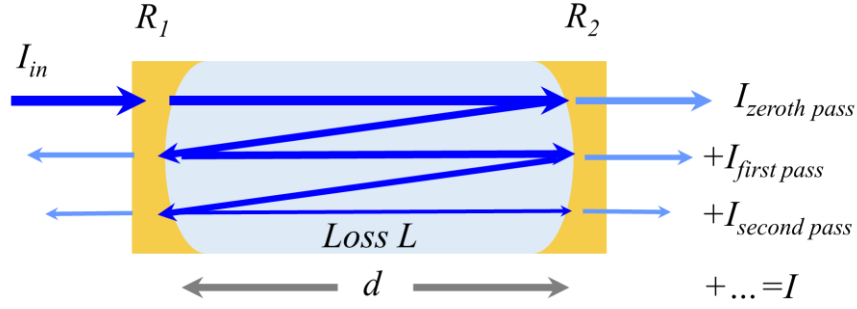


Figure II-1 Light transmission in an optical cavity.

Assuming no light absorption by the cavity mirrors, the transmission of the cavity mirror is then $(1 - R)$. Considering that optical losses per pass through the cavity is L due to absorption losses by absorbers, the light transmission factor inside the cavity is thus $(1 - L)$. The total leaking light intensity from the cavity, I , can be expressed as the sum of each individual light intensity leaked from the cavity [1]:

$$\begin{aligned}
 I &= I_{in} (1 - R_1)(1 - L)(1 - R_2) + \\
 &\quad I_{in} (1 - R_1)(1 - L)R_2(1 - L)R_1(1 - L)(1 - R_2) \\
 &\quad + \dots + \\
 &\quad I_{in} (1 - R_1)(1 - L)R_1^n R_2^n (1 - L)^{2n} (1 - R_2) \\
 &\quad + \dots + \\
 &= I_{in} (1 - R_1)(1 - R_2)(1 - L) \sum_{n=0}^{\infty} R_1^n R_2^n (1 - L)^{2n}
 \end{aligned} \tag{Eq.2}$$

Since $R < 1$ and $L < 1$, according to the geometric progression, Eq.2 can be transformed into the following equation [1]:

$$I = I_{in} \frac{(1 - R_1)(1 - L)(1 - R_2)}{1 - R_1 R_2 (1 - L)^2} \tag{Eq.3}$$

When the cavity is *empty* (without any absorber), $L = 0$ and I_0 can be retrieved:

$$I_0 = I_{in} \frac{(1 - R_1)(1 - R_2)}{1 - R_1 R_2} \tag{Eq.4}$$

Dividing Eq.4 by Eq.3, the single-pass loss $(1-L)$ can be expressed as the difference between the light intensity measured in a cavity filled with absorbers (I) and that without the absorbers (I_0) :

$$\frac{I_0}{I} = \frac{I_{in} \frac{(1-R_1)(1-R_2)}{1-R_1R_2}}{I_{in} \frac{(1-R_1)(1-R_2)(1-L)}{1-R_1R_2(1-L)^2}} = \frac{1-R_1R_2(1-L)^2}{(1-R_1R_2)(1-L)}$$

which can be converted to

$$(1-L)^2 + \frac{I_0}{I} \frac{(1-R_1R_2)}{R_1R_2} (1-L) - \frac{1}{R_1R_2} = 0$$

for which the roots are

$$(1-L) = \pm \sqrt{\frac{1}{4} \left(\frac{I_0}{I} \frac{1-R_1R_2}{R_1R_2} \right)^2} + \frac{1}{R_1R_2} - \frac{1}{2} \frac{I_0}{I} \frac{1-R_1R_2}{R_1R_2} \quad (\text{Eq.5})$$

As $0 < L < 1$, the negative root is unrealistic.

Assuming the loss per pass only lies in the Lambert–Beer law, i.e. $1 - L = \exp(-\alpha d)$ and $R_1 = R_2 = R$, the absorption coefficient α , can be written in the following general form:

$$\alpha = \frac{1}{d} \left| \ln \left(\frac{1}{2R^2} \left(\sqrt{4R^2 + \left(\frac{I_0}{I} (R^2 - 1) \right)^2} + \frac{I_0}{I} (R^2 - 1) \right) \right) \right| \quad (\text{Eq.6})$$

It should be noted that no approximation regarding of either α or R was made to derive Eq.6, which is thus applicable in the condition of a large absorption and a small reflectivity. In case of a small loss per pass ($L \rightarrow 0$), and a high reflectivity ($R \rightarrow 1$), the absorption coefficient in Eq. 6 can be approximated by [2]:

$$\alpha \approx \frac{1}{d} \left(\frac{I_0}{I} - 1 \right) (1-R) \quad (\text{Eq.7})$$

This equation Eq.7 implies an effective optical length $L_{eff} = d/(1 - R)$, increasing by a factor of $(1-R)^{-1}$ compared with the single pass length d , and it will be $(1 - (R_1 R_2)^{0.5})^{-1}$ times d in case of a more common condition $R_1 \neq R_2$. Moreover, the signal-to-noise ratio (SNR) is increased by a maximum factor of $[2(1-R)]^{-1/2}$ [3].

Compared to the minimum absorption that can be detected by conventional single pass absorption spectroscopy (Eq.8) [1],

$$a_{min,single} = \frac{I}{d} \left(1 - \frac{I_{min,single}}{I_{0,single}} \right) \quad (\text{Eq.8})$$

IBBCEAS technique has a minimum absorption coefficient of (Eq.8) approximating $(I_0 - I)/I_0 \approx (I_0 - I)/I$:

$$a_{min,IBBCEAS} = \frac{I}{d} \left(1 - \frac{I_{min,IBBCEAS}}{I_{0,IBBCEAS}} \right) (1 - R) \quad (\text{Eq.9})$$

$I_{min,single}$ and $I_{min,IBBCEAS}$ are the minimum detectable light intensities by absorption for single pass spectroscopy and IBBCEAS. Assuming the same path length d , the IBBCEAS detection limit would be lowered by a factor of $(1-R)^{-1}$ due to the improvement of effective length. An IBBCEAS cavity with a mirror reflectivity of 99.5% will correspond to an enhancement factor of 200 compared to the single pass method.

1.2 Retrieval of trace gas concentrations and aerosol extinction coefficients

The IBBCEAS technique has been widely used for highly sensitive measurement of trace gas concentrations and aerosol extinction. The main advantages of this method is its capacity of simultaneous detection of multiple species using one single instrument involving a broadband light.

The single pass loss was assumed to be caused by absorption of sampled absorber in the discussion above. In fact, in addition to the gas absorption, the Rayleigh scattering by the gas and the Mie scattering by the aerosol particles inside the cavity both contribute to

the total light losses. Therefore, in order to accurately invert the concentration of the absorber, it is vital to take the effects of Rayleigh and Mie scatterings into account.

Let's consider an optical cavity of a length d and formed with two high reflectivity ($R(\lambda)$) mirrors. The cavity is continuously illuminated by a broadband light source I_{source} . The light intensity I_{cavity} inside the cavity depends on the losses due to mirror reflectivity ($R(\lambda)$), extinctions of gas $\alpha_{ext,gas}(\lambda)$ and aerosol $\alpha_{ext,aerosol}(\lambda)$ inside the cavity. The light intensity I_{cavity} can be expressed as Eq.10 [4, 5]:

$$\frac{dI_{cavity}(\lambda)}{dt} = c \left(-\frac{1-R(\lambda)}{d} - \alpha_{ext,gas}(\lambda) - \alpha_{ext,aerosol}(\lambda) \right) I_{cavity}(\lambda) + ck_s I_{source}(\lambda) \quad (\text{Eq.10})$$

where c is the speed of light in vacuum and k_s is an arbitrary constant to describe the coupling efficiency of the light intensity into the cavity. The differential dt is the finite time step of a single pass within the cavity, and the differential dI_{cavity} stands for the finite light intensity step of a single pass within the cavity.

The intensity transmitted by the cavity $I(\lambda)$ is observed when Eq.10 has reached a steady state between the source input and the cavity losses, which results in the differential equal to zero. With $dI_{cavity}/dt = 0$, the transmitted intensity $I(\lambda)$ having a proportionality constant (k_c) to I_{cavity} is given as [4]:

$$I(\lambda) = k_c I_{cavity}(\lambda) = \frac{k_c k_s I_{source}(\lambda)}{\frac{1-R(\lambda)}{d} + \alpha_{ext,gas}(\lambda) + \alpha_{ext,aerosol}(\lambda)} \quad (\text{Eq.11})$$

where the gas extinction coefficient $\alpha_{ext,gas}(\lambda)$ is the sum of gas absorption coefficient $\alpha_{abs,gas}(\lambda)$ and scattering coefficient $\alpha_{scat,gas}(\lambda)$, and the aerosol extinction $\alpha_{ext,aerosol}(\lambda)$ is the sum of aerosol absorption coefficient $\alpha_{abs,aerosol}(\lambda)$ and aerosol scattering coefficient $\alpha_{scat,aerosol}(\lambda)$.

When the cavity is *empty* (with only N_2 inside the cavity), both the aerosol extinction $\alpha_{ext,aerosol}(\lambda)$ and the air absorption $\alpha_{abs,air}(\lambda)$ will be zero. Because the Rayleigh scattering cross section of air (78.1% N_2 and 20.9% O_2) is close to that of N_2 , air scattering coefficient $\alpha_{scat,air}(\lambda)$ can be considered as the same with that of gas $\alpha_{scat,gas}(\lambda)$ and N_2

$\alpha_{Ray,N_2}(\lambda)$ [6], such that $\alpha_{scat,gas}(\lambda) = \alpha_{scat,air}(\lambda) = \alpha_{Ray,N_2}(\lambda)$. And the reference intensity $I_0(\lambda)$ will be:

$$I_0(\lambda) = \frac{k_c k_s I_{source}(\lambda)}{\frac{1-R(\lambda)}{d} + \alpha_{scat,gas}(\lambda)} = \frac{k_c k_s I_{source}(\lambda)}{\frac{1-R(\lambda)}{d} + \alpha_{Ray,N_2}(\lambda)} \quad (\text{Eq.12})$$

Combining Eq.11 and Eq.12, we can obtain Eq.13:

$$\frac{I_0(\lambda) - I(\lambda)}{I(\lambda)} = \frac{\alpha_{abs,gas}(\lambda) + \alpha_{ext,aerosol}(\lambda)}{\frac{1-R(\lambda)}{d} + \alpha_{Ray,N_2}(\lambda)} \quad (\text{Eq.13})$$

and a linear relationship to the sum of the trace gas and aerosol extinction coefficients can be derived as (Eq.14) :

$$\begin{aligned} \alpha_{abs,gas}(\lambda) + \alpha_{ext,aerosol}(\lambda) &= \sum_i \alpha_i(\lambda) \\ &= \left(\frac{1-R(\lambda)}{d} + \alpha_{Ray,N_2}(\lambda) \right) \left(\frac{I_0(\lambda) - I(\lambda)}{I(\lambda)} \right) \end{aligned} \quad (\text{Eq.14})$$

The absorption of trace gas and extinction of aerosol are governed by the Lambert-Beer's Law [7]:

$$\alpha_{abs,gas}(\lambda) + \alpha_{ext,aerosol}(\lambda) = \sum_i n_i \sigma_i(\lambda) + P(\lambda) \quad (\text{Eq.15})$$

where n_i and σ_i are the number concentration and the reference cross section for the i^{th} gas species, respectively. $P(\lambda)$, a polynomial offset varying from linear to fifth order, is used to account for the sum of variation in spectral baseline $P_0(\lambda)$ and aerosol extinction $\alpha_{ext,aerosol}(\lambda)$.

Trace gas concentrations n_i can be simultaneously quantified by fitting the right side of Eq.15 to the right side (experimental data) of Eq.14. Aerosol extinction $\alpha_{ext,aerosol}(\lambda)$ will be retrieved by the difference of $P(\lambda)$ and spectral baseline $P_0(\lambda)$, which are the polynomial in Eq.15 when cavity is filled with sample and N_2 , respectively.

1.3 Development of two IBBCEAS systems for field and chamber measurements

During my PhD work, two systems based on IBBCEAS have been developed for the measurement of aerosol extinction and NO₃ radical, respectively.

1.3.1 A portable IBBCEAS for field measurement of aerosol extinction

The development of this setup is based on previous works at the LPCA [8]. As shown in Fig.II-2, a light emitting diode (LED) (Nichia, NCSU033AT), emitting ~250 mW optical power in the UV spectral region around 365 nm, was used as broadband (350 - 400 nm) light source. The UV LED was mounted on a temperature controlled copper plate to stabilize the optical intensity and LED spectral distribution. The temperature of the copper plate was stabilized at 20 °C \pm 0.01 °C with the help of a temperature sensor (Analog Device, AD590) and a single stage thermoelectric cooler (TEC, Supercool). A laser diode controller (Stanford Research System, LDC501) was used to power both the TEC and the UV LED. The optical cavity was formed with two high reflectivity mirrors (Layertec GmbH) separated by a distance of ~182 cm. The mirrors had 25 mm in diameter, 2 m radius of curvature and a reflectivity of ~99.97% between 340 and 370 nm (as specified by the manufacturer). The light from the LED was directly focused into the cavity with a UV lens ($f = 75$ mm). In order to avoid CCD saturation, a UV band-pass filter (Semrock) was placed between the focusing lens and the cavity to block the light at undesirable wavelengths (<364 nm and >378 nm). Light transmitted through the cavity was collected using a second UV lens ($f = 75$ mm) into a multimode optical fiber (1000 μ m in diameter with a numerical aperture of 0.22), and then transferred to a CCD spectrometer (Oceanoptics, QE 65000) for spectral dispersion and absorption signal measurement. The spectrometer was equipped with a 25 μ m entrance slit, a 600 grooves/mm grating and a 2048 pixels linear CCD array, which allowed covering the whole 290-480 nm wavelength range with a spectral resolution of 0.53 nm around 360 nm. The characterization and performances of the setup will be described in Chapter III.

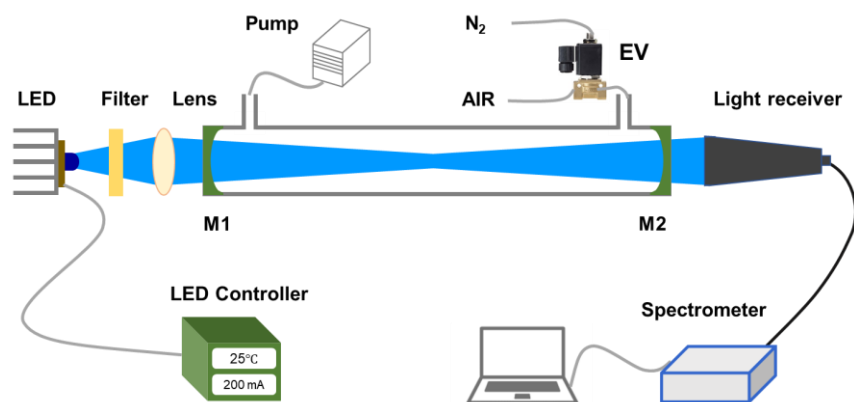


Figure II-2 Setup of IBBCEAS for field measurement. M1, M2, cavity mirrors; EV, electronic valve.

1.3.2 Open-path IBBCEAS in CHARME chamber for monitoring NO_3 radicals

Another IBBCEAS system (Fig.II-3) was designed and installed in an atmospheric simulation chamber called CHARME (CHamber for the Atmospheric Reactivity and the Metrology of the Environment) for NO_3 detection during study of NO_3 oxidation of VOCs.

A commercial high-power red LED (Thorlabs, M660L4) emitting around 660 nm with 940 mW optical power was used as broadband light source for IBBCEAS. The red LED was powered with a current driver (Thorlabs, LEDD18) at 1200 mA and mounted on an Ø30.5 mm heat sink to stabilize the output optical intensity and spectral distribution of the LED. High optical finesse cavity was composed of two mirrors facing each other on the simulation chamber walls with a distance of 482 cm. The LED light was focused into the center of the chamber cavity. The cavity mirrors had an estimated reflectivity of >99.99% by vendor for the region of 620-680 nm (Layertec). In order to avoid spectrometer saturation, a band-pass filter (Semrock, FF01-655/40-25) was placed between the lens and the cavity mirror to pass the light of wavelength from 635 nm to 675 nm with > 93% transmission. The light beam (diameter ~20 mm) transmitted through the cavity was first collected with a lens ($f = 100$ mm) into a single multimode optical fiber (1000 μm in diameter with a numerical aperture of 0.22), and then transferred to a CCD spectrometer (Oceanoptics, QE Pro) for spectral dispersion and absorption signal

measurement. The spectrograph was equipped with a 50 μm entrance slit, a 600 grooves/mm grating and a 1024 pixels linear CCD array, which allowed covering the whole 570-732 nm spectral range with a spectral resolution of 0.42 nm. The characterization and performances of the setup will be described in Chapter IV.

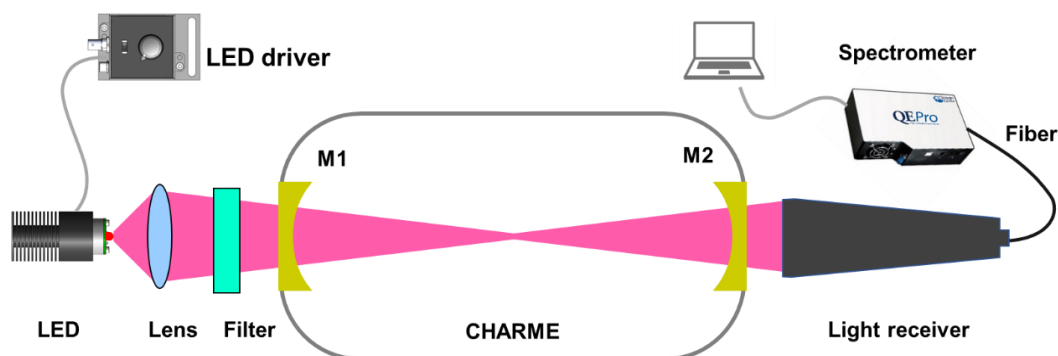


Figure II-3 Setup of IBBCEAS for chamber application. M1, M2: cavity mirrors.

2 The atmospheric simulation chamber CHARME

2.1 Description and features

Since it is tricky to separate the chemistry from the complex meteorology and reaction processes in the atmosphere, an atmospheric simulation chamber is one of the most direct tools to investigate the relationships between the formation and the evolution of atmospheric compounds, by providing a relatively controllable environment and focusing on the specific compounds of interest.

As mentioned in the previous section, such a chamber called CHARME (CHamber for the Atmospheric Reactivity and the Metrology of the Environment) aiming at studying atmospheric physical and chemical processes has been developed in the Laboratoire de Physico-Chimie de l'Atmosphère (LPCA), Dunkirk, France in 2010 as presented in Fig.II-4 (a).

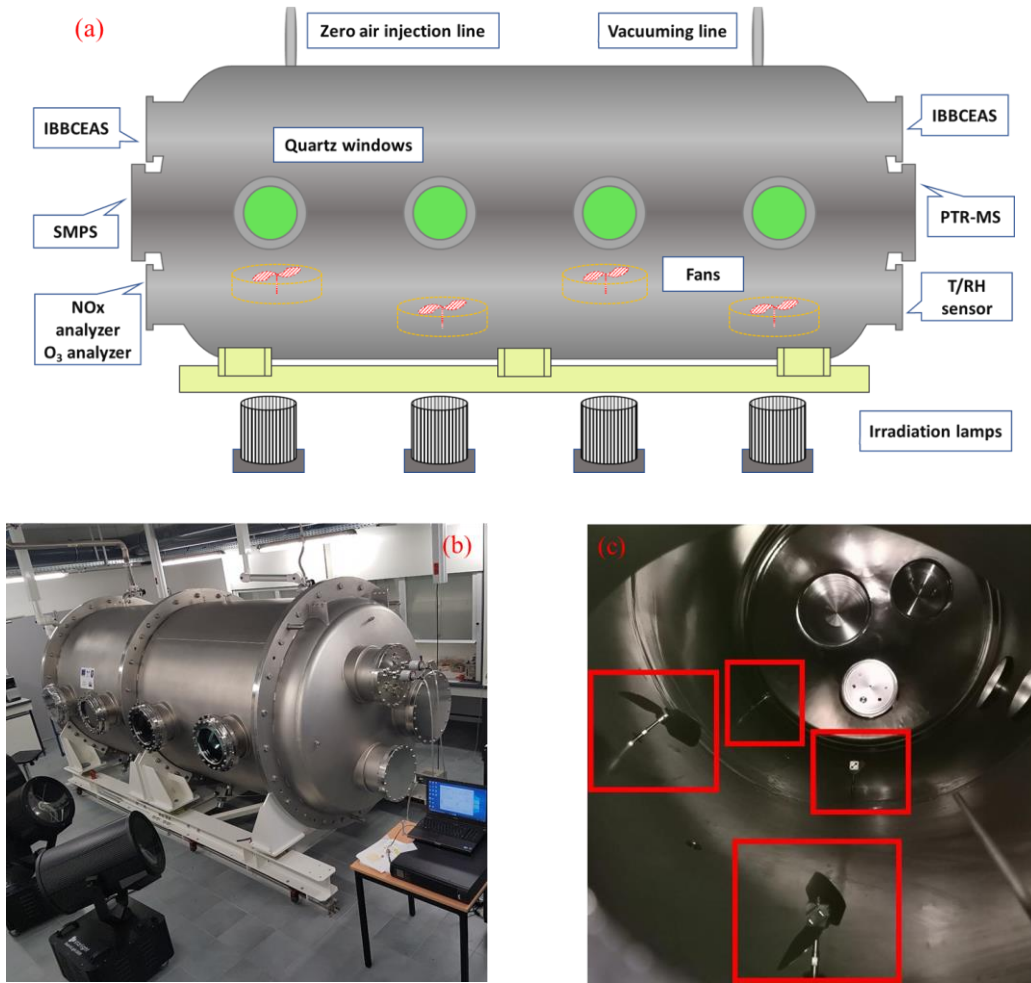


Figure II-4 Installation of CHARME: (a) Schematic of CHARME with main design; (b) Irradiation systems and general view; (c) Mixing fans inside CHARME.

The 9.2 m³ chamber reactor is made of stainless steel type 304 L to be chemically inert, and it has a cylindrical shape with horizontal linear structure by the dimensions of 4.40 m × Ø 1.68 m. CHARME has an internal surface of 30-32 m² (with ports and flanges).

The walls of CHARME consist of double layers allowing circulation of thermal fluids to vary the chamber temperature between -20 and +50 °C (available in the medium term), and the rigid steel within 4~40 mm thickness allows the chamber to reach a vacuum without deformation of the flange (pressure ranging from 0.4 mbar to 1 bar). The inner surface of CHARME has been polished and electrochemically treated, which increase the

light reflection inside the chamber and reduce the interaction between compounds and the walls materials.

Four windows with dimension of $\varnothing 25 \text{ cm} \times 24 \text{ mm}$ thickness, made of quartz shown in Fig.II-4 (b), are installed on the longitudinal side of the chamber and used to introduce the radiation into the chamber, which allows transmission of spectrum between 230 and 3600 nm. The irradiating emission spectrum of correctly-filtered lamps is shown in Fig.II-5(a), which matches the solar spectrum well in the visible wavelength range. The quartz material transmission is almost higher than 90% for the range of 230 ~ 2500 nm, shown in Fig.II-5(b). Also the quartz material can withstand vacuum without deformation or breakage. The irradiation source consists of 4 Xenon arc lamps (5 kW, SKY TRACER 5000). The light projectors have been adjusted and fixed at a proper distance ($\sim 0.7 \text{ m}$) from the quartz windows and a proper height ($\sim 1.2 \text{ m}$) from the ground to directly point at the windows, which is to have wide projected spots and get rid of the concentrated warming effect on one point on the inner wall.

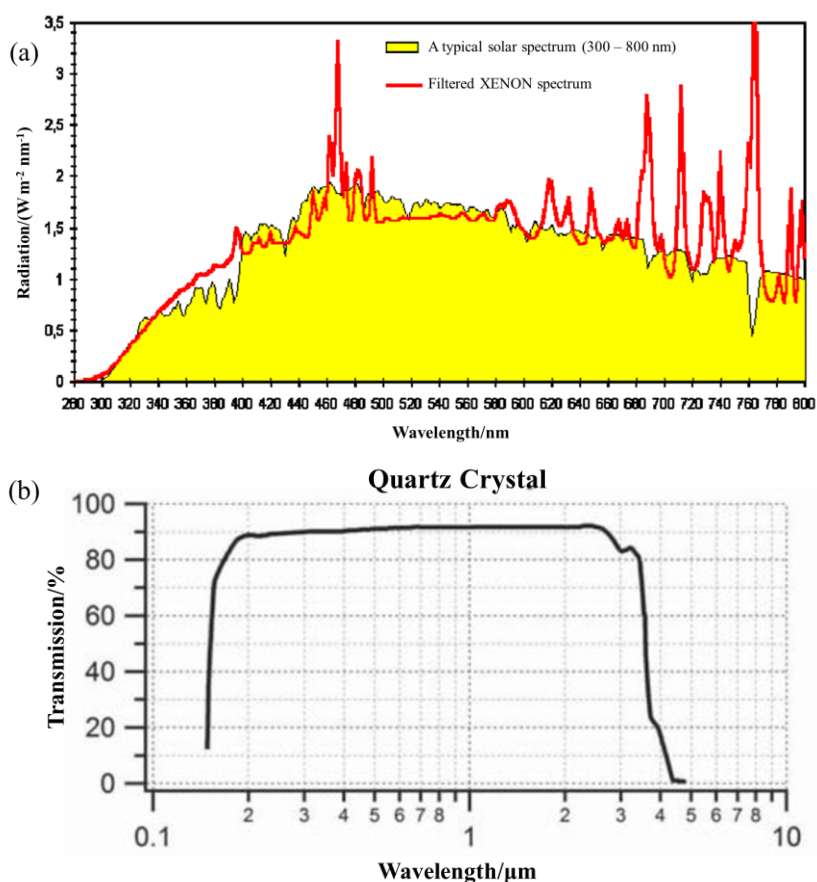


Figure II-5 (a) Comparison of solar and filtered xenon spectra; (b) Quartz material transmission (<https://www.vacom.de/en/downloads/vacom-product-catalog>).

To have a good homogeneity, four stainless steel fans are installed at the bottom of the reactor, shown in Fig.II-4 (c). The rotating speed of each fan (maximum of 330 revolutions per minute - RPM) can be controlled by the input power voltage.

Table II-1 Characteristics of CHARME.

Charateristics	
Material	Electropolished 304 L stainless steel
Shape	Cylindrical
Volume	9.2 m ³ (Ø 1.68 m × L 4.40 m)
Surface-to-volume ratio	3.5 m ⁻¹
Irradiation	4 xenon arc lamps (5 kW)
Air source	Air generator (Parker KA-1-MT8)
Agitation	4 fans (Ø 50 cm), RPM= 330
Temperature	Indoor temperature (293 ± 1 K) Medium term: -20 to + 50 °C (double layer)
Pressure	Evacuable, 0.4 mbar - 1 bar
Pumping system	110 m ³ /h, Cobra NC0100-0300B

2.2 Associated instruments

The instruments associated to the chamber to measure the gaseous and particulate compounds are listed in Tab.II-2 and their specific parameters are described in the following sections.

Table II-2 Analytical instruments associated to CHARME.

Instruments	Target	Range
-------------	--------	-------

T/RH Sensor (Vaisala HUMICAP HMT330)	Temperature; Relative Humidity (RH)	-70 °C - 180 °C 0 - 100%
O ₃ analyzer (photometry UV) (Thermo Scientific 49i)	O ₃	0.5 ppbv - 200 ppmv
NO _x analyzer (chemiluminescence using a molybdenum convertor) (Thermo Scientific 42i)	NO, NO ₂	0.4 ppbv - 100 ppmv
Turbomatrix - GC (Autosystem XL) - FID, off-line Perkin Elmer	VOCs Organic Aerosols (denuder / filter)	pptv - ppmv
PTR-ToF-MS (Ionicon 1000) On-line	VOCs	pptv - ppmv
SMPS (CPC TSI 3775 - DMA 3082)	Aerosols	4 - 1000 nm 10 - 3000 nm; 10 ⁴ Particles/cm ³
CPC (TSI 3010) LC-MS (Agilent LC 1100 - MS 6540)	Aerosols	Chemical compositions

2.2.1 Gas-phase analysis

2.2.1.1 Proton Transfer Reaction-Time of Flight Mass Spectrometry (PTR-ToF-MS)

The PTR-ToF-MS (Ionicon 1000) is used to monitor the VOC concentrations in CHARME. The fundamental ionization process in a PTR-ToF-MS instrument can be written as:



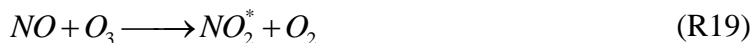
During the reaction of protonated water (H_3O^+) with VOC molecule R (R18), a proton H^+ transfers from hydronium ion to R , leading to a protonated and ionized molecule RH^+ and a neutral water molecule. This reaction is energetically possible for all VOCs, whose proton affinity is higher than that of water (691 kJ/mol [10]). Then the VOCs concentration in the sample could be theoretically calculated using Eq.16,

$$[VOCs]_{ppbv} = \frac{1}{k \cdot t} \cdot \frac{[RH^+]}{[H_3O^+]} \quad (Eq.16)$$

where k is a reaction rate coefficient of R 18, t is the reaction time that the ions need to pass the drift tube. Normally the value of k could be found in literature for many substances (alternatively it also can be calculated or experimentally determined). The ToF-MS analyzer will record the mass-to-charge (m/z) ratio and the abundance of various ions.

2.2.1.2 Chemiluminescence NO_x analyzer

Chemiluminescence [11] is the reference method recommended by the European legislation [12] and the US EPA [13] to measure NO_x atmospheric concentrations, and it is a commonly used technique for the measurement of NO₂ in monitoring networks. It is based on the reaction of nitric oxide (NO) with ozone which generates nitric dioxide (NO₂, reaction R19) in an electronically excited state and it then falls back to the ground state by emitting light (reaction R20):



In this process the emitted luminescence is proportional to the NO concentration. This technique can also measure NO₂, but it has first to be transformed into NO by a molybdenum converter heated to about 325 °C. The NO and sum of NO + NO₂ concentrations are determined in the NO and NO_x modes, and the concentration of NO₂ could be deduced from the difference of the values from these two modes. A photomultiplier tube installed on in the reaction chamber detects the luminescence generated during this reaction.

Chemiluminescence has a sensitivity of ~ 0.40 ppbv within 1 min, its main drawback is that NO_y (HONO, HNO₃ and other active nitrogen oxides) may introduce interferences, as they may also be converted into NO by the molybdenum convertor.

2.2.1.3 Ozone analyzer

The Thermo Scientific™ Model 49i ozone analyzer uses UV photometric technology to measure the concentrations of ozone in air from 0.05 ppbv to 200 ppmv.

This instrument operates on the principle that O_3 molecules absorb UV light at a wavelength of 254 nm. The air is pumped into the analyzer and split into two streams, one flows through an ozone scrubber to reference cell, and the other one directly flows to sample cell. The degree to which the UV light is absorbed is directly related to the ozone concentration as described by the Beer-Lambert Law [14]:

$$\frac{I}{I_0} = e^{-\alpha \cdot L \cdot C} \quad (\text{Eq.17})$$

where α is the molecular absorption coefficient, (at 0 °C and 1 atmosphere), L is the length of cells (38 cm), C stands for ozone concentration in parts per million (ppmv), I is the UV light intensity of the sample (with ozone) in the sample cell and I_0 is the UV light intensity of zero air in the reference cell. The UV light intensities of each cell are measured by two photo-diode detectors, respectively.

2.2.1.4 GC-MS

Off-line analysis of VOCs sampled in the CHARME are performed with the coupling Thermodesorber (ATD - 400, Perkin Elmer) - Gas Chromatograph (GC, Autosystem XL) - Mass Spectrometer (MS) (Turbomass), Perkin Elmer.

The sampling and analyzing routine is:

- 1) The organic compounds are sampled on Tenax TA tubes at $Q = 100$ ml/min during 30 - 120 min.
- 2) GC-MS program: The tubes are thermally desorbed by the ATD for 15 min at 300 °C under helium stream and cryofocused in a trap cooled down to -30 °C. The trap is afterwards heated within a few seconds to 300 °C allowing a fast injection of the VOCs into the chromatographic column. They are then separated using the following program: isotherm 5 min at 50 °C; 5 °C min⁻¹ step to 110 °C; 45 °C min⁻¹ step to 250 °C and hold at 250 °C for 5 min (total programming of 25.1 min). The qualitative analyses are performed by a mass spectrometer (quadrupole) using the TIC (Total Ion Count) mode, and an acquisition of the masses between 33 and 500 amu (atomic mass units). The energy of the ionizing electrons is 70 eV which

allows an identification of the detected compounds by comparison with those of the NIST library (the National Institute of Standards and Technology, 2005 [15]).

2.2.1.5 Liquid chromatography-mass spectrometry (LC-MS)

To determine the chemical composition of SOAs, before analyzed by LC-MS (Agilent LC 1100 - MS 6540) using the negative ionization mode (proton abstraction) the aerosol samples are collected on treated quartz fiber filters.

The chromatographic column used in this work was a ZORBAX Extend-C18 (50 mm long \times 2.1 mm i. d., 1.8 μ m pore size) one thermostated at 40 °C. The MS analysis allows to access the molar mass of the identified products and the MS/MS (the first mass analyzer is set to pass only precursor ions of a single m/z to the collision cell, and the second MS is set to pass the product ions of a single m/z to the detector) analyses, performed at three different energies (10 eV, 20 eV and 40 eV) permit to identify the functional groups of the compounds and to propose chemical structures.

2.2.2 Particle-phase analysis

For the measurement of particles in CHARME, a Scanning Mobility Particle Sizer (SMPS) consisting of a Differential Mobility Analyzer (Model 3081 Long DMA, TSI Inc.) and a Condensation Particle Counter (CPC Model 3775, TSI Inc.) is used (Fig.II-6(a)).

As illustrated in Chapter I, the SMPS is based on the principle of the electrical mobility, which is the ability of a charged particle to move in an electric field. As shown in Fig.II-6(b) the reaction generated particles are sampled from the chamber with a short conductive silicon line to reduce particles losses. The particles pass through an impactor and into the electrostatic classifier where they are neutralized with a radioactive source. Afterwards, particles are introduced with the sheath air into the DMA, which has an electric field between the two rods in DMA. Due to the created electric field and according to their electrical mobility, aerosols drift down the annular space between the electrodes with a stable flow (to avoid uncertainties in the particle number concentration and sizing). Consequently, positively charged particles move across the sheath flow towards the central rod and then enter into the CPC, negatively charged ones are repelled

to the wall and uncharged particles exit the DMA with excess air through the exhaust flow [16]. In the particle counter, butanol vapor condensation takes place to grow particles into droplets with optically detectable size. The CPC counts the number of particles to provide a particle concentration value that is displayed as the number of particles detected per cubic centimeter ($\#/cm^3$) of sample air.

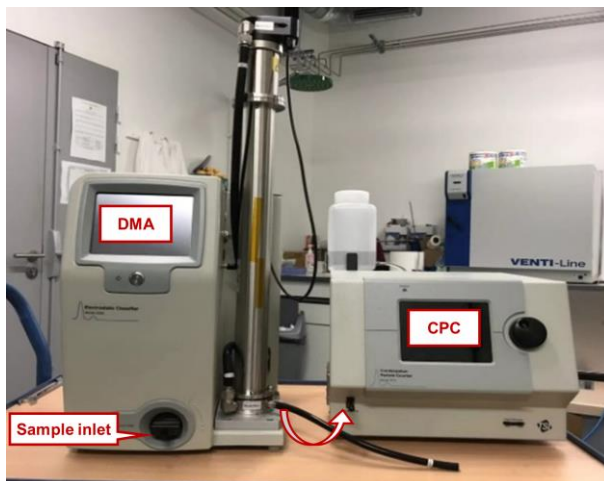


Figure II-6 The DMA and the CPC coupled to CHARME.

Throughout the experiments, the DMA was operated with an aerosol and sheath flows of 0.3 and 3.0 L min^{-1} , respectively. Aerosol number concentration and size distribution, are measured over a range of 10 to 680 nm diameter for every 120 s . Based on the assumption that the particles are spherical, the aerosol instrument manager software provides the volume (in $\text{nm}^3 \text{ cm}^{-3}$) and mass concentration (in $\mu\text{g m}^{-3}$) if the aerosol density is known.

3 Conclusion of the chapter

In this chapter, the development of two IBBCEAS systems has been described as well as the simulation chamber CHARME with the associated instruments.

In brief, IBBCEAS instruments can be used both for field campaigns and laboratory studies to measure trace gases concentrations (like NO_2 , HONO and NO_3 radicals) and

aerosol extinction. Results obtained with the develop setups are presented in Chapter III and IV.

The chamber CHARME has been employed to investigate the gas phase reaction of guaiacol (2-methoxyphenol) with NO_3 radicals (rate constant determination and study of the formation of secondary organic aerosols). The results are shown in Chapter IV.

References

- [1] S. E. Fiedler, A. Hese, A. A. Ruth. Incoherent broad-band cavity-enhanced absorption spectroscopy. *Chemical Physics Letters*, 2003, 371(3-4): 284-294. **10.1016/s0009-2614(03)00263-x**
- [2] G. Berden, R. Peeters, G. Meijer. Cavity ring-down spectroscopy: experimental schemes and applications. *International Reviews in Physical Chemistry*, 2010, 19(4): 565-607. **10.1080/014423500750040627**
- [3] S. E. Fiedler, A. Hese, A. A. Ruth. Incoherent broad-band cavity-enhanced absorption spectroscopy of liquids. *Review of Scientific Instruments*, 2005, 76(2): 023107. **10.1063/1.1841872**
- [4] R. Washenfelder, A. Langford, H. Fuchs, S. Brown. Measurement of glyoxal using an incoherent broadband cavity enhanced absorption spectrometer. *Atmospheric Chemistry and Physics*, 2008, 8(24): 7779-7793. **10.5194/acp-8-7779-2008**
- [5] R. A. Washenfelder, J. M. Flores, C. A. Brock, S. S. Brown, Y. Rudich. Broadband measurements of aerosol extinction in the ultraviolet spectral region. *Atmospheric Measurement Techniques*, 2013, 6(4): 861-877. **10.5194/amt-6-861-2013**
- [6] K. Suhail, M. George, S. Chandran, R. Varma, D. S. Venables, M. Wang, J. Chen. Open path incoherent broadband cavity-enhanced measurements of NO₃ radical and aerosol extinction in the North China Plain. *Spectrochimica Acta Part A: Molecular and Biomolecular Spectroscopy*, 2019, 208: 24-31. **10.1016/j.saa.2018.09.023**
- [7] W. Zhao, X. Xu, M. Dong, W. Chen, X. Gu, C. Hu, Y. Huang, X. Gao, W. Huang, W. Zhang. Development of a cavity-enhanced aerosol albedometer. *Atmospheric Measurement Techniques*, 2014, 7(8): 2551-2566. **10.5194/amt-7-2551-2014**
- [8] L. Meng, G. Wang, P. Augustin, M. Fourmentin, Q. Gou, E. Fertein, T. Nguyen Ba, C. Coeur, A. Tomas, W. Chen. Incoherent broadband cavity enhanced absorption spectroscopy (IBBCEAS)-based strategy for direct measurement of aerosol extinction in a lidar blind zone. *Optics Letters*, 2020, 45(7): 1611-1614. **10.1364/OL.389093**
- [9] T. Wu, Q. Zha, W. Chen, Z. Xu, T. Wang, X. He. Development and deployment of a cavity enhanced UV-LED spectrometer for measurements of atmospheric HONO and NO₂ in Hong Kong. *Atmospheric Environment*, 2014, 95: 544-551. **10.1016/j.atmosenv.2014.07.016**
- [10] A. Bodi, J. Csontos, M. Kálai, S. Borkar, B. Szűcs. On the protonation of water. *Chemical Sciences*, 2014, 5(8): 3057-3063. **10.1039/c4sc00791c**
- [11] R. S. Gao, E. Keim, E. L. Woodbridge, S. J. Ciciora, M. Proffitt, T. L. Thompson, R. McLaughlin, D. W. Fahey. New photolysis system for NO₂ measurements in the

- lower stratosphere. *Journal of Geophysical Research*, 1994, 99(D10): 20673-20681. **10.1029/94JD01521**
- [12] M. D. Minarro, E. G. Ferradas. Performance evaluation of two commercial chemiluminescence NO_x analysers according to European Standard EN 14211. *Journal of Environmental Monitoring*, 2012, 14(2): 383-390. **10.1039/c1em10601e**
- [13] K. Demerjian. A review of national monitoring networks in North America. *Atmospheric Environment*, 2000, 34(12-14): 1861-1884. **10.1016/s1352-2310(99)00452-5**
- [14] Thermo scientific Model 49i Manual (2011). <http://tools.thermofisher.com/content/sfs/manuals/epm-manual-model%2049i.pdf>
- [15] The NIST Mass Spectrometry Data Center. NIST Standard Reference Database 1A.
- [16] A. Wiedensohler, W. Birmili, A. Nowak, A. Sonntag, K. Weinhold, M. Merkel, B. Wehner, T. Tuch, S. Pfeifer, M. Fiebig, A. M. Fj äraa, E. Asmi, K. Sellegri, R. Depuy, H. Venzac, P. Villani, P. Laj, P. Aalto, J. A. Ogren, E. Swietlicki, P. Williams, P. Roldin, P. Quincey, C. Hüglin, R. Fierz-Schmidhauser, M. Gysel, E. Weingartner, F. Riccobono, S. Santos, C. Gröning, K. Faloon, D. Beddows, R. Harrison, C. Monahan, S. G. Jennings, C. D. Dowd, A. Marinoni, H. G. Horn, L. Keck, J. Jiang, J. Scheckman, P. H. McMurry, Z. Deng, C. S. Zhao, M. Moerman, B. Henzing, G. de Leeuw, G. Löschau, S. Bastian. Mobility particle size spectrometers: harmonization of technical standards and data structure to facilitate high quality long-term observations of atmospheric particle number size distributions. *Atmospheric Measurement Techniques*, 2012, 5(3): 657-685. **10. 5194/amt-5-657-2012**
- [17] M. Gysel, G. B. McFiggans, H. Coe. Inversion of tandem differential mobility analyser (TDMA) measurements. *Journal of Aerosol Science*, 2009, 40(2): 134-151. **10.1016/j.jaerosci.2008.07.013**

Chapter III Portable IBBCEAS instrument for field measurement of aerosol extinction

LIDAR (Light detection and ranging) systems are widely used in different disciplines ranging from physics, Earth study to archaeology, vehicle automation and forest survey. In particular, in the field of atmospheric studies, LIDAR is a suitable tool for remote sensing of optical characteristics of aerosol particles. But by reason of its geometric structure, LIDAR has a blind range in the near field which causes the loss of information in this area.

To compensate for the lack of LIDAR information in this blind range, IBBCEAS technique has been introduced to perform complementary measurement in this LIDAR blind area in the present PhD work.

1 Introduction and objectives

Due to the layering of the atmosphere, a large negative vertical gradient of aerosol concentration is often observed between the Earth's surface and the first kilometers of the troposphere. Knowledge of the aerosol vertical distribution is crucial for meteorological and atmospheric chemistry models, and thus for forecasting and warning air pollution events.

Aerosol LIDAR systems are used for remote sensing of atmospheric aerosols through the measurements of backscattered light from nanosecond laser pulses emitted into the atmosphere. Atmospheric backscattering and extinction coefficients, which are correlated to particle concentrations, are retrieved from the backscattering LIDAR signals. Various LIDAR techniques have been developed to deduce spatial aerosol optical properties from standard elastic backscatter LIDAR signal, such as multiangle LIDAR method [1], stable near-end solution [2] or Fernald-Klett inversion method [3]. However, due to incomplete geometric overlap between the laser emission beam and the field of view

(FOV) of receiver telescope in the near range [4] (Fig.III-1), retrieval of aerosol optical properties using LIDAR is restricted in the first lowest hundreds of meters of the atmosphere [5]. The overlap factor η is a characteristic parameter describing the different overlapping relation between the FOV of the telescope and the laser beam. When the laser beam is out of the telescope's FOV, the overlap factor η is 0, where is called blind region; when the beam is partially inside the the FOV of the telescope, the overlap factor is between 0 and 1; when the laser beam is completely contained in the FOV, $\eta = 1$.

This issue could be partially addressed by measuring the overlap function or adjusting the alignment for near and far range measurements [6]. The measurement of aerosol distributions near ground ($\eta = 0$) is, however, crucial because of various ground surface emission sources (industries, traffic, fires, etc.) and their potential effects on human health [7].

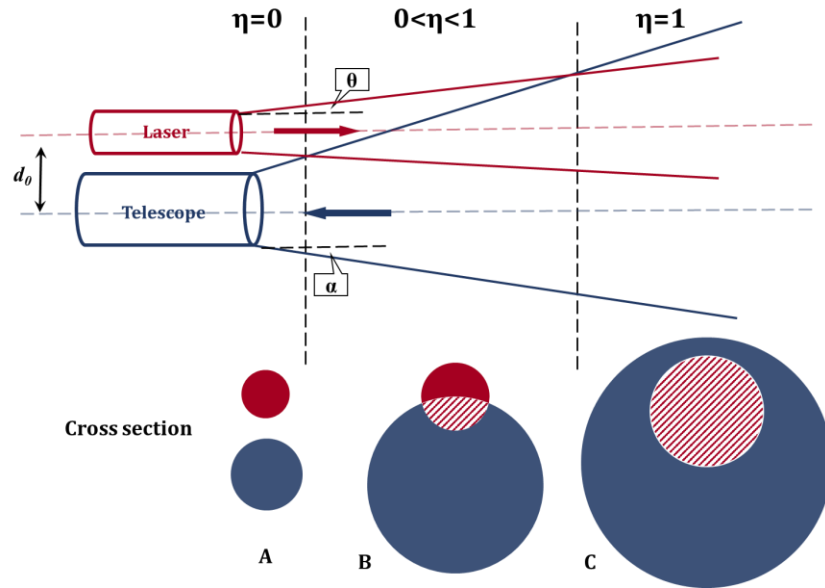


Figure III-1 Schematic diagram of LIDAR's geometric overlap factor η . θ and α are the width transmitter angle and the receiver acceptance angle, respectively. d_0 is the separation distance between the two axes. The overlap factor η is related to the θ , α , d_0 , and the diameters of both cross sections of laser beam and telescope FOV at the same distance.

In the past decades, the LIDAR blind zone has been reduced from several kilometers (micro pulse LIDAR, MPL) to a few hundreds of meters (approximately 200 m for ALS300 LIDAR, Leosphere) [8] by enlarging the FOV with optimized optical design (like enlarging the receiver angle α , reducing the distance between laser and receiver, etc...), which almost reaches the instrumental limit. Considerable endeavors have been conducted through experimental methods [9] or analytical approaches [10, 11].

For the missing informations in the blind zone near the ground surface, indirect *in situ* measurement of scattering or extinction coefficient would be supportive for extracting aerosol optical parameter as well as for determination of the solution boundary value from the near-end inversion method or for the correction of aerosol's optical depth in the blind zone [2]. Nephelometer [12, 13] is the most commonly used instrument for the measurement of aerosol concentrations using light scattering to provide supplementary near ground data.

A new alternative optical method is proposed in the present PhD work to directly measure aerosol extinction near the ground surface, instead of aerosol scattering. Optical methods have been widely used to measure aerosol extinction, such as multi-axis differential optical absorption spectroscopy (MAX-DOAS) [14, 15] for measurements over long-path length, and cavity attenuated phase shift (CAPS) [16, 17], cavity ring-down spectroscopy (CRDS) [18, 19] and incoherent broadband cavity enhanced absorption spectroscopy (IBBCEAS) [18, 19] for local point measurements. To our knowledge, using IBBCEAS to measure aerosol extinction near ground surface in synergy with LIDAR remote sensing has been previously reported.

In the present work, a custom-designed IBBCEAS-based instrument coupled to a broadband UV light emitting diode (LED) was developed for measuring aerosol extinction over a relatively large spectral band (355-380 nm) with high spatial resolution.

The objective of the present work is to provide a new optical measurement method to complete the missing information on aerosol extinction in the LIDAR blind range which allows to use the aerosol extinction data measured by the method being located close to the LIDAR measurement site, for near-end LIDAR calibration to compensate for missing data in its blind zone, in particular near the ground face. Comparison of the

IBBCEAS measured aerosol extinction was compared with that measured by LIDAR remote sensing at the same location near ground surface to validate the proposed strategy for further application to LIDAR measurement of aerosol extinction with calibration by IBBCEAS measurement.

2 Description of the involved instruments

2.1 LIDAR system and measurements

The scanning LIDAR used in the present work is an ALS300 manufactured by the LEOSPHERE Company (Fig.III-2). This LIDAR operates with a third harmonic of an Nd-YAG laser at 355 nm wavelength. The energy pulse is about 16 mJ with a repetition rate of 20 Hz, and the spatial resolution is 15 m along each beam. The theoretical LIDAR blind distance for optimal near field overlap is about 250 m. In order to reduce the blind distance, a geometrical form factor (GFF) has been deduced by using horizontal profile measurements in a homogeneous clear atmosphere area before the start of the measurements [20]. The GFF, deduced experimentally, has been applied in each profile obtained during the burning period, to reduce the blind distance from 250 m to 105 m. The LIDAR signal was inverted to derive aerosol extinction coefficients using the Klett–Fernald method [21, 22]. At the beginning of the measurements, the Hamilton’s slant LIDAR technique [23] was applied on single range-height indicator measurements (from 0° to 84° zenith angle with a step of 5°) to deduce the aerosol optical thickness in the blind zone. A sun photometer located in the close environment of the measurements site, integrated in the international Aerosol Robotic Network (<https://aeronet.gsfc.nasa.gov>), was used to constrain the LIDAR signal in order to determine the LIDAR ratio.



Figure III-2 LIDAR system installed in an atmospheric mobile unit.

2.2 IBBCEAS instrument

The IBBCEAS used in this campaign has been described in Section 1.3.1 of Chapter II.

Both aerosol and NO_2 have absorption in the UV wavelength range [24]. In the present work, a LED (Nichia, NCSU033AT) was used as light source, with center wavelength at ~ 365 nm. The main parameters of LED are listed in Tab.III-1. The spectrum of LED is shown in Fig.III-3(a) and the absorption cross section of NO_2 is shown in Fig.III-3(b).

Table III-1 Main parameters of LED

LED power /mW	Forward current/mA	Forward voltage/V	Peak wavelength/nm	Full width at half maximum (FWHM) /nm
190~310	700	3.2~4.4	365	9

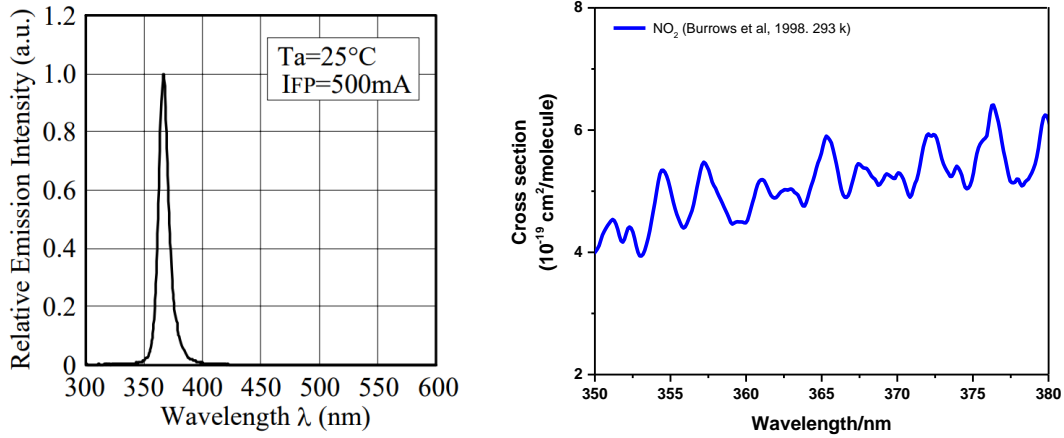


Figure III-3 (a) Emission spectrum of the LED used (<https://www.alldatasheet.com/datasheet-pdf/pdf/240025/NICHIA/NCSU033AT.html>); (b) Absorption spectrum of NO_2 from 350 nm to 380 nm [25].

To minimize the interference of ambient light, a UV band-pass filter (Semrock, FF01-360/23-25) is placed between the LED and the cavity to block the light at undesirable wavelength. The performance of the filter is shown in Fig.III-4.

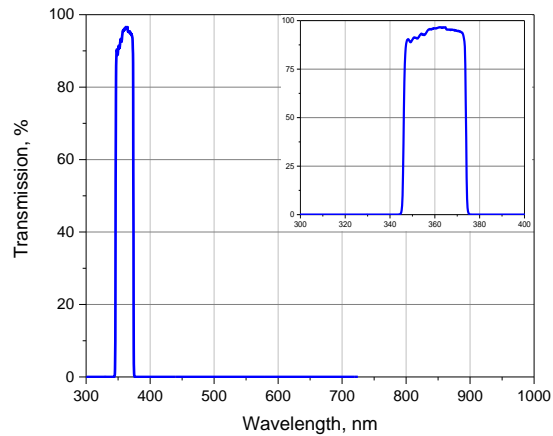


Figure III-4 Band-pass filter transmission. Transmission in the range of 320-1120 nm is noise limited to be near or below $3 \times 10^{-5}\%$, and transmission in the wavelength of < 320 nm or > 1120 nm is near or below $3 \times 10^{-4}\%$. (<http://www.semrock.com/FilterDetails.aspx?id=FF01-360/23-25>)

QE 65000 spectrometer from Ocean Optics for spectral dispersion and absorption signal measurement was used in this study. The main parameters are listed in Tab.III-2.

Table III-2 Parameters for QE 65000 spectrometer.

	Main parameter
Focal length	101 mm
Spectral range	290 - 480 nm
Resolution	~ 0.5 nm
Entrance slit	25 μ m
CCD pixels	2048
Detector	Hamamatsu S7031-1006
Dimensions (L×W×H)	185 mm × 115 mm × 50 mm

3 Measurement details

3.1 Measurement by IBBCEAS

3.1.1 Calibration of the IBBCEAS instrument

As shown in Eq.14, cavity mirror reflectivity must be firstly determined over the whole working wavelength range for accurate quantitative measurement. In the present work, the mirror reflectivity $R(\lambda)$ was determined using a known concentration of NO₂ by rearranging Eq.14 as follows:

$$R(\lambda) = 1 - d \times \left(\frac{n_{NO_2} \sigma_{NO_2}(\lambda) \cdot I(\lambda)}{I_0(\lambda) - I(\lambda)} - \alpha_{Ray, N_2}(\lambda) \right) \quad (\text{Eq.18})$$

where d is the cavity length (142 cm), n_{NO_2} is the number concentration of a reference NO₂ cylinder (361 ppbv \pm 10%), $\sigma_{NO_2}(\lambda)$ is the absorption cross section of NO₂ (5.42×10^{-19} cm² molecule⁻¹ at 370 nm), $\alpha_{Ray, N_2}(\lambda)$ is the Rayleigh scattering coefficient,

calculated as $6.02 \times 10^{-7} \text{ cm}^{-1}$ at 370 nm wavelength at 1 atm [26], $I_0(\lambda)$ and $I(\lambda)$ are the measured light intensities when cavity is with N_2 and with absorber, respectively.

Fig.III-5 (a) shows the original cavity output spectra of pure N_2 and 361 ppbv NO_2 for $I_0(\lambda)$ and $I(\lambda)$, respectively, as well as the theoretical Rayleigh scattering coefficient. Fig.III-5 (b) displays the reference absorption cross sections of NO_2 around 365 nm reported by Burrows et al. [25], and also the experimentally determined mirror reflectivity. Fig.III-5 (c) is the NO_2 (361 ppbv) absorption spectrum being used to determine the mirror reflectivity in Fig.III-5 (b). Considering the wavelength where NO_2 has large absorption band, the cavity shows high output intensity and the mirrors present a fifth-order polynomial, therefore the working wavelength was confirmed from 364 nm to 377 nm.

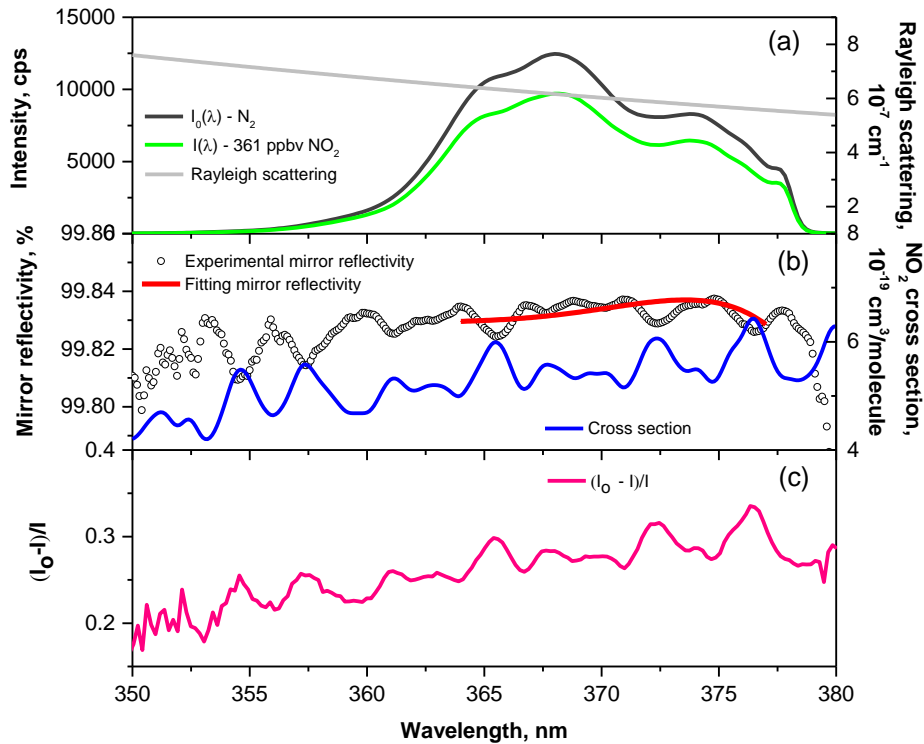


Figure III-5 (a) Cavity output spectra for pure N_2 and standard NO_2 mixture, and the Rayleigh scattering coefficient for N_2 [26]; (b) Absorption cross sections of NO_2 [25] and the experimentally determined mirror reflectivity; (c) 361 ppbv NO_2 absorption spectrum.

In the working wavelength region of 364-377 nm, the maximum mirror reflectivity (~5% uncertainty) was found to be ~99.84% at 374.5 nm, leading to an effective optical pathlength of ~ 860 m.

3.1.2 Performance characteristics

The measurement accuracy of an instrument system usually depends on calibration, and the measurement precision may be improved by data averaging in case where white noise is dominant. The acquisition time of the spectrum is determined by the integration time and the number of averaging times. If the integration time is too long, the acquisition time also increases, but the CCD is easily saturated; if the integration time is too short, the measured spectral signal-to-noise ratio is very poor. In this case, the maximum averaging number (or optimal averaging time), limited by the stability of the LED emission and the stability of the CCD spectrometer system, can be determined by an Allan variance analysis [27].

System stability of the developed instrument was characterized by means of the Allan variance analysis. The optimal integration (averaging) time can be obtained using time series IBBCEAS spectra of N₂ through Allan variance analysis. The cavity was flushed with pure nitrogen and the cavity output intensity was recorded over 200 consecutive 2.4-s spectra (i.e. 4 averaged spectra with a 600 ms integration time provided one spectral data). Typical Allan variance analysis results (expressed in Allan deviation) by Origin is shown in Fig.III-6, illustrating a maximum instrument stabilization time of 69.6 s by 600 ms integration time with averaging number of 116, which gives a measurement precision (1 σ) of 1.5 ppbv for NO₂. Considering the calculation and comparison with associated instruments' time responses, the used averaging time was 60 s (leading to an averaging number of 100).

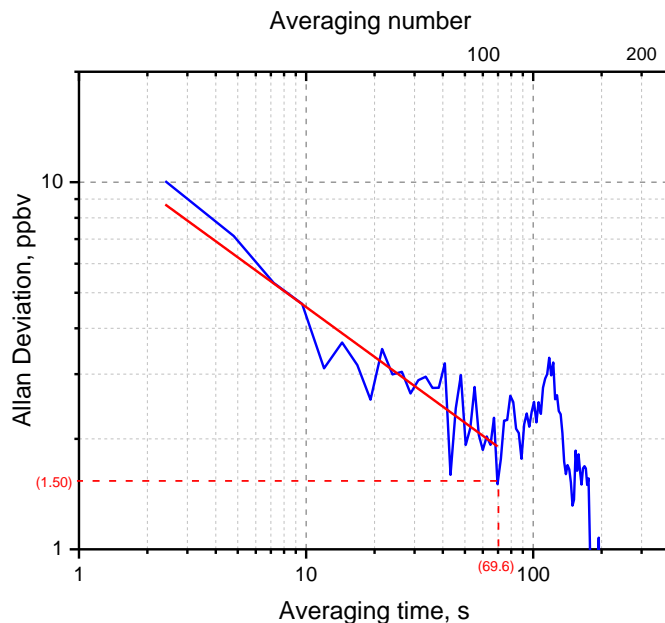


Figure III-6 Allan variance plot as a function of averaging time. The optimum averaging time was found to be 69.6 s with an estimate of the measurement precision of 1.5 ppbv for NO_2 , corresponding to an optimum averaging number of 116 with 600 ms integration time per spectrum.

The measurement precision of the IBBCEAS instrument was assessed by flushing N_2 into the cavity. The time resolution for IBBCEAS was 1 min (600 ms integration time, averaging 100 times). A time series of 200 data were recorded. The mean value of the NO_2 concentration for the data was 0.22 ppbv, indicating the instrumental accuracy. Fig.III-7 shows the distribution histogram of the estimated NO_2 concentrations by the IBBCEAS instrument, and the distribution histogram was fitted with a Gaussian model, resulting in the measurement precision of 2.19 ppbv from the FWHM of the fit Gaussian profile.

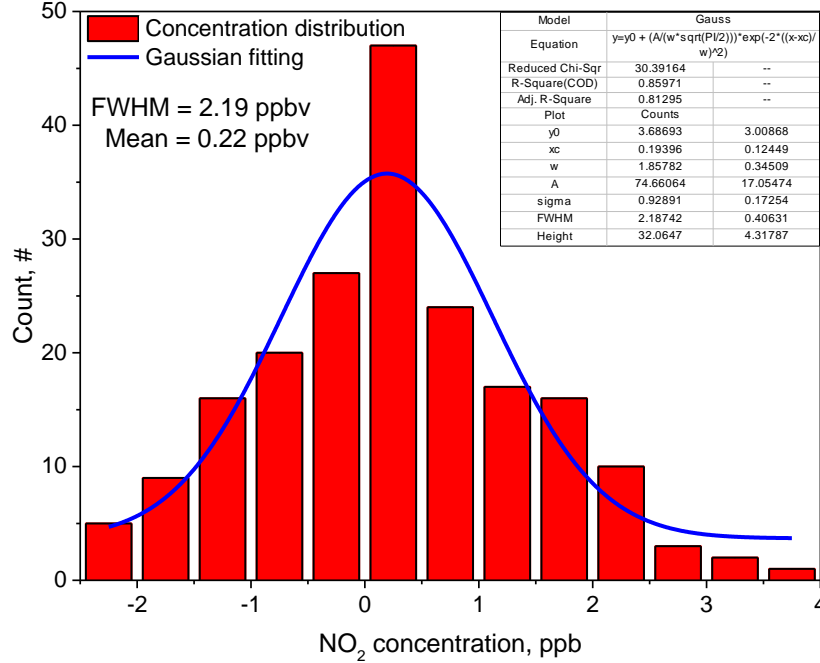


Figure III-7 Histogram showing the distribution of the estimated 0 ppbv NO₂ concentrations by N₂ flushing.

Based on Eq. 14, considering the uncertainties in the used NO₂ absorption cross section [25] (5%), in the cavity length (1%), in $\Delta I/I$ (0.5%), in the factor of (1 - R) (5%), uncertainty in the total measurement extinction were approximately estimated to be 5.2%.

3.1.3 Simultaneous measurement of aerosol extinction and NO₂ concentration in ambient air

As indicated in Eq.15, the knowledge of baseline variation over time is crucial for accurately retrieving aerosol extinction $\alpha_{ext,aerosol}(\lambda)$ as both contributions are accounted by a polynomial function $P(\lambda)$ determined from the slow variation feature in the measured IBBCEAS spectrum.

In the current work, the spectral baseline $P_0(\lambda)$ was regularly measured through the following operation protocol (Fig.III-8 (c)): 6-min measurement with pure N₂ (for baseline $P_0(\lambda)$) and 24-min measurement with air sample (providing information on gas absorption $\alpha_{abs,gas}$, aerosol extinction $\alpha_{ext,aerosol}$ and baseline $P_0(\lambda)$). Switching was controlled with an electronic valve (Fig.III-8 (a) and Fig.III-8 (b)). N₂ or ambient air was continuously sampled, at a flow rate of 2 L/min, to the IBBCEAS cavity working at

atmospheric pressure. A case of one cycle to show the process to achieve aerosol extinction $\alpha_{\text{ext,aerosol}}$ is given in Fig.III-8 (d).

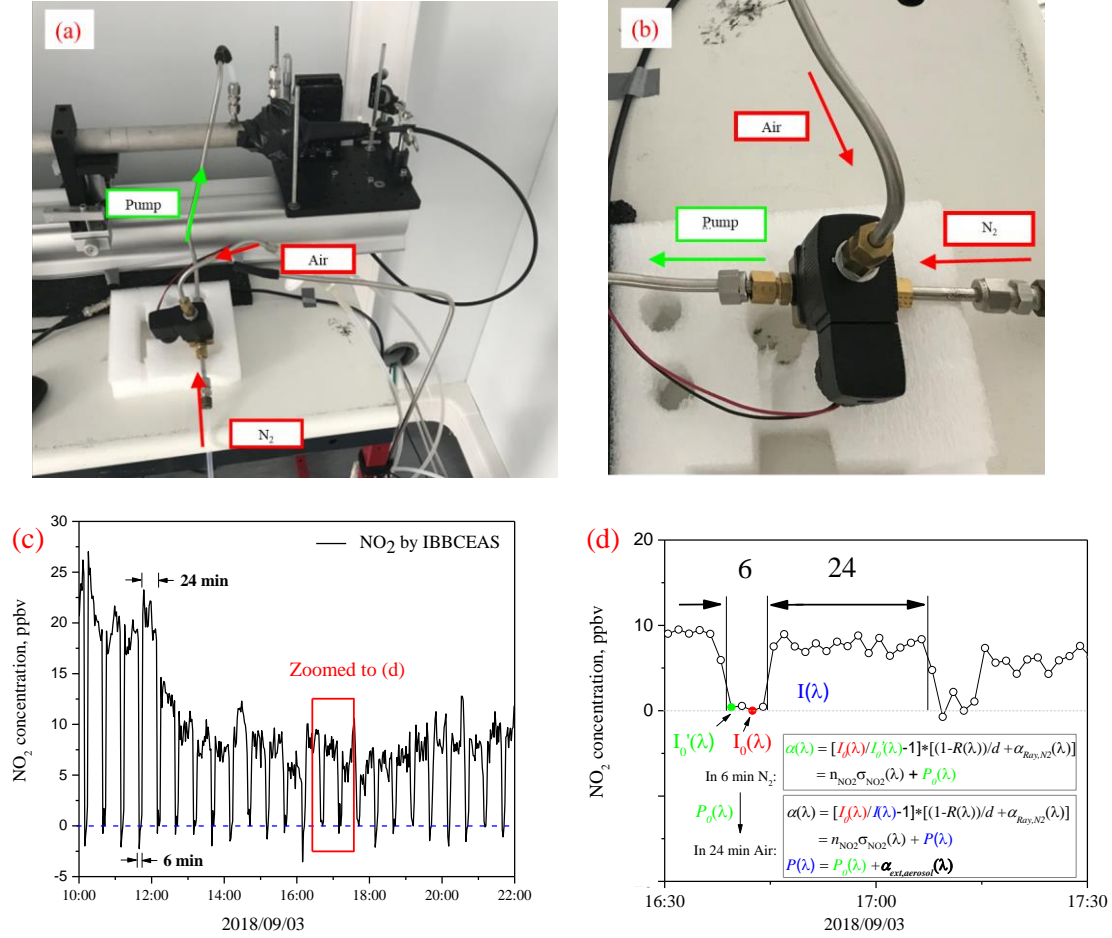


Figure III-8 (a) and (b) The electronic valve in the experiment; (c) Working time sequence of the valve in the experiment; (d) Process to retrieve the aerosol extinction $\alpha_{\text{ext,aerosol}}(\lambda)$. In each 30-min cycle, the flow was switched between N₂ and air. The system baseline was retrieved by the difference between two successive N₂ spectra. In N₂ flow sequence, four spectra of N₂ were recorded, one of which was selected as reference background intensity $I_0(\lambda)$ (red dot in Fig.III-8 (d)) and another spectrum (green dot in Fig.III-8 (d)) was the sample intensity $I_0'(\lambda)$, then based on Eq.15, the fitting result came with nearly 0 ppbv NO₂, and a baseline $P_0(\lambda)$ was deduced from the IBBCEAS spectrum of $I_0(\lambda)/I_0'(\lambda)$, and this baseline $P_0(\lambda)$ was regarded as stable in the following 24 min. Thus in the following air flow, the aerosol extinction could be separated from the polynomial $P(\lambda)$: $\alpha_{\text{ext,aerosol}} = P(\lambda) - P_0(\lambda)$.

A representative case of data retrieval is shown in Fig.III-9, depicting measured (black circles) and fitted (red curve) IBBCEAS spectra of 10.8 ppbv NO₂ in air containing aerosols. The acquisition time for each spectrum was 60 s (average of 100 spectra with an integration time of 600 ms per spectrum). Wavelength-dependent aerosol extinction coefficients $\alpha_{ext.aerosol}(\lambda)$ (orange line) were deduced from the subtraction of regularly measured $P_0(\lambda)$ (dark green line) from the fitted polynomial function $P(\lambda)$, as shown in Eq.15.

Limit of detection (LoD) of the present IBBCEAS instrument was evaluated using the following expression:

$$Limit\ of\ Detection = \frac{[NO_2]_{measured}}{SNR} = \frac{[NO_2]_{measured}}{(\alpha_{max} - \alpha_{min}) / SD_{residual}} \quad (Eq.21)$$

where $[NO_2]_{measured}$ is the measured NO₂ concentration, the SNR stands for the signal-to-noise ratio and was estimated by the ratio of the maximal absorption difference by absorption of the measured NO₂ to the standard deviation of the residual [28].

Based on the standard deviation of the fit residual in Fig.III-9, a minimum detectable extinction coefficient of $4.3 \times 10^{-9} \text{ cm}^{-1}$ (corresponding to a minimum detectable NO₂ concentration of 1.5 ppbv were deduced.

$$[NO_2]_{LoD} = \frac{[NO_2]_{measured}}{SNR} = \frac{[NO_2]_{measured}}{(\alpha_{max} - \alpha_{min}) / SD_{residual}} = 1.5 \text{ ppb}$$

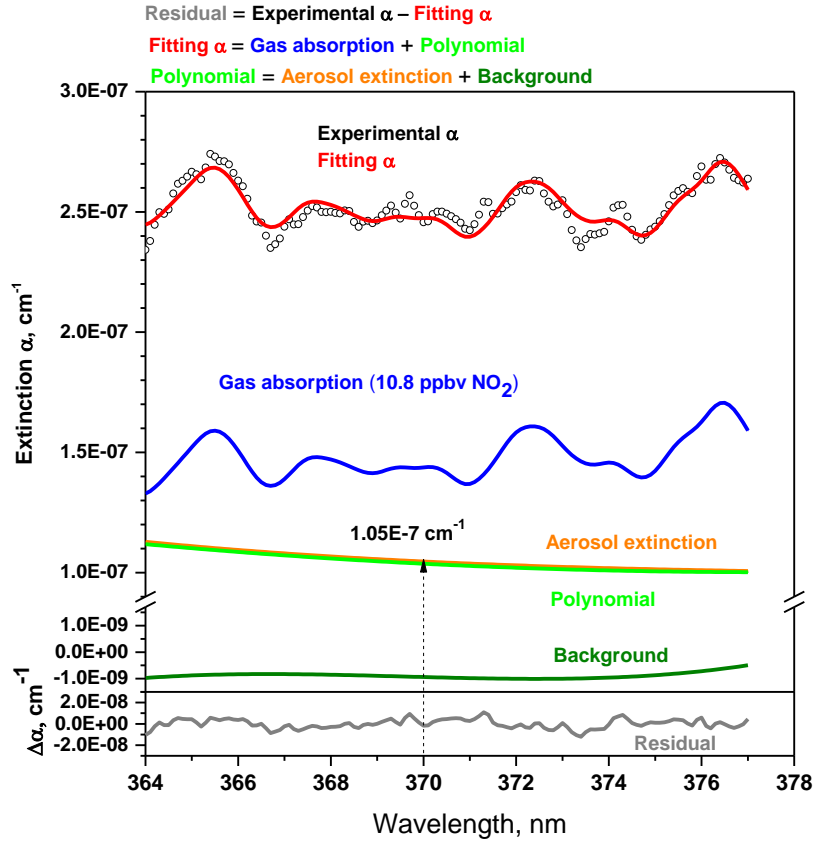


Figure III-9 Typical data retrieval of NO_2 (10.8 ppbv) and wavelength-dependent aerosol extinction coefficients ($1.05 \times 10^{-7} \text{ cm}^{-1}$ at 370 nm) from a measured IBBCEAS spectrum of ambient air.

3.1.4 Sampling site

An inter-comparison campaign was organized in the morning of September 14, 2018 in an urban and industrialized coastal area in Dunkirk (North France). Combined measurements of aerosol extinction at the same location (as illustrated in Fig.III-10) near ground surface were performed using LIDAR remote sensing and IBBCEAS *in situ* monitoring. The LIDAR system was located in UMA (Unité Mobile Atmosphérique) situated at ground level about 0.4 km away from the building where a UV LED-IBBCEAS system was installed (in an air-conditioned shelter) on the roof at ~14 m high. The meteorology parameters were recorded during the measurement as shown in Fig.III-11. Measurement of aerosol extinction for the comparison was performed at 400 m away from the LIDAR (outside its blind zone) at a zenith angle around 84° .

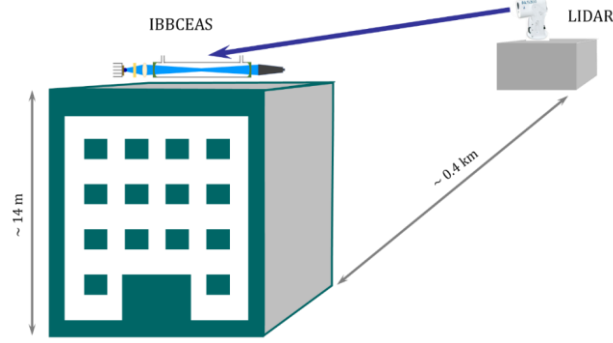


Figure III-10 Schematic of combined measurements of aerosol extinction near ground surface.

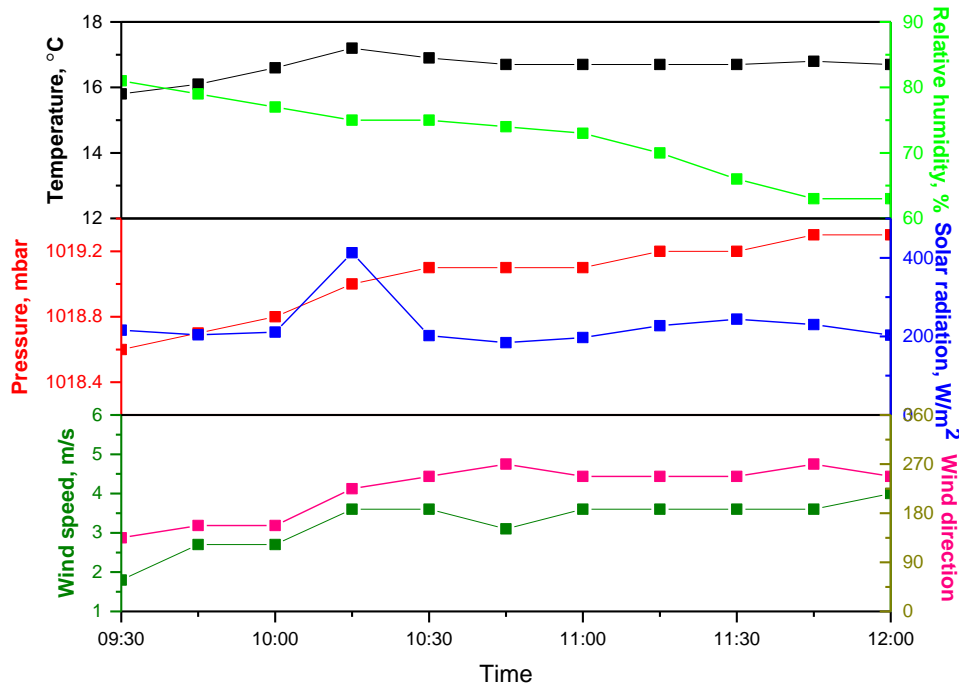


Figure III-11 Time series of meteorological parameters (such as temperature, relative humidity, atmospheric pressure, solar radiation, wind speed and direction) during the measurement period at the measurement site (9:30-11:30, 14 September 2018). During the 2.5 hours measurement, the local temperature and pressure presents a relatively stable condition without significant variation. The solar radiation has an increase around 10:15, which may enhance vertical dispersion of aerosols which may "dilute" aerosols so that it may decrease extinction coefficient, and the wind has a mild change from south to southwest as RH decreased, which may bring the different air masses and aerosol sources.

3.1.5 Potential interferences

Besides absorption from NO₂ and aerosol particles in air sample, there are other gaseous species exhibiting structured absorption features in the relevant wavelength range (364-378 nm), such as HONO, CH₂O, O₃, BrO, IO, OClO and glyoxal.

(1) The typical concentration for CH₂O and O₃ in the atmosphere are up to tens of ppbv levels, but their low absorption cross sections ($< 10^{-22}$ cm² molecule⁻¹ [29, 30], compared to the cross sections of more than 10^{-19} cm² molecule⁻¹ for NO₂, make their absorption magnitudes ($\sim 10^{-10}$ cm⁻¹) lower than NO₂, and undetectable by the minimum detectable extinction coefficient of the current IBBCEAS instrument (4.3×10^{-9} cm⁻¹).

(2) Although the absorption cross sections of BrO ($\sim 10^{-18}$ cm² molecule⁻¹ [31]), IO ($\sim 10^{-18}$ cm² molecule⁻¹ [32]) and OClO ($\sim 10^{-17}$ cm² molecule⁻¹ [33]) are one or even two orders higher than that of NO₂ in this spectral region, their concentrations are only several pptv for BrO and IO, tens of pptv for OClO [34], nearly three orders of magnitude lower than NO₂ concentration in ambient air making their absorption magnitudes ($\sim 10^{-10}$ cm⁻¹ for BrO and IO, $\sim 10^{-9}$ cm⁻¹ for OClO) lower than the minimum detectable extinction coefficient of the IBBCEAS, they are below the detection limit.

(3) Regarding glyoxal with a typical cross section of $< 10^{-20}$ cm² molecule⁻¹ [35] in this spectral region, as its concentration in urban areas ranges from 10 pptv to 1 ppbv, its absorption ($\sim 10^{-12}$ - 10^{-10} cm⁻¹) is about 10-100 times weaker than that of NO₂ and hence can be ignored.

3.2 Intercomparison of results from the IBBCEAS and the LIDAR

The LIDAR-derived aerosol extinction coefficients and those simultaneously measured by the UV LED-IBBCEAS (Fig.III-9) are plotted in Fig.III-12 (a). The measurements were carried out in the morning of 14 September 2018 from 9:30 to 11:30.

A good agreement with a correlation coefficient of $R^2 = 0.90$ (Fig.III-12 (b)) is obtained between the aerosol extinctions measured using the two different techniques. Both results have a consistent variation tendency during the sampling period.

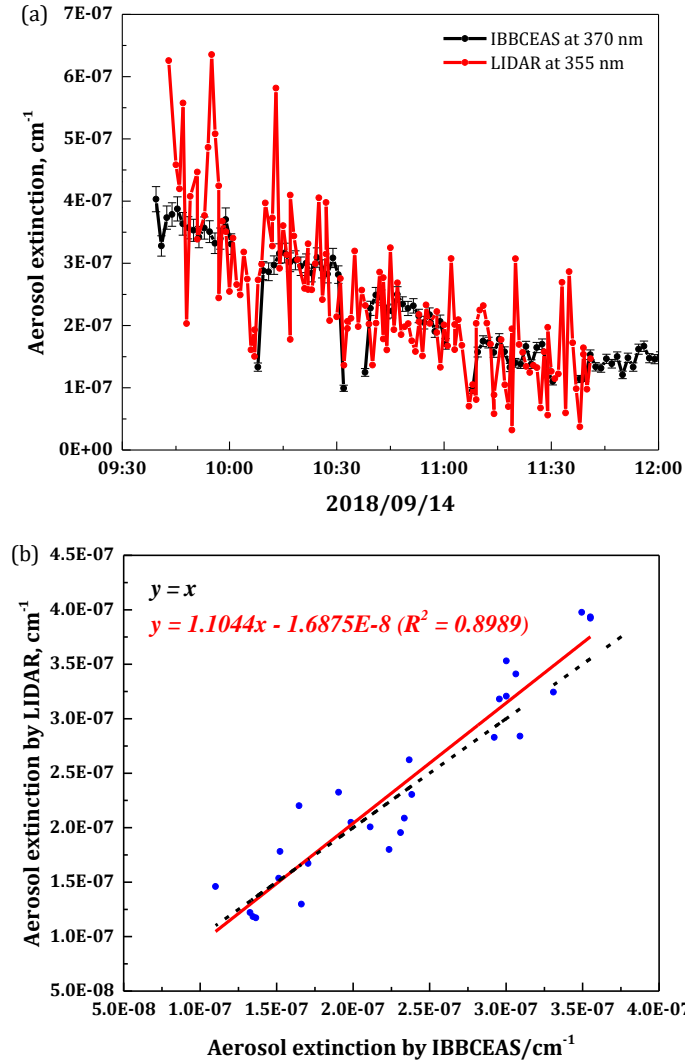


Figure III-12 (a) Time-series measurements of aerosol extinctions by LIDAR (red) and by UV LED-IBBCEAS (black); (b) Correlation plot of time-series measurement results. Time resolutions for LIDAR and IBBCEAS measurements are 1.5 min and 1 min, respectively. Time resolution for the correlation plot is 3 min.

Some discrepancies were however observed between 09:40 and 10:00. The strongest fluctuations measured with LIDAR can be explained by the fact that its measurements were performed over a 400-m open-path which could be significantly influenced by the ambient meteorological conditions (RH, wind direction, wind speed, etc.), while the UV LED-IBBCEAS sampled local air into its optical cavity for the measurement, which led to more stable measurement conditions.

4 Conclusion

In conclusion, LED-based IBBCEAS operating around 370 nm wavelength has been applied, for the first time, to address the issue of missing data in the LIDAR blind zone (lowest hundreds of meters of the atmosphere). Combined measurements of aerosol extinction coefficients have been performed using LIDAR remote sensing and IBBCEAS in situ monitoring at the same location near ground surface. Good correlation ($R^2=0.90$) between the data obtained with these two different measurement techniques was obtained. This work demonstrates the potential of using aerosol extinction data measured by IBBCEAS located close to the LIDAR measurement site, for near-end LIDAR calibration to compensate for missing data in its blind zone, in particular near ground surface. It would be useful to refine LIDAR signal inversion and thus to improve the reliability and accuracy of atmospheric aerosol data. The present work also shows the interest of developing a low-cost, compact and robust IBBCEAS instrument (currently not commercially available) for UV-borne measurements to determine the vertical profile of the LIDAR ratio for near-end calibration.

References

- [1] H. Rivera, J. A. Ogren, E. Andrews, O. L. Mayol-Bracero. Variations in the physicochemical and optical properties of natural aerosols in Puerto Rico - Implications for climate. *Atmospheric Chemistry and Physics Discussions*, 2018, 1-28. **10.5194/acp-2018-791**
- [2] D. Zhao, J. Xin, C. Gong, X. Wang, Y. Ma, Trends of aerosol optical properties over the heavy industrial zone of northeastern Asia in the past decade (2004–15). *Journal of the Atmospheric Sciences*, 2018, 75(6): 1741-1754. **10.1175/jas-d-17-0260.1**
- [3] S. M. Lor á-Salazar, W. P. Arnott, H. Moosmüller. Accuracy of near-surface aerosol extinction determined from columnar aerosol optical depth measurements in Reno, NV, USA. *Journal of Geophysical Research: Atmospheres*, 2014, 119(19): 11,355-311,374. **10.1002/2014jd022138**
- [4] C. Talbot, P. Augustin, C. Leroy, V. Willart, H. Delbarre, G. Khomenko. Impact of a sea breeze on the boundary-layer dynamics and the atmospheric stratification in a coastal area of the North Sea. *Boundary-Layer Meteorology*, 2007, 125(1): 133-154. **10.1007/s10546-007-9185-6**
- [5] J. Wang, W. Liu, C. Liu, J. Liu, Z. Chen, Y. Xiang, X. Meng. The determination of aerosol distribution by a no-blind-zone scanning LIDAR. *Remote Sensing*, 2020, 12: 626. **10.3390/rs12040626**
- [6] A. Rognmo, U. P. Hoppe. Measuring the Transmitter beam divergence and controlling the beam alignment in a LIDAR instrument. *In European Rocket and Balloon Programs and Related Research*, 1999, 437:191-195. **1999ESASP.437..191R**
- [7] D. Painemal, M. Clayton, R. Ferrare, S. Burton, D. Josset, M. Vaughan. Novel aerosol extinction coefficients and LIDAR ratios over the ocean from CALIPSO-CloudSat: evaluation and global statistics. *Atmospheric Measurement Techniques*, 2019, 12(4): 2201-2217. **10.5194/amt-12-2201-2019**
- [8] G. Sun, L. Qin, Z. Hou, X. Jing, F. He, F. Tan, S. Zhang. Small-scale Scheimpflug LIDAR for aerosol extinction coefficient and vertical atmospheric transmittance detection. *Optics Express*, 2018, 26(6): 7423-7436. **10.1364/OE.26.007423**
- [9] J. Shen, N. Cao. Accurate inversion of tropospheric aerosol extinction coefficient profile by Mie-Raman LIDAR. *Optik*, 2019, 184: 153-164. **10.1016/j.ijleo.2018.12.151**
- [10] J. Zalach, C. von Savigny, A. Langenbach, G. Baumgarten, F. Lübken, A. Bourassa. Challenges in retrieving stratospheric aerosol extinction and particle size from

- ground-based RMR- LIDAR observations. *Atmospheric Measurement Techniques Discussions*, 2019: 1-21. **10.5194/amt-2019-267**
- [11] T. Halldorsson, J. Langerholc. Geometrical form factors for the LIDAR function. *Applied Optics*, 1978, 17(2): 240-244. **10.1364/AO.17.000240**
- [12] S. Lolli, L. Sauvage, S. Loaec, M. Lardier. EZ LIDAR™: A new compact autonomous eye-safe scanning aerosol LIDAR for extinction measurements and PBL height detection. Validation of the performances against other instruments and intercomparison campaigns. *Optica Pura y Aplicada*, 2011, 44(1): 33-41. **hal-01119142**
- [13] A. W. Strawa, R. Elleman, A. G. Hallar, D. Covert, K. Ricci, R. Provencal, T. W. Owano, H. H. Jonsson, B. Schmid, A. P. Luu, K. Bokarius, E. Andrews. Comparison of in situ aerosol extinction and scattering coefficient measurements made during the Aerosol Intensive Operating Period. *Journal of Geophysical Research*, 2006, 111(D5S03). **10.1029/2005jd006056**
- [14] P. Massoli, D. M. Murphy, D. A. Lack, T. Baynard, C. A. Brock, E. R. Lovejoy. Uncertainty in Light Scattering Measurements by TSI Nephelometer: Results from Laboratory Studies and Implications for Ambient Measurements. *Aerosol Science and Technology*, 2009, 43(11): 1064-1074. **10.1080/02786820903156542**
- [15] W. R. Espinosa, L. A. Remer, O. Dubovik, L. Ziemba, A. Beyersdorf, D. Orozco, G. Schuster, T. Lapyonok, D. Fuertes, J. V. Martins. Retrievals of aerosol optical and microphysical properties from imaging polar nephelometer scattering measurements. *Atmospheric Measurement Techniques*, 2017, 10(3): 811-824. **10.5194/amt-10-811-2017**
- [16] J. Saturno, C. Pöhlker, D. Massabò, J. Brito, S. Carbone, Y. Cheng, X. Chi, F. Ditas, I. Hrabě de Angelis, D. Morán-Zuloaga, M. L. Pöhlker, L. V. Rizzo, D. Walter, Q. Wang, P. Artaxo, P. Prati, M. O. Andreae. Comparison of different aethalometer correction schemes and a reference multi-wavelength absorption technique for ambient aerosol data. *Atmospheric Measurement Techniques*, 2017, 10(8): 2837-2850. **10.5194/amt-10-2837-2017**
- [17] T. Müller, J. S. Henzing, G. de Leeuw, A. Wiedensohler, A. Alastuey, H. Angelov, M. Bizjak, M. Collaud Coen, J. E. Engström, C. Gruening, R. Hillamo, A. Hoffer, K. Imre, P. Ivanow, G. Jennings, J. Y. Sun, N. Kalivitis, H. Karlsson, M. Komppula, P. Laj, S. M. Li, C. Lunder, A. Marinoni, S. Martins dos Santos, M. Moerman, A. Nowak, J. A. Ogren, A. Petzold, J. M. Pichon, S. Rodriguez, S. Sharma, P. J. Sheridan, K. Teinilä, T. Tuch, M. Viana, A. Virkkula, E. Weingartner, R. Wilhelm, Y. Q. Wang. Characterization and intercomparison of aerosol absorption photometers: result of two intercomparison workshops. *Atmospheric Measurement Techniques*, 2011, 4(2): 245-268. **10.5194/amt-4-245-2011**

- [18] P. Zieger, E. Weingartner, J. Henzing, M. Moerman, G. de Leeuw, J. Mikkilä, M. Ehn, T. Petäjä, K. Cléner, M. van Roozendaal, S. Yilmaz, U. Frieß, H. Irie, T. Wagner, R. Shaiganfar, S. Beirle, A. Apituley, K. Wilson, U. Baltensperger. Comparison of ambient aerosol extinction coefficients obtained from in-situ, MAX-DOAS and LIDAR measurements at Cabauw. *Atmospheric Chemistry and Physics*, 2011, 11(6): 2603-2624. **10.5194/acp-11-2603-2011**
- [19] A. Petzold, T. Onasch, P. Keegan, A. Freedman. Intercomparison of a Cavity Attenuated Phase Shift-based extinction monitor (CAPS PMex) with an integrating nephelometer and a filter-based absorption monitor. *Atmospheric Measurement Techniques*, 2013, 6(5): 1141-1151. **10.5194/amt-6-1141-2013**
- [20] Y. Sasano, H. Shimizu, N. Takeuchi, M. Okuda. Geometrical form factor in the laser radar equation: an experimental determination. *Applied Optics*, 1979, 18: 3908-3910. **10.1364/AO.18.003908**
- [21] J. D. Klett. Stable analytical inversion solution for processing LIDAR returns. *Applied Optics*, 1981, 20: 211-220. **10.1364/AO.20.000211**
- [22] F. G. Fernald. Analysis of atmospheric LIDAR observations: Some comments. *Applied Optics*, 1984, 23: 652-653. **10.1364/AO.23.000652**
- [23] P. M. Hamilton. LIDAR measurement of backscatter and attenuation of atmospheric aerosol. *Atmospheric Environment*, 1967, 3(2): 221-223. **10.1016/0004-6981(69)90010-9**
- [24] W. Zhao, X. Xu, M. Dong, W. Chen, X. Gu, C. Hu, Y. Huang, X. Gao, W. Huang, W. Zhang. Development of a cavity-enhanced aerosol albedometer. *Atmospheric Measurement Techniques*, 2014, 7(8): 2551-2566. **10.5194/amt-7-2551-2014**
- [25] J. P. Burrows, A. Dehn, B. Deters, S. Himmelman, A. Richter, S. Voigt, J. Orphal. Atmospheric remote-sensing reference data from GOME: part 1. temperature-dependent absorption cross-sections of NO₂ in the 231-794 nm range. *Journal of Quantitative Spectroscopy and Radiative Transfer*, 1998, 60(6): 1025-1031. **10.1016/S0022-4073(97)00197-0**
- [26] R. Thalman, K. J. Zarzana, M. A. Tolbert, R. Volkamer. Rayleigh scattering cross-section measurements of nitrogen, argon, oxygen and air. *Journal of Quantitative Spectroscopy and Radiative Transfer*, 2014, 147: 171-177. **10.1016/j.jqsrt.2014.05.030**
- [27] J. M. Langridge, S. M. Ball, A. J. Shillings, R. L. Jones. A broadband absorption spectrometer using light emitting diodes for ultrasensitive, in situ trace gas detection. *Review of Scientific Instruments*, 2008, 79(12): 123110. **10.1063/1.3046282**
- [28] O. C. Fleischmann, M. Hartmann, J. P. Burrows, J. Orphal. New ultraviolet absorption cross-sections of BrO at atmospheric temperatures measured by time-

- windowing Fourier transform spectroscopy. *Journal of Photochemistry and Photobiology A: Chemistry*, 2004, 168(1-2): 117-132. **10.1016/j.jphotochem.2004.03.026**
- [28] C. A. Cantrell, J. A. Davidson, A. H. McDaniel, R. E. Shetter, J. G. Calvert. Temperature-dependent formaldehyde cross sections in the near-ultraviolet spectral region. *The Journal of Physical Chemistry*, 1990, 94(10): 3902-3908. **10.1021/j100373a008**
- [29] J. P. Burrows, A. Richter, A. Dehn, B. Deters, S. Himmelmann, S. Voigt, J. Orphal. Atmospheric remote-sensing reference data from GOME2. temperature-dependent absorption cross sections of O₃ in the 231-794 nm range. *Journal of Quantitative Spectroscopy and Radiative Transfer*, 1999, 61(4): 509-517. **10.1016/s0022-4073(98)00037-5**
- [30] O. C. Fleischmann, M. Hartmann, J. P. Burrows, J. Orphal. New ultraviolet absorption cross-sections of BrO at atmospheric temperatures measured by time-windowing Fourier transform spectroscopy. *Journal of Photochemistry and Photobiology A: Chemistry*, 2004, 168(1-2): 117-132. **10.1016/j.jphotochem.2004.03.026**
- [31] Y. Bedjanian, G. Le Bras, G. Poulet. Kinetic study of the Br⁺IO, I⁺BrO and Br⁺I₂ reactions. Heat of formation of the BrO radical. *Chemical Physics Letters*, 1997, 266(1-2): 233-238. **10.1016/s0009-2614(97)01530-3**
- [32] H. Kromminga, J. Orphal, P. Spietz, S. Voigt, J. P. Burrows. New measurements of OClO absorption cross-sections in the 325-435 nm region and their temperature dependence between 213 and 293 K. *Journal of Photochemistry and Photobiology A: Chemistry*, 2003, 157(2-3): 149-160. **10.1016/s1010-6030(03)00071-6**
- [33] C. Peters, S. Pechtl, J. Stutz, K. Hebestreit, G. Hönninger, K. G. Heumann, A. Schwarz, J. Winterlik, U. Platt. Reactive and organic halogen species in three different European coastal environments. *Atmospheric Chemistry and Physics, European Geosciences Union*, 2005, 5(12): 3357-3375. **hal-00295805**
- [34] R. Volkamer, P. Spietz, J. Burrows, U. Platt. High-resolution absorption cross-section of glyoxal in the UV-vis and IR spectral ranges. *Journal of Photochemistry and Photobiology A: Chemistry*, 2005, 172(1): 35-46. **10.1016/j.jphotochem.2004.11.011**
- [35] T. Wu, C. Coeur-Tourneur, G. Dhont, A. Cassez, E. Fertein, X. He, W. Chen. Simultaneous monitoring of temporal profiles of NO₃, NO₂ and O₃ by incoherent broadband cavity enhanced absorption spectroscopy for atmospheric application. *Journal of Quantitative Spectroscopy & Radiative Transfer*, 2014, 133: 199-205. **10.1016/j.jqsrt.2013.08.002**

Chapter IV Laboratory studies of the reactions of VOCs with nitrate radicals

Since the finding of the importance of nitrate radical in nocturnal chemistry, many laboratory studies on the reactions of VOCs with NO_3 have been carried out. Regarding the determination of reaction rate constants, the relative rate method has been much largely used in those studies, because direct, time-resolved detection of NO_3 has been very challenging. Yet, since the relative rate method implies the use of reference compounds with known nitrate rate constants, this increases the uncertainties in the rate constant obtained.

In the following chapter, we present the results of laboratory studies using an IBBCEAS instrument coupled to the environmental chamber CHARME. In the first part, the kinetics of NO_3 with guaiacol (2-methoxyphenol, 2MP) was investigated by using the pseudo-first order method with an excess of 2-MP and tracking the NO_3 concentrations profiles. In a second part, the chemical mechanism for the reaction of guaiacol with NO_3 was studied. Note that the results on guaiacol have been accepted for publication in the journal *Atmospheric Environment* (Meng et al., 2020) and the corresponding parts are reproduced *in extenso* in the present chapter.

1 Context of the study

Biomass combustion is a one of the major source of both gases and particulates in many parts of the world. It is estimated to contribute approximately 10 - 50% of the total organic fraction of aerosols [1], and it can be inferred that biomass combustion has a direct influence on both ambient air quality and climate change [2]. Some earlier studies showed that wood smoke exposure can lead to many adverse health effects, such as acute respiratory infections, asthma, lung cancer and cataracts [3, 4].

Natural wood consists of three basic polymers, cellulose, lignin, and hemicelluloses. Lignin is estimated to account for 18 - 35% by mass [5] and methoxyphenols are emitted from the pyrolysis of lignin.

The reactivity of methoxyphenols with hydroxyl radicals [6-9], chlorine atoms [10], ozone [11] and nitrate radicals [12-14] has been investigated. The determination of the rate coefficients for these reactions demonstrates the high reactivity of methoxyphenols toward OH, Cl and NO₃ and their low reactivity with O₃. In the nocturnal atmosphere, the nitrate radical is the dominant oxidant, and its reactivity with VOCs is similar to that of OH during daytime [15]. Because of the fast diurnal photolysis of NO₃, appreciable [NO₃] can only accumulate at night, with concentrations ranging from 5×10^7 to 1×10^{10} molecules cm⁻³ [16, 17]. Based on literature data, a recent study [12] estimated the lifetime of 13 ~ 174 s for methoxyphenols with respects to their reaction with NO₃ (for [NO₃] = 5×10^8 molecules cm⁻³ [18]), the large range of lifetimes reflecting disagreements in rate constants for the reaction of guaiacol with NO₃. Complementary investigations are thus clearly needed for this class of compounds.

2 Kinetics of the reaction of NO₃ radical with guaiacol

2.1 Experimental section

2.1.1 Experimental system

The experiments were performed in the dark in CHARME chamber at room temperature (294 ± 2 K), atmospheric pressure and low relative humidity (RH < 2%).

Purified and dried air was introduced into the chamber using a generator (Parker Zander KA-MT 1-8) connected to a compressor (SLM-S 7.5 - Renner SCROLLLine). CHARME is coupled to a vacuum pump (Cobra NC0100-0300B), which allows to reduce the pressure down to 0.4 mbar. The time required to evacuate and fill the reactor was around 1 h.

Guaiacol (2-methoxyphenol) was introduced into the simulation chamber under vacuum (~ 0.04 mbar) and then NO_3 was introduced.

2.1.2 Chemicals

The compounds used in this study, their manufacturer and stated purity were: guaiacol (Alpha Aesar, 98 %), m-cresol (Merck Schuchardt, 99%), o-cresol (Merck Schuchardt, 99%), p-cresol (Merck Schuchardt, 98%), water (VWR, > 99.9 %), dioxygen (Praxair, 99.5 %) and nitrogen dioxide (Praxair, 99 %).

In this study, the NO_3 radicals were generated by two methods:

a) *in situ* formation of NO_3 from reactions (R18):



NO_2 was injected first with a gas syringe and O_3 generated using an ozone generator (by Corona discharge in O_2 , Model C-Lasky, C-010-DTI) was then introduced. The injection of both gases were performed in a few seconds. The nitrogen dioxide and ozone concentrations were measured with a chemiluminescence NO_x analyzer (Thermo Scientific, 42i) and a photometric ozone analyzer (Thermo Scientific, 49i), respectively.

b) thermal decomposition of dinitrogen pentoxide (N_2O_5) [19, 20]:

N_2O_5 was first synthesized in a vacuum line through the reaction of NO_2 with an excess of O_3 according to the forward reaction of R19, which is followed by the reverse reaction:



A setup presented in Fig.IV-1 (a) for N_2O_5 has been installed and the process of formation of N_2O_5 is :

- 1) Prepare the ethanol bath ($-80 \sim 85$ °C) in the dewar (Fig.IV-1 (b));
- 2) Vacuum the setup in Fig.IV-1 (a);

- 3) Connect the NO_2 cylinder to the setup, and trap the NO_2 in a glass tube with the ethanol bath in the form of white crystals, which correspond to nitrogen peroxide (N_2O_4), if blue colour appears then nitric acid is formed;
- 4) To trap the N_2O_5 move the ethanol bath to another trap and flush the first trap with O_3 , which leads to the formation of N_2O_5 and store the crystal products (Fig.IV-1 (c)) in a refrigerator of $T = -80\text{ }^\circ\text{C}$.

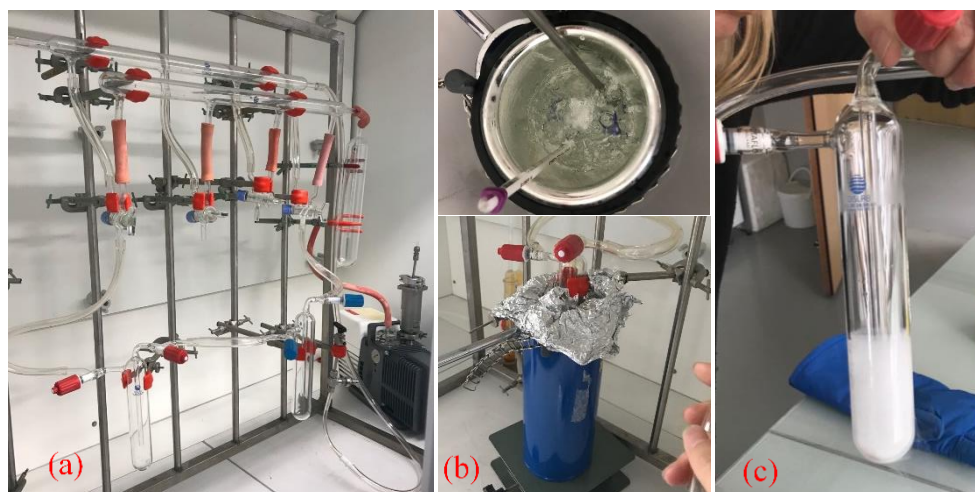


Figure IV-1 Setups of N_2O_5 formation: (a) Setups for the formation process; (b) Ethanol bath in dewar vessel; (c) N_2O_5 crystal in the trap.

2.1.3 Kinetic study methods

The rate constants for the reactions of NO_3 radical with guaiacol could be measured using two methods: the pseudo-first order (absolute) method and the relative method.

2.1.3.1 Pseudo-first-order method

In the pseudo-first order method, NO_3 was generated by the *in situ* method and its decay was measured with the IBBCEAS setup mounted on the chamber. For these experiments, guaiacol concentrations were in excess compared to those of nitrate radicals (about a factor of 10 higher).

During this process, NO_3 , O_3 and NO_2 are in equilibrium; therefore, the rate coefficient can be obtained by fitting NO_3 temporal profiles using the Facsimile software [21]. Besides the reactions R18 and R19, the relevant reactions are:



Under pseudo-first-order conditions, the rate of disappearance of NO_3 followed a simple exponential rate law:

$$[\text{NO}_3]_t = [\text{NO}_3]_0 \times e^{-k't} \quad (\text{Eq.20})$$

where $k' = k \times [\text{guaiacol}] + k'_{\text{loss}}$ is the total radical decay caused by its wall loss (first-order rate coefficient for NO_3 removal in the absence of guaiacol) and its reaction with guaiacol. Using Facsimile, the k and k'_{loss} would be fitted out.

2.1.3.2 Relative rate method

This method is based on the measurement of the loss of a reactant, guaiacol in this study, relative to that of a reference compound in the presence of an oxidant [17, 22]. Ideally, the ratio of the rate constants between the reference and the reactant with the same oxidant should be in the range of 0.2 ~ 5. NO_3 was produced by the two methods cited above.

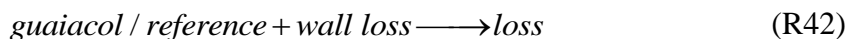
In this study on the NO_3 reaction with guaiacol, three reference compounds were used: o-cresol, m-cresol, and p-cresol. Their rate constants with NO_3 (in units of $\text{cm}^3 \text{ molecule}^{-1} \text{ s}^{-1}$) are: $k_{\text{o-cresol}} = (1.40 \pm 0.16) \times 10^{-11}$ [23], $k_{\text{m-cresol}} = (1.10 \pm 0.13) \times 10^{-11}$ [23] and $k_{\text{p-cresol}} = (1.10 \pm 0.13) \times 10^{-11}$ [23].

For both NO_3 production methods, reactions between the VOCs and the NO_3 radical will take place simultaneously:





Preliminary tests have shown that the wall losses for guaiacol and reference VOCs were not negligible. Thus, wall loss reactions need to be taken into account:



Kinetic analysis of the reactions R36, R41 and R42 leads to the following relationship for the relative rate method:

$$\ln \frac{[guaiacol]_0}{[guaiacol]_t} - k'_{loss} \cdot t = \frac{k_{guaiacol}}{k_{reference}} \left\{ \ln \frac{[reference]_0}{[reference]_t} - k'_{ref} \cdot t \right\} \quad (Eq.21)$$

where $k_{guaiacol}$ and $k_{reference}$ are the rate constants for the reactions R36 and R41; k'_{loss} and k'_{ref} are the wall loss rate constants for guaiacol and reference in reactions R42; $[guaiacol]_0$, $[guaiacol]_t$ and $[reference]_0$, $[reference]_t$ are the concentrations of guaiacol and reference in the beginning and at any time t of the reaction, respectively.

Hence, by plotting $\ln\{[guaiacol]_0/[guaiacol]_t\} - k'_{loss}(t)$ against $\ln\{[reference]_0/[reference]_t\} - k'_{ref}(t)$, a straight line with the slope of $k_{guaiacol}/k_{reference}$ should be obtained.

2.2 Results and discussion

2.2.1 Specifications of IBBCEAS

An IBBCEAS system has been installed in CHARME, as described in Section 1.3.2 of Chapter II. The mirror reflectivity was determined from Eq.14 by injection of NO_2 (1295 ppbv) in zero air into the simulation chamber (shown in Fig.IV-2 (b)). The NO_2 concentration was monitored by a chemiluminescence NO_x analyzer. The mirror reflectivity $R(\lambda)$ was thus determined from Eq.14 and fitted by a fifth-order polynomial:

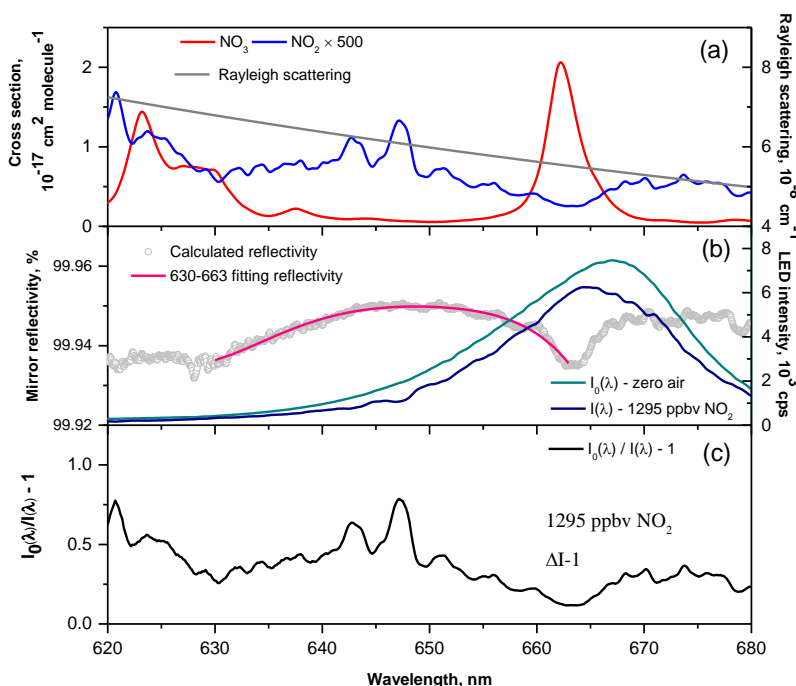
$$R = 1 - d \times \left(\frac{n_{NO_2} \sigma_{NO_2}(\lambda) \cdot I(\lambda)}{I_0(\lambda) - I(\lambda)} - \alpha_{Ray, N_2}(\lambda) \right) \quad (Eq.22)$$

where d is the chamber length (482 cm), n_{NO_2} is the number concentration of NO_2 (3.29×10^{13} molecules cm^{-3} at 1 atm and 18 °C), $\sigma_{NO_2}(\lambda)$ is the absorption cross section of NO_2

($6.51 \times 10^{-21} \text{ cm}^2 \text{ molecule}^{-1}$ at 660 nm and 1 atm), $\alpha_{\text{Ray}, \text{N}_2}(\lambda)$ is the Rayleigh scattering coefficient, which is calculated as $5.62 \times 10^{-8} \text{ cm}^{-1}$ at 660 nm and 1 atm [24], $I_0(\lambda)$ and $I(\lambda)$ are the intensities when cavity is with zero air and with NO_2 , respectively.

Fig.IV-2 (a) shows the cross sections of NO_2 [25], NO_3 [26] and Rayleigh scattering coefficient used in this work for the calibration of mirror reflectivity and concentration retrieval, Fig.IV-2 (b) and (d) shows the mirror reflectivity determined for NO_3 measurement around 660 nm in CHARME and the LED emission spectrum, respectively, and Fig.IV-2 (c) is the NO_2 (1295 ppbv) absorption characteristic determined in the mirror reflectivity calculation in Fig.IV-2 (b). Normally, the working wavelength should include the largest absorption band of NO_3 (660 nm – 665 nm). However in CHARME, the calibration result showed the mirrors do not present a good fifth-order polynomial between 660 nm and 665 nm, therefore to have the smooth mirror reflectivity, the fitting wavelength was confirmed from 630 nm to 663 nm.

The maximum mirror reflectivity was 99.95% at ~650 nm, which led to an effective optical absorption length of 9.14 km. The upper panel shows NO_2 and NO_3 spectra in the same region for comparison. Each spectrum was recorded with a total acquisition time of 15 s (integrated time of 600 ms \times 25 average times).



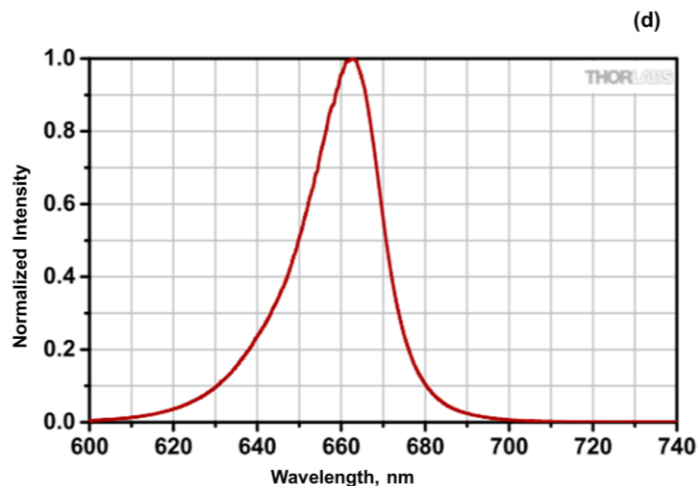


Figure IV-2 (a) NO_2 [25] and NO_3 [26] absorption cross sections around 650 nm, and Rayleigh scattering coefficient [24]; (b) Light intensities and mirror reflectivity; (c) 1295 ppbv NO_2 absorption characteristic; (d) LED emission spectrum.

A representative data retrieval is shown in Fig.IV-3, depicting measured (black circles) and fitted (magenta curve) IBBCEAS spectra of 445.5 ppbv NO_2 and 2.0 ppbv NO_3 in the chamber sample.

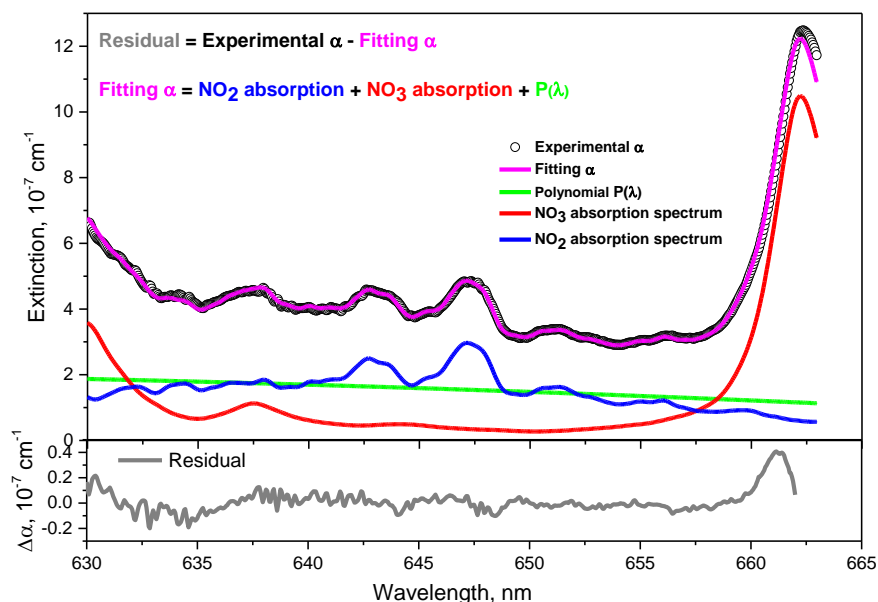


Figure IV-3 Typical data retrieval of NO_2 (445.4 ppbv) and NO_3 (2.0 ppbv) from a measured IBBCEAS spectrum of chamber sample.

LoD for NO₂ of the IBBCEAS instrument coupled to CHARME was evaluated using Eq.19. And similarly LoD of NO₃ was retrieved. Based on the standard deviation of the fit residual in Fig.IV-3, and SNR of 23.2 for NO₂ and 81.5 for NO₃, the detection limits for NO₂ and NO₃ were 19.2 ppbv and 24.5 pptv, respectively with an integration time of 15 s.

An example showing NO₃ formation after successive additions of NO₂ and O₃ is given in Fig.IV-4. Time series of NO₃ and NO₂ were simultaneously measured by IBBCEAS and chemiluminescence analyzer for 3.5 h after an initial injection of 2000 ppbv NO₂. Then, after about 30 min for NO₂ concentration stabilization, 1600 ppbv O₃ were introduced to generate NO₃ *in situ*.

The concentrations of the different gaseous species were simulated using the Facsimile software and these data were compared to those experimentally measured. The corresponding reaction mechanism is shown in Tab.IV-1:

Table IV-1 Chemical reaction system used to simulate the temporal profiles of NO₃, NO₂, O₃ and N₂O₅ concentrations with Facsimile.

Chemical reaction	<i>k</i> (at 296 K)	Units
$NO_2 + O_3 \longrightarrow NO_3 + O_2$	3.33×10^{-17} $\Delta \log k = \pm 0.06^a$	cm ³ molecule ⁻¹ s ⁻¹
$NO_2 + NO_3 \xrightleftharpoons{M} N_2O_5$	1.25×10^{-12} $\Delta \log k = \pm 0.2^a$	cm ³ molecule ⁻¹ s ⁻¹
	3.48×10^{-2} $\Delta \log k = \pm 0.3^a$	s ⁻¹
$NO_3 + wall\ loss \longrightarrow loss$	$1.48 \times 10^{-2}^b$	s ⁻¹
$N_2O_5 + wall\ loss \longrightarrow loss$	$2.17 \times 10^{-5}^b$	s ⁻¹
$O_3 + wall\ loss \longrightarrow loss$	$3.36 \times 10^{-5}^c$	s ⁻¹
$NO_2 + wall\ loss \longrightarrow loss$	$1.91 \times 10^{-5}^c$	s ⁻¹

^a Recommended values at 296 K [27].

^b Rate constants adjusted using the Facsimile software to match the experimental concentrations of NO₃ and NO₂. These constants depend on the chamber properties.

^c Rate constants directly measured.

The simulated concentration-time profile of NO_2 displays good agreement with IBBCEAS measurements, while chemiluminescence NO_2 measurements rapidly disagree after O_3 addition. This was expected, as it is known that other nitrogen species (i.e. NO_3 , N_2O_5 ...) interfere in chemiluminescence analyzers [28]. Before the injection of ozone, the correlation between the NO_2 concentrations measured by IBBCEAS and chemiluminescence is $y = 1.077x - 180.0$ with $R^2 = 0.90$ which validates the measurements of NO_2 performed with the developed IBBCEAS as shown in Fig.IV-5.

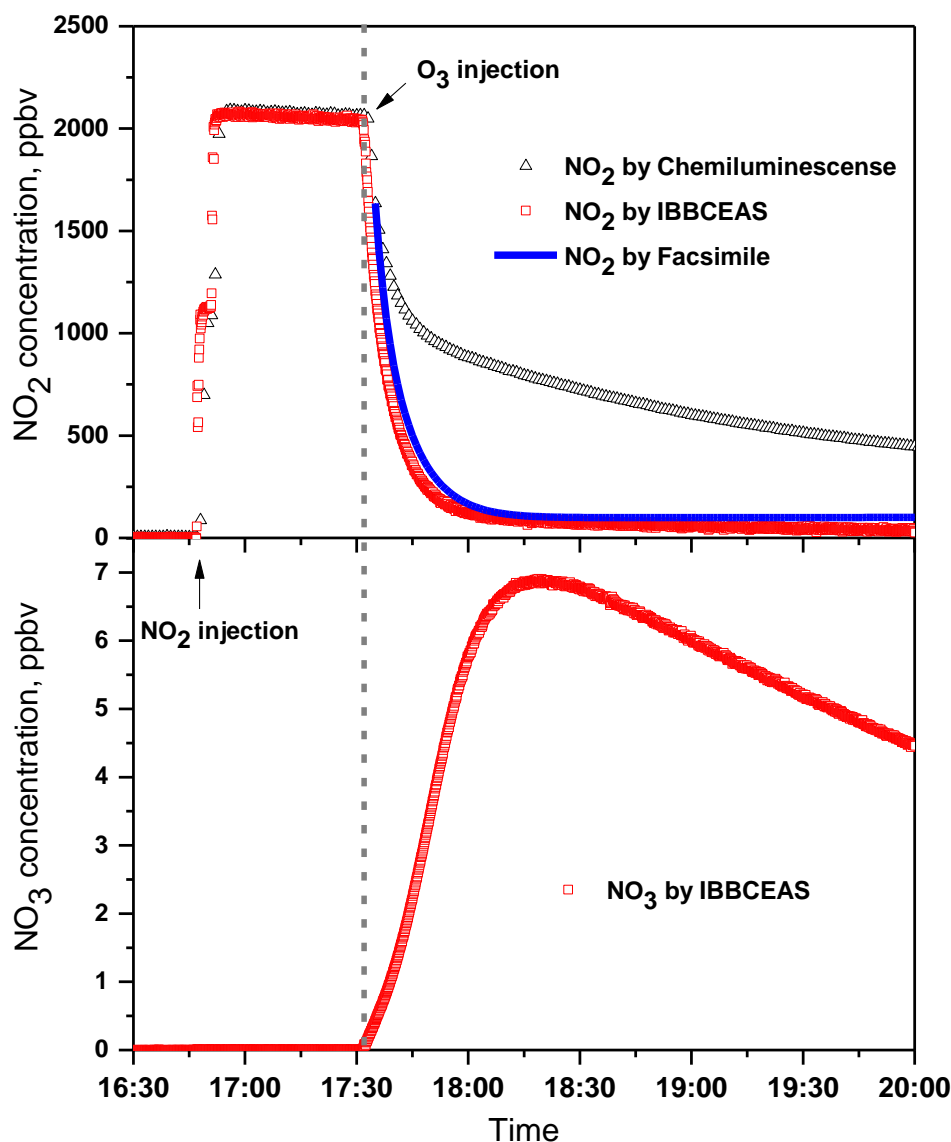


Figure IV-4 NO_2 (upper panel) and NO_3 (lower panel) time profiles following injection of 2000 ppbv NO_2 , ~30 min stabilization and injection of 1600 ppbv O_3 .

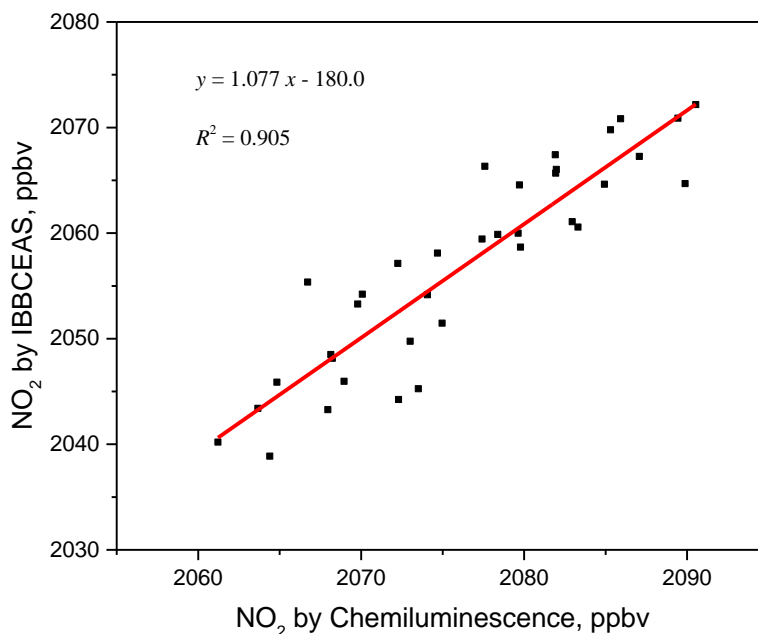


Figure IV-5 Correlation plot of NO_2 measured by IBBCEAS vs. NO_2 measured by chemiluminescence before O_3 injection.

2.2.2 NO_3 + guaiacol kinetics using the pseudo-first order method

A first, preliminary experiment was carried out with initial concentrations of ~ 2200 ppbv NO_2 and ~ 1800 ppbv O_3 , as shown in Fig.IV-6. NO_2 was introduced in the chamber by several injections and O_3 was flushed into the chamber after half an hour. By simulation using Facsimile, the maximum of $[\text{NO}_3]$ was estimated after ~ 40 min, consistent with the measurements. The experimental maximum $[\text{NO}_3]$ was observed ~ 40 min after the mixing of $\text{NO}_2 + \text{O}_3$.

450 ppbv guaiacol were then injected into the chamber and NO_3 immediately falls down to zero in ~ 2 min due to the fast reaction between guaiacol and NO_3 radical. This extremely fast decay makes it impossible to retrieve the $\text{NO}_3 + \text{guaiacol}$ rate constant.

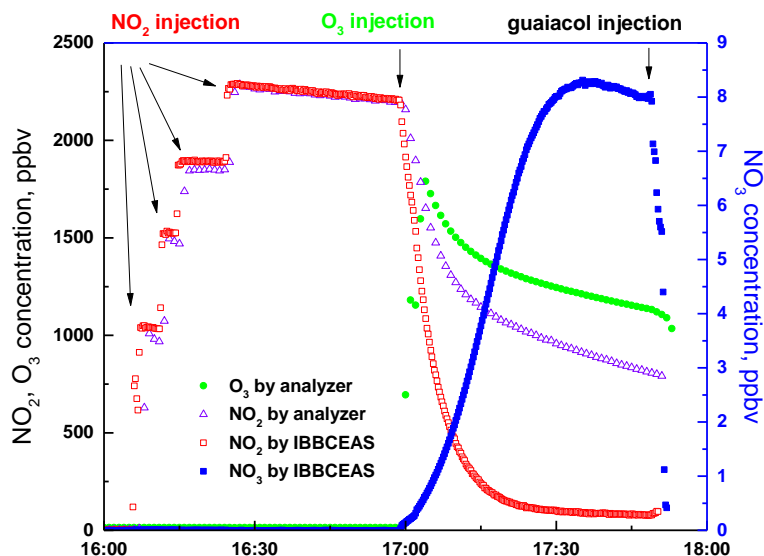


Figure IV-6 Time series of NO_2 , O_3 and NO_3 in experiment of NO_3 + guaiacol.

Thus, determining the rate constant of NO_3 + guaiacol by the pseudo-first order method is not possible, due to the fast reaction. Attention should be taken when applying this method for NO_3 + VOC rate constant determination, which appears to be more applicable for less reactive VOCs having k values lower than that of NO_3 + guaiacol (rate constant magnitude $10^{-11} \text{ cm}^3 \text{ molecule}^{-1} \text{ s}^{-1}$).

One thought to slow down the reaction rate, is to reduce the initial concentration of reactants. But due to the pseudo-first order method needs the concentration of one reactant in excess, which is difficult to control. If trying to lower the initial concentration of guaiacol, for the guaiacol injection needs some time to vapor in the chamber, during this period NO_3 would have been totally consumed for the fast rate constant.

2.2.3 NO_3 + guaiacol kinetics using the relative rate method

During the experimental study of the rate constant of NO_3 + guaiacol by relative rate method, experiments were performed using two methods to produce NO_3 radicals, by *in situ* production and through N_2O_5 decomposition.

In experiments with *in situ* NO_3 formation, the experiments followed the process:

- 1) Vacuum the chamber, and inject the guaiacol and reference VOCs with a syringe with the similar estimated concentration;

- 2) Fill the chamber with zero air to atmospheric pressure;
- 3) after ~ 30 min wall losses for guaiacol and reference, inject the NO_2 with a gas syringe, and introduce ozone by the O_3 generator.

In experiments with N_2O_5 decomposition method, the experiments process would be:

- 1) Vacuum chamber and then fill the chamber with zero air;
- 2) Inject the guaiacol and reference VOCs;
- 3) Until the concentrations of guaiacol and reference were in stable wall loss, take out the N_2O_5 crystal trap out of the refrigerator and keep the trap in the ethanol bath;
- 4) When NO_3 is needed, keep the indoor lights off, and take out the trap from the ethanol bath, flush the N_2O_5 trap with N_2 flow into the chamber.

Three isomers of cresol were used as reference compounds. The initial concentrations of guaiacol and references were in the range of 20 ~ 200 ppbv. Fig.IV-7 displays the decay losses of guaiacol vs. those of the reference compounds. The ratios $k_{\text{guaiacol}}/k_{\text{reference}}$ were derived from the linear-least square analysis which enables to obtain k_{guaiacol} . Tab.IV-2 summarizes the data obtained. The quoted errors on the rate coefficients k_{guaiacol} from each individual experiment were 2σ of $k_{\text{guaiacol}}/k_{\text{reference}}$ using the method recommended by Brauers and Finlayson-Pitts [29].

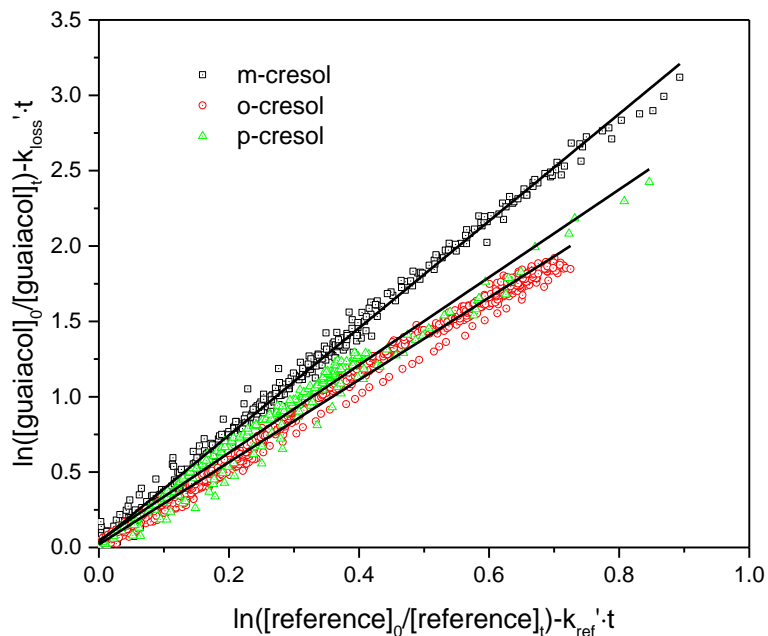


Figure IV-7 Plots of relative kinetics for NO_3 reaction with guaiacol using cresols as references.

Table IV-2 Experimental rate constants for the reaction of NO_3 radicals with guaiacol at 294 ± 2 K.

Ref. compound	$k_{\text{reference}} \times 10^{-11}$ ($\text{cm}^3 \text{ molecule}^{-1} \text{ s}^{-1}$)	$k_{\text{guaiacol}}/k_{\text{reference}}$	$k_{\text{guaiacol}} \times 10^{-11}$ ($\text{cm}^3 \text{ molecule}^{-1} \text{ s}^{-1}$)
m-cresol	1.10 ± 0.13	3.55 ± 0.03	3.91 ± 0.46
o-cresol	1.40 ± 0.16	2.73 ± 0.07	3.82 ± 0.45
p-cresol	1.10 ± 0.10	2.91 ± 0.02	3.20 ± 0.29

The rate constant for the reaction of guaiacol with NO_3 radical determined with the relative rate method using the three references are in good agreement, leading to an average value of $k_{\text{guaiacol}} = (3.77 \pm 0.39) \times 10^{-11} \text{ cm}^3 \text{ molecule}^{-1} \text{ s}^{-1}$. The observed consistency between the k_{guaiacol} obtained from the three references provides confidence in the rate constant measured in this work.

The present value of $(3.77 \pm 0.39) \times 10^{-11} \text{ cm}^3 \text{ molecule}^{-1} \text{ s}^{-1}$ is about 40% higher than a previous one obtained from the same lab: $(2.69 \pm 0.57) \times 10^{-11} \text{ cm}^3 \text{ molecule}^{-1} \text{ s}^{-1}$ [12].

The reasons for the discrepancy is not known. Besides, our result disagrees with the recent study of Yang et al. [13] who found $(0.32 \pm 0.14) \times 10^{-11} \text{ cm}^3 \text{ molecule}^{-1} \text{ s}^{-1}$. Yang et al. used N_2O_5 decomposition to generate NO_3 and 2-methyl-2-butene as reference compound. However, wall losses for both VOCs were neglected (which is especially surprising for such a sticky compound as guaiacol) which may explain the disagreement.

3 SOAs formation from the gas-phase reaction of guaiacol with NO_3 radicals

The formation of SOAs from guaiacol with respect to its reaction with OH has been investigated in the literature [7, 8]. In most environments, atmospheric aerosol concentrations of around $5 \mu\text{g m}^{-3}$ can be found and in these atmospheric conditions, the OH reactions of guaiacol contribute for a minor part to SOAs production. The objective of this work was to study the reaction of guaiacol with NO_3 radicals in order to investigate its potential to form SOAs and discuss atmospheric implications of the reaction of guaiacol with NO_3 radicals.

3.1 Experimental section

3.1.1 Experimental system and method

The experiments were conducted in two simulation chambers: LPCA-ONE and CHARME. LPCA-ONE is a cubic, rigid PMMA (PolyMethyl Methacrylate) reactor with volume of 8.0 m^3 ($2 \text{ m} \times 2 \text{ m} \times 2 \text{ m}$) and a surface-to-volume ratio of 3 m^{-1} . It is equipped with a Teflon fan (diameter 30 cm) located in the center of the lower face to ensure homogeneous mixing of the reactants. Prior to each experiment, the reaction chamber was flushed with purified air for about 12 h. More details about the LPCA-ONE can be found in [30]. Note that these experiments with LPCA-ONE were performed by another PhD student [30].

Guaiacol was introduced into the simulation chambers using an inlet system in which measured amounts of the substances were gently heated ($50 \text{ }^\circ\text{C}$) in a small flow of purified air.

The experiments were performed with guaiacol initial concentrations in the range (84 - 537 ppbv). After allowing a few minutes for guaiacol mixing, NO₂ (500 - 1500 ppbv) and O₃ (500 -1000 ppbv) or N₂O₅ were then introduced (within a few seconds) into the chambers. The concentration of guaiacol was recorded every 10 s with PTR-ToF-MS. Air samples were collected through a heated (333 K) peek inlet tube with a flow of 50 mL min⁻¹ into the PTR-ToF-MS drift tube and guaiacol was monitored from the peak at m/z 125.

Aerosol formation was followed with an SMPS using a 120 s scan time and a 16 s delay between samples, providing a size distribution from 15 to 661 nm. The aerosol mass concentration M₀ was calculated assuming a density of 1.4 for the organic aerosol (recommended value, [31]).

Preliminary experiments were performed to verify that guaiacol ozonolysis was negligible in the experiments where NO₃ was formed in-situ from NO₂ + O₃ (this was expected as the rate constant for the ozone reaction with guaiacol is low ($k_{(\text{guaiacol}+\text{O}_3)} = 4 \times 10^{-19} \text{ cm}^3 \text{ molecule}^{-1} \text{ s}^{-1}$, [11])).

Background aerosol formation could occur from the reaction of nitrate radicals with impurities in the purified air and/or with offgasing of compounds from the reactor walls. To characterize this particle formation, purified air was left in the dark in the presence of NO₃ for ≈ 1 h. These test experiments yielded aerosol mass concentrations of 0.2 $\mu\text{g m}^{-3}$, which is negligible compared to the SOAs mass concentrations observed from the reaction of NO₃ with guaiacol (between 7 and 547 $\mu\text{g m}^{-3}$).

SOAs wall loss rates were determined by monitoring the aerosol mass concentrations over a period of ≈ 1 h at the end of each experiment. SOA wall losses are described by a first order law, with a dependence on the aerosol size. The decay rates estimated in this study were in the range 5 - 44% h⁻¹. These values are within the range reported for other chamber experiments [7, 8, 32-36].

To determine the chemical composition of SOAs, quartz fiber filters were sampled at 7.5 L min⁻¹ during 3 h (47 mm diameter Whatman 1851-047 QMA). Before the sample collection, filters were fired at 500 °C for 12 h, and were then stored in an aluminum foil

< 4 °C until analysis. For the experiments performed with higher initial concentrations of guaiacol (2 ppmv), SOA masses and yields were not determined because a high fraction of the particles was outside the measurement range of the SMPS.

The collected aerosols were analyzed by ESI-LC-QToF-MS/MS (Agilent LC 1100 - MS 6540) using the negative ionization mode (proton abstraction). The chromatographic column used was a ZORBAX Extend-C18 (50 mm long × 2.1 mm i.d., 1.8 µm pore size) thermostated at 40 °C. The MS analyses allow to access the molar mass of the identified products and the MS/MS analyses, performed at three different energies (10 eV, 20 eV and 40 eV) permit to identify the functional groups of the compounds and to propose chemical structures.

The filters were ultrasonically extracted twice during 30 min in 5 mL of methanol. The solution was then filtered (pore sizes 0.45 µm; PTFE Membrane, Whatman) and the volume was gently reduced to 100 µL under a flow of gaseous nitrogen. Finally, the volume was diluted to 1 mL with ultrapure water in order to improve the separation of the compounds during the chromatographic analysis. The mobile phase used is a mixture of water (+0.1% formic acid) and acetonitrile (+5 mM ammonium formate); the gradient varied from 90% water / 10% acetonitrile at the beginning of the analysis to 100% acetonitrile at the end.

3.1.2 Chemicals

4-nitroguaiacol and 5-nitroguaiacol were both commercially available, so their identification was confirmed by the correlation of the LC retention times and the mass spectra recorded under the same chromatographic conditions.

The compounds used in this study, their manufacturer and stated purity were: guaiacol (Alpha Aesar, 98 %), 4-nitroguaiacol (Acros Organics, 97 %), 5-nitroguaiacol (TCI, 97 %), methanol (Aldrich, 99.9%), acetonitrile (VWR, > 99.9 %), water (VWR, > 99.9 %), sodium formate (VWR, > 99 %), formic acid (Acros Organics, 99 %), dioxygene (Praxair, 99.5 %) and nitrogen dioxide (Praxair, 99 %).

3.2 Results and discussion

3.2.1 SOA yields

A series of guaiacol/NO₃ experiments were carried out in the dark, at atmospheric pressure, room temperature (294 ± 2) K and low relative humidity (< 2 %). The initial concentrations of NO₂ ([NO₂]₀), O₃ ([O₃]₀) and guaiacol ([guaiacol]₀), the guaiacol reacted concentrations corrected for wall losses (Δ[guaiacol]), the organic aerosol mass concentrations corrected for wall losses (M₀) and the overall SOA yields (Y defined below) are summarized in Tab.IV-3. Guaiacol was totally consumed (within 15-60 min) in all experiments, so the reacted concentrations Δ[guaiacol] correspond to [guaiacol]₀ corrected for wall losses.

All experiments investigating SOA yields were achieved without inorganic seed aerosol and were conducted until the suspended aerosol mass (corrected for wall losses) M₀ was stable.

Typical time profiles of guaiacol and SOA mass concentrations are presented in Fig.IV-8 together with time-dependent aerosol size distributions (experiment guaiacol #10; initial conditions: guaiacol (276 ppbv; 1429 μg m⁻³); NO₂ (750 ppbv) and O₃ (500 ppbv)). The formation of particles started after about 45 min when almost all guaiacol has reacted. The first aerosol size distributions were centered on a few tens of nm. Then, particle number concentrations as well as SOA mass rapidly increased to reach a plateau after ~ 2h reaction time, consistent with a slower reaction rate due to the total consumption of the organic precursor. These observations suggest that the aerosol formation is due to the NO₃ reaction with guaiacol as well as with its first and second (or even further) generation products. The organic aerosol yield Y was experimentally determined as the ratio of the SOA formed (M₀ in μg m⁻³) to the reacted guaiacol concentration (Δ[guaiacol] in μg m⁻³) at the end of each experiment:

$$Y = \frac{M_0}{\Delta[\text{guaiacol}]} \quad (\text{Eq.23})$$

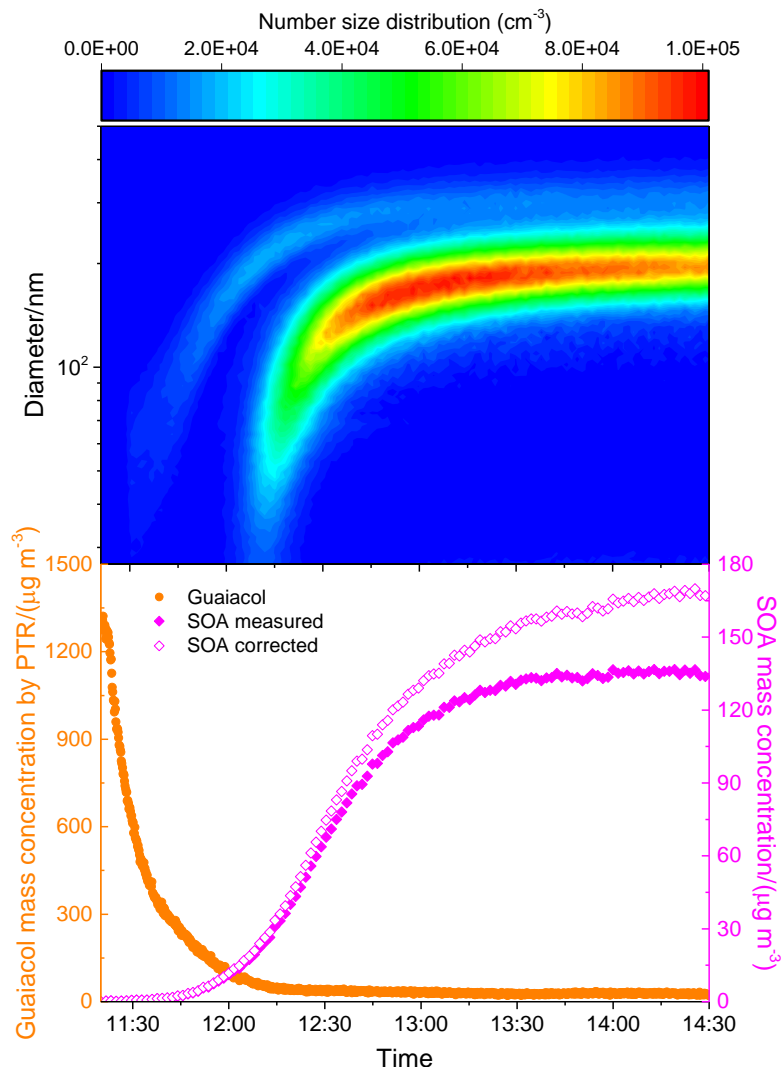


Figure IV-8 Typical concentration-time profiles obtained for guaiacol (PTR-ToF-MS) and SOAs (SMPS; measured and corrected for wall losses). Experiment guaiacol#10 (initial mixing ratios: guaiacol (276 ppbv; $1429 \mu\text{g m}^{-3}$); NO_2 (750 ppbv) and O_3 (500 ppbv)).

The uncertainty on the SOA yield values can be estimated at about 30%, due to statistical and possible systematic errors on M_0 and $\Delta[\text{guaiacol}]$. The results reported in Tab.IV-2 indicate that the initial concentration of guaiacol influenced the aerosol mass concentration formed: a higher guaiacol initial concentration led to higher SOA yields. Furthermore, as the organic aerosol mass directly affects the gas/particle partitioning by

acting as the medium into which oxidation products can be absorbed, higher SOA mass leads to higher SOA yields.

Table IV-3 Experimental conditions and results.

Expt.	[guaiacol] ₀ ^a (ppbv)	NO ₃ formation		Δ[guaiacol] ^b (μg m ⁻³)	M ₀ ^c (μg m ⁻³)	Y ^d
		[NO ₂] ₀ (ppbv)	[O ₃] ₀ (ppbv)			
In LPCA-ONE						
guaiacol #1	84	N ₂ O ₅ decomposition		436	13	0.03
guaiacol #2	158	N ₂ O ₅ decomposition		818	98	0.12
guaiacol #3	206	N ₂ O ₅ decomposition		1063	109	0.10
guaiacol #4	244	N ₂ O ₅ decomposition		1263	182	0.14
guaiacol #5	290	N ₂ O ₅ decomposition		1501	300	0.20
guaiacol #6	420	N ₂ O ₅ decomposition		2171	452	0.21
In CHARME						
guaiacol #7	117	N ₂ O ₅ decomposition		604	7	0.01
guaiacol #8	218	785 ^e	896 ^f	1130	92	0.08
guaiacol #9	228	535 ^e	620 ^f	1181	94	0.08
guaiacol #10	276	750 ^g	500 ^h	1429	170	0.12
guaiacol #11	288	1239 ^e	798 ^f	1492	314	0.21
guaiacol #12	537	1500 ^g	1000 ^h	2778	547	0.20

^a Initial guaiacol volume ratio.

^b Reacted guaiacol concentration (guaiacol was totally consumed in all experiments and the guaiacol wall losses were in the order of magnitude 10^{-6} or 10^{-5} s^{-1} which were neglected, so the reacted concentrations $\Delta[\text{guaiacol}]$ correspond to $[\text{guaiacol}]_0$).

^c Organic aerosol mass concentration (corrected for wall losses and assuming a particle density of 1.4 g/cm^3).

^d Overall SOA yield (Y) calculated as the ratio of M_0 to the total reacted guaiacol concentration.

^e Initial NO₂ volume ratio measured in the chamber (chemiluminescence NO_x analyzer).

^f Initial O₃ volume ratio measured in the chamber (photometric O₃ analyzer).

^g Initial injected NO₂ volume ratio.

^h Initial injected O₃ volume ratio.

The aerosol growth curve, represented by a plot of M_0 versus $\Delta[\text{guaiacol}]$ at the end of the experiments is shown in Fig.IV-9. Each experiment is represented by a single data point. The figure displays a linear correlation ($R^2 = 0.92$), with a slope of 0.25. This latter

value can be compared with the highest SOA yields determined for the reaction of guaiacol with NO_3 ($Y = 0.21$; see Tab.IV-3) and seems to represent the high-limit aerosol yield for this reaction. Extrapolation of the data shown in Fig.IV-9 suggests that the SOA production would be negligible for guaiacol reacted concentrations lower than $\approx 550 \mu\text{g m}^{-3}$ ($\approx 110 \text{ ppbv}$). This observation is corroborated by the results obtained for the less concentrated experiments (guaiacol #1 and guaiacol #7 with initial guaiacol concentrations of $436 \mu\text{g m}^{-3}$ and $604 \mu\text{g m}^{-3}$, respectively) in which the aerosol mass concentrations M_0 were low (around $10 \mu\text{g m}^{-3}$).

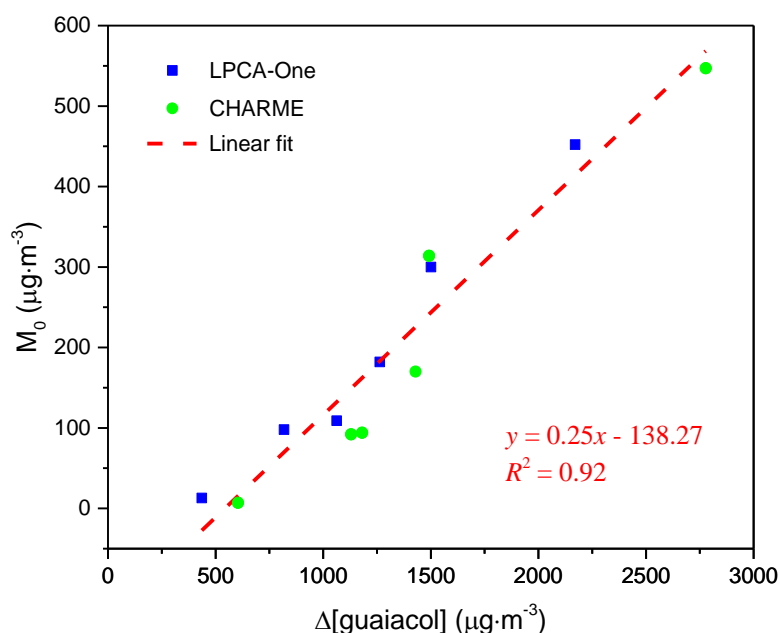


Figure IV-9 Aerosol growth curve: SOA mass concentration (M_0) against the reacted guaiacol concentration ($\Delta[\text{guaiacol}]$) measured at the end of the experiments. Each data point represents a separate experiment.

A widely-used semi-empirical model based on absorptive gas-particle partitioning of semi-volatile products (Odum et al., 1996; Pankow, 1994a,b) allows to describe the SOA yields. In this model, the SOA yield (Y) of a particular hydrocarbon (i) is given by:

$$Y = \sum_i M_0 \frac{\alpha_i K_{om,i}}{1 + K_{om,i} M_0} \quad (\text{Eq.24})$$

where α_i is the mass-based stoichiometric coefficient of the semi-volatile product i and $K_{om,i}$ is the gas-particle partitioning equilibrium constant. In this study, since no organic aerosol seed was used, the total aerosol mass is equal to the mass of the SOAs formed. Eq.24 can be fitted to the guaiacol experimental data to determine the values for α_i and $K_{om,i}$ (see Fig.IV-10). The simulation of Y versus M_0 with the one-product model is able to satisfactorily reproduce the experimental data ($R^2 = 0.94$). The two-products model was not retained as it leads to high uncertainties on the values of α_i and $K_{om,i}$ (sometimes more than 100% error). The fitting parameters α and K_{om} corresponding to the one-product semi-empirical model are 0.32 ± 0.04 and $(4.2 \pm 1.0) \times 10^{-3} \text{ m}^3 \mu\text{g}^{-1}$, respectively. Many studies on SOA yields from aromatic compounds have reported that the aerosol yields data should be fitted assuming two hypothetical products [37, 38]. However, a number of recent works have shown that the organic aerosol yields formed in aromatic photo-oxidation systems could be well described by assuming only one hypothetical product [7, 8, 32-34, 36, 39]. Although the organic aerosol-phase is often composed of many oxidation products, the present simulation with the one-product model indicates either that one semi-volatile organic compound is the major component of the condensed phase or that the few organics present in SOAs have similar α_i and $K_{om,i}$ values. In this latter case, the obtained constants α_i and $K_{om,i}$ would not have any intrinsic physical meaning but would rather represent mean values.

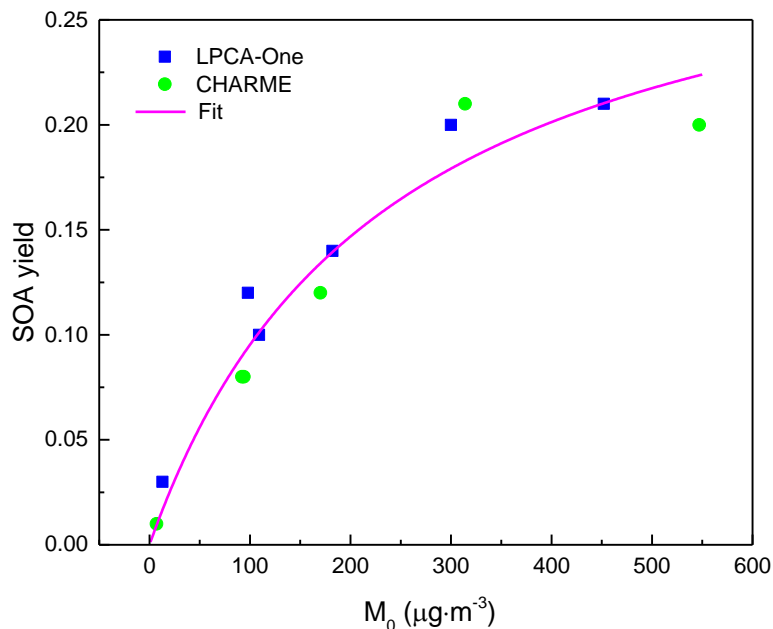


Figure IV-10 Yield curve (SOA yield Y vs. the organic aerosol mass formed M_0) for guaiacol/ NO_3 experiments in LPCA-One (blue squares) and in CHARME (green circles). The line represents the best fit to the data considering one semi-volatile major product. The fitting parameters used are $\alpha = 0.32 \pm 0.04$ and $K_{om} = (4.2 \pm 1.0) \times 10^{-3} \text{ m}^3 \mu\text{g}^{-1}$.

In their study on the reaction of guaiacol with OH performed under high NO_x conditions, Lauraguais et al. [8] reported a gas-particle partitioning equilibrium constant K_{om} of $(4.7 \pm 1.2) \times 10^{-3} \text{ m}^3 \mu\text{g}^{-1}$, which is very close to the value determined in the present study for the reaction of guaiacol with NO_3 . So, it can be assumed that the products formed in the particle phase from the gas-phase oxidation of guaiacol with both oxidants have probably similar chemical compositions, including nitrate compounds. In contrast, the mass-based stoichiometric coefficient determined for the semi-volatile products formed from the reaction of guaiacol with OH ($\alpha = 0.83$) is more than twice the value of α obtained for the reaction with NO_3 . This suggests that the reaction products from guaiacol + OH are less volatile in general compared to those from guaiacol + NO_3 . This lower volatility makes them prone to go readily into the condensed phase.

It is interesting to compare α (0.32) to the slope in Fig.IV-10 (0.25). α represents the total amount of the semi-volatile products formed both in the gas- and aerosol- phases,

whereas *Y* corresponds to the semi-volatile products that have been formed in the particle phase only. So, this suggests that about 80% of the low-volatile compounds formed in the guaiacol reaction with NO₃ radicals are transferred into the particle-phase.

3.2.2 SOA chemical composition

ESI-LC-QTOF-MS/MS analyses were performed to characterize the composition of the SOAs formed from the gas-phase reaction of NO₃ with guaiacol. A typical chromatogram is presented in Fig.IV-11. Once the molar mass of one product is determined (by LC-QTOF-MS), the corresponding peak is fragmented using three energy values (10 eV, 20 eV and 30 eV; MS/MS analysis). A higher energy value leads to a greater fragmentation of the molecules which allows to identify the functional groups and thus to assess the chemical structures of the compounds.

The compounds detected in the SOAs are listed in Tab.IV-4 (major compounds, relative abundance > 4 %) and Tab.S1 (minor compounds, relative abundance ≤ 2 %); the indicated masses correspond to the [M-H] product ions. The relative abundances (expressed in %) were calculated from the ratio of the sum of the chromatographic peak areas of the different isomers to the total chromatographic peak area of all the peaks. This approach assumes that the mass spectrometer has the same response for every detected chemical compound. The main compounds observed in the SOAs are nitrated aromatic compounds (see Tab.IV-4): nitromethoxybenzenes ($m/z = 152$, 2 isomers, 9.3%); nitrocatechol(s) ($m/z = 154$, 1 or 2 isomers (the peak width suggests the presence of two isomers, but this hypothesis could not be confirmed), 18.0%); nitroguaiacols ($m/z = 168$, 4 isomers, 11.7%); dinitromethoxybenzene ($m/z = 197$, 2 isomers, 7.6%); dinitrocatechols ($m/z = 199$, 3 isomers, 4.7%); dinitroguaiacols ($m/z = 213$, 6 isomers, 9.0%); dimeric compounds formed via the association of 1 nitroguaiacol and 1 nitrocatechol ($m/z = 321$, 12 isomers, 5.4%) or via the association of 2 nitroguaiacols ($m/z = 335$, 5 isomers, 18.1 %), and 2 unidentified compounds ($m/z = 531$, 8.2% and $m/z = 584$, 4.3%). So, this confirms that the oxidation products formed in the aerosols from the reaction of NO₃ radicals with guaiacol are both first and second generation products, as suggested by the data shown in Fig.IV-11. However, as more than ≈75% of the SOA mass is generated after complete depletion of guaiacol, it is highly probable that the

aerosol products are formed through reactions in the gas-phase and/or in the condensed phase (in the chamber or on the filter during the sampling). Additional experiments using lower initial guaiacol concentrations would probably reduce potential reactions occurring in the condensed phase. Figures S1-S8 (see Appendix I) display $[M-H]^+$ product ions MS/MS spectra obtained at 20 eV for the major compounds identified in the SOAs ($m/z = 152$, Fig.S1; $m/z = 154$, Fig.S2; $m/z = 168$, Fig.S3; $m/z = 197$, Fig.S4; $m/z = 199$, Fig.S5; $m/z = 213$, Fig.S6; $m/z = 321$, Fig.S7 and $m/z = 335$, Fig.S8). The different fragments allowed to propose consistent chemical structures for the oxidation products of $\text{NO}_3 + \text{guaiacol}$ found in the particle phase.

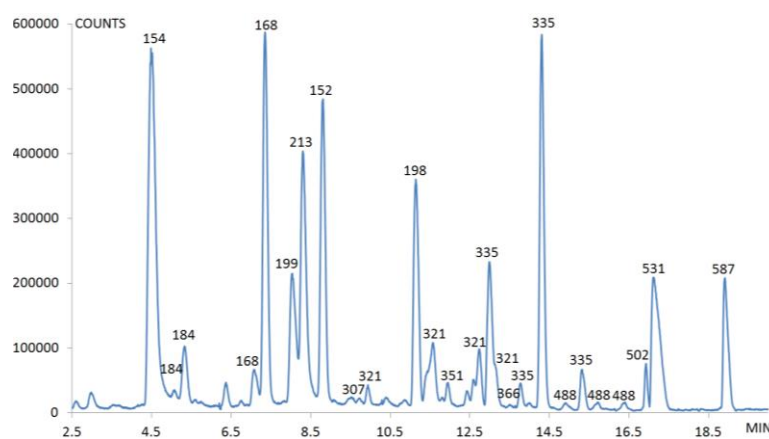
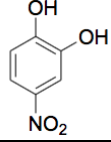
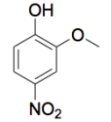
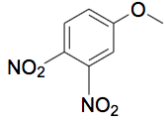
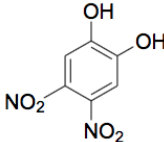
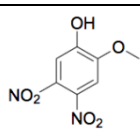
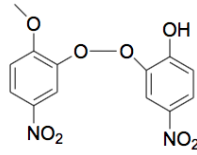
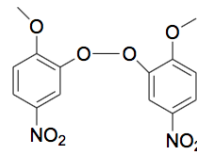


Figure IV-11 Chromatogram (ESI-LC-QToF-MS/MS analysis) of the SOAs formed from the gas-phase reaction of guaiacol with NO_3 radicals. The compounds corresponding to the labelled peaks are displayed in Tab.IV-4. The indicated masses correspond to the $[M-H]^+$ product ions.

Table IV-4 Major compounds observed in the SOAs (ESI-LC-QToF-MS/MS analyses) formed from the gas-phase reaction of guaiacol with NO_3 radicals. The main fragments obtained by MS/MS analyses (see Fig.S1-S8 in Appendix I) and the relative abundances (R, in %) are also indicated.

Molecular ion ^a	Main fragments	Brut Formula	Name ^e	Structure ^f	R (%) ^g
152	46 $[\text{NO}_2]^-$ 93 $[\text{C}_6\text{H}_5\text{O}]^-$ 122 $[\text{C}_7\text{H}_6\text{O}_2]^-$	$\text{C}_7\text{H}_6\text{NO}_3^d$	Nitromethoxybenzene ₂		9.3

154	69 [C ₃ HO ₂] ⁻ 95 [C ₅ H ₃ O ₂] ⁻ 123 [C ₆ H ₃ O ₃] ⁻	C ₆ H ₄ NO ₄ ^d	Nitrocatechol ¹⁻²		18.0
168	95 [C ₅ H ₃ O ₂] ⁻ 123 [C ₆ H ₃ O ₃] ⁻ 153 [C ₆ H ₃ NO ₄] ⁻	C ₇ H ₆ NO ₄ ^b	Nitroguaiacol ⁴		11.7
197	76 [C ₅ H ₂ N] ⁻ 109 [CH ₅ N ₂ O ₄] ⁻ 123 [C ₆ H ₅ NO ₂] ⁻	C ₇ H ₅ N ₂ O ₅ ^c	Dinitromethoxybenzene ²		7.6
199	67 [C ₄ H ₃ O] ⁻ 95 [C ₅ H ₃ O ₂] ⁻ 153 [C ₆ H ₃ NO ₄] ⁻	C ₆ H ₃ N ₂ O ₆ ^b	Dinitrocatechol ³		4.7
213	66 [C ₃ NO] ⁻ 78 [C ₅ H ₂ O] ⁻ 198 [C ₆ H ₂ N ₂ O ₆] ⁻	C ₇ H ₅ N ₂ O ₆ ^b	Dinitroguaiacol ⁶		9.0
321	153 [C ₆ H ₃ NO ₄] ⁻ 168 [C ₇ H ₆ NO ₄] ⁻ 306 [C ₁₂ H ₆ N ₂ O ₈] ⁻	C ₁₃ H ₉ N ₂ O ₈ ^b	Association of 1 nitroguaiacol and 1 nitrocatechol ¹²		5.4
335	153 [C ₆ H ₃ NO ₄] ⁻ 168 [C ₇ H ₆ NO ₄] ⁻ 320 [C ₁₆ H ₆ N ₃ O ₅] ⁻	C ₁₄ H ₁₁ N ₂ O ₈ ^b	Association of 2 nitroguaiacols ⁵		18.1
531	-	-	-	-	8.2
587	-	-	-	-	4.3

^a The indicated masses correspond to the [M-H] product ions.

^b Probability given by the software between 98 and 100 %.

^c Probability given by the software between 90 and 97 %.

^d Probability given by the software between 70 and 89%.

^e Number of detected isomers.

^f The drawn structure correspond to one isomer only.

^g The relative abundances (in %) were calculated from the ratio of the sum of the chromatographic areas of the different isomers to the total chromatographic area of all the peaks.

The minor compounds detected in the aerosols are shown in Tab.S1.

Among the major reaction products, 4-nitroguaiacol and 5-nitroguaiacol were clearly identified by comparing their chromatographic retention times and their MS-MS spectra to those of standards commercially available. The most abundant nitroguaiacol formed in the particle phase was 4-nitroguaiacol (91.5%), in large excess compared to 5-nitroguaiacol (5.4%) and 3-nitroguaiacol and/or 6-nitroguaiacol (3.1% for both; the standards of these two isomers do not exist, so it was not possible to distinguish them).

The mechanism leading to the main oxidation products identified in the SOAs is proposed in Fig.IV-12. It has been postulated by Atkinson et al., [40], that the NO_3 radical initiated reaction of aromatic compounds may first proceed by an ipso-addition to the OH substituent which forms a six-membered transition state intermediacy. A second mechanism starts with the electrophilic addition of the nitrate radical on the aromatic ring. These two ways lead to the formation of nitric acid and a phenoxy radical, which then react with NO_2 to produce nitroguaiacol isomers. Similarly, the formation of dinitroguaiacols and trinitroguaiacol can be explained by the reaction of nitroguaiacols with NO_3 and NO_2 .

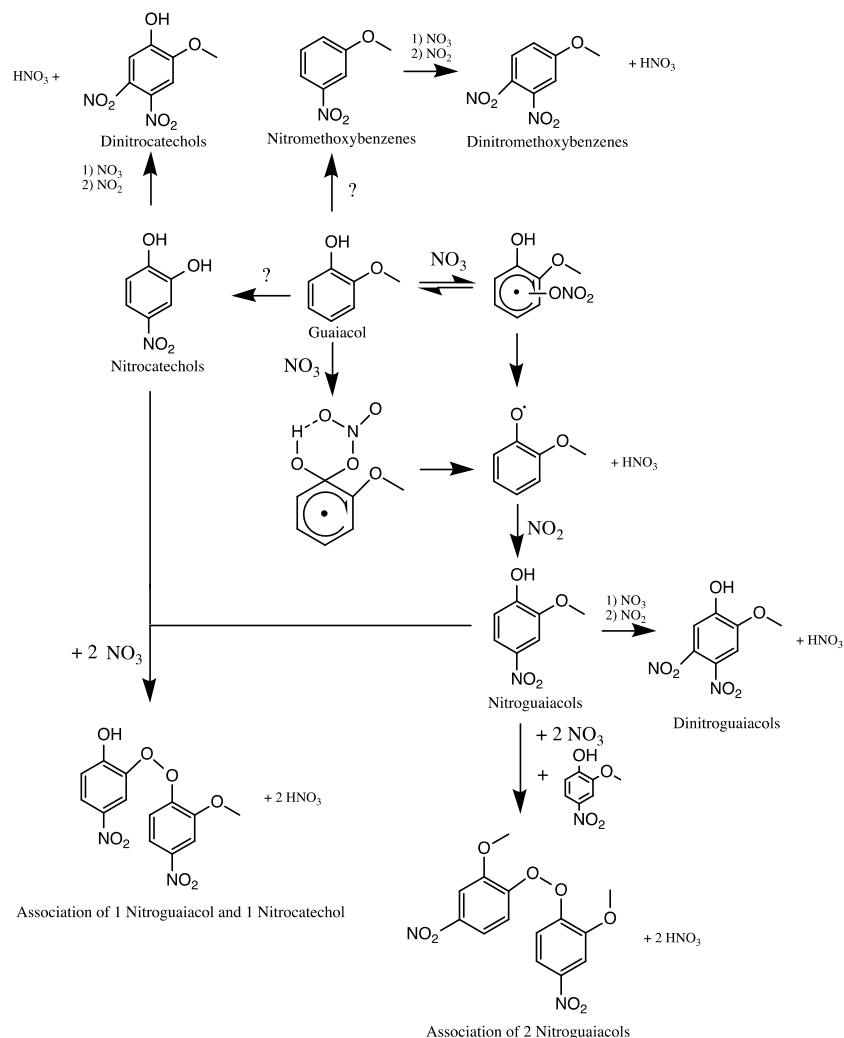


Figure IV-12 Detailed chemical mechanism leading to the main products observed in the SOAs formed from the gas-phase reaction of guaiacol with NO_3 radicals.

The initial oxidation steps starting from guaiacol and going to nitromethoxybenzenes and nitrocatechols are not known, as indicated in Fig.IV-12. Since the present gas-phase chemistry knowledge of aromatic compounds is not able to address these issues, we suggest that an oxidation chemistry could take place in the condensed phase and produce the observed nitromethoxybenzenes and nitrocatechols. Investigations of the liquid-phase guaiacol oxidation would be very useful to support this assumption. In their study on gas-phase reaction products of NO_3 + guaiacol, Yang et al. [13] also reported the presence of nitroguaiacols (4-nitroguaiacol and 6-nitroguaiacol; 4-nitroguaiacol being the most

abundant), dinitroguaiacol (4,6-dinitroguaiacol), catechol (1,2-dihydroxybenzene) and nitromethoxybenzene in the products formed from the gas-phase of NO_3 reaction guaiacol. They also identified catechols from the oxidation of creosol (4-methyl-guaiacol) and syringol (6-methoxy-guaiacol). The formation of catechols was reported by Zhang et al. (2016) as well, who studied the reaction of eugenol (4-allyl-guaiacol) and ethyl-guaiacol with NO_3 radicals. The mechanism leading to catechols from guaiacol and its derivatives was not explained in both previous articles.

The formation of nitrocatechols and dinitrocatechols can then result from the reaction of NO_3 and NO_2 with catechol and nitrocatechols, respectively. The compounds with high molecular masses ($m/z > 300$) display 2 to 3 aromatic cycles; they can be produced from the combination of phenoxy radicals formed from nitroguaiacol(s) and/or nitrocatechol(s).

For the main identified products, one isomer was always more abundant than the others (the corresponding relative abundances vary from 85 % to 99 %; see Tab.S2).

The oxidation products formed in the aerosols from the gas-phase reaction of guaiacol with nitrate radicals can also be compared to those identified for the reaction of guaiacol with hydroxyl radicals under high NO_x conditions [41]. The ATR-FTIR analyses performed by Ahmad et al. [41] also reveal the presence of 4-nitroguaiacol in the SOAs. So, this observation suggests that the oxidation products generated in the particulate phase, via the oxidation of guaiacol by NO_3 or OH/NO_x reaction, are probably similar as it has been previously postulated from the comparison of the gas-particle partitioning equilibrium constants ($K_{om,i}$) obtained with both oxidants.

4 Conclusion

The rate constant for the reaction of guaiacol with nitrate radicals has been studied in CHARME using relative rate method. The consistency of the data determined with three reference VOCs, o-cresol, m-cresol and p-cresol provided confidence in the rate constant presented in this work. The experiments carried out with guaiacol in excess (pseudo-first order method) showed that this method is only applicable for VOCs having moderate

NO₃ reactivity (k_{NO_3} lower than that $(3.77 \pm 0.39) \times 10^{-11} \text{ cm}^3 \text{ molecule}^{-1} \text{ s}^{-1}$), for the fast reaction consumes the reactant too fast to get the time profiles. Determining the rate constant of NO₃ + guaiacol by the pseudo-first order method is challenging, due to the fast reaction. Attention should be taken when applying this method for NO₃ + VOC rate constant determination.

The determined rate coefficient k_{guaiacol} allowed to calculate the atmospheric lifetime of guaiacol with respect to its reaction with NO₃ assuming a concentration of $[\text{NO}_3] = 5 \times 10^8 \text{ molecule cm}^{-3}$ ([18]). We can estimate the contribution of NO₃ reaction to the loss of guaiacol by applying the rate constant measured in this work.

$$\tau = \frac{1}{k_{\text{guaiacol}} [\text{NO}_3]} \quad (\text{Eq.25})$$

An atmospheric lifetime of about 53 s is obtained.

The formation of SOAs from the reaction of guaiacol with nitrate radicals has been studied in two simulation chambers. The SOAs yields have been shown to be influenced by the initial guaiacol concentration, which leads to aerosol yields ranging from 0.01 to 0.21. A very good agreement was observed between the experiments performed in both chambers which gives confidence in the data obtained in this study. The aerosols data have been fitted with the absorptive gas-particle partitioning model developed by Pankow [42, 43] and Odum et al. [44] using the one-product model.

Aerosol organic carbon concentration is typically $5 \mu\text{g m}^{-3}$ in many environments, though it can occasionally rise to $50 \mu\text{g m}^{-3}$ or more in highly polluted areas. Extrapolating to a particle loading of $5 \mu\text{g m}^{-3}$ from the yield data (Fig.IV-10) gives a 2% SOA yield. Based on this result, one can infer that the contribution of the reaction between guaiacol and NO₃ radicals to SOAs production under atmospheric conditions is probably relatively minor. However, in polluted areas this reaction can be an important source of secondary aerosols.

ESI-LC-QToF-MS/MS analyses were performed to characterize the chemical composition of the aerosols. Nitro-aromatics compounds were identified as the main

oxidation products, confirming previous studies [13, 14] on the products formed from the gas-phase reaction of NO_3 radicals with guaiacol derivatives.

A well-established tracer for primary biomass burning aerosols (BBA) is levoglucosan (1,6-anhydro- β -anhydroglucose), which originates from the pyrolysis of cellulose or hemicelluloses [45]. Several nitro-aromatic compounds were detected in urban aerosols, and nitrocatechols as well as nitroguaiacols are recognized to be suitable tracers for secondary BBA [46, 47]. Further research efforts on the reactivity of these compounds would allow to measure their rate constants with the main oxidants and to determine the corresponding lifetimes. To our knowledge, only a few data are available in the literature concerning the atmospheric reactivity of nitro-aromatics [48, 49].

References

- [1] M. A. Bari, G. Baumbach, B. Kuch, G. Scheffknecht. Temporal variation and impact of wood smoke pollution on a residential area in southern Germany. *Atmospheric Environment*, 2010, 44(31): 3823-3832. **10.1016/j.atmosenv.2010.06.031**
- [2] L. P. Naeher, M. Brauer, M. Lipsett, J. T. Zelikoff, C. D. Simpson, J. Q. Koenig, K. R. Smith. Woodsmoke health effects: a review. *Inhalation Toxicology*, 2007, 19(1): 67-106. **10.1080/08958370600985875**
- [3] A. K. Bolling, J. Pagels, K. E. Yttri, L. Barregard, G. Sallsten, P. E. Schwarze, C. Boman. Health effects of residential wood smoke particles: the importance of combustion conditions and physicochemical particle properties. *Part Fibre Toxicol*, 2009, 6(1): 29. **10.1186/1743-8977-6-29**
- [4] M. Ezzati, D. M. Kammen. The health impacts of exposure to indoor air pollution from solid fuels in developing countries: knowledge, gaps, and data needs. *Environmental Health Perspectives*, 2002, 110(11): 1057-1068. **10.1289/ehp.021101057**
- [5] C. G. Nolte, J. J. Schauer, G. R. Cass, B. R. Simoneit. Highly polar organic compounds present in wood smoke and in the ambient atmosphere. *Environmental Science & Technology*, 2001, 35(10): 1912-1919. **10.1021/es001420r**
- [6] C. Coeur-Tourneur, A. Cassez, J. C. Wenger. Rate coefficients for the gas-phase reaction of hydroxyl radicals with 2-methoxyphenol (guaiacol) and related compounds. *The Journal of Physical Chemistry A*, 2010, 114(43): 11645-11650. **10.1021/jp1071023**
- [7] A. Lauraguais, C. Coeur-Tourneur, A. Cassez, A. Seydi. Rate constant and secondary organic aerosol yields for the gas-phase reaction of hydroxyl radicals with syringol (2,6-dimethoxyphenol). *Atmospheric Environment*, 2012, 55: 43-48. **10.1016/j.atmosenv.2012.02.027**
- [8] A. Lauraguais, C. Coeur-Tourneur, A. Cassez, K. Deboudt, M. Fourmentin, M. Chođ. Atmospheric reactivity of hydroxyl radicals with guaiacol (2-methoxyphenol), a biomass burning emitted compound: Secondary organic aerosol formation and gas-phase oxidation products, *Atmospheric Environment*, 2014, 86: 155-163. **10.1016/j.atmosenv.2013.11.074**
- [9] A. Lauraguais, I. Bejan, I. Barnes, P. Wiesen, C. Coeur. Rate coefficients for the gas-phase reactions of hydroxyl radicals with a series of methoxylated aromatic compounds. *The Journal of Physical Chemistry A*, 2015, 119(24): 6179-6187. **10.1021/acs.jpca.5b03232**

- [10] A. Lauraguais, I. Bejan, I. Barnes, P. Wiesen, C. Coeur-Tourneur, A. Cassez. Rate coefficients for the gas-phase reaction of chlorine atoms with a series of methoxylated aromatic compounds. *The Journal of Physical Chemistry A*, 2014, 118(10): 1777-1784. **10.1021/jp4114877**
- [11] A. E. Zein, C. Coeur, E. Obeid, A. Lauraguais, T. Fagniez. Reaction kinetics of catechol (1,2-benzenediol) and guaiacol (2-methoxyphenol) with ozone. *Journal of Physical Chemistry A*, 2015, 119(26): 6759-6765. **10.1021/acs.jpca.5b00174**
- [12] A. Lauraguais, A. Zein, C. Coeur, E. Obeid, A. Cassez, M. T. Rayez, J. C. Rayez. Kinetic study of the gas-phase reactions of nitrate radicals with methoxyphenol compounds: experimental and theoretical approaches. *The Journal of Physical Chemistry A*, 2016, 120(17): 2691-2699. **10.1021/acs.jpca.6b02729**
- [13] B. Yang, H. Zhang, Y. Wang, P. Zhang, J. Shu, W. Sun, P. Ma. Experimental and theoretical studies on gas-phase reactions of NO_3 radicals with three methoxyphenols: Guaiacol, creosol, and syringol. *Atmospheric Environment*, 2016, 125: 243-251. **10.1016/j.atmosenv.2015.11.028**
- [14] H. Zhang, B. Yang, Y. Wang, J. Shu, P. Zhang, P. Ma, Z. Li. Gas-phase reactions of methoxyphenols with NO_3 radicals: kinetics, products, and mechanisms. *The Journal of Physical Chemistry*, 2016, 120(8): 1213-1221. **10.1021/acs.jpca.5b10406**
- [15] F. Karagulian, C. Santschi, M. J. Rossi. The heterogeneous chemical kinetics of N_2O_5 on CaCO_3 and other atmospheric mineral dust surrogates. *Atmospheric Chemistry and Physics Discussions*, 2005, 5(5): 10369-10408. **hal-00301869**
- [16] U. F. Platt, A. M. Winer, H. W. Biermann, R. Atkinson, J. N. Pitts. Measurement of nitrate radical concentrations in continental air. *Environmental Science & Technology*, 1984, 18(5): 365-369. **10.1021/es00123a015**
- [17] R. Atkinson. Kinetics and mechanisms of the gas - phase reactions of the NO_3 radical with organic compounds. *Journal of Physical and Chemical Reference Data*, 1991, 20(3): 459-507. **10.1063/1.555887**
- [18] Y. Shu, R. Atkinson. Atmospheric lifetimes and fates of a series of sesquiterpenes. *Journal of Geophysical Research*, 1995, 100(D4): 7275-7281. 10.1029/ 95jd00368
- [19] G. Schott, N. Davidson. Shock waves in chemical kinetics: the decomposition of N_2O_5 at high temperatures. *Journal of the American Chemical Society*, 1958, 80(8): 1841-1853. **10.1021/ja01541a019**
- [20] R. Atkinson, W. P. L. Carter, C. N. Plum, A. M. Winer, J. N. Pitts. Kinetics of the gas-phase reactions of NO_3 radicals with a series of aromatics at 296 ± 2 K. *International Journal of Chemical Kinetics*, 1984, 16(7): 887-898. **10.1002/kin.550160709**

- [21] FACSIMILE for Windows.MPCA Software. < <https://www.mcpa-software.com>>
- [22] R. Atkinson. Kinetics and mechanisms of the gas-phase reactions of the hydroxyl radical with organic compounds under atmospheric conditions. *Chemical Reviews*, 1986, 86(1): 69-201. **10.1021/cr00071a004**
- [23] R. J. Calvert, K. H. Becker, R. M. Kamens, T. J. Seinfeld, G. Yarwood. *The Mechanisms of Atmospheric Oxidation of Aromatic Hydrocarbons*. Oxford University Press, New York, 2002.
- [24] R. Thalman, K. J. Zarzana, M. A. Tolbert, R. Volkamer. Rayleigh scattering cross-section measurements of nitrogen, argon, oxygen and air. *Journal of Quantitative Spectroscopy and Radiative Transfer*, 2014, 147: 171-177. **10.1016/j.jqsrt.2014.05.030**
- [25] J. P. Burrows, A. Dehn, B. Deters, S. Himmelmann, A. Richter, S. Voigt, J. Orphal. Atmospheric remote-sensing reference data from gome: part 1. temperature-dependent absorption cross-sections of NO₂ in the 231-794 nm range. *Journal of Quantitative Spectroscopy and Radiative Transfer*, 1998, 60(6): 1025-1031. **10.1016/s0022-4073(97)00197-0**
- [26] D. S. Venables, T. Gherman, J. Orphal, J. C. Wenger, A. A. Ruth. High sensitivity *in situ* monitoring of NO₃ in an atmospheric simulation chamber using incoherent broadband cavity-enhanced absorption spectroscopy. *Environmental Science & Technology*, 2006, 40(21): 6758-6763. **10.1021/es061076j**
- [27] R. Atkinson, D. L. Baulch, R. A. Cox, J. N. Crowley, R. F. Hampson, R. G. Hynes, M. E. Jenkin, M. J. Rossi, J. Troe. Evaluated kinetic and photochemical data for atmospheric chemistry: Volume I - gas phase reactions of O_x, HO_x, NO_x and SO_x species. *Atmospheric Chemistry and Physics*, 2004, 4(6): 1461-1738. **10.5194/acp-4-1461-2004**
- [28] E. J. Dunlea, S. C. Herndon, D. D. Nelson, R. M. Volkamer, F. San Martini, P. M. Sheehy, M. S. Zahniser, J. H. Shorter, J. C. Wormhoudt, B. K. Lamb, E. J. Allwine, J. S. Gaffney, N. A. Marley, M. Grutter, C. Marquez, S. Blanco, B. Cardenas, A. Retama, C. R. Ramos Villegas, C. E. Kolb, L. T. Molina, M. J. Molina. Evaluation of nitrogen dioxide chemiluminescence monitors in a polluted urban environment. *Atmospheric Chemistry and Physics Discussions*, 2007, 7 (1):569-604. **10.5194/acp-7-2691-2007**
- [29] T. Brauers, B. J. Finlayson-Pitts. Analysis of relative rate measurements. *International Journal of Chemical Kinetics*, 1997, 29(9): 665-672. **10.1002/(sici)1097-4601(1997)29:9<665::Aid-kin3>3.0.Co;2-s**

- [30] A. Lauraguais (2014) Contribution from burning wood to air quality and study of atmospheric reactivity of simulation chamber methoxyphenols. (Université du Littoral Côte d'Opale). **tel-01259183**
- [31] M. Hallquist, J. C. Wenger, U. Baltensperger, Y. Rudich, D. Simpson, M. Claeys, J. Dommen, N. M. Donahue, C. George, A. H. Goldstein, J. F. Hamilton, H. Herrmann, T. Hoffmann, Y. Iinuma, M. Jang, M. E. Jenkin, J. L. Jimenez, A. Kiendler-Scharr, W. Maenhaut, G. McFiggans, T. F. Mentel, A. Monod, A. Prévôt, J. H. Seinfeld, J. D. Surratt, R. Szmigielski, J. Wildt. The formation, properties and impact of secondary organic aerosol: current and emerging issues. *Atmospheric Chemistry and Physics*, 2009, 9(14): 5155-5236. **10.5194/acp-9-5155-2009**
- [32] C. Coeur-Tourneur, A. Tomas, A. Guilleateau, F. Henry, F. Ledoux, N. Visez, V. Riffault, J. C. Wenger, Y. Bedjanian. Aerosol formation yields from the reaction of catechol with ozone. *Atmospheric Environment*, 2009, 43(14): 2360-2365. **10.1016/j.atmosenv.2008.12.054**
- [33] C. Coeur-Tourneur, V. Foulon, M. Laréal. Determination of aerosol yields from 3-methylcatechol and 4-methylcatechol ozonolysis in a simulation chamber. *Atmospheric Environment*, 2010, 44(6): 852-857. **10.1016/j.atmosenv.2009.11.027**
- [34] F. Henry, C. Coeur-Tourneur, F. Ledoux, A. Tomas, D. Menu. Secondary organic aerosol formation from the gas-phase reaction of hydroxyl radicals with m-, o- and p-cresol. *Atmospheric Environment*, 2008, 42: 3035-3045. **10.1016/j.atmosenv.2007.12.043**
- [35] M. D. Hurley, O. Sokolov, T. J. Wallington, H. Takekawa, M. Karasawa, B. Klotz, I. Barnes, K. H. Becker. Organic aerosol formation during the atmospheric degradation of toluene. *Environmental Science & Technology*, 2001, 35(7): 1358-1366. **10.1021/es0013733**
- [36] H. Takekawa, H. Minoura, S. Yamazaki. Temperature dependence of secondary organic aerosol formation by photo-oxidation of hydrocarbons. *Atmospheric Environment*, 2003, 37(24): 3413-3424. **10.1016/s1352-2310(03)00359-5**
- [37] J. R. Odum, T. Jungkamp, R. J. Griffin, H. Forstner, R. C. Flagan, J. H. Seinfeld. Aromatics, reformulated gasoline, and atmospheric organic aerosol formation. *Environmental Science & Technology*, 1997, 31(7): 1890-1897. **10.1021/es960535I**
- [38] C. Song, K. Na, D. R. Cocker. Impact of the hydrocarbon to NO_x ratio on secondary organic aerosol formation. *Environmental Science & Technology*, 2005, 39(9): 3143-3149. **10.1021/es0493244**
- [39] R. I. Olariu, A. Tomas, I. Barnes, K. Wirtz. Atmospheric ozone degradation reaction of 1,2-dihydroxybenzene: Aerosol formation study. The European Photoreactor EUPHORE, 2003, 47-63.

- [40] R. Atkinson, S. M. Aschmann, J. Arey. Reactions of hydroxyl and nitrogen trioxide radicals with phenol, cresols, and 2-nitrophenol at 296 ± 2 K. *Environmental Science & Technology*, 1992, 26(7): 1397-1403. **10.1021/es00031a018**
- [41] W. Ahmad, C. Coeur, A. Tomas, T. Fagniez, J. B. Brubach, A. Cuisset. Infrared spectroscopy of secondary organic aerosol precursors and investigation of the hygroscopicity of SOA formed from the OH reaction with guaiacol and syringol. *Applied Optics*, 2017, 56(11): E116-E122. **10.1364/AO.56.00E116**
- [42] J. F. Pankow. An absorption model of gas/particle partitioning of organic compounds in the atmosphere. *Atmospheric Environment*, 1994, 28(2): 185-188. **10.1016/1352-2310(94)90093-0**
- [43] J. F. Pankow. An absorption model of the gas/aerosol partitioning involved in the formation of secondary organic aerosol. *Atmospheric Environment*, 1994, 28(2): 189-193. **10.1016/1352-2310(94)90094-9**
- [44] J. R. Odum, T. Hoffmann, F. Bowman, D. Collins, R. C. Flagan, J. H. Seinfeld. Gas/particle partitioning and secondary organic aerosol yields. *Environmental Science & Technology*, 1996, 30(8): 2580-2585. **10.1021/es950943+**
- [45] B. Simoneit. Biomass burning- a review of organic tracers for smoke from incomplete combustion. *Applied Geochemistry*, 2002, 17(3): 129-162. **10.1016/S0883-2927(01)00061-0**
- [46] Y. Iinuma, O. Boge, R. Grafe, H. Herrmann. Methyl-nitrocatechols: atmospheric tracer compounds for biomass burning secondary organic aerosols. *Environmental Science & Technology*, 2010, 44(22): 8453-8459. **10.1021/es102938a**
- [47] Z. Kitanovski, I. Grgic, F. Yasmeen, M. Claeys, A. Cusak. Development of a liquid chromatographic method based on ultraviolet-visible and electrospray ionization mass spectrometric detection for the identification of nitrocatechols and related tracers in biomass burning atmospheric organic aerosol. *Rapid communications in mass spectrometry: RCM*, 2012, 26(7): 793-804. **10.1002/rcm.6170**
- [48] I. Bejan, I. Barnes, R. Olariu, S. Zhou, P. Wiesen, T. Benter. Investigations on the gas-phase photolysis and OH radical kinetics of methyl-2-nitrophenols. *Physical chemistry chemical physics: PCCP*, 2007, 9(42): 5686-5692. **10.1039/b709464g**
- [49] I. Bejan, M. Duncianu, R. Olariu, I. Barnes, P. W. Seakins, P. Wiesen. Kinetic study of the gas-phase reactions of chlorine atoms with 2-chlorophenol, 2-nitrophenol, and four methyl-2-nitrophenol isomers. *The Journal of Physical Chemistry A*, 2015, 119(20): 4735-4745. **10.1021/acs.jpca.5b02392**

Conclusions and perspectives

The aim of this thesis was to develop IBBCEAS instruments dedicated to the measurement of aerosol extinction and NO_3 radicals, for field and laboratory applications.

Aerosol extinction is an important optical property. In traditional LIDAR measurement of aerosol extinction, a blind area exists in the near field due to the inherent geometric structure of the LIDAR technique, resulting in the loss of remote sensing information in this area. In the present work, a portable LED-based IBBCEAS operating around 370 nm wavelength was developed in an effort to tackle the issue of missing data in LIDAR's blind zone. Combined *in situ* measurements of aerosol extinction coefficients using LIDAR and IBBCEAS were performed at the same location near ground surface. A good correlation ($R^2 = 0.90$) between the data arising from these two different measurement techniques was obtained, demonstrating the potential of the use of an IBBCEAS located close to the LIDAR measurement site, to record data in its LIDAR blind zone, particularly near the ground surface. This work has been published in *Optics Letters*, 2020, 45(7): 1611-1614.

The nitrate radical NO_3 is a crucial species for atmospheric chemistry, as during the night it reacts with a number of VOCs, mainly unsaturated ones. The short NO_3 life time (from a few seconds [1] to dozens of minutes [2]) as well as its low concentrations (from a few pptv to a few hundred pptv) make atmospheric NO_3 measurement challenging. Kinetics and mechanistic studies on NO_3 -initiated oxidation of VOCs are also much less abundant in the literature compared to OH radical chemistry, thus limiting the understanding of NO_3 impact in atmospheric chemistry. In the present work, an IBBCEAS setup was developed and installed on the simulation chamber CHARME, aiming at investigating NO_3 chemistry with biogenic VOCs. Chamber studies were performed to validate the IBBCEAS instrument by following nitrate radical concentrations during its production by reaction of NO_2 with O_3 in the simulation

chamber. Furthermore, the reaction of guaiacol (2-methoxyphenol, a VOC emitted by biomass burning) with nitrate radicals was investigated in both LPCA simulation chambers (CHARME and LPCA-ONE). The SOAs yield and products of $\text{NO}_3 + \text{guaiacol}$ have been studied.

The rate coefficient determined using the relative rate method $((3.77 \pm 0.39) \times 10^{-11} \text{ cm}^3 \text{ molecule}^{-1} \text{ s}^{-1})$ leads to an atmospheric lifetime of about 53 s with respect to the oxidation of NO_3 with guaiacol. The formation of secondary organic aerosols from the reaction of guaiacol with nitrate radicals was also observed. The SOAs yields were shown to be influenced by the initial guaiacol concentration, leading to aerosol yields ranging from 0.01 to 0.21. A very good agreement was observed between the experiments performed in both chambers which gives confidence in the data obtained in this study. The aerosol data were fitted with the absorptive gas-particle partitioning model developed by Pankow [1, 2] and Odum et al. [3] using the one-product model. Aerosol organic carbon concentration is typically $5 \mu\text{g m}^{-3}$ in many environments, though it can occasionally rise to $50 \mu\text{g m}^{-3}$ or more in highly polluted areas. Extrapolating to a particle loading of $5 \mu\text{g m}^{-3}$ from the yield data gives a 2% SOA yield. Based on this result, one can infer that the contribution of the reaction between guaiacol and NO_3 radicals to SOAs production under atmospheric conditions is probably relatively minor. However, in polluted areas this reaction can be an important source of secondary aerosols. This work has been published in *Atmospheric Environment*, (2020) DOI: 10.1016/j.atmosenv.2020.117740.

The development of these two IBBCEAS setups offer large perspectives of future research studies. The portable instrument designed for aerosol extinction measurements will be extended to other species, like HONO and NO_2 measurement. Besides, NO_2 measurement by the traditional chemiluminescence method is known to be subjected to interferences from other N-containing species. The present IBBCEAS instrument will enable accurate atmospheric measurements to be performed.

Due to the high reactivity of NO_3 toward guaiacol, the absolute determination of the rate constant is challenging. The IBBCEAS instrument installed on CHARME has been applied for investigation of absolute determination of the rate constants of guaiacol with

NO₃ radicals. The fast reaction rate made it not applicable to track the NO₃ concentration time profiles for the reactive compound like guaiacol. Attention should be taken when applying the absolute rate method for NO₃ + VOCs rate constant determination, and less reactive VOCs should be taken into consideration.

By the way, kinetic databases will be completed, structure-activity relationships could be developed and explicit atmospheric chemistry models like GECKO-A could be improved. Product and SOA formation studies will also be carried out on BVOCs coming from combustion sources, for which literature data are scarce.

References

- [1] A. Geyer, B. Alicke, R. Ackermann, M. Martinez, H. Harder, W. Brune, P. di Carlo, E. Williams, T. Jobson, S. Hall, R. Shetter, J. Stutz. Direct observations of daytime NO_3 : implications for urban boundary layer chemistry. *Journal of Geophysical Research*, 2003, 108(D12), 4368. **10.1029/2002JD002967**
- [2] S. S. Brown, H. Stark, A. R. Ravishankara. Applicability of the steady state approximation to the interpretation of atmospheric observations of NO_3 and N_2O_5 . *Journal of Geophysical Research*, 2003, 108(D17), 4539. **10.1029/2003JD003407**
- [3] J. F. Pankow. An absorption model of gas/particle partitioning of organic compounds in the atmosphere. *Atmospheric Environment*, 1994, 28(2): 185-188. **10.1016/1352-2310(94)90093-0**
- [4] J. F. Pankow. An absorption model of the gas/aerosol partitioning involved in the formation of secondary organic aerosol. *Atmospheric Environment*, 1994, 28(2): 189-193. **10.1016/1352-2310(94)90094-9**
- [5] J. R. Odum, T. Hoffmann, F. Bowman, D. Collins, R. C. Flagan, J. H. Seinfeld. Gas/particle partitioning and secondary organic aerosol yields. *Environmental Science & Technology*, 1996, 30(8): 2580-2585. **10.1021/es950943+**

R é s u m é

Les radicaux NO_3 jouent un rôle important dans la chimie de la troposphère nocturne, à la fois en tant qu'agent oxydant pour un grand nombre d'espèces organiques et en tant que voie d'élimination des NO_x . Bien qu'il ait une concentration atmosphérique assez faible (de quelques pptv à quelques centaines de pptv), le radical nitrate contrôle l'oxydation de nombreux gaz traces, en particulier les terpènes et les alcènes. De plus, le NO_3 peut également contribuer à la formation et à la croissance d'aérosols organiques secondaires (AOS).

Les études sur réactivité des radicaux nitrate avec les composés organiques volatils (COV) ne sont pas très répandues, et de nombreuses incertitudes subsistent sur les constantes cinétiques, les mécanismes réactionnels et la formation des AOS. Les études se limitent souvent à la détermination des nitrates organiques totaux et des rendements en AOS sans aucune détection ou quantification des espèces individuelles. Ainsi, la chimie des NO_3 reste beaucoup moins connue que celle des OH.

Les aérosols atmosphériques jouent un rôle central dans les processus liés au changement climatique et à la qualité de l'air et ils affectent la santé humaine. Les études sur les aérosols atmosphériques suscitent un intérêt croissant en raison de leur impact sur le climat, de leurs réactions chimiques hétérogènes dans l'atmosphère, qui affectent particulièrement la qualité de l'air dans l'environnement, et des problèmes de visibilité et de santé associés.

Une bonne compréhension de la physico-chimie atmosphérique est nécessaire pour réaliser des expériences en laboratoire, des campagnes sur le terrain et des modélisations.

Bien qu'il s'agisse de bases de données de cinétique chimique assez complètes pour les réactions en phase gazeuse et hétérogènes, comme l'évaluation des données cinétiques des gaz d'IUPAC (<http://iupac.pole-ether.fr/>) et JPL (<https://jpldataeval.jpl.nasa.gov/download.html>), il existe encore de nombreuses lacunes pour la chimie atmosphérique réaliste et complexe. Les études en laboratoire fournissent une bonne approche pour

isoler et se concentrer sur une réaction chimique individuelle entre des composants simples dans des conditions atmosphériques pertinentes. Et il fournit également une méthode efficace pour mener des études cinétiques et mécaniques. De telles études fournissent un moyen très utile d'examiner initialement la relation émissions-qualité de l'air dans des conditions contrôlées.

Dans l'atmosphère, les concentrations en gaz traces dépendent des taux de production et de perte de produits chimiques, ainsi que du transport physique. Les mesures sur le terrain de la composition atmosphérique fournissent des données et des informations essentielles sur le mécanisme de la source, qui peuvent être utilisées pour tester le complément et la précision des mécanismes chimiques impliqués dans les modèles atmosphériques et aider à améliorer le modèle.

Comme présenté ci-dessus, ce travail se concentrera sur le radical NO_3 et les aérosols. L'instrument de spectroscopie d'absorption en cavité résonante par une source incohérente large bande (en anglais, incoherent broadband cavity-enhanced absorption spectroscopy, IBBCEAS) peut être utilisé pour la mesure multi-espèces. Compte tenu de la sensibilité du coût, du fonctionnement, il peut être utilisé pour plusieurs espèces, qui se concentreront sur le NO_3 et les aérosols dans ce travail. Pour mieux comprendre les sources, la distribution et les puits de NO_3 et d'aérosols, les concentrations atmosphériques sont importantes pour entreprendre une étude plus approfondie.

Une compréhension et une explication de l'impact des aérosols sur la transmission de la lumière dans l'atmosphère nécessitent une connaissance des propriétés optiques des aérosols. Comme présenté ci-dessus, de nombreuses techniques sont consacrées à la détection des paramètres des aérosols. La technique LIDAR est une méthode largement utilisée pour la mesure sur le terrain de l'extinction des aérosols. Cependant, en raison de sa structure géométrique, des informations sont manquantes dans sa zone aveugle c'est à dire entre le sol et les premières centaines de mètres d'altitude. L'un des principaux objectifs de ce projet consiste à développer un instrument IBBCEAS portable pour les mesures sur le terrain des propriétés optiques des aérosols et à tester son accord avec les résultats de mesure LIDAR, afin de fournir une solution potentielle pour les informations manquantes d'extinction des aérosols dans la zone aveugle du LIDAR.

Un autre objectif de la thèse est de construire un système IBBCEAS pour les études en laboratoire des réactions $\text{NO}_3 + \text{COV}$, qui pourrait être utilisé pour mesurer les profils temporels de NO_3 .

i. Instrument IBBCEAS portable pour la mesure sur le terrain de l'extinction des aérosols

Pour compenser le manque d'informations LIDAR dans la zone aveugle, la technique IBBCEAS a été introduite pour effectuer des mesures complémentaires (dans cette partie, se référer au Chapitre III pour les figures, tableaux et formules).

En raison d'un chevauchement géométrique incomplet entre le faisceau d'émission laser et le champ de vision (FOV) du télescope récepteur dans la plage proche (Fig.III-1), la récupération des propriétés optiques des aérosols avec le LIDAR est limitée dans les premières centaines de mètres de l'atmosphère. Le facteur de recouvrement η est un paramètre caractéristique décrivant la relation de recouvrement différente entre le FOV du télescope et le faisceau laser. Lorsque le faisceau laser est hors du champ de vision du télescope, le facteur de chevauchement η est égal à 0, où est appelée zone aveugle; lorsque le faisceau est partiellement à l'intérieur du FOV du télescope, le facteur de recouvrement est compris entre 0 et 1; lorsque le faisceau laser est complètement contenu dans le FOV, $\eta = 1$.

Une nouvelle méthode optique alternative est proposée dans le présent travail de doctorat pour mesurer directement l'extinction des aérosols près de la surface du sol, au lieu de la diffusion des aérosols. Un instrument développé au LPCA basé sur la technique IBBCEAS couplé à une diode électroluminescente UV (LED) à large bande a été développé pour mesurer l'extinction des aérosols sur une bande spectrale relativement large (355-380 nm) avec une résolution spatiale élevée. Les données d'extinction des aérosols mesurées par IBBCEAS ont été comparées à celles obtenues avec le LIDAR au même endroit près de la surface du sol.

i.1 Mesure par IBBCEAS

i.1.1 Calibrage de l'instrument IBBCEAS

La Figure III-5 (a) montre les spectres de N₂ pur et de NO₂ (361 ppbv) pour I₀ (λ) et I (λ), respectivement, ainsi que le coefficient de diffusion de Rayleigh théorique. La Figure III-5 (b) affiche les sections efficaces d'absorption de référence de NO₂ autour de 365 nm rapportées par Burrows et al. (1998), ainsi que la réflectivité du miroir déterminée expérimentalement. La Figure III-5 (c) présente le spectre d'absorption de NO₂ (361 ppbv) utilisé pour déterminer la réflectivité du miroir sur la Figure III-5 (b).

Dans la gamme de longueur d'onde de travail (364 - 377 nm), la réflectivité maximale du miroir est de ~ 99,84% (incertitude ~ 5%) à 374,5 nm, conduisant à une longueur de trajet optique effective de ~ 860 m.

i.1.2 Caractéristiques et performances

La stabilité de l'instrument développé a été caractérisée au moyen de l'analyse de la variance Allan. Le temps d'intégration optimal peut être obtenu en utilisant les spectres IBBCEAS de séries chronologiques de N₂ grâce à l'analyse de la variance Allan. La cavité a été balayée avec de l'azote pur et l'intensité de sortie de la cavité a été enregistrée sur 200 spectres consécutifs de 2,4 s (c'est-à-dire 4 spectres moyennés avec un temps d'intégration de 600 ms). Des résultats typiques de l'analyse de la variance d'Allan (exprimés en écart d'Allan) sont présentés sur la Figure III-6. Le temps de stabilisation maximal de l'instrument est de 69,6 s pour un temps d'intégration de 600 ms avec un nombre moyen de 116, ce qui donne une précision de mesure (1σ) de 1,5 ppbv pour le NO₂. Compte tenu du calcul et de la comparaison avec les réponses temporelles des instruments associés, le temps moyen utilisé était de 60 s (conduisant à un nombre moyen de 100).

La précision de mesure de l'instrument IBBCEAS a été évaluée avec N₂ dans la cavité. La résolution temporelle pour l'IBBCEAS était de 1 min (temps d'intégration de 600 ms, en moyenne 100 fois). Une série chronologique de 200 données a été enregistrée. La valeur moyenne de la concentration de NO₂ pour les données était de 0,22 ppbv, ce qui indique la précision instrumentale. La Figure III-7 montre l'histogramme de distribution des concentrations estimées de NO₂ par l'instrument IBBCEAS. Celui-ci a

été ajusté avec un modèle gaussien, ce qui donne une précision de mesure de 2,19 ppbv à partir du FWHM du profil gaussien d'ajustement.

i.1.3 Mesure simultanée de l'extinction des aérosols et de la concentration de NO₂ dans l'air ambiant

Dans le travail actuel, la ligne de base spectrale $P_0(\lambda)$ a été régulièrement mesurée à travers le protocole d'opération suivant (Fig.III-8 (c)): mesure de 6 minutes avec N₂ pur (pour la ligne de base $P_0(\lambda)$) suivi d'une mesure pendant 24 minutes avec échantillon d'air (fournissant des informations sur l'absorption de gaz $\alpha_{\text{abs,gaz}}$, l'extinction des aérosols $\alpha_{\text{ext, aérosols}}$ et la ligne de base $P_0(\lambda)$). La commutation a été contrôlée avec une valve électronique (Fig.III-8 (a) et Fig.III-8 (b)). Le N₂ ou l'air ambiant ont été échantillonnés en continu, à un débit de 2 L/min, vers la cavité IBBCEAS fonctionnant à pression atmosphérique. Un cycle montrant le processus pour parvenir à l'extinction de l'aérosol $\alpha_{\text{ext, aérosols}}$ est donné sur la Figure III-8 (d).

Sur la base de l'écart type du résidu d'ajustement (Figure III-9), un coefficient d'extinction minimum détectable de $4,3 \times 10^{-9} \text{ cm}^{-1}$ correspondant à une concentration détectable minimum de NO₂ de 1,5 ppbv a été déduit.

i.1.4 Site d'échantillonnage

Une campagne d'inter-comparaison a été organisée dans la matinée du 14 septembre 2018 dans une zone côtière urbaine et industrialisée à Dunkerque (Nord de la France). Des mesures combinées de l'extinction des aérosols réalisées (comme illustrées sur la Figure III-10) près de la surface du sol ont été effectuées à l'aide de la télédétection LIDAR et de la surveillance in situ IBBCEAS. Le système LIDAR était situé dans l'UMA (Unité Mobile Atmosphérique) située au niveau du sol à environ 0,4 km du bâtiment où un système UV LED-IBBCEAS a été installé (dans un abri climatisé) sur le toit à ~ 14 m de hauteur. Les paramètres météorologiques ont été enregistrés pendant la période de mesure comme indiqué sur la Figure III-11. La mesure de l'extinction des aérosols a été réalisée à 400 m du LIDAR (en dehors de sa zone aveugle) avec un angle zénithal d'environ 84 °.

i.1.5 Interférences potentielles

Outre l'absorption du NO_2 et des aérosols dans l'échantillon d'air, il existe d'autres espèces gazeuses présentant des caractéristiques d'absorption structurées dans la gamme de longueurs d'onde pertinente (364-378 nm), telles que HONO, CH_2O , O_3 , BrO, IO, OCIO et glyoxal. En raison de leur faible concentration et/ou de leur faible section efficace d'absorption leurs extinctions sont indétectables par l'instrument IBBCEAS.

i.2 Comparaison des résultats de l'IBBCEAS et du LIDAR

Les coefficients d'extinction des aérosols dérivés du LIDAR et ceux mesurés simultanément par la LED UV-IBBCEAS (Fig.III-9) sont représentés sur la Fig.III-12 (a). Les mesures ont été effectuées dans la matinée du 14 septembre 2018 de 9h30 à 11h30.

Un bon accord (coefficient de corrélation $R^2 = 0,90$ (Fig.III-12 (b)) est obtenu entre les extinctions d'aérosols mesurées à l'aide des deux techniques.

Quelques écarts ont cependant été observés entre 09h40 et 10h00. Les fluctuations les plus fortes mesurées avec LIDAR s'expliquent par le fait que ses mesures ont été effectuées sur un trajet ouvert de 400 m qui pourrait être significativement influencé par les conditions météorologiques ambiantes (HR, direction du vent, vitesse du vent, etc.), tandis que le UV LED-IBBCEAS a échantillonné l'air local dans sa cavité optique, ce qui a conduit à des conditions de mesure plus stables.

i.3 Conclusion

En conclusion, la technique LED-IBBCEAS fonctionnant autour de 370 nm a été utilisée pour la première fois pour résoudre le problème des données manquantes dans la zone aveugle du LIDAR (les premières centaines de mètres de l'atmosphère). Des mesures combinées des coefficients d'extinction des aérosols ont été effectuées à l'aide de la télédétection LIDAR et de l'IBBCEAS. Une bonne corrélation ($R^2 = 0,90$) entre les données obtenues avec ces deux techniques a été obtenue. Ce travail démontre le potentiel de l'utilisation des données d'extinction des aérosols mesurées par IBBCEAS, pour compenser celles manquantes dans la zone aveugle du LIDAR.

ii. Etudes en laboratoire des réactions des COV avec les radicaux nitrate

Nous présentons ici les résultats d'études en laboratoire utilisant un instrument IBBCEAS couplé à la chambre de simulation atmosphérique CHARME (CHamber for the Atmospheric Reactivity and the Metrology of the Environment) pour la mesure du radical NO_3 .

Dans la première partie, la cinétique du NO_3 avec le gaiacol (2-méthoxyphénol, 2MP) a été étudiée en utilisant la méthode du pseudo-premier ordre avec un excès de 2-MP et en suivant les profils de concentrations de NO_3 . Dans une seconde partie, le mécanisme chimique de la réaction du gaiacol avec le NO_3 a été étudié (se référer au Chapitre IV pour les figures, tableaux et formules).

ii.1 Cinétique de la réaction du radical NO_3 avec le gaiacol

Les constantes de vitesse pour les réactions du radical NO_3 avec le gaiacol peuvent être mesurées en utilisant deux méthodes: la méthode du pseudo-premier ordre et la méthode relative.

Dans la méthode du pseudo-premier ordre, les concentrations en NO_3 sont suivies par un dispositif IBBCEAS monté sur la chambre de simulation atmosphérique CHARME. Pour ces expériences, les concentrations en gaiacol sont en excès par rapport à celles en radicaux nitrate (environ d'un facteur 10).

La méthode relative est basée sur la mesure de la perte d'un réactif par rapport à celle d'un composé de référence. Idéalement, le rapport des constantes de vitesse entre la référence et le réactif devrait être compris entre 0,2 à 5. Le NO_3 a été produit par deux méthodes : insitu par la réaction entre O_3 et NO_2 et via la décomposition du N_2O_5 .

Pour la méthode relative, trois composés de référence ont été utilisés : l'o-crésol, le m-crésol et le p-crésol.

ii.1.1 Spécifications d'IBBCEAS

La Fig.IV-2 (a) montre les profils de NO_2 , NO_3 et le coefficient de diffusion de Rayleigh utilisés dans ce travail pour l'étalonnage de la réflectivité du miroir et la détermination des concentrations en radical nitrate. Les Fig.IV-2 (b) et (d) montrent la réflectivité du miroir déterminée autour de 660 nm dans la chambre de simulation CHARME ainsi que

le spectre d'émission des LED, respectivement. Sur la Fig. IV-2 (c) montre les caractéristiques d'absorption de NO₂ (1295 ppbv) déterminées dans le calcul de la réflectivité du miroir de la Fig. IV-2 (b).

La réflectivité maximale du miroir est de 99,95% à ~ 650 nm, ce qui a conduit à une longueur d'absorption optique effective de 9,14 km. Le panneau supérieur montre les spectres NO₂ et NO₃ dans la même région à des fins de comparaison. Chaque spectre a été enregistré avec un temps d'acquisition total de 15 s (temps intégré de 600 ms × 25).

Les limites de détection pour NO₂ et NO₃ de l'instrument IBBCEAS couplé à CHARME ont été évaluées en utilisant l'Eq.19. Sur la base des écarts-types du résidu d'ajustement (Figure IV-3), et des rapports signal sur bruit (23,2 pour NO₂ et 81,5 pour NO₃), celles-ci sont de 19,2 ppbv pour NO₂ et 24,5 pptv pour NO₃, pour un temps d'intégration de 15 s.

Les concentrations des différentes espèces gazeuses ont été simulées à l'aide du logiciel FACSIMILE et les données obtenues ont été comparées à celles mesurées expérimentalement.

Avant l'ajout d'ozone, les profils temporels de concentration de NO₂ simulés sont en bon accord avec ceux mesurés par l'IBBCEAS ($y = 1,077x - 180,0$ avec $R^2 = 0,90$; Figure IV-5). En revanche, après l'ajout de O₃, celles obtenues par chimiluminescence présentent en désaccord. Ce résultat était attendu car il est connu que d'autres espèces azotées (par exemple NO₃, N₂O₅...) interfèrent avec NO₂ dans les analyseurs par chimiluminescence.

ii.1.2 Cinétique du NO₃ + gaiacol utilisant la méthode du pseudo-premier ordre

Une expérience préliminaire a été réalisée avec des concentrations initiales de ~ 2200 ppbv NO₂ et ~ 1800 ppbv O₃, comme le montre la Figure IV-6. Par simulation (à l'aide du logiciel FACSIMILE), le maximum de [NO₃] a été estimé après ~ 40 min, de réaction; conformément aux mesures.

450 ppbv de gaiacol ont ensuite été injectés dans la chambre et le NO₃ a été rapidement totalement consommé (en ~ 2 min) en raison de sa réaction avec le gaiacol, ce

qui rend impossible la mesure de la constante de vitesse à partir du suivi des concentrations en NO_3 .

Cela suggère que l'utilisation de l'IBBCEAS pour la détermination des constantes de vitesse des réactions $\text{NO}_3 + \text{COV}$ doit être limitée à des COV moins réactifs que le gaiacol.

ii.1.3 Cinétique du $\text{NO}_3 + \text{gaiacol}$ par la méthode relative

Trois isomères du crésol ont été utilisés comme composés de référence. Les concentrations initiales de gaiacol et les références se situaient entre 20 et 200 ppbv. La Figure IV-7 affiche la consommation du gaiacol par rapport à celles des composés de référence. Le tableau IV-2 résume les données obtenues. Les incertitudes indiquées pour k_{gaiacol} correspondent à 2σ sur la régression linéaire et ne tiennent pas compte des incertitudes sur $k_{\text{référence}}$.

Les valeurs des constantes de vitesse pour la réaction du gaiacol avec le radical NO_3 déterminées par la méthode de la vitesse relative en utilisant les trois références sont en bon accord et conduisent à une valeur moyenne de $k_{\text{gaiacol}} = (3,77 \pm 0,39) \times 10^{-11} \text{ cm}^3 \text{ molécule}^{-1} \text{ s}^{-1}$.

La valeur déterminée dans ce travail est environ 40% plus élevée que celle mesurée précédemment dans le même laboratoire: $(2,69 \pm 0,57) \times 10^{-11} \text{ cm}^3 \text{ molécule}^{-1} \text{ s}^{-1}$ [2]. En outre, ce résultat est en également en désaccord avec l'étude récente de Yang et al. (2016) qui ont trouvé une valeur de $(0,32 \pm 0,14) \times 10^{-11} \text{ cm}^3 \text{ molécule}^{-1} \text{ s}^{-1}$ pour la constante. Yang et al.(2016) ont utilisé la décomposition de N_2O_5 pour générer du NO_3 et du 2-méthyl-2-butène comme composé de référence. Cependant, les pertes de paroi pour les deux COV ont été négligées (ce qui est particulièrement surprenant pour un composé aussi collant que le gaiacol), ce qui peut expliquer le désaccord.

ii.2 Formation de AOS à partir de la réaction en phase gazeuse du gaiacol avec les radicaux NO_3

L'objectif de ce travail était d'étudier la formation d'AOS à partir de la réaction du gaiacol avec les radicaux NO_3 . Les expériences ont été menées dans deux chambres de simulation: LPCA-ONE et CHARME.

LPCA-ONE est un réacteur cubique rigide en PMMA (PolyMethyl Methacrylate) de 8,0 m³ (2 m × 2 m × 2 m; rapport surface/volume ≈ 3 m⁻¹). Il est équipé d'un ventilateur en Téflon (diamètre 30 cm) situé au centre de la face inférieure pour assurer un mélange homogène des réactifs. Avant chaque expérience, la chambre de réaction est balayée par de l'air purifié pendant environ 12 h.

Les expériences ont été réalisées avec des concentrations initiales en gaiacol de 84 à 537 ppbv. Après quelques minutes, le NO₂ (500 - 1 500 ppbv) et l'O₃ (500 - 1 000 ppbv) ou du N₂O₅ sont introduits. La concentration de gaiacol a été enregistrée (m/Z 125) toutes les 10 s avec le PTR-ToF-MS. Les échantillons d'air ont été collectés avec un débit de 50 ml min⁻¹ à travers un tube en peek chauffé (333 K).

La formation en aérosols organiques secondaires a été suivie avec un SMPS en utilisant un temps de balayage de 120 s et un délai de 16 s entre les échantillons, fournissant une distribution de taille entre 15 à 661 nm. La concentration massique de l'aérosol M₀ a été calculée en supposant une densité de 1,4 pour l'aérosol organique.

Des expériences préliminaires ont été effectuées pour vérifier que l'ozonolyse du gaiacol était négligeable dans les expériences où le NO₃ était formé in situ à partir de la réaction NO₂ + O₃ (cela était attendu car la constante de vitesse pour la réaction de l'ozone avec le gaiacol est faible ($k_{(\text{gaiacol} + \text{O}_3)} = 4 \times 10^{-19} \text{ cm}^3 \text{ molécule}^{-1} \text{ s}^{-1}$)).

Une formation d'aérosols pourrait se produire à partir de la réaction des radicaux nitrate avec des impuretés présents dans l'air purifié et/ou avec le dégazage de composés provenant des parois des réacteurs. Pour caractériser cette formation de particules, de l'air purifié a été laissé dans l'obscurité en présence de NO₃ pendant ~ 1 h. Ces tests ont conduit à des concentrations massiques en aérosols de 0,2 µg m⁻³, ce qui est négligeable par rapport aux concentrations massiques en AOS observées à partir de la réaction du NO₃ avec le gaiacol (entre 7 et 547 µg m⁻³).

Les pertes des AOS sur les parois des 2 chambres ont été déterminées en suivant les concentrations massiques en aérosols sur une période d'environ 1 h à la fin de chaque expérience. Celles-ci sont décrites par une loi de premier ordre, avec une dépendance de

la taille de l'aérosol; les valeurs obtenues varient entre 5 et 44% h⁻¹; elles correspondent à celles obtenues dans d'autres chambres.

Pour déterminer la composition chimique des AOS, des filtres en fibre de quartz ont été prélevés à 7,5 L min⁻¹ pendant 3 h. Pour ces expériences, les concentrations initiales en gaiacol étaient de ≈ 2 ppmv. Les aérosols collectés ont été analysés par ESI-LC-QToF-MS/MS en utilisant le mode d'ionisation négative (abstraction de protons).

ii.2.1 Rendements en AOS

Une série d'expériences gaiacol/NO₃ a été réalisée dans l'obscurité à pression atmosphérique, température ambiante (294 ± 2) K et faible humidité relative (<2%). Les concentrations initiales en NO₂ ([NO₂]₀), O₃ ([O₃]₀) et gaiacol ([gaiacol]₀), les concentrations consommées en gaiacol corrigées des pertes sur les parois (Δ [gaiacol]), les concentrations massiques en aérosols organiques corrigées des pertes de paroi (M_0) et les rendements globaux AOS sont résumés dans le tableau IV-3. Toutes les expériences ont été réalisées sans particules d'ensemencement et ont été menées jusqu'à ce que la masse d'aérosol formé soit stable.

Les profils temporels typiques de concentrations massiques du gaiacol et des AOS sont présentés sur la Figure IV-8 (expérience gaiacol # 10; conditions initiales: gaiacol (276 ppbv; 1429 $\mu\text{g m}^{-3}$); NO₂ (750 ppbv) et O₃ (500 ppbv)). La formation de particules est observée environ 45 minutes après le début de la réaction et atteint un plateau après un temps de réaction d'environ 2 h. Les rendements en AOS (Y) ont été déterminés expérimentalement à partir du rapport entre la concentration massique en AOS obtenue (M_0 en $\mu\text{g m}^{-3}$) et la concentration en gaiacol consommé (Δ [gaiacol] en $\mu\text{g m}^{-3}$) à la fin de chaque expérience (Éq. 23).

L'incertitude sur les valeurs des rendements des AOS peut être estimée à environ 30%, en raison d'erreurs statistiques et systématiques possibles sur M_0 et Δ [gaiacol]. Les résultats reportés dans le tableau IV-2 indiquent que la concentration initiale en gaiacol influence les rendements : une concentration initiale plus élevée en gaiacol entraîne un rendement en AOS plus élevé.

Le tracé de M_0 en fonction de $\Delta[\text{gaiacol}]$ obtenu à la fin des expériences est représenté sur la Figure IV-9. Celle-ci présente une corrélation linéaire ($R^2 = 0,92$), avec une pente de 0,25. Cette dernière valeur peut être comparée au rendement maximum en AOS déterminés pour la réaction du gaiacol avec NO_3 ($Y_{\text{max}} = 0,21$; voir le tableau IV-3) et semble représenter la limite haute pour cette réaction. L'extrapolation des données présentées sur la Figure IV-9 suggère que la production d'AOS serait négligeable pour des concentrations en gaiacol consommées inférieures à $\approx 550 \mu\text{g m}^{-3}$ (110 ppbv).

Un modèle semi-empirique basé sur la répartition gaz-particules de produits semi-volatils (Odum et al., 1996; Pankow, 1994a, b) permet de décrire les rendements de AOS obtenus (Eq.24).

ii.2.2 Composition chimique AOS

Des analyses ESI-LC-QTOF-MS/MS ont été réalisées pour caractériser la composition chimiques des AOS formés à partir de la réaction en phase gazeuse de NO_3 avec le gaiacol. Un chromatogramme typique est présenté sur la Figure IV-11. Une fois la masse molaire d'un produit déterminée (par LC-QTOF-MS), le pic correspondant est fragmenté en utilisant trois valeurs d'énergie (10 eV, 20 eV et 30 eV; analyse MS/MS). Une valeur énergétique plus élevée conduit à une plus grande fragmentation des molécules ce qui permet d'identifier les groupes fonctionnels et ainsi d'évaluer les structures chimiques des composés.

Les composés détectés dans les AOS sont listés dans les tableaux IV-4 (composés majeurs, abondance relative $> 4\%$) et Tab.S1 (composés mineurs, abondance relative $\leq 2\%$). Les abondances relatives (exprimées en %) ont été calculées à partir du rapport entre les aires chromatographiques des différents isomères et l'aire totale de tous les pics. Cette approche suppose que le spectromètre de masse a la même réponse pour chaque composé chimique détecté. Les principaux composés observés dans les AOS sont les composés aromatiques nitrés (voir Tab.IV-4): nitrométhoxybenzènes ($m/z = 152$, 2 isomères, 9,3%); nitrocatéchol(s) ($m/z = 154$, 1 ou 2 isomères (la largeur du pic suggère la présence de deux isomères, mais cette hypothèse n'a pas pu être confirmée), 18,0%); nitrogaiacols ($m/z = 168$, 4 isomères, 11,7%); dinitrométhoxybenzène ($m/z = 197$, 2 isomères, 7,6%); dinitrocatéchols ($m/z = 199$, 3 isomères, 4,7%); dinitrogaiacols ($m/z =$

213, 6 isomères, 9,0%); composés dimères formés via l'association de 1 nitroguaiacol et 1 nitrocatechol ($m/z = 321$, 12 isomères, 5,4%) ou via l'association de 2 nitroguaiacols ($m/z = 335$, 5 isomères, 18,1%), et 2 composés non identifiés ($m/z = 531$, 8,2% et $m/z = 584$, 4,3%). Ainsi, cela confirme que les produits d'oxydation formés dans les aérosols à partir de la réaction des radicaux NO_3 avec le guaiacol sont à la fois des produits de première et de deuxième génération, comme le suggèrent les données présentées sur la Figure IV-11. Cependant, comme plus de 75% de la masse de l'AOS est formée lorsque tout le guaiacol est consommé, il est fort probable que les produits observés en phase condensée proviennent de l'oxydation en phases gazeuse et/ou en particulaire des produits de première génération. Des expériences supplémentaires utilisant des concentrations initiales en guaiacol inférieures permettraient de réduire ces réactions secondaires. Les Figures S1-S8 (voir annexe I) présentent les spectres MS/MS obtenus à 20 eV pour les principaux composés identifiés dans les AOS ($m/z = 152$, Fig.S1; $m/z = 154$, Fig .S2; $m/z = 168$, Figure S3; $m/z = 197$, Figure S4; $m/z = 199$, Figure S5; $m/z = 213$, Figure S6; $m/z = 321$, Figure .S7 et $m/z = 335$, Figure S8). Les différents fragments ont permis de proposer des structures chimiques cohérentes pour les produits d'oxydation de la réaction $\text{NO}_3 + \text{guaiacol}$ observés dans la phase particulaire.

Le 4-nitroguaiacol et le 5-nitroguaiacol ont été clairement identifiés dans les AOS en comparant leurs temps de rétention chromatographique et leurs spectres MS-MS à ceux des standards disponibles dans le commerce. Le nitroguaiacol le plus abondant formé dans la phase particulaire était le 4-nitroguaiacol (91,5%), en grand excès par rapport au 5-nitroguaiacol (5,4%) et au 3-nitroguaiacol et/ou 6-nitroguaiacol (3,1% pour les deux; les standards de ces deux isomères n'existent pas, il n'a donc pas été possible de les distinguer).

Le mécanisme conduisant aux principaux produits d'oxydation identifiés dans les AOS est proposé sur la Figure IV-12. Il a été suggéré par Atkinson et al. (1992), que la réaction entre le radical NO_3 et les composés phénoliques peut débuter par une addition en ipso du substituant OH, conduisant à la formation d'un intermédiaire stable avec un cycle à six atomes. Une autre possibilité est l'addition de NO_3 sur le cycle aromatique. Ces deux voies conduisent à la formation d'acide nitrique et d'un radical phénoxy, qui

réagit ensuite avec le NO_2 pour produire des isomères du nitroguaiacol. De même, la formation de dinitroguaiacols et trinitroguaiacols peut être expliquée par la réaction des nitroguaiacols et dinitroguaiacols avec NO_3 puis NO_2 .

Les étapes d'oxydation initiales formant des nitrométhoxybenzènes et nitrocatechols à partir du guaiacol et de NO_3 ne sont pas encore élucidées, comme indiqué sur la Figure IV-12. Étant donné que les connaissances actuelles sur la réactivité chimique en phase gazeuse des composés aromatiques ne permet pas d'identifier ce mécanisme, cela suggère qu'une chimie d'oxydation pourrait avoir lieu dans la phase condensée et produire les nitrométhoxybenzènes et nitrocatechols observés. Des études sur l'oxydation du guaiacol en phase liquide seraient très utiles pour étayer cette hypothèse. Dans leur étude sur les produits de réaction en phase gazeuse du NO_3 + guaiacol, Yang et al. (2016) ont également signalé la présence de nitroguaiacols (4-nitroguaiacol et 6-nitroguaiacol; le 4-nitroguaiacol étant le plus abondant), dinitroguaiacol (4,6-dinitroguaiacol), catéchol (1,2-dihydroxybenzène) et nitrométhoxybenzène dans les produits formés à partir de l'oxydation en phase gazeuse du guaiacol par NO_3 .

La formation de nitrocatechols et de dinitrocatechols peut également résulter de la réaction de NO_3 puis NO_2 avec le catéchol et les nitrocatechols, respectivement. Les composés à masse moléculaire élevée ($m/z > 300$) présentent 2 à 3 cycles aromatiques; ils peuvent être produits à partir de l'association de radicaux phénoxy formés à partir de nitroguaiacol (s) et/ou nitrocatechol (s).

Pour les principaux produits identifiés, un isomère a toujours été plus abondant que les autres (les abondances relatives correspondantes varient entre 85% à 99%; voir Tab.S2).

Les produits d'oxydation formés en phase condensée à partir de la réaction en phase gazeuse du guaiacol avec des radicaux nitrate peuvent également être comparés à ceux identifiés lors de la réaction du guaiacol avec des radicaux hydroxyles dans des conditions de NO_x élevée. Les analyses ATR-FTIR réalisées par Ahmad et al. (2017) révèlent également la présence de 4-nitroguaiacol dans les AOS. Ainsi, cette observation suggère que les produits d'oxydation générés en phase particulaire, via l'oxydation du guaiacol par NO_3 ou OH/NO_x , sont probablement similaires comme cela a été précédemment postulé.

à partir de la comparaison des constantes de répartition gaz-particules obtenus avec les deux oxydants.

ii.3 Conclusion

La constante de vitesse pour la réaction du gaiacol avec les radicaux nitrate a été étudiée dans CHARME en utilisant la méthode relative. Un bon accord a été obtenu en utilisant trois COV de référence (l'o-crésol, le m-crésol et le p-crésol), ce qui donne une valeur moyenne $k_{\text{guaicol}} = (3,77 \pm 0,39) \times 10^{-11} \text{ cm}^3 \text{ molécule}^{-1} \text{ s}^{-1}$.

Les expériences réalisées avec le gaiacol en excès (méthode du pseudo-premier ordre) ont montré que cette méthode n'est pas applicable pour le guaiaicol qui présente une réactivité trop élevée avec NO_3 . D'autres COV moins réactifs avec cet oxydant seront testés.

La constante de vitesse k_{gaiacol} déterminée dans cette étude a permis de calculer la durée de vie atmosphérique du gaiacol par rapport à sa réaction avec le radical NO_3 . Celle-ci est égale à 53 s, si on suppose une concentration en NO_3 de $5 \times 10^8 \text{ molécule cm}^{-3}$.

La formation de AOS à partir de la réaction du gaiacol avec des radicaux nitrate a été étudiée dans deux chambres de simulation. Il a été démontré que les rendements en AOS sont influencés par la concentration initiale en gaiacol, ce qui conduit à des rendements en aérosols allant de 0,01 à 0,21. Un très bon accord a été observé entre les expériences réalisées dans les deux chambres, ce qui valide les résultats obtenus dans cette étude. Les données sur les aérosols ont été ajustées avec le modèle de répartition gaz-particules développé par Pankow (1994) et Odum et al. (1996) en utilisant le modèle à un seul produit.

Les concentrations atmosphériques en aérosols sont de $\approx 5 \text{ } \mu\text{g m}^{-3}$ dans de nombreux environnements, bien qu'elle puisse parfois atteindre $50 \text{ } \mu\text{g m}^{-3}$ voire plus dans des zones fortement polluées. L'extrapolation à une charge particulaire de $5 \text{ } \mu\text{g m}^{-3}$ des valeurs de rendement en aérosols obtenues dans cette étude (Figure IV-10) donne un rendement en AOS de 2% pour la réaction $\text{guaiaicol} + \text{NO}_3$. On peut donc conclure que la contribution à la production d'AOS de la réaction entre le gaiacol et les radicaux NO_3 est probablement

relativement mineure dans de nombreux environnements. Cependant, dans les zones polluées, cette réaction peut être une source importante d'aérosols organiques secondaires.

Des analyses ESI-LC-QToF-MS/MS ont été réalisées pour caractériser la composition chimique des aérosols. Des composés nitro-aromatiques ont été identifiés comme les principaux produits d'oxydation, confirmant des études antérieures sur les produits formés à partir de la réaction en phase gazeuse des radicaux NO_3 avec les dérivés du gaiacol.

Le lévoglucosan (1,6-anhydro- β -anhydroglucose), qui provient de la pyrolyse de la cellulose ou des hémicelluloses, est un traceur bien établi des aérosols primaires de combustion de la biomasse (BB). Plusieurs composés nitro-aromatiques ont été détectés dans les aérosols urbains, et les nitrocatechols ainsi que les nitroguaiacols sont reconnus comme des traceurs appropriés pour le BB secondaire [2,3]. Des efforts de recherche supplémentaires sur la réactivité de ces composés permettraient de mesurer leurs constantes de vitesse avec les principaux oxydants et de déterminer les durées de vie correspondantes. À notre connaissance, seules quelques données sont disponibles dans la littérature concernant la réactivité atmosphérique des nitro-aromatiques.

Mots clés : spectroscopie d'absorption en cavité résonante par une source incohérente spectrale large bande (IBBCEAS); extinction d'aérosol; radical nitrate; chambre de simulation atmosphérique; gaiacol; rendements en AOS.

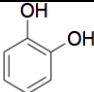
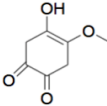
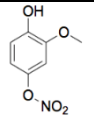
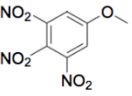
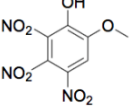
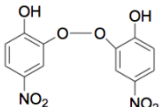
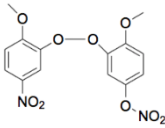
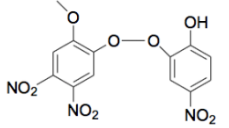
Reference

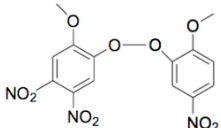
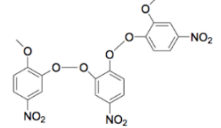
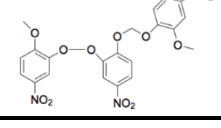
- [1] A. Lauraguais, A. Zein, C. Coeur, E. Obeid, A. Cassez, M. T. Rayez, J. C. Rayez. Kinetic study of the gas-phase reactions of nitrate radicals with methoxyphenol compounds: experimental and theoretical approaches. *The Journal of Physical Chemistry A*, 2016, 120(17): 2691-2699. **10.1021/acs.jpca.6b02729**
- [2] Y. Iinuma, O. Boge, R. Grafe, H. Herrmann. Methyl-nitrocatechols: atmospheric tracer compounds for biomass burning secondary organic aerosols. *Environmental Science & Technology*, 2010, 44(22): 8453-8459. **10.1021/es102938a**
- [3] Z. Kitanovski, I. Grgic, F. Yasmeen, M. Claeys, A. Cusak. Development of a liquid chromatographic method based on ultraviolet-visible and electrospray ionization mass spectrometric detection for the identification of nitrocatechols and related tracers in biomass burning atmospheric organic aerosol. *Rapid communications in mass spectrometry: RCM*, 2012, 26(7): 793-804. **10.1002/rcm.6170**

Appendices

Appendix I Minor/major compounds observed in the SOAs and LC/MS/MS product ion spectra for major compounds

Table S1 Minor compounds observed in the SOAs (ESI-LC-QToF-MS/MS analyses) formed from the gas-phase reaction of guaiacol with NO₃ radicals. The relative abundances (R, in %) are also indicated.

Molecular ion ^a	Main fragments	Brut Formula	Name ^c	Structure ^f	R (%) ^g
109	69 [C ₃ HO ₂] ⁻	C ₆ H ₅ O ₂ ^d	Catechol ¹		<0.2
155	-	C ₇ H ₇ O ₄ ^d	Hydroxymethoxy-cyclohexenedione ¹		<0.2
184	65 [C ₄ HO] ⁻ 152 [C ₆ H ₂ NO ₄] ⁻ 169 [C ₆ H ₃ NO ₅] ⁻	C ₇ H ₆ NO ₅ ^b	Hydroxymethoxy-phenylnitrate ⁴		2.0
242	-	C ₇ H ₄ N ₃ O ₇ ^b	Trinitromethoxybenzene ²		0.7
258	93 [C ₅ HO ₂] ⁻ 153 [C ₆ H ₃ NO ₄] ⁻ 213 [C ₆ HN ₂ O ₇] ⁻	C ₇ H ₄ N ₃ O ₈ ^d	Trinitroguaiacol ¹		<0.2
307	-	C ₁₂ H ₇ N ₂ O ₈ ^c	Association of 2 nitrocatechols ⁶		<0.2
351	-	C ₁₄ H ₁₁ N ₂ O ₉ ^b	Association of 1 nitroguaiacol and 1 Hydroxymethoxy-phenylnitrate ⁷		0.2
366	-	C ₁₃ H ₈ N ₃ O ₁₀ ^b	Association of 1 dinitroguaiacol and 1 nitrocatechol ⁶		<0.2

380	-	$C_{14}H_{10}N_3O_{10}$ ^c	Association of 1 nitroguaiacol and 1 dinitroguaiacol ¹		<0.2
488	153 $[C_6H_3NO_4]^-$ 168 $[C_7H_6NO_4]^-$ 319 $[C_{13}H_7N_2O_8]^-$	$C_{20}H_{14}N_3O_{12}$ ^b	Association of 2 nitroguaiacol and 1 nitrocatechol ¹⁴		<0.2
502	153 $[C_6H_3NO_4]^-$ 168 $[C_7H_6NO_4]^-$	$C_{21}H_{16}N_3O_{12}$ ^c	Association of 3 nitroguaiacols ⁷		0.9

^a The indicated masses correspond to the $[M-H]$ product ions.

^b Probability given by the software between 98 and 100 %.

^c Probability given by the software between 90 and 97 %.

^d Probability given by the software between 70 and 89 %.

^e Number of detected isomers.

^f The drawn structure correspond to one isomer only.

^g The relative abundances (in %) were calculated from the ratio of the sum of the chromatographic areas of the different isomers to the total chromatographic area of all the peaks.

Table S2 Major compounds observed in the SOAs (ESI-LC-QToF-MS/MS analyses) formed from the gas-phase reaction of guaiacol with NO₃ radicals. Relative abundances (isomers, in %) and retention times (RT, in min) of the different isomers.

Molecular ions ^a	Name	Isomers RT (min) ^b	Isomers (%)
152	Nitromethoxybenzene	8.82	99.0
		9.56	1.0
154	Nitrocatechol	4.49	100.0
168	Nitroguaiacol	6.38	5.4 (5-Nitroguaiacol)
		6.76	1.3 (3 or 6-Nitroguaiacol)
		7.35	91.5 (4-Nitroguaiacol)
		8.12	1.8 (3 or 6 - Nitroguaiacol)
197	Dinitromethoxybenzene	10.86	2.4
		11.16	97.6
199	Dinitrocatechol	8.03	97.2
		8.97	2.8
213	Dinitroguaiacol	8.31	96.5
		9.43	0.1
		9.70	1.0
		10.39	1.8
		8.99	0.4
		10.17	0.3
321	Association of 1 nitroguaiacol and 1 nitrocatechol	9.94	7.6
		10.30	1.2
		11.41	1.0
		11.59	28.0
		11.94	10.5
		12.22	0.2
		12.42	3.9
		12.59	8.7
		12.75	22.7
		12.15	14.3
		13.50	1.6
		11.81	0.4
335	Association of 2 nitroguaiacols	14.88	0.2
		13.00	4.1
		13.78	5.4
		14.31	85.1
		15.31	5.2

^a The indicated masses correspond to the [M–H] product ions.

^b Retention time (in Fig.IV-10).

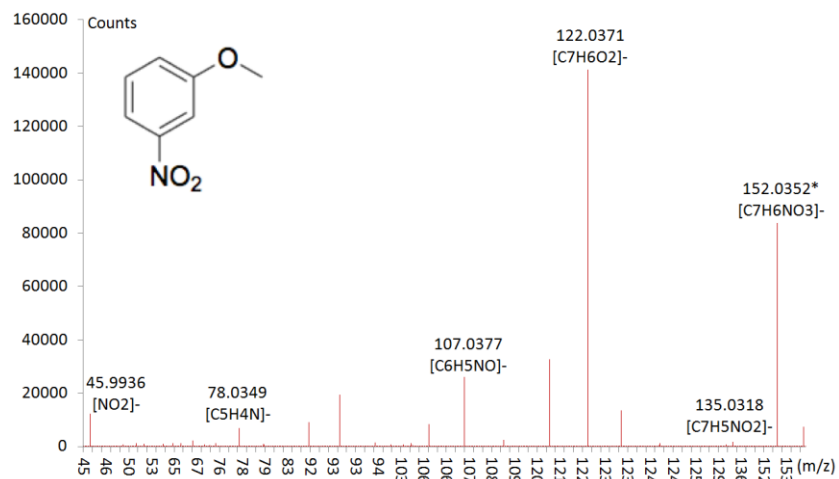


Figure S1 LC/MS/MS product ion spectra of m/z 152 compound: nitromethoxybenzene at RT = 8.82 min (Fig.IV-10).

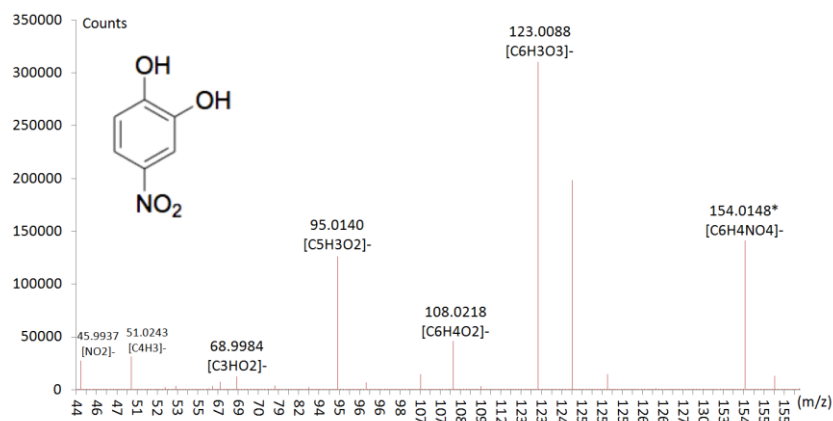


Figure S2 LC/MS/MS product ion spectra of m/z 154 compound: nitrocatechol at RT = 4.58 min (Fig.IV-10).

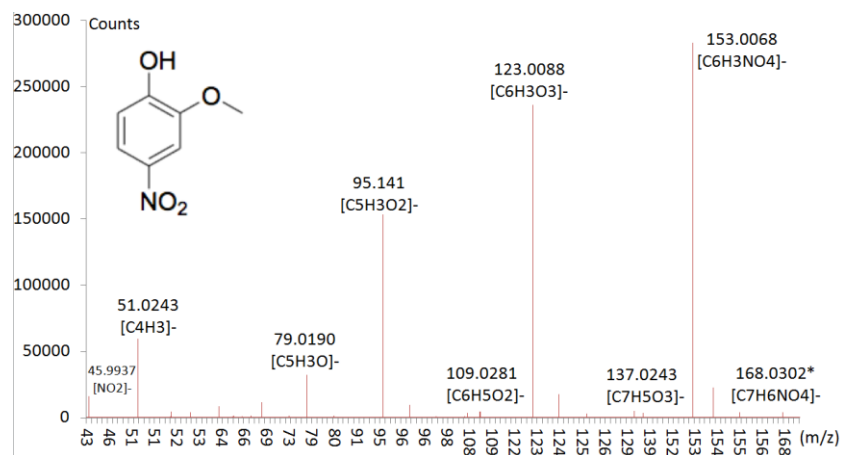


Figure S3 LC/MS/MS product ion spectra of m/z 168 compound: nitroguaiacol at RT = 7.33 min (Fig.IV-10).

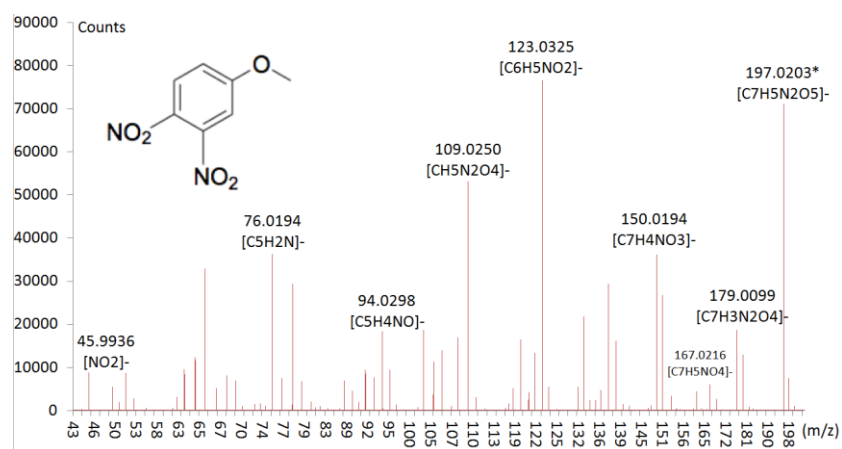


Figure S4 LC/MS/MS product ion spectra of m/z 197 compound: dinitromethoxybenzene at RT = 11.16 min (Fig.IV-10).

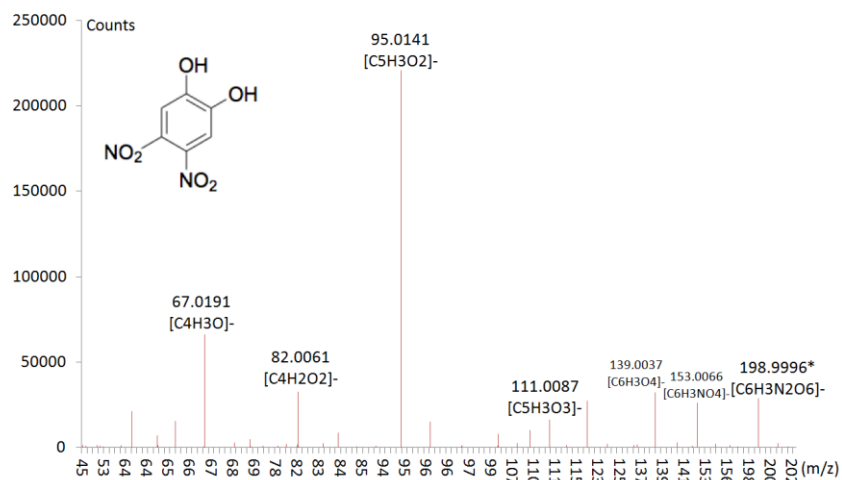


Figure S5 LC/MS/MS product ion spectra of m/z 199 compound: dinitrocatechol at RT = 8.03 min (Fig.IV-10).

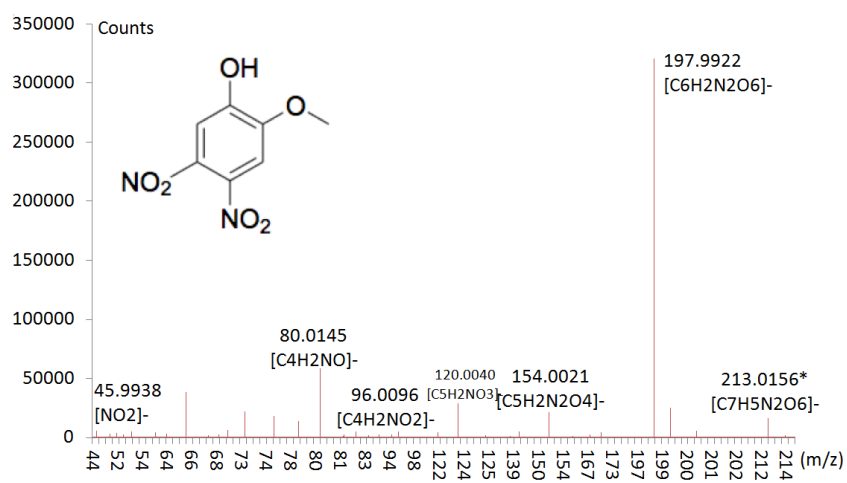


Figure S6 LC/MS/MS product ion spectra of m/z 213 compound: dinitroguaiacol at RT = 8.34 min (Fig.IV-10).

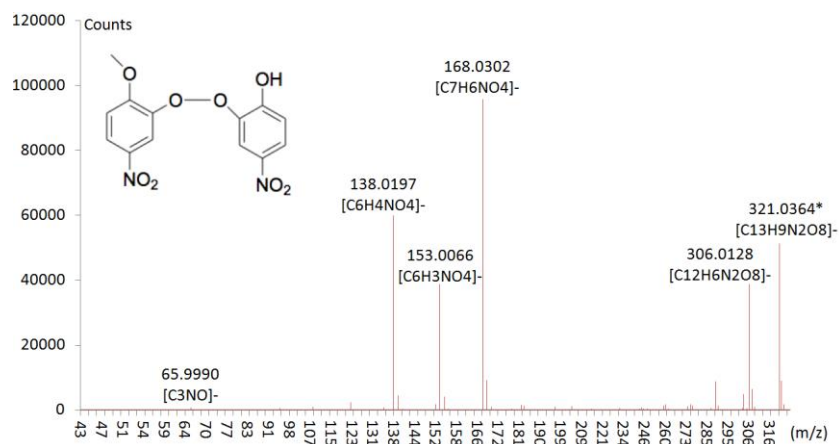


Figure S7 LC/MS/MS product ion spectra of m/z 321 compound: association of 1 nitroguaiacol and 1 nitrocatechol at RT = 11.82 min (Fig.IV-10).

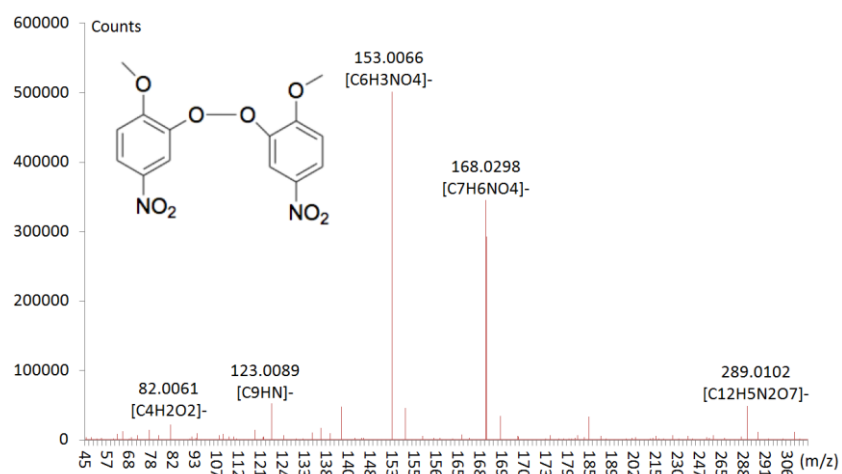


Figure S8 LC/MS/MS product ion spectra of m/z 335 compound: association of 2 nitroguaiacols at RT = 14.26 min (Fig.IV-10).

Appendix II Airticle 1

Published in *Atmospheric Environment*, (2020)

DOI: 10.1016/j.atmosenv.2020.117740.

Secondary organic aerosol formation from the gas-phase reaction of guaiacol (2- methoxyphenol) with NO₃ radicals

Lingshuo MENG^(1,2), Cécile COEUR^{(1)*}, Layal FAYAD⁽¹⁾, Nicolas HOUZEL⁽¹⁾, Paul GENEVRAY⁽³⁾, Hichem BOUZIDI⁽¹⁾, Alexandre TOMAS^(2,3), Weidong CHEN⁽¹⁾

⁽¹⁾ *Laboratoire de Physico-Chimie de l'Atmosphère, Université du Littoral Côte d'Opale, Dunkerque 59140, France*

⁽²⁾ *IMT Lille Douai, Univ. Lille, SAGE – Sciences de l'Atmosphère et Génie de l'Environnement, 59000 Lille, France*

⁽³⁾ *Centre Commun de Mesures, Université du Littoral Côte d'Opale, Dunkerque 59140, France*

*Corresponding author. Tel.: +33328 23 76 42.

Address: Université du Littoral Côte d'Opale, Bâtiment IREnE, 189A, Avenue Maurice Schumann, 59140 DUNKERQUE - FRANCE.

Email address: coeur@univ-littoral.fr (C. Coeur).

Keywords: guaiacol, NO₃ radicals, secondary organic aerosols, simulation chamber, nitro-aromatics.

Abstract

Methoxyphenols are oxygenated aromatic compounds emitted by wood combustion (consequently to the pyrolysis of lignin). The atmospheric reaction of nitrate radical (NO₃) with guaiacol (2-methoxyphenol), one of the principal representatives of this class of compounds has been investigated in the dark at (294 ± 2) K, atmospheric pressure and low

relative humidity ($RH < 2\%$). The formation of secondary organic aerosols (SOAs) has been studied in two simulation chambers. The concentrations time profiles of guaiacol were followed with a PTR-ToF-MS (Proton Transfer Mass Reaction – Time of Flight – Mass Spectrometer) and those of SOAs by an SMPS (Scanning Mobility Particle Sizer). Aerosol yields (Y) were calculated from the ratio of the suspended aerosol mass concentration corrected for wall losses (M_0), to the total reacted guaiacol concentration assuming a particle density of 1.4 g cm^{-3} . The aerosol yield increases as the initial guaiacol concentration rises, leading to yield values ranging from 0.01 to 0.21. A very good agreement was observed between the experiments performed in both chambers which gives confidence in the data obtained in this study. The organic aerosol formation can be represented by a one-product gas/particle partitioning absorption model with a stoichiometric coefficient $\alpha = 0.32 \pm 0.04$ and an equilibrium constant $K = (4.2 \pm 1.0) \times 10^{-3}\text{ m}^3\text{ }\mu\text{g}^{-1}$. The chemical composition of the aerosols formed was studied after sampling on quartz fiber filter, ultrasonic extraction and analysis by ESI-LC-QToF-MS-MS (ElectroSpray Ionization - Liquid Chromatography - Quadrupole - Time of Flight – Tandem Mass Spectrometry). The oxidation products observed in the condensed phase are mostly nitro-aromatics; they display chemical structures with one, two and three aromatic rings. A reaction mechanism leading to these products has been proposed. To our knowledge, this work represents the first study on the SOAs formation from the reaction of guaiacol with NO_3 radicals.

1. Introduction

During the last decades, air pollution has been a major issue and environmental policies have been developed to reduce its impacts on climate and air quality (Gurjar et al. 2010). Some field campaigns have shown that aromatic compounds represent about 20% of non-methane hydrocarbons in urban areas. These volatile organic compounds (VOCs) contribute to the formation of photo-oxidants (Derwent et al., 1996; Derwent et al., 1998) and Secondary Organic Aerosols (SOAs) (Calvert et al., 2002; Hallquist et al., 2009) and may involve risks for human health (Hanson et al., 1996).

The use of renewable energy is encouraged by environmental policies to help to decrease the dependence to fossil fuels. Biomass burning is one of the major alternative energy sources; nevertheless, it is well recognized that it also contributes to important emissions of atmospheric aerosols (Fourtziou et al., 2017), VOCs (Bruns et al., 2017) and have significant impacts on human health (Lighty et al., 2000; Sarigiannis 2015), regional and global air quality (Lelieveld et al., 2001) and climate (Chen et al., 2010; Langmann et al., 2009). Natural fires, human-initiated burning of vegetation and residential wood combustion are included in the term of “biomass burning” (Hays et al., 2002; Mazzoleni et al., 2007; McDonald et al., 2000; Schauer et al., 2001; Simpson et al., 2005).

The pyrolysis of lignin, one of the major components of wood, produces methoxyphenols. The principal atmospheric representatives of this class of compounds are guaiacol (2-methoxyphenol), syringol (2,6-dimethoxyphenol) and their derivatives (Hays et al., 2002; Mazzoleni et al., 2007; McDonald et al., 2000; Schauer et al., 2001; Simpson et al., 2005). They are semi-volatile compounds with high molecular weight and are distributed between gas- and particle- phases.

The reactivity of methoxyphenols toward hydroxyl radicals (Coeur-Tourneur et al., 2010a; Lauraguais et al., 2012, 2014a, 2015), chlorine atoms (Lauraguais et al., 2014b), ozone (El Zein et al., 2015) and nitrate radicals (Lauraguais et al., 2016; Yang et al., 2016; Zang et al., 2016) has been investigated. The determination of the rate coefficients for these reactions has demonstrated their high reactivity toward OH, Cl and NO₃ and their low reactivity with O₃. The corresponding atmospheric lifetimes are about 2 h (OH), 20 h (Cl), 1 min (NO₃) and 12 days (O₃), respectively. Therefore, under atmospheric conditions, the main degradation pathways for the methoxyphenols are their reactions with hydroxyl radicals in the daytime and with NO₃ radicals, during the night.

The formation of secondary organic aerosols from guaiacol and syringol with respect to their reaction with OH has also been investigated (Lauraguais et al., 2012; Lauraguais et al., 2014a). In most environments, atmospheric aerosol concentrations of around 5 µg m⁻³ can be found and in these atmospheric conditions the OH reactions of guaiacol and syringol contribute for a minor part to SOAs production.

The objective of this work was to study the reaction of guaiacol, a wood burning emitted compound, with NO_3 radicals in order to investigate its potential to form SOAs. The experiments were performed in the dark, in two simulation chambers at (294 ± 2) K, atmospheric pressure and low relative humidity ($\text{RH} < 2\%$). The SOA yields were measured and the data analyzed according to the absorptive gas-particle partitioning model developed by Pankow (1994a,b) and Odum et al. (1996). The oxidation products formed in the aerosols were analyzed by ESI-LC-QToF-MS-MS (ElectroSpray Ionization - Liquid Chromatography - Quadrupole - Time of Flight - Tandem Mass Spectrometry). The atmospheric implications of the reaction of guaiacol with NO_3 radicals were also discussed. To our knowledge, this work represents the first study on the formation of SOAs from the reaction of guaiacol with nitrate radicals.

2. Material and method

The experiments were performed in the dark in two simulation chambers, LPCA-ONE and CHARME at room temperature (294 ± 2 K), atmospheric pressure and low relative humidity ($\text{RH} < 2\%$).

LPCA-ONE is an 8.0 m^3 ($2 \text{ m} \times 2 \text{ m} \times 2 \text{ m}$) PMMA (PolyMethyl Methacrylate) cubic reactor stirred by a Teflon fan (diameter 30 cm) located in the center of the lower face. A detailed description of the chamber is available in Lauraguais et al. (2012). CHARME (Chamber for the Atmospheric Reactivity and the Metrology of the Environment) is a 9.2 m^3 evacuable cylinder (diameter $\approx 1.7 \text{ m}$ and length $\approx 4.0 \text{ m}$) made in stainless steel (304 L) and electropolished. Four fans (in stainless steel; diameter 50 cm) located in the bottom assure a fast homogenization of the reactive mixture.

Purified and dried air was introduced into both chambers using a generator (Parker Zander KA-MT 1-8) connected to a compressor (SLM-S 7.5 - Renner SCROLLLine). LPCA-ONE was flushed for a minimum of 12 h before each experiment and CHARME is coupled to a vacuum pump (Cobra NC0100-0300B), which allows to reduce the pressure down to 0.4 mbar. The time required to evacuate and fill this latter reactor was around 1 h. After cleaning the chambers, satisfactory background particle number concentrations below $10 \text{ particles cm}^{-3}$ could be detected by a Scanning Mobility Particle Sizer (SMPS TSI, CPC 3775 / DMA 3081).

Guaiacol was introduced into the simulation chambers using an inlet system in which measured amounts of the substances were gently heated in a small flow of purified air.

Nitrate radicals were generated using two methods:

- (i) *in situ* formation of NO₃ from reactions (1):



NO₂ was injected first with a gas syringe and O₃ was then introduced using an ozone generator (by Corona discharge in O₂, Model C-Lasky, C-010-DTI). The injection of both gases were performed in a few seconds. The nitrogen dioxide and ozone concentrations were controlled with a chemiluminescence NO_x analyzer (Thermo Scientific, 42i) and a photometric ozone analyzer (Thermo Scientific, 49i), respectively.

- (ii) thermal decomposition of dinitrogen pentoxide (N₂O₅) (Atkinson et al., 1984):



N₂O₅ was first synthesized in a vacuum line through the reaction of NO₂ with an excess of O₃ according to reaction (1) followed by reaction (-2):



The first phase of the synthesis consisted in trapping NO₂ (in the form of N₂O₄ crystals) at 193 K in a cold tube. In a second phase, the tube was flushed with ozone (C-Lasky C-010-DTI) to form N₂O₅. Dinitrogen pentoxide crystals were gathered in a second cold trap and kept for several weeks at 188 K.

The experiments were performed with guaiacol initial concentrations in the range (84 - 537 ppb). After allowing a few minutes for guaiacol mixing, NO₂ (500 - 1500 ppb) and O₃ (500 -1000 ppb) or N₂O₅ were then introduced (in a few seconds) into the chambers. The concentration of guaiacol was monitored every 10 s with a Proton Transfer Reaction - Time of Flight - Mass Spectrometer (PTR-ToF-MS 1000, Ionicon Analytik GmbH). The air samples were collected through a heated (333 K) peek inlet tube with a flow of 50 mL min⁻¹ into the PTR-ToF-MS drift tube and guaiacol was monitored from the peak at m/z 125.

The aerosol formation was followed with a SMPS using a 2 min scan time and a 16 s delay between samples, providing a size distribution from 15 to 661 nm. The aerosol mass concentration M_0 was calculated assuming a density of 1.4 for the organic aerosol (recommended value, Hallquist et al., 2009).

Preliminary experiments were performed to verify that the guaiacol ozonolysis was negligible in the experiments where NO_3 was formed in-situ from $\text{NO}_2 + \text{O}_3$ (this was expected as the rate constant for the ozone reaction with guaiacol is low ($k_{(\text{guaiacol}+\text{O}_3)} = 4 \times 10^{-19} \text{ cm}^3 \text{ molecule}^{-1} \text{ s}^{-1}$, El Zein et al., 2015)).

Background aerosol formation could occur from the reaction of nitrate radicals with impurities in the purified air and/or with offgasing of compounds from the reactor walls. To characterize this particle formation, purified air was left in the dark in the presence of NO_3 for ≈ 1 h. These test experiments yielded aerosol mass concentrations of $0.2 \mu\text{g m}^{-3}$, which is negligible compared to the SOAs mass concentrations observed from the reaction of NO_3 with guaiacol (between 7 and $547 \mu\text{g m}^{-3}$).

The SOAs wall loss rates were determined by monitoring the aerosol mass concentrations over a period of ≈ 1 h at the end of each experiment. SOA wall losses are described by a first order law, with a dependence on the aerosol size. The decay rates estimated in this study were in the range 5 - 44 % h^{-1} . These values are within the range reported for other chamber experiments (Coeur-Tourneur et al., 2009, 2010b; Henry et al., 2008; Hurley et al., 2001; Lauraguais et al., 2012, 2014a; Takekawa et al., 2003).

To determine the chemical composition of SOAs, quartz fiber filters were sampled at 7.5 L min^{-1} during 3 h (47 mm diameter Whatman 1851-047 QMA). Before the sample collection, filters were fired at 500°C for 12 h, and were then stored in an aluminum foil below 4°C until analysis. For these experiments performed with higher initial concentrations of guaiacol (2 ppm), SOA masses and yields were not determined because a high fraction of the particles was outside the measurement range of the SMPS.

The collected aerosols were analyzed by ESI-LC-QToF-MS/MS (Agilent LC 1100 - MS 6540) using the negative ionization mode (proton abstraction). The chromatographic column used was a ZORBAX Extend-C18 (50 mm long \times 2.1 mm i.d., $1.8 \mu\text{m}$ pore size)

thermostated at 40 °C. The MS analyses allow to access the molar mass of the identified products and the MS/MS analyses, performed at three different energies (10 eV, 20 eV and 40 eV) permit to identify the functional groups of the compounds and to propose chemical structures.

The filters were ultrasonically extracted twice during 30 min in 5 mL of methanol. The solution was then filtered (pore sizes 0.45 µm; PTFE Membrane, Whatman) and the volume was gently reduced to 100 µL under a flow of gaseous nitrogen. Finally, the volume was diluted to 1 mL with ultrapure water in order to improve the separation of the compounds during the chromatographic analysis. The mobile phase used is a mixture of water (+0.1 % formic acid) and acetonitrile (+5 mM ammonium formate); the gradient varied from 90 % water / 10 % acetonitrile at the beginning of the analysis to 100 % acetonitrile at the end.

4-nitroguaiacol and 5-nitroguaiacol were both commercially available, so their identification was confirmed by the correlation of the LC retention times and the mass spectra recorded under the same chromatographic conditions.

The compounds used in this study, their manufacturer and stated purity were: guaiacol (Alpha Aesar, 98 %), 4-nitroguaiacol (Acros Organics, 97 %), 5-nitroguaiacol (TCI, 97 %), methanol (Aldrich, 99.9%), acetonitrile (VWR, > 99.9 %), water (VWR, > 99.9 %), sodium formate (VWR, > 99 %), formic acid (Acros Organics, 99 %), dioxygene (Praxair, 99.5 %) and nitrogen dioxide (Praxair, 99 %).

3. Results and Discussion

3.1. SOA yields

A series of guaiacol/NO₃ experiments were carried out in the dark, at atmospheric pressure, room temperature (294 ± 2) K and low relative humidity (< 2 %). The initial concentrations of NO₂ ([NO₂]₀), O₃ ([O₃]₀) and guaiacol ([guaiacol]₀), the guaiacol reacted concentrations corrected for wall losses (Δ[guaiacol]), the organic aerosol mass concentrations corrected for wall losses (M₀) and the overall SOA yields (Y defined below) are summarized in Table 1. Guaiacol was totally consumed (within 15-60 min) in all experiments, so the reacted concentrations Δ[guaiacol] correspond to [guaiacol]₀.

All experiments investigating SOA yields were achieved without inorganic seed aerosol and were conducted until the suspended aerosol mass (corrected for wall losses) M_0 was stable.

Table 1. Experimental conditions and results.

Expt.	[guaiacol] ₀ ^a (ppb)	NO ₃ formation		Δ[guaiacol] ^b (μg m ⁻³)	M ₀ ^c (μg m ⁻³)	Y ^d
		[NO ₂] ₀ (ppb)	[O ₃] ₀ (ppb)			
In LPCA-ONE						
guaiacol #1	84	N ₂ O ₅ decomposition		436	13	0.03
guaiacol #2	158	N ₂ O ₅ decomposition		818	98	0.12
guaiacol #3	206	N ₂ O ₅ decomposition		1063	109	0.10
guaiacol #4	244	N ₂ O ₅ decomposition		1263	182	0.14
guaiacol #5	290	N ₂ O ₅ decomposition		1501	300	0.20
guaiacol #6	420	N ₂ O ₅ decomposition		2171	452	0.21
In CHARME						
guaiacol #7	117	N ₂ O ₅ decomposition		604	7	0.01
guaiacol #8	218	785 ^e	896 ^f	1130	92	0.08
guaiacol #9	228	535 ^e	620 ^f	1181	94	0.08
guaiacol #10	276	750 ^g	500 ^h	1429	170	0.12
guaiacol #11	288	1239 ^e	798 ^f	1492	314	0.21
guaiacol #12	537	1500 ^g	1000 ^h	2778	547	0.20

^a Initial guaiacol volume ratio.

^b Reacted guaiacol concentration (guaiacol was totally consumed in all experiments and the guaiacol wall losses were in the order of magnitude 10^{-6} or 10^{-5} s^{-1} which were neglected, so the reacted concentrations Δ [guaiacol] correspond to [guaiacol]₀).

^c Organic aerosol mass concentration (corrected for wall losses and assuming a particle density of 1.4 g cm^{-3}).

^d Overall SOA yield (Y) calculated as the ratio of M_0 to the total reacted guaiacol concentration.

^e Initial NO₂ volume ratio measured in the chamber (chemiluminescence NO_x analyser).

^f Initial O₃ volume ratio measured in the chamber (photometric O₃ analyser).

^g Initial injected NO₂ volume ratio.

^h Initial injected O₃ volume ratio.

Typical time profiles of guaiacol and SOA mass concentrations are presented in Fig. 1 together with time-dependent aerosol size distributions (experiment guaiacol #10; initial conditions: guaiacol (276 ppb; $1429 \mu\text{g m}^{-3}$); NO₂ (750 ppb) and O₃ (500 ppb). The

formation of particles started after about 45 min when almost all guaiacol has reacted. The first aerosol size distributions were centered on a few tens of nm. Then, particle number concentrations as well as SOA mass rapidly increased to reach a plateau after ~ 2h reaction time, consistent with a slower reaction rate due to the total consumption of the organic precursor.

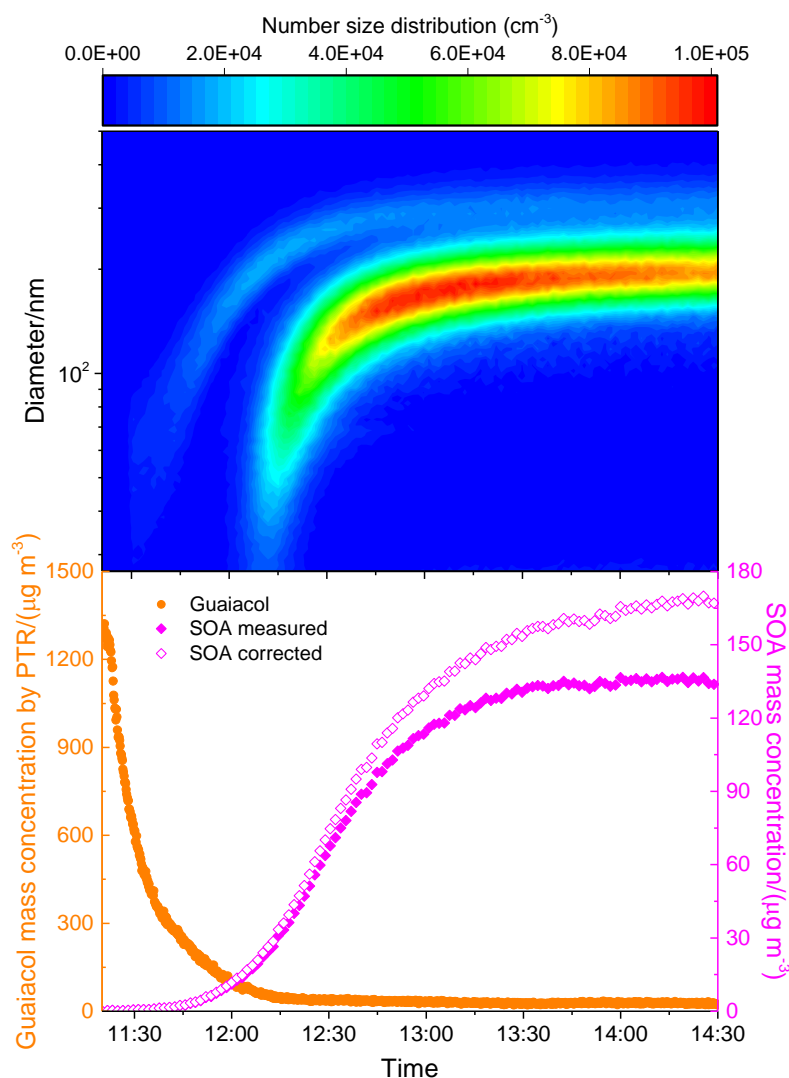


Fig. 1. Typical concentration-time profiles obtained for guaiacol (PTR-ToF-MS) and SOAs (SMPS; measured and corrected for wall losses). Experiment guaiacol #10 (initial mixing ratios: guaiacol (276 ppb; 1429 $\mu\text{g m}^{-3}$); NO₂ (750 ppb) and O₃ (500 ppb)).

These observations suggest that the aerosol formation is due to the NO₃ reaction with guaiacol as well as with its first and second (or even further) generation products. The

organic aerosol yield Y was experimentally determined as the ratio of the SOA formed (M_0 in $\mu\text{g m}^{-3}$) to the reacted guaiacol concentration ($\Delta[\text{guaiacol}]$ in $\mu\text{g m}^{-3}$) at the end of each experiment:

$$Y = \frac{M_0}{\Delta[\text{guaiacol}]} \quad (\text{I})$$

The uncertainty on the SOA yield values can be estimated at about 30%, due to statistical and possible systematic errors on M_0 and $\Delta[\text{guaiacol}]$. The results reported in Table 1 indicate that the initial concentration of guaiacol influenced the aerosol mass concentration formed: a higher guaiacol initial concentration led to higher SOA yields. Furthermore, as the organic aerosol mass directly affects the gas/particle partitioning by acting as the medium into which oxidation products can be absorbed, higher SOA mass leads to higher SOA yields.

The aerosol growth curve, represented by a plot of M_0 versus $\Delta[\text{guaiacol}]$ at the end of the experiments is shown in Fig. 2. Each experiment is represented by a single data point. The figure displays a linear correlation ($R^2 = 0.92$), with a slope of 0.25. This latter value can be compared with the highest SOA yields determined for the reaction of guaiacol with NO_3 ($Y = 0.21$; see Table 1) and seems to represent the high-limit aerosol yield for this reaction. Extrapolation of the data shown in Fig. 2 suggests that the SOA production would be negligible for guaiacol reacted concentrations lower than $\approx 550 \mu\text{g m}^{-3}$ ($\approx 110 \text{ ppb}$). This observation is corroborated by the results obtained for the less concentrated experiments (guaiacol #1 and guaiacol #7 with initial guaiacol concentrations of $436 \mu\text{g m}^{-3}$ and $604 \mu\text{g m}^{-3}$, respectively) in which the aerosol mass concentrations M_0 was low (around $10 \mu\text{g m}^{-3}$).

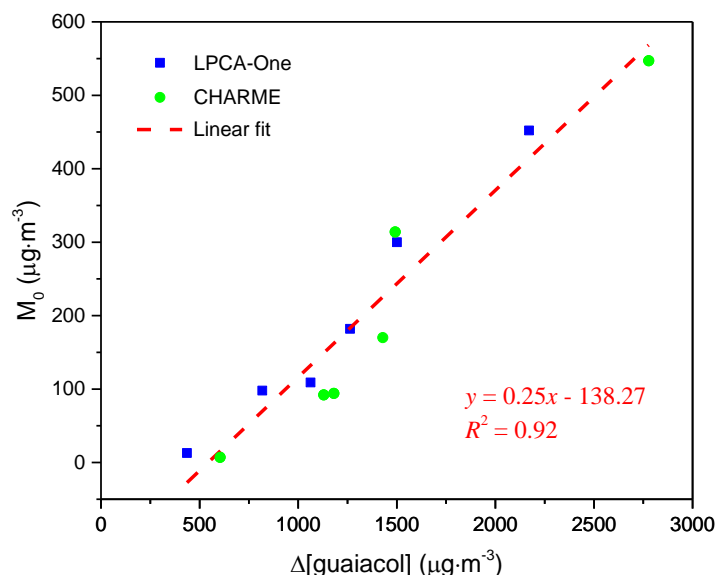


Fig. 2. Aerosol growth curve: SOA mass concentration (M_0) against the reacted guaiacol concentration ($\Delta[\text{guaiacol}]$) measured at the end of the experiments. Each data point represents a separate experiment.

A widely-used semi-empirical model based on absorptive gas-particle partitioning of semi-volatile products (Odum et al., 1996; Pankow, 1994a,b) allows to describe the SOA yields. In this model, the SOA yield (Y) of a particular hydrocarbon (i) is given by:

$$Y = \sum_i M_0 \frac{\alpha_i K_{om,i}}{1 + K_{om,i} M_0} \quad (\text{II})$$

where α_i is the mass-based stoichiometric coefficient of the semi-volatile product i and $K_{om,i}$ is the gas-particle partitioning equilibrium constant. In this study, since no organic aerosol seed was used, the total aerosol mass is equal to the mass of the SOAs formed. Eq. II can be fitted to the guaiacol experimental data to determine the values for α_i and $K_{om,i}$ (see Fig. 3). The simulation of Y versus M_0 with the one-product model is able to satisfactorily reproduce the experimental data ($R^2 = 0.94$). The two-products model was not retained as it leads to high uncertainties on the values of α_i and $K_{om,i}$ (sometimes more than 100% error). The fitting parameters α and K_{om} corresponding to the one-product semi-empirical model are 0.32 ± 0.04 and $(4.2 \pm 1.0) \times 10^{-3} \text{ m}^3 \mu\text{g}^{-1}$, respectively. Many studies on SOAs yields from aromatic compounds have reported that the aerosol yields

data should be fitted assuming two hypothetical products (Odum et al., 1997; Song et al., 2005). However, a number of recent works have shown that the organic aerosol yields formed in aromatic photo-oxidation systems could be well described by assuming only one hypothetical product (Coeur-Tourneur et al., 2009, 2010a; Henry et al., 2008; Lauraguais et al., 2012, 2014a; Olariu et al., 2003; Takekawa et al., 2003). Although the organic aerosol-phase is often composed of many oxidation products, the present simulation with the one-product model indicates either that one semi-volatile organic compound is the major component of the condensed phase or that the few organics present in SOAs have similar α_i and $K_{om,i}$ values. In this latter case, the obtained constants α_i and $K_{om,i}$ would not have any intrinsic physical meaning but would rather represent mean values.

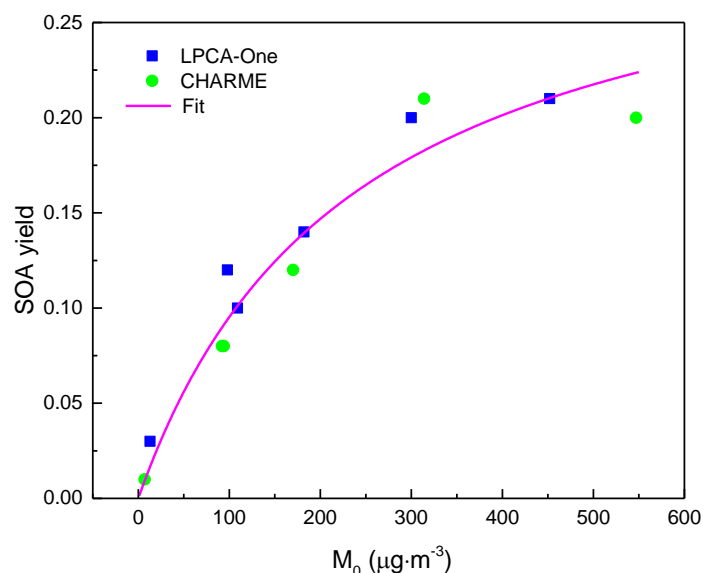


Fig. 3. Yield curve (SOA yield Y versus the organic aerosol mass formed M_0) for guaiacol/ NO_3 experiments in LPCA-One (blue squares) and in CHARME (green circles). The line represents the best fit to the data considering one semi-volatile major product. The fitting parameters used are $\alpha = 0.32 \pm 0.04$ and $K_{om} = (4.2 \pm 1.0) \times 10^{-3} \text{ m}^3 \mu\text{g}^{-1}$.

In their study on the reaction of guaiacol with OH performed under high NO_x conditions, Lauraguais et al. (2014a) reported a gas-particle partitioning equilibrium constant K_{om} of $(4.7 \pm 1.2) \times 10^{-3} \text{ m}^3 \mu\text{g}^{-1}$, which is very close to the value determined in

the present study for the reaction of guaiacol with NO_3 . So, it can be assumed that the products formed in the particle phase from the gas-phase oxidation of guaiacol with both oxidants have probably similar chemical compositions, including nitrate compounds. In contrast, the mass-based stoichiometric coefficient determined for the semi-volatile products formed from the reaction of guaiacol with OH ($\alpha = 0.83$) is more than twice the value of α obtained for the reaction with NO_3 . This suggests that the reaction products from guaiacol + OH are less volatile in general compared to those from guaiacol + NO_3 . This lower volatility makes them prone to go readily into the condensed phase.

It is interesting to compare α (0.32) to the slope in Fig. 2 (0.25). α represents the total amount of the semi-volatile products formed both in the gas- and aerosol- phases, whereas Y corresponds to the semi-volatile products that have been formed in the particle phase only. So, this suggests that about 80% of the low-volatile compounds formed in the guaiacol reaction with NO_3 radicals are transferred into the particle-phase.

3.2. SOA chemical composition

ESI-LC-QTOF-MS/MS analyses were performed to characterize the composition of the SOAs formed from the gas-phase reaction of NO_3 with guaiacol. A typical chromatogram is presented in Fig. 4. Once the molar mass of one product is determined (by LC-QTOF-MS), the corresponding peak is fragmented using three energy values (10 eV, 20 eV and 30 eV; MS/MS analysis). A higher energy value leads to a greater fragmentation of the molecules which allows to identify the functional groups and thus to assess the chemical structures of the compounds.

The compounds detected in the SOAs are listed in Table 2 (major compounds, relative abundance > 4 %) and Table S1 (minor compounds, relative abundance ≤ 2 %); the indicated masses correspond to the $[\text{M}-\text{H}]$ product ions. The relative abundances (expressed in %) were calculated from the ratio of the sum of the chromatographic peak areas of the different isomers to the total chromatographic peak area of all the peaks. This approach assumes that the mass spectrometer has the same response for every detected chemical compound.

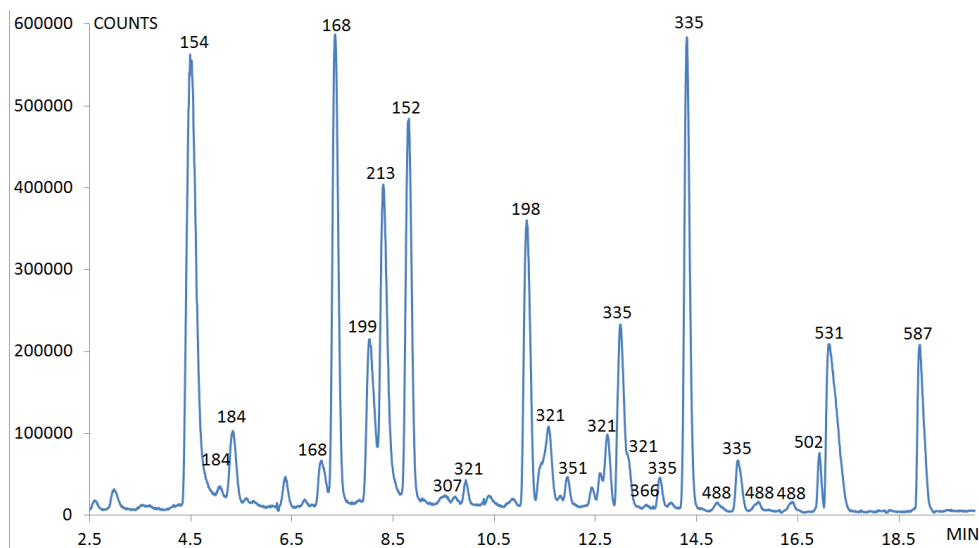
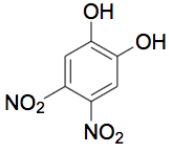
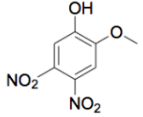
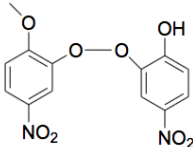
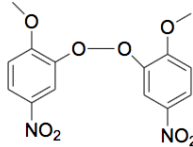


Fig. 4. Chromatogram (ESI-LC-QToF-MS/MS analysis) of the SOAs formed from the gas-phase reaction of guaiacol (2-methoxyphenol) with NO_3 radicals. The compounds corresponding to the labelled peaks are displayed in table 2. The indicated masses correspond to the $[\text{M}-\text{H}]^+$ product ions.

Table 2. Major compounds observed in the SOAs (ESI-LC-QToF-MS/MS analyses) formed from the gas-phase reaction of guaiacol with NO_3 radicals. The main fragments obtained by MS/MS analyses (see Fig.S1-S8 in Appendix I) and the relative abundances (R, in %) are also indicated.

Molecular ion ^a	Main fragments	Brut Formula	Name ^c	Structure ^f	R (%) ^g
152	46 $[\text{NO}_2]^-$ 93 $[\text{C}_6\text{H}_5\text{O}]^-$ 122 $[\text{C}_7\text{H}_6\text{O}_2]^-$	$\text{C}_7\text{H}_6\text{NO}_3^{\text{d}}$	Nitromethoxybenzene ₂		9.3
154	69 $[\text{C}_3\text{HO}_2]^-$ 95 $[\text{C}_5\text{H}_3\text{O}_2]^-$ 123 $[\text{C}_6\text{H}_3\text{O}_3]^-$	$\text{C}_6\text{H}_4\text{NO}_4^{\text{d}}$	Nitrocatechol ¹⁻²		18.0
168	95 $[\text{C}_5\text{H}_3\text{O}_2]^-$ 123 $[\text{C}_6\text{H}_3\text{O}_3]^-$ 153 $[\text{C}_6\text{H}_3\text{NO}_4]^-$	$\text{C}_7\text{H}_6\text{NO}_4^{\text{b}}$	Nitroguaiacol ⁴		11.7
197	76 $[\text{C}_5\text{H}_2\text{N}]^-$ 109 $[\text{CH}_5\text{N}_2\text{O}_4]^-$ 123 $[\text{C}_6\text{H}_5\text{NO}_2]^-$	$\text{C}_7\text{H}_5\text{N}_2\text{O}_5^{\text{c}}$	Dinitromethoxybenzene ₂		7.6

199	67 [C ₄ H ₃ O] ⁻ 95 [C ₅ H ₃ O ₂] ⁻ 153 [C ₆ H ₃ NO ₄] ⁻	C ₆ H ₃ N ₂ O ₆ ^b	Dinitrocatechol ³		4.7
213	66 [C ₃ NO] ⁻ 78 [C ₅ H ₂ O] ⁻ 198 [C ₆ H ₂ N ₂ O ₆] ⁻	C ₇ H ₅ N ₂ O ₆ ^b	Dinitroguaiacol ⁶		9.0
321	153 [C ₆ H ₃ NO ₄] ⁻ 168 [C ₇ H ₆ NO ₄] ⁻ 306 [C ₁₂ H ₆ N ₂ O ₈] ⁻	C ₁₃ H ₉ N ₂ O ₈ ^b	Association of 1 nitroguaiacol and 1 nitrocatechol ¹²		5.4
335	153 [C ₆ H ₃ NO ₄] ⁻ 168 [C ₇ H ₆ NO ₄] ⁻ 320 [C ₁₆ H ₆ N ₃ O ₅] ⁻	C ₁₄ H ₁₁ N ₂ O ₈ ^b	Association of 2 nitroguaiacols ⁵		18.1
531	-	-	-	-	8.2
587	-	-	-	-	4.3

^a The indicated masses correspond to the [M-H] product ions.

^b Probability given by the software between 98 and 100 %.

^c Probability given by the software between 90 and 97 %.

^d Probability given by the software between 70 and 89%.

^e Number of detected isomers.

^f The drawn structure correspond to one isomer only.

^g The relative abundances (in %) were calculated from the ratio of the sum of the chromatographic areas of the different isomers to the total chromatographic area of all the peaks.

The main compounds observed in the SOAs are nitrated aromatic compounds (see Table 2): nitromethoxybenzenes (m/z = 152, 2 isomers, 9.3%); nitrocatechol(s) (m/z = 154, 1 or 2 isomers (the peak width suggests the presence of two isomers, but this hypothesis could not be confirmed), 18.0%); nitroguaiacols (m/z = 168, 4 isomers, 11.7%); dinitromethoxybenzene (m/z = 197, 2 isomers, 7.6%); dinitrocatechols (m/z = 199, 3 isomers, 4.7%); dinitroguaiacols (m/z = 213, 6 isomers, 9.0%); dimeric compounds formed via the association of 1 nitroguaiacol and 1 nitrocatechol (m/z = 321, 12 isomers, 5.4%) or via the association of 2 nitroguaiacols (m/z = 335, 5 isomers, 18.1 %), and 2 unidentified compounds (m/z = 531, 8.2% and m/z = 584, 4.3%). So, this

confirms that the oxidation products formed in the aerosols from the reaction of NO_3 radicals with guaiacol are both first and second generation products, as suggested by the data shown in Fig. 1. However, as more than $\approx 75\%$ of the SOA mass is generated after complete depletion of guaiacol, it is highly probable that the aerosol products are formed through reactions in the gas-phase and/or in the condensed phase (in the chamber or on the filter during the sampling). Additional experiments using lower initial guaiacol concentrations would probably reduce potential reactions occurring in the condensed phase. Figures S1-S8 (see supporting information) display $[\text{M}-\text{H}]^+$ product ions MS/MS spectra obtained at 20 eV for the major compounds identified in the SOAs ($m/z = 152$, Fig. S1; $m/z = 154$, Fig. S2; $m/z = 168$, Fig. S3; $m/z = 197$, Fig. S4; $m/z = 199$, Fig. S5; $m/z = 213$, Fig. S6; $m/z = 321$, Fig. S7 and $m/z = 335$, Fig. S8). The different fragments allowed to propose consistent chemical structures for the oxidation products of NO_3 + guaiacol found in the particle phase.

The minor compounds detected in the aerosols are shown in Table S1.

Among the major reaction products, 4-nitroguaiacol and 5-nitroguaiacol were clearly identified by comparing their chromatographic retention times and their MS-MS spectra to those of standards commercially available. The most abundant nitroguaiacol formed in the particle phase was 4-nitroguaiacol (91.5%), in large excess compared to 5-nitroguaiacol (5.4%) and 3-nitroguaiacol and/or 6-nitroguaiacol (3.1% for both; the standards of these two isomers do not exist, so it was not possible to distinguish them).

The mechanism leading to the main oxidation products identified in the SOAs is proposed in Fig. 5. It has been postulated by Atkinson et al., (1992), that the NO_3 radical initiated reaction of aromatic compounds may first proceed by an ipso-addition to the OH substituent which forms a six-membered transition state intermediacy. A second mechanism starts with the electrophilic addition of the nitrate radical on the aromatic ring. These two ways lead to the formation of nitric acid and a phenoxy radical, which then react with NO_2 to produce nitroguaiacol isomers. Similarly, the formation of dinitroguaiacols and trinitroguaiacol can be explained by the reaction of nitroguaiacols with NO_3 and NO_2 .

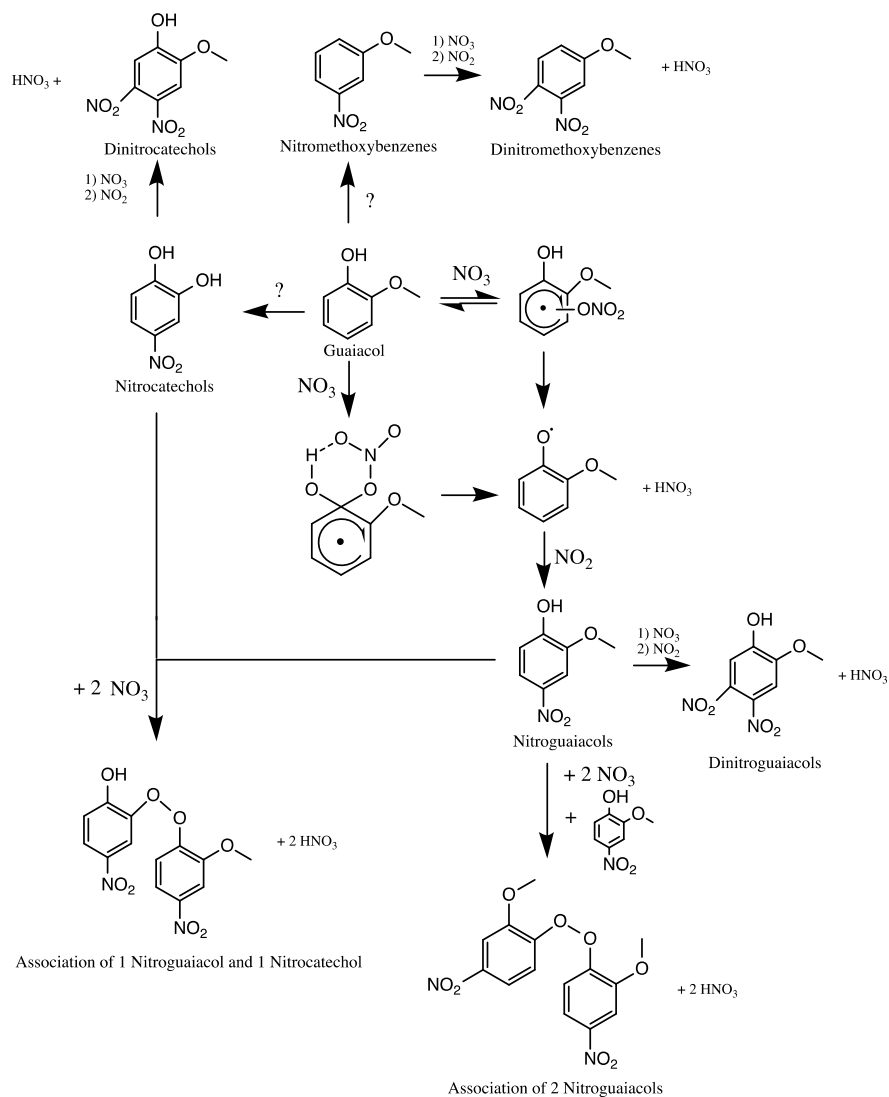


Fig.5. Detailed mechanism leading to the main products observed in the SOAs formed from the gas-phase reaction of guaiacol (2-methoxyphenol) with NO_3 radicals.

The initial oxidation steps starting from guaiacol and going to nitromethoxybenzenes and nitrocatechols are not known, as indicated in Fig. 5. Since the present gas-phase chemistry knowledge of aromatic compounds is not able to address these issues, we suggest that an oxidation chemistry could take place in the condensed phase and produce the observed nitromethoxybenzenes and nitrocatechols. Investigations of the liquid-phase guaiacol oxidation would be very useful to support this assumption. In their study on gas-phase reaction products of NO_3 + guaiacol, Yang et al. (2016) also reported the presence

of nitroguaiacols (4-nitroguaiacol and 6-nitroguaiacol; 4-nitroguaiacol being the most abundant), dinitroguaiacol (4,6-dinitroguaiacol), catechol (1,2-dihydroxybenzene) and nitromethoxybenzene in the products formed from the gas-phase of NO_3 reaction guaiacol. They also identified catechols from the oxidation of creosol (4-methyl-guaiacol) and syringol (6-methoxy-guaiacol). The formation of catechols was reported by Zhang et al. (2016) as well, who studied the reaction of eugenol (4-allyl-guaiacol) and ethyl-guaiacol with NO_3 radicals. The mechanism leading to catechols from guaiacol and its derivatives was not explained in both previous articles.

The formation of nitrocatechols and dinitrocatechols can then result from the reaction of NO_3 and NO_2 with catechol and nitrocatechols, respectively. The compounds with high molecular masses ($m/z > 300$) display 2 to 3 aromatic cycles; they can be produced from the combination of phenoxy radicals formed from nitroguaiacol(s) and/or nitrocatechol(s).

For the main identified products, one isomer was always more abundant than the others (the corresponding relative abundances vary from 85 % to 99 %; see table S2).

The oxidation products formed in the aerosols from the gas-phase reaction of guaiacol with nitrate radicals can also be compared to those identified for the reaction of guaiacol with hydroxyl radicals under high NO_x conditions (Ahmad et al., 2017). The ATR-FTIR analyses performed by Ahmad et al., (2017) also reveal the presence of 4-nitroguaiacol in the SOAs. So, this observation suggests that the oxidation products generated in the particulate phase, via the oxidation of guaiacol by NO_3 or OH/NO_x reaction, are probably similar as it has been previously postulated from the comparison of the gas-particle partitioning equilibrium constants ($K_{\text{om},i}$) obtained with both oxidants.

4. Conclusions

The formation of secondary organic aerosols from the reaction of guaiacol (2-methoxyphenol) with nitrate radicals has been studied in two simulation chambers. The SOAs yields have been shown to be influenced by the initial guaiacol concentration, which leads to aerosol yields ranging from 0.01 to 0.21. A very good agreement was observed between the experiments performed in both chambers which gives confidence in the data obtained in this study. The aerosols data have been fitted with the absorptive

gas-particle partitioning model developed by Pankow (1994a,b) and Odum et al. (1996) using the one-product model.

Aerosol organic carbon concentration is typically $5 \mu\text{g m}^{-3}$ in many environments, though it can occasionally rise to $50 \mu\text{g m}^{-3}$ or more in highly polluted areas. Extrapolating to a particle loading of $5 \mu\text{g m}^{-3}$ from the yield data (Fig. 3) gives a 2% SOA yield. Based on this result, one can infer that the contribution of the reaction between guaiacol and NO_3 radicals to SOAs production under atmospheric conditions is probably relatively minor. However, in polluted areas this reaction can be an important source of secondary aerosols.

ESI-LC-QToF-MS/MS analyses were performed to characterize the chemical composition of the aerosols. Nitro-aromatics compounds were identified as the main oxidation products, confirming previous studies (Yang et al., 2016; Zhang et al., 2016) on the products formed from the gas-phase reaction of NO_3 radicals with guaiacol derivatives.

A well-established tracer for primary biomass burning aerosols (BBA) is levoglucosan (1,6-anhydro- β -anhydroglucose), which originates from the pyrolysis of cellulose or hemicelluloses (Simoneit et al., 2002). Several nitro-aromatic compounds were detected in urban aerosols, and nitrocatechols as well as nitroguaiacols are recognized to be suitable tracers for secondary BBA (Iinuma et al., 2010; Kitanovsky et al., 2012). Further research efforts on the reactivity of these compounds would allow to measure their rate constants with the main oxidants and to determine the corresponding lifetimes. To our knowledge, only a few data are available in the literature concerning the atmospheric reactivity of nitro-aromatics (Bejan et al., 2007; 2015).

Acknowledgements

This work was supported by the CaPPA project (Chemical and Physical Properties of the Atmosphere) funded by the French National Research Agency (ANR-11-LABX-0005-01) and the CLIMIBIO program supported by the Hauts-de-France Regional

Council, the French Ministry of Higher Education and Research and the European Regional Development Fund.

References

- Atkinson, R., Carter, W.P.L., Plum, C.N., Winer, A.M., Pitts, J.N., 1984. Kinetics of the gas-phase reactions of NO₃ radicals with a series of aromatics at 296 ± 2 K. *Int. J. Chem.* 16, 887-898.
- Atkinson R., Aschmann S. M., Arey J, 1992. Reactions of hydroxyl and nitrogen trioxide radicals with phenol, cresols, and 2-nitrophenol at 296 ± 2 K. *Environ. Sci. Technol.* 26, 1397-1403.
- Ahmad, W., Coeur C., Tomas A., Fagniez T., Brubach J-B., Cuisset A., 2017. Infrared spectroscopy of secondary organic aerosol precursors and investigation of the hygroscopicity of SOA formed from the OH reaction with guaiacol and syringol. *Appl. Opt.*, 56, 116-122.
- Bejan, J., Barnes, I., Olariu, O., Zhou, S., Wiesen, P., Bentera, T., 2007. Investigations on the gas-phase photolysis and OH radical kinetics of methyl-2-nitrophenols. *Phys. Chem. Chem. Phys.*, 9, 5686-5692.
- Bejan, J., Duncianu, M., Olariu, O., Barnes, I., Seakins, P., Wiesen, P., 2015. Kinetic study of the gas-phase reactions of chlorine atoms with 2-chlorophenol, 2-nitrophenol, and four methyl-2-nitrophenol isomers. *J. Phys. Chem. A*, 2015, 20, 4735-4745.
- Bruns E.A. , Slowik J.G., El Haddad I., Kilic D., Klein F., Dommen J., Temime-Roussel B., Marchand N., Baltensperger U., Prévôt A.S.H. 2017. Characterization of gas-phase organics using proton transfer reaction time-of-flight mass spectrometry: fresh and aged residential wood combustion emissions. *Atmos. Chem. Phys.*, 17, 705-720.
- Calvert, J.G., Atkinson, R., Becker, K.H., Kamens, R.M., Seinfeld, J.H., Wallington, T.J., Yarwood, G., 2002. *The mechanisms of atmospheric oxidation of aromatic hydrocarbons*, Oxford University Press, New York, N.Y.
- Chen Y., Bond T.C., 2010. Light absorption by organic carbon from wood combustion. *Atmos. Chem. Phys.* 10, 1773–1787.
- Coeur-Tourneur, C., Tomas, A., Guilloteau, A., Henry, F., Ledoux, F., Visez, N., Riffault, V., Wenger, J.C., Bedjanian, Y., 2009. Aerosol formation yields from the reaction of catechol with ozone. *Atmos. Environ.* 43, 2360-2365.

- Coeur-Tourneur C., Cassez A., Wenger J.C., 2010a. Rate constants for the gas-phase reaction of hydroxyl radicals with 2-methoxyphenol (guaiacol) and related compounds, *J. Phys. Chem. A* 114, 11645-11650.
- Coeur-Tourneur C., Foulon V., Laréal M., 2010b. Determination of aerosol yields from 3-methylcatechol and 4-methylcatechol ozonolysis in a simulation chamber, *Atmos. Environ.* 44, 852-857.
- Derwent, R.G., Jenkin, M.E., Saunders, S., 1996. Photochemical ozone creation potentials for a large number of reactive hydrocarbons under European conditions. *Atmos. Environ.* 30, 181–199.
- Derwent, R.G., Jenkin, M.E., Saunders, S.M., Pillings, M. J., 1998. Photochemical ozone creation potentials for organic compounds in northwest Europe calculated with a master chemical mechanism. *Atmos. Environ.* 32, 2429–2441.
- El Zein, A., Coeur, C., Obeid, E., Lauraguais, A., Fagniez, T., 2015. Reaction kinetics of catechol (1,2-Benzenediol) and guaiacol (2-Methoxyphenol) with ozone. *J. Phys. Chem. A* 119, 6759-6765.
- Fourtziou L., Liakakou E., Stavroulas I., Theodosi C., Zarnpas P., Psiloglou B., Sciare J., Maggos T., Bairachtari K., Bougiatioti A., Gerasopoulos E., Sarda-Estève R., Bonnaire N., Mihalopoulos N. 2017. Multi-tracer approach to characterize domestic wood burning in Athens (Greece) during wintertime. *Atmos. Environ.*, 148, 89-101.
- Gurjar B.R., Molina L.T., Ojha C.S.P. 2010. *Air Pollution: Health and Environmental Impacts*. CRC Press Taylor & Francis Group.
- Hallquist M., Wenger J. C., Baltensperger U., Rudich Y., Simpson D., Claeys M., Dommen J., Donahue N. M., George C., Goldstein A. H., Hamilton J. F., Herrmann H., Hoffmann T., Iinuma Y., Jang M., Jenkin M. E., Jimenez J. L., Kiendler-Scharr A., Maenhaut W., McFiggans G., Mentel Th. F., Monod A., Prévôt A. S. H., Seinfeld J. H., Surratt J. D., R. Szmigielski R., Wildt J., 2009. The formation, properties and impact of secondary organic aerosol: current and emerging issues. *Atmos. Chem. Phys.* 9, 5155–5236.
- Hanson D.J., 1996. Toxics release inventory report shows chemical emissions continuing to fall. *Chem. Eng. News*, July 15, 29-30.
- Hays, M.D., Geron, C.D., Linna, K.J., Smith, N.D., Schauer, J. J., 2002. Speciation of gas-phase and fine particle emissions from burning of foliar fuels. *Environ. Sci. Technol.* 36, 2281-2295.

- Henry, F., Coeur-Tourneur, C., Ledoux, F., Tomas, A., Menu, D., 2008. Secondary organic aerosol formation from the gas phase reaction of hydroxyl radicals with m-, o- and p-cresol. *Atmos. Environ.* 42, 3035–3045.
- Hurley, M.D., Sokolov, O., Wallington, T.J., Takekawa, H., Karasawa, M., Klotz, B., Barnes, I., Becker, K.H., 2001. Organic aerosol formation during the atmospheric degradation of toluene. *Environ. Sci. Technol.* 35, 1358–1366.
- Iinuma, Y., Böge, O., Agräfe R., Herrmann H., 2010. Methyl-Nitrocatechols: Atmospheric tracer compounds for biomass burning secondary organic aerosols. *Environ. Sci. Technol.*, 44, 8453-8459.
- Kitanovsky, Z., Grgi, I., Yasmeen, F., Claeys, M., A., 2012. Development of a liquid chromatographic method based on ultraviolet-visible and electrospray ionization mass spectrometric detection for the identification of nitrocatechols and related tracers in biomass burning atmospheric organic aerosol, *Rapid Commun. Mass Sp.*, 26, 793-804.
- Langmann, B., Duncan, V., Textor, C., Trentmann, J., van der Werfe, G.R., 2009. Vegetation fire emissions and their impact on air pollution and climate. *Atmos. Environ.* 43, 107-116
- Lauraguais, A., Coeur-Tourneur, C., Cassez, A., Seydi, A., 2012. Rate constant and secondary organic aerosol yields for the gas-phase reaction of hydroxyl radicals with syringol (2,6-dimethoxyphenol). *Atmos. Environ.* 55, 43-48.
- Lauraguais, A., Bejan, I., Coeur-Tourneur, C., Cassez, A., Deboudt, K., Fourmentin, M., Chođ, M., 2014a. Atmospheric reactivity of hydroxyl radicals with guaiacol (2-methoxyphenol), a biomass burning emitted compound: secondary organic aerosol formation and gas-phase oxidation products. *J. Phys. Chem. A* 86, 155-163.
- Lauraguais, A., Bejan, I., Barnes, I., Wiesen, P., Coeur-Tourneur, C., Cassez, A., 2014b. Rate coefficient for the gas-phase reaction of chlorine atoms with a series of methoxylated aromatic compounds. *J. Phys. Chem. A* 118, 1777-1784.
- Lauraguais, A., Bejan, I., Barnes, I., Wiesen, P., Coeur, C., 2015. Rate coefficients for the gas-phase reaction of hydroxyl radicals with a series of methoxylated aromatic compounds. *J. Phys. Chem. A* 119, 6179-6187.
- Lauraguais, A., El Zein, A., Coeur, C., Obeid, E., Rayez, M-T., Rayez, J-C., 2016. Rate coefficient for the gas-phase reaction of nitrate radicals with a series of methoxyphenol compounds: experimental and theoretical approaches. *J. Phys. Chem. A*, 120, 2691-2699 (2016).

- Lelieveld, J., Crutzen, P.J., Ramanathan, V., Andreae, M.O., Brenninkmeijer, C.A.M., Campos, T., Cass, G.R., Dickerson, R.R., Fischer, H., de Gouw, J.A., Hansel, A., Jefferson, A., Kley, D., de Laat, A.T.J., Lal, S., Lawrence, M.G., Lobert, J.M., Mayol-Bracero, O.L., Mitra, A.P., Novakov, T., Oltmans, S.J., Prather, K.A., Reiner, T., Rodhe, H., Scheeren, H.A., Sikka, D., Williams, J., 2001. The Indian ocean experiment: widespread air pollution from South and Southeast Asia. *Science* 291, 1031-1036.
- Lighty, J.S., Veranth, J.M., Sarofim, A.F., 2000. Combustion aerosols: factors governing their size and composition and implications to human health. *J. Air Waste Manag.* 50, 1565-1618.
- Mazzoleni, L.R., Zielinska, B., Moosmüller, H., 2007. Emissions of levoglucosan, methoxyphenols, and organic acids from prescribed burns, laboratory combustion of wildland fuels, and residential wood combustion. *Environ. Sci. Technol.* 41, 2115-2122.
- McDonald, J.D., Zielinska, B., Fujita, E.M., Sagebiel, J.C., Chow, J.C., Watson, J.G., 2000. Fine particle and gaseous emission rates from residential wood combustion. *Environ. Sci. Technol.* 34, 2080-2091.
- Odum, J.R., Hoffmann, T., Bowman, F.M., Collins, D., Flagan, R.C., Seinfeld, J.H., 1996. Gas/particle partitioning and secondary organic aerosol yields. *Environ. Sci. Technol.* 3, 2580-2585.
- Odum, J.R., Jungkamp, T.P.W., Griffin, R.J., Forstner, H.J.L., Flagan, R.C., Seinfeld, J.H., 1997. Aromatics, reformulated gasoline, and atmospheric organic aerosol formation. *Environ. Sci. Technol.* 31, 1890–1897.
- Olariu, R.I., Tomas, A., Barnes, I., Wirtz, K., 2003. Atmospheric ozone degradation reaction of 1,2-dihydroxybenzene: aerosol formation study. In: *The European Photoreactor EUPHORE, fourth report 2001*. Ed. Institute of Physical Chemistry, Bergische Universität Wuppertal, Germany, 54–71.
- Pankow, J.F., 1994a. An absorption model of gas/particles partitioning of organic compounds in the atmosphere. *Atmos. Environ.* 28, 185–188.
- Pankow, J.F., 1994b. An absorption model of the gas/aerosol partitioning involved in the formation of secondary organic aerosol. *Atmos. Environ.* 28, 189–193.
- Sarigiannis D.A., Karakitsios S.P., Kermenidou, M.V. 2015. Health impact and monetary cost of exposure to particulate matter emitted from biomass burning in large cities. *Sci. Total Environ.*, 15, 319-330.

- Schauer, J.J., Kleeman, M.J., Cass, G.R., Simoneit, B.R.T., 2001. Measurement of emissions from air pollution sources. 3. C₁-C₂₉ organic compounds from fireplace combustion of wood. *Environ. Sci. Technol.* 35, 1716-1728.
- Simoneit, B. R. T., 2002. Biomass burning - a review of organic tracers for smoke from incomplete combustion. *Appl. Geochem.* 17, 129-162.
- Simpson, C.D., Paulsen, M., Dills, R.L., Liu, L.J.S., Kalman, D.A., 2005. Determination of methoxyphenols in ambient atmospheric particulate matter: tracers for wood combustion. *Environ. Sci. Technol.* 39, 631-637.
- Song, C., Na, K., Cocker, D.R., 2005. Impact of the hydrocarbon to NO_x ratio on secondary organic aerosol formation. *Environ. Sci. Technol.* 39, 3143-3149.
- Takekawa, H., Minoura, H., Yamazaki, S., 2003. Temperature dependence of secondary organic aerosol formation by photo-oxidation of hydrocarbons. *Atmos. Environ.* 37, 3413-3424.
- Yang, B., Zhang, H., Wang, Y., Zhang P., Shu, J., Sun, W., Ma, P., 2016. Experimental and theoretical studies on gas-phase reactions of NO₃ radicals with three methoxyphenols: guaiacol, creosol, and syringol. *Atmos. Environ.*, 125, 243-251.
- Zhang H., Yang, B., Wang, Y., Shu, J., Zhang, P., Ma, P., Li, Z. 2016. Gas-phase reactions of methoxyphenols with NO₃ radicals: kinetics, products, and mechanisms. *J. Phys. Chem. A*, 120, 1213-1221.

Appendix III Airticle 2

Published in *Optics Letters*, 2020, 45(7): 1611-1614.

Incoherent broadband cavity enhanced absorption spectroscopy (IBBCEAS)-based strategy for direct measurement of aerosol extinction in lidar blind zone

Lingshuo Meng,^{1,2} Gaoxuan Wang,¹ Patrick Augustin,^{1,5} Marc Fourmentin,¹ Qian Gou,^{3,*} Eric Fertein,¹ Tong Nguyen Ba,¹ Cécile Coeur,¹ Alexandre Tomas,² Weidong Chen^{1,4}

¹ *Laboratoire de Physico-Chimie de l'Atmosphère, Université du Littoral Côte d'Opale, Dunkerque 59140, France*

² *IMT Lille Douai, Univ. Lille, SAGE – Sciences de l'Atmosphère et Génie de l'Environnement, 59000 Lille, France*

³ *Department of Chemistry, School of Chemistry and Chemical Engineering, Chongqing University, Chongqing 401331, China*

⁴ email: chen@univ-littoral.fr

⁵ email: augustin@univ-littoral.fr

*Corresponding authors: qian.gou@cqu.edu.cn

Abstract

In this Letter, the development of a custom-designed incoherent broadband cavity enhanced absorption spectrometer (IBBCEAS) and its application to *in situ* measurement of aerosol extinction near ground surface is described, in an effort to address the issue of missing data in the lidar blind zone in the first hundreds of meters of the observation range. Combined measurements of aerosol extinction at the same location using lidar remote sensing and *in situ* IBBCEAS operating in the UV spectral region around 370 nm showed results with a good correlation ($R^2=0.90$) between the two measurement techniques. This work highlights a new strategy for near-end lidar calibration, using a ground-based compact and robust IBBCEAS located at the lidar measurement site, to determine the vertical profile of the aerosol extinction coefficient with a higher accuracy.

Atmospheric aerosols show a considerable and growing interest due to their effects on regional air quality and global climate change, through their direct or indirect effects [1] impacting cloud formation and hydrological cycle [2], or modifying the radiation balance [3]. Due to the layering of the atmosphere, a large negative vertical gradient of aerosol concentration is often observed between the Earth's surface and the first kilometers of the troposphere. Knowledge of the aerosol vertical distribution is crucial for meteorological and atmospheric chemistry models, and thus for forecasting and warning of air pollution events.

Aerosol lidars (light detection and ranging) are used for remote sensing of atmospheric aerosols through the measurements of backscattered light from nanosecond laser pulses emitted into the atmosphere. Atmospheric backscattering and extinction coefficients, which are correlated to particle concentrations, are retrieved from the backscattering lidar signals. Various lidar techniques have been developed to deduce spatial aerosol optical properties from standard elastic backscatter lidar, such as multiangle lidar method [4], stable near-end solution [5] or Fernald-Klett inversion method [6]. However, due to incomplete geometric overlap between laser emission beam and the field of view (FOV) of receiver telescope in the near range [7], retrieval of aerosol optical properties using lidar is restricted in this blind zone in the first lowest hundreds of meters of the atmosphere. The measurement of aerosol distributions near ground is, however, crucial because of various ground surface emission sources (industries, traffic, fires, *et al.*) and their potential effects on human health [8]. This issue could be partially addressed by measuring the overlap function or adjusting the alignment for near and far range measurements. In the past decades, the lidar blind zone has been reduced from several kilometers (micro pulse lidar, MPL) to a few hundreds of meters (approximately 200 m for ALS300 LIDAR, Leosphere) [9] by enlarging the FOV with optimized optical design, which almost reaches the instrumental limit. Considerable endeavors have been conducted through experimental methods [10] or analytical approaches [11,12]. For the missing informations in the blind zone near the ground surface, indirect *in situ* measurement of scattering or extinction coefficient would be supportive for extracting aerosol optical parameter as well as for determination of the solution boundary value from the near-end inversion method or for the correction of

aerosol's optical depth in the blind zone [5]. Nephelometer [13,14] is the most commonly used instrument for the measurement of aerosol concentrations using light scattering to provide supplementary near ground data.

In this letter, a new alternative method is proposed to directly measure aerosol extinction near the ground surface, instead of aerosol scattering, which would be possible to apply in the lidar's blind zone to obtain extra aerosol information. Optical methods have been widely used to measure aerosol extinction, such as multi-axis differential optical absorption spectroscopy (MAX-DOAS) [15,16] for long path measurements, and cavity attenuated phase shift (CAPS) [17,18], cavity ring-down spectroscopy (CRDS) [19,20] and incoherent broadband cavity enhanced absorption spectroscopy (IBBCEAS) [19,21] for local point measurements. But, to our knowledge, no measurement of aerosol extinction by IBBCEAS near ground surface in synergy with lidar remote sensing has been previously reported. In the present work, an custom-designed IBBCEAS-based instrument coupled to a broadband UV light emitting diode (LED) was developed for measuring aerosol extinction over a relatively large spectral band (355-380 nm) with high spatial resolution. The IBBCEAS method, first introduced by Fiedler and co-worker in 2003 [22], eliminates the need for optical mode matching and electronic locking of the cavity resonant mode to the laser wavelength, as required for CRDS. In addition, IBBCEAS does not require particular optical alignment as needed for CRDS. All of these make IBBCEAS device rather simple, stable and robust, very suitable and attractive for field-campaign measurements [23].

The objective of the present work is to compare the aerosol extinction measured by *in situ* IBBCEAS with that measured by lidar remote sensing at the same location near ground surface.

A LED-based IBBCEAS operating in the UV range of 355-380 nm (UV LED-IBBCEAS) was designed and developed (Figure 1). Two high reflectivity mirrors (Layertec) were used to form a linear high finesse optical cavity. The used LED (Nichia, NCSU033AT) provided ~250 mW optical power around 370 nm with a full width at half maximum (FWHM) of ~15 nm. The LED temperature and current were controlled and stabilized with a laser diode controller (LDC501, Stanford Research System). Spectral

signal from the cavity was recorded using a grating spectrometer (QE65000, Ocean Optics) with a spectral resolution of ~ 0.53 nm.

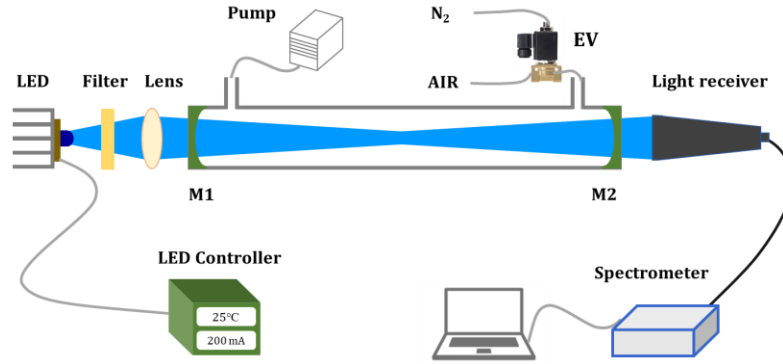


Figure 1 Schematic diagram of the developed UV LED-IBBCEAS setup. M1, M2 : cavity mirrors; EV: electronic valve.

In IBBCEAS measurement approach, gas absorption $\alpha_{\text{abs.gas}}(\lambda)$ and aerosols extinction $\alpha_{\text{ext.aerosol}}(\lambda)$ from air samples can be determined through the following equation [24]:

$$\left(\frac{1-R(\lambda)}{d} + \alpha_{\text{Ray.N}_2}(\lambda) \right) \times \left(\frac{I_0(\lambda) - I(\lambda)}{I(\lambda)} \right) = \sum_i n_i \times \sigma_i(\lambda) + P(\lambda) \quad (1)$$

where $I(\lambda)$ and $I_0(\lambda)$ are the transmitted light intensities with air samples and with nitrogen N_2 (for baseline) inside the cavity, respectively; $R(\lambda)$ is the mirror reflectivity, d (cm) is the distance between two cavity mirrors and $\alpha_{\text{Ray.N}_2}(\lambda)$ is the Rayleigh scattering coefficient of N_2 . The 1st term on the right-hand side is related to $\alpha_{\text{abs.gas}}(\lambda)$ based on the Lambert-Beer law:

$$\sum_i n_i \times \sigma_i(\lambda) = \alpha_{\text{abs.gas}}(\lambda) \quad (2)$$

where n_i and σ_i are the number concentration and the reference cross section for the i^{th} gas species, respectively. Whereas the 2nd term $P(\lambda)$ is a polynomial function used to account for the sum of aerosol extinction $\alpha_{\text{ext.aerosol}}(\lambda)$ and variation in the spectral baseline $\alpha_{\text{baseline}}(\lambda)$:

$$P(\lambda) = \alpha_{\text{ext.aerosol}}(\lambda) + \alpha_{\text{baseline}}(\lambda) \quad (3)$$

Based on the IBBCEAS measurements, trace gas concentration n_i and aerosol extinction $\alpha_{\text{ext.aerosol}}(\lambda)$ can be simultaneously retrieved by fitting the experimental data (left-hand of Eq. (1)) to reference cross-section $\sigma_i(\lambda)$ and the polynomial function $P(\lambda)$ (right-hand of Eq. (1)).

As shown in Eq. (1), cavity mirror reflectivity must be firstly determined over the whole working wavelength range for accurate quantitative analysis. In the present work, the mirror reflectivity $R(\lambda)$ was determined from a known concentration (361 ppb) of nitrogen dioxide (NO_2) by rearranging Eq. (1) as follows:

$$R(\lambda) = 1 - d \times \left(\frac{n_{\text{NO}_2} \sigma_{\text{NO}_2}(\lambda) \cdot I(\lambda)}{I_0(\lambda) - I(\lambda)} - \alpha_{\text{Ray.N}_2}(\lambda) \right) \quad (4)$$

Figure 2(a) shows the reference absorption cross sections of NO_2 around 365 nm reported by Burrows et al. [25]. Figure 2(b) displays the experimentally determined mirror reflectivity in association with the LED emission spectrum. The maximum mirror reflectivity was $\sim 99.84\%$ at 374.5 nm, leading to an effective optical length of ~ 860 m.

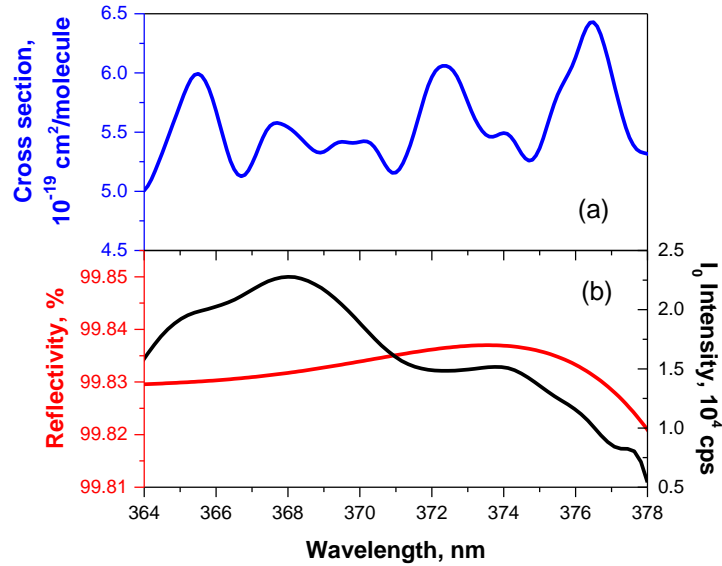


Figure 2 (a): NO_2 absorption cross sections from 364 nm to 378 nm; (b): cavity mirror reflectivity and LED emission spectrum.

As indicated by Eq. (3), the knowledge of baseline variation $\alpha_{\text{baseline}}(\lambda)$ over time is crucial for accurately retrieving aerosol extinction $\alpha_{\text{ext.aerosol}}(\lambda)$. In the current work,

spectral baseline was regularly measured with the following protocol: 6-min measurement with pure N₂ (for baseline) and 24-min measurement with air sample, switching controlled by an electronic valve. N₂ or ambient air was continuously sampled, at a flow rate of 2 L/min, into the IBBCEAS cavity working at atmospheric pressure.

A representative case of data retrieval is shown in Figure 3, which depicts measured (black circles) and fitted (red curve) spectra of 10.8 ppb NO₂ in air containing aerosols. The acquisition time for each spectrum was 60 s (average of 100 spectra with 0.6 s of integration time per spectrum). Wavelength-dependent aerosol extinction coefficients $\alpha_{\text{ext.aerosol}}(\lambda)$ (orange line) were deduced from the subtraction of regularly measured $\alpha_{\text{baseline}}(\lambda)$ (green line) from the fitted polynomial function $P(\lambda)$, as shown in Eq. (3).

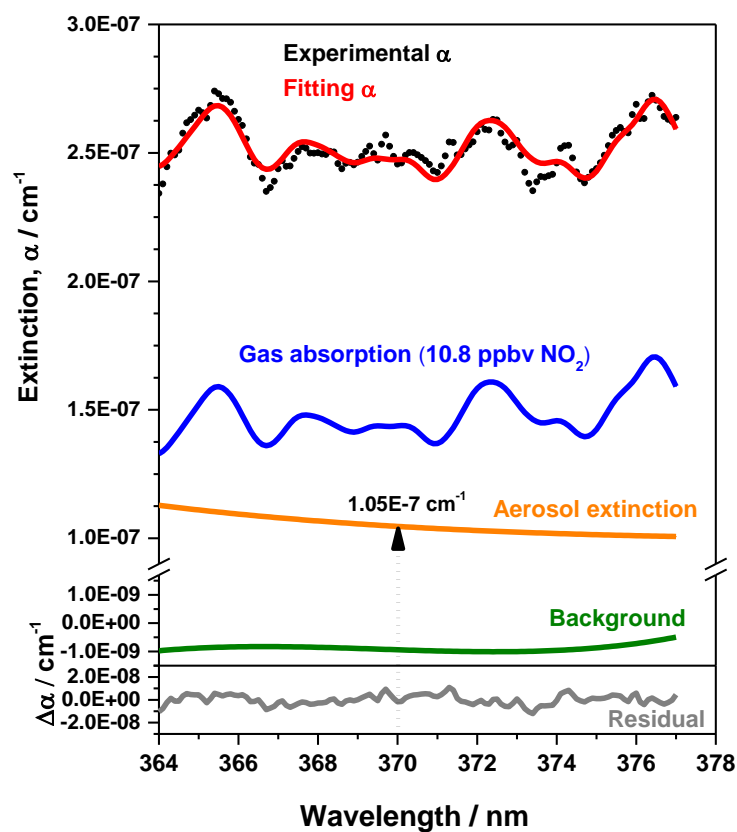


Figure 3 Typical data retrieval of NO₂ (10.8 ppb) and wavelength-dependent aerosol extinction coefficients ($1.05 \times 10^{-7} \text{ cm}^{-1}$ at 370 nm) from a measured IBBCEAS spectrum of ambient air.

Based on the standard deviation of the fit residual, a minimum detectable extinction coefficient of $4.3 \times 10^{-9} \text{ cm}^{-1}$ and a minimum detectable NO_2 concentration of 1.5 ppb were deduced. The aerosol extinction measured at 370 nm by the UV LED-IBBCEAS (where NO_2 absorption is relatively small) was used for comparison with the measurement by lidar.

Combined measurements of aerosol extinction at the same location (as illustrated in Figure 4) near ground surface were performed using lidar remote sensing and IBBCEAS *in situ* monitoring. An inter-comparison campaign was organized at the end of 2018 summer in a urban and industrialized coastal area (Dunkirk, North France). A 355 nm (pulsed tripled Nd:YAG laser) scanning lidar (ALS300, LEOSPHERE) [26] was deployed in combination with the custom-made UV LED-IBBCEAS instrument operating around 370 nm.

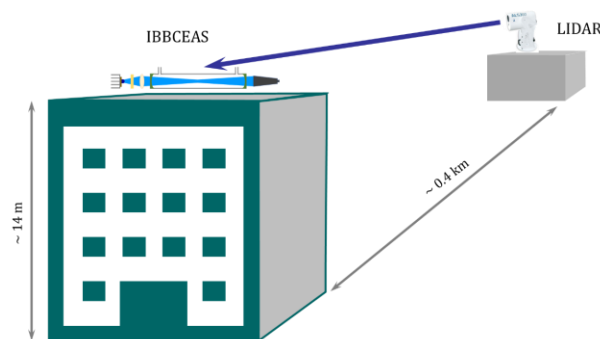


Figure 4 Schematic of combined measurements of aerosol extinction near ground surface. The lidar system is located in a truck situated at ground level and the UV LED-IBBCEAS system is kept in a shelter on the roof of a ~14 m high building. The horizontal distance between the two instruments was ~ 0.4 km.

The lidar-derived aerosol extinction coefficients and those simultaneously measured by the UV LED-IBBCEAS are plotted in Figure 5(a). The measurements were carried out in the morning of 14th September 2018 from 9:30 to 11:30.

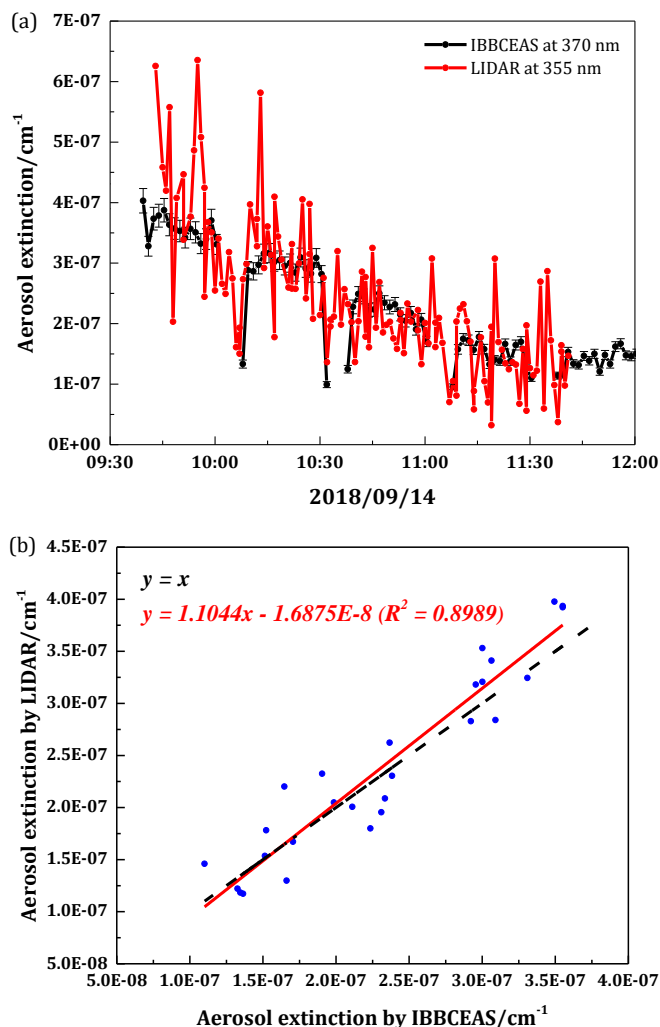


Figure 5 (a) Time-series measurements of aerosol extinctions by lidar (red) and by UV LED-IBBCEAS (black); (b) Correlation plot of time-series measurement results. Time resolutions for the lidar and the IBBCEAS measurements are 1.5 min and 1 min, respectively. Time resolution for the correlation plot is 3 min.

A good agreement with a correlation coefficient $R^2=0.90$ (Figure 5(b)) was obtained between the aerosol extinctions measured using the two different techniques. Both results have a consistent variation tendency during the sampling period.

Some discrepancies were however observed between 09:40 and 10:00. The strongest fluctuations measured with lidar can be explained by the fact that its measurements were performed over a 400-m open-path which could be significantly influenced by the ambient meteorological conditions (RH, wind direction, wind speed, etc), while the UV

LED-IBBCEAS sampled local air into its optical cavity for the measurement, which led to more stable measurement conditions.

In conclusion, a LED-based IBBCEAS operating around 370 nm wavelength was developed in an effort to address the issue of missing data in the lidar blind zone (lowest hundreds of meters of the atmosphere). Combined measurements of aerosol extinction coefficients have been performed using lidar remote sensing and IBBCEAS *in situ* monitoring at the same location near ground surface. Good correlation ($R^2=0.90$) between the data obtained with these two different measurement techniques were obtained. This result demonstrates the potential of using the aerosol extinction data measured by IBBCEAS, being located close to the lidar measurement site, for near-end lidar calibration to compensate for missing data in its blind zone, in particular near ground surface. It would be useful to refine lidar signal inversion and thus to improve the reliability and accuracy of atmospheric aerosol data. The present work also shows the interest of developing a low-cost, compact and robust IBBCEAS instrument (currently not commercially available) for UAV-borne measurements to determine the vertical profile of the lidar ratio for near-end calibration.

Funding. The CaPPA project (ANR-10-LABX005), the National Natural Science Foundation of China (Grant Nos. 21703021 and U1931104), the BQR program from the ULCO, the regional CPER IRENE and CLIMIBIO programs.

Disclosures. The authors declare no conflicts of interest.

References

1. B. H. Samset, C. W. Stjern, E. Andrews, R. A. Kahn, G. Myhre, M. Schulz, and G. L. Schuster, *Curr. Clim. Change Rep.* **4**, 83 (2018).
2. V. Ramanathan, P. Crutzen, J. T. Kiehl, and D. Rosenfeld, *Science* **294**, 2124 (2001).
3. R. Zhang, K. Ho, and Z. Shen, *Atmos. Sci. Lett.* **5**, 161 (2011).

4. M. Adam, V. A. Kovalev, C. Wold, J. Newton, M. Pahlow, W. M. Hao, M. B. Parlange, *J. Atmos. Ocean. Technol.* **24**, 2014 (2007).
5. A. Kovalev, *Appl. Opt.* **42**, 585 (2003).
6. A. Comerón, C. Muñoz-Porcar, F. Rocadenbosch, A. Rodríguez-Gómez, and M. Sicard, *Sensors* **17**, 1450 (2017).
7. G. Sun, L. Qin, Z. Hou, X. Jing, F. He, F. Tan, and S. Zhang, *Opt. Express* **26**, 7436 (2018).
8. T. Shiina, in *Asia Communications and Photonics Conference and Exhibition 2011* (Optical Society of America, 2011), 1-6.
9. S. Lolli, L. Sauvage, S. Loaec, and M. Lardier, *Opt. Pura. Appl.* **44**, 41 (2011).
10. W. Gong, F. Mao, and J. Li, *Opt. Commun.* **284**, 2971 (2011).
11. R. Chen, Y. J. L. Wen, and D. Wen, *Appl. Opt.* **56**, 4645 (2017).
12. U. Wandinger and A. Ansmann, *Appl. Opt.* **41**, 514 (2002).
13. A. Mariana, M. Pahlow, V. Kovalev, M. Parlange, and N. Nair, *J Geophys. Res. Atmos.* **109**, D16 (2004).
14. W. R. Espinosa, L. A. Remer, O. Dubovik, L. Ziemba, A. Beyersdorf, D. Orozco, G. Schuster, T. Lapyonok, D. Fuertes, and J. Martins, *Atmos. Meas. Tech.* **10**, 824 (2017).
15. P. Zieger, E. Weingartner, J. Henzing, M. Moerman, G. de Leeuw, J. Mikkilä, M. Ehn, T. Petäjä, K. Cléner, M. van Roozendaal, S. Yilmaz, U. Frieß, H. Irie, T. Wagner, R. Shaiganfar, S. Beirle, A. Apituley, K. Wilson, and U. Baltensperger, *Atmos. Chem. Phys.* **11**, 2624 (2011).
16. Z. Davis, U. Frieß, K. B. Strawbridge, M. Aggarwaal, S. Baray, E. G. Schnitzler, A. Lobo, V. E. Fioletov, I. Abboud, C. A. McLinden, J. Whiteway, M. D. Willis, A. K. Y. Lee, J. Brook, J. Olfert, J. O'Brien, R. Staebler, H. D. Osthoff, C. Mihele, and R. McLaren, *Atmos. Meas. Tech. Discuss.* <https://doi.org/10.5194/amt-2019-296>
17. A. Petzold, T. Onasch, P. Kebabian, and A. Freedman, *Atmos. Meas. Tech.* **6**, 1151 (2013).
18. R. M. Varma, S. M. Ball, T. Brauers, H. P. Dorn, U. Heitmann, R. L. Jones, U. Platt, D. Pöhler, A. A. Ruth, A. J. L. Shillings, J. Thieser, A. Wahner, and D. S. Venables, *Atmos. Meas. Tech.* **6**, 3130 (2013).
19. A. W. Strawa, R. Elleman, A. G. Hallar, D. Covert, K. Ricci, R. Provencal, T. W. Owano, H. H. Jonsson, B. Schmid, A. P. Luu, K. Bokarius, and E. Andrews, *J. Geophys. Res.* **111**, D05 (2006).

20. T. D. Gordon, N. L. Wagner, M. S. Richardson, D. C. Law, D. Wolfe, E. W. Eloranta, C. A. Brock, F. Erdesz, and D. M. Murphy, *Aerosol Sci. Tech.* **49**, 726 (2015).
21. W. Zhao, M. Dong, W. Chen, X. Gu, C. Hu, and X. Gao, W. Huang, and W. Zhang, *Anal. Chem.* **85**, 2260 (2013).
22. S. E. Fiedler, A. Hese, and A. A. Ruth, *Chem. Phys. Lett.* **371**, 294 (2003).
23. H. Yi, T. Wu, G. Wang, W. Zhao, E. Fertein, C. Coeur, X. Gao, W. Zhang, and W. Chen, *Opt. Express* **24**, A790 (2016).
24. G. Wang, "Development of photonic instruments for measurement of Aerosol optical properties", PhD thesis, Université Littoral Côte d'Opale, France (2018).
25. J. Burrows, A. Dehn, B. Deters, S. Himmelmann, A. Richter, S. Voigt, and J. Orphal, *J. Quant. Spectrosc. & Radiat. Transfer* **60**, 1031 (1998).
26. N. Boyouk, J. L. ón, H. Delbarre, P. Augustin, and M. Fourmentin, *Atmos. Res.* **101**, 910 (2011).